

CHEMICALLY TUNED VIRUS LIKE PARTICLES: FROM CANCER THERAPY TO
TARGETED DELIVERY

by

Arezoo Shahriarkevishahi

APPROVED BY SUPERVISORY COMMITTEE:

Dr. Jeremiah J. Gassensmith, Chair

Dr. Jie Zheng

Dr. Sheel C. Dodani

Dr. Jung-Mo Ahn

Copyright 2021

Arezoo Shahrivarkevishahi

All Rights Reserved

To my husband, Khashayar Rajabimoghadam and my family

CHEMICALLY TUNED VIRUS LIKE PARTICLES: FROM CANCER THERAPY TO
TARGETED DELIVERY

by

AREZOO SHSHRIVSRKEVISHAHI, MS

DISSERTATION

Presented to the Faculty of
The University of Texas at Dallas
in Partial Fulfillment
of the Requirements
for the Degree of

DOCTOR OF PHILOSOPHY IN
CHEMISTRY

THE UNIVERSITY OF TEXAS AT DALLAS

December 2021

ACKNOWLEDGMENTS

I would like to first thank my advisor, Dr Jeremiah Gassensmith, for all his continued support, guidance, and encouragement throughout the years. He always had confidence in my abilities and gave me the opportunity to plan and execute the research I wanted to do and supported me through all the difficulties I came across. He encouraged me to always pursue my goals and supported me through my internships time. He was always available, always there, always listened and always cared. He cheered me up when I was feeling down after failing in an experiment or an interview or whatever personal problems I had. He and his wife Katie never let me feel away from home. They always invited us over to celebrate holidays and were with us in all difficult days too. Without his trust, support and encouragement this journey would be impossible. (Thank you Jeremiah).

I would also like to thank my committee members, Dr. Sheel Dodani, Dr. Jie Zheng and Dr. Jung-Mo Ahn. Your guidance, comments, and advice taught me to think critically and shaped my technical and scientific ability to convey science in a direct and approachable manner.

I am thankful for my extraordinary lab members, who became my best friends. You always supported me with your kindness, love, and amazing science and didn't let me to give up on tough days. I was so lucky having you guys in my life these past years and I will miss all of you. I would also like to give thanks to my wonderful and talented undergraduate researchers Chayton Alisia Tumac, Abhinay Adlooru and Sindhu Ponnampallil for all your help. Finally, I wish to thank my husband, Khashayar, for all his love and support throughout this difficult journey. He always was there for me, helped me to stay motivated and follow my dream and never let me feel alone. Thank you so much Khash for your patience and endless support. I also would like to say thanks to my family and friends for their love and support throughout the time it took to finish this journey.

November 2021

CHEMICALLY TUNED VIRUS LIKE PARTICLES: FROM CANCER THERAPY TO TARGETED DELIVERY

Arezo Shahriarkevisahi, PhD
The University of Texas at Dallas, 2021

Supervising Professor: Jeremiah J. Gassensmith

In recent years, nanoparticle-based therapeutics have been increasingly applied in broad range of clinical applications from diagnosis to treatment of many diseases such as cancer, diabetes and neurodegenerative disorders. A wide range of synthetic and naturally occurring materials such as polymers, metal oxides, silicate, liposome, and carbon nanotubes have been developed to overcome some of the key barriers in free therapeutics including intracellular trafficking, cell/tissue targeting, poor biodistribution, and low efficiency. However, despite all achievements in creating these nanomaterials with different chemical and physical properties such as size, shape and surface properties, developing a nanoparticle to surmount these limitations all in one is a big challenge. Virus like particle (VLP) as protein-based nanomaterials that closely mimic the highly symmetrical and polyvalent conformation of viruses while lack the viral genomes have emerged as a solution for these limitations. Their unique features such as high biocompatibility, biodegradability, monodispersity, intrinsic immunogenicity, and safety combined with interior and exterior modification capability offer new tool to scientists for careful design and engineering of multi-component therapeutic agent with intended biological behavior and pharmacological

profiles. Herein, various chemistry strategies are introduced in combination with biology and immunology to turn virus like particle to a favorable engineered biomaterial for several functions such as cancer therapy and intracellular delivery. We showed how by modifying surface of VLP Q β with NIR organic molecule we can make a highly efficient and stable photothermal agent that can cause thermal ablation of tumor while simultaneously activating the immune response. We found this immunophotothermal agent, suppress primary tumor, control metastasis, and prolong survival time in mice bearing breast cancer. We also addressed one of the biggest challenges in biologic delivery which is direct delivery of therapeutic cargo into cell cytoplasm. Using organic chemistry we designed a cytosolic targeting linker that when attached to surface of VLP Q β , helps to escape endosomes and be released into cytoplasm, Moreover, this proteinaceous material is shown to have a great potential in combination with other materials such as metal organic framework to construct a multimodal cancer therapeutic agent enabling delivering multiple therapeutic agents such as immunotherapeutic drugs while taking advantage of all unique features of virus like particles. These works clearly show the significant potential of VLP in design and modification of new therapeutic platform.

TABLE OF CONTENTS

ACKNOWLEDGMENTS	v
ABSTRACT.....	vi
LIST OF FIGURES	x
CHAPTER 1 VIRUS LIKE PARTICLES: A SELF-ASSEMBLED TOOLBOX FOR CANCER THERAPY	1
1.1 Introduction.....	1
1.2 Surface Modification	5
1.3 Phototherapy	11
1.4 Immunotherapy	17
1.5 Encapsulation.....	21
1.6 Gene Therapy	24
1.7 Chemotherapy	27
1.8 Conclusion	31
CHAPTER 2 PHOTOTHERMALPHAGE: A VIRUS-BASED PHOTOTHERMAL THERAPEUTIC AGENT.....	32
2.1 Introduction.....	33
2.2 Results and Discussion	36
2.3 Conclusions.....	52
CHAPTER 3 INTRACELLULAR DELIVERY OF VIRUS-LIKE PARTICLES USING A SHEDDABLE LINKER	53
3.1 Introduction.....	53
3.2 Results and Discussion	56
3.3 Conclusions.....	67
CHAPTER 4 MULTIFUNCTIONAL PHOTO-IMMUNO METAL-ORGANIC FRAMEWORK: COMBINATIONAL STRATEGY TOWARD CANCER TREATMENT	68
4.1 Introduction.....	68
4.2 Results and Discussion	72
4.3 Conclusions.....	76

CHAPTER 5 CONCLUSION AND FUTURE WORK	78
5.1 Conclusions.....	78
5.2 Future Directions	79
APPENDIX A EXTENDED DATA FOR CHAPTER 2	80
APPENDIX B EXTENDED DATA FOR CHAPTER 3.....	105
APPENDIX C EXTENDED DATA FOR CHAPTER 4.....	139
REFERENCES	142
BIOGRAPHICAL SKETCH	167
CURRICULUM VITAE.....	168

LIST OF FIGURES

- Figure 1.1. The structure function relationship of VLPs and their associated cellular uptake is innately related to their shape (noted by the arrows) while the chemical modification and loading capacities allows access to further targeted delivery of drugs, therapeutics, and biomaterials to specific cell types, such as cancer cells and immune cells, and regions, such as tumor microenvironments and passage to the blood brain barrier.3
- Figure 1.2. Common strategies employed for surface modification of VLPs associated with specific amino acid residues. The schematic represents an icosahedral VLP. Many methods for bioconjugations can be used in multiple ways such as the Lys and Asp for either ends of carbodiimide couplings as well as forming synthetic analogues of amino acids which are commonly used to attached azide or alkyne moieties for click reactions.6
- Figure 1.3. A) Reduction of disulfide bonds with TCEP and addition of dibromo maleimide to form maleimide conjugates demonstrated on icosahedral Q β .⁶³ B) Cu-catalyzed azide-alkyne click chemistry demonstrated in fluorescein alkyne dye conjugation to icosahedral Q β .⁶⁶ C) Functionalization of the rod-like VLP, TMV, with CB6 through reaction with formed triazole. ⁶⁵9
- Figure 1.4. A) Azide-functionalized metalloporphyrin derivatives **1** and **2** and glycan ligands **3** and **4** for B) surface functionalization onto alkyne-modified Q β VLPs through CuAAC. C) Dose-response phototoxicity induced by zinc porphyrin-loaded Q β particles on CHO-CD22 cells, under full-spectrum irradiation (IC50 \approx 80 nM in porphyrin, 1.6 nM in particle) (top) and with filtered irradiation (430 \pm 10 nm, IC50 \approx 230 nM in porphyrin, 4.6 nM in particle) (bottom). D) Comparison of CD22-negative and positive cells at 10 nM particle concentration (0.5 μ M in porphyrin), under full-spectrum irradiation (top) and with 50 nM particles (2.5 μ M in porphyrin), under irradiation at 430 \pm 10 nm (bottom). The MTT assay was performed 24 h after light exposure. E) Phase contrast and fluorescent microscope images of CHO (a, c and e) and CHO-CD22+ cells (b, d and f) incubated with PBS (a and b), 9@GFP16 (c and d), and 8@GFP16 (e and f) at 37 °C for 4 hours. Each particle was used at 1 nM (50 nM in porphyrin); the @ symbol denotes the encapsulation of multiple copies of GFP inside the particle. Reproduced with permission from reference 91.....14
- Figure 1.5. A) Experimental design of synergistic immunophotothermal therapy. B) Tumor growth curves of 4T1 tumor-bearing mice treated with PBS, Q β , Croc, and PTPhage with and without laser radiation showing the most effective therapeutic approach is attributed to PTPhage, which exhibited the greatest restriction to tumor growth. C) Tumor weight as a representation of tumor suppression verified high antitumor performance of PTPhage compared to Croc, Q β , and PBS groups. D) Survival study of 4T1 tumor-bearing BALB/c mice (n = 5). E) Number of lung nodules after India ink staining showed PTT modified VLP has significant effect in controlling metastasis. F) Representative images of India ink-infused lungs of irradiated Croc, PTPhage, and PBS mice with white spots clearly

demonstrate number of metastatic nodules per each group. Reproduced with permission from reference 42.....	16
Figure 1.6. A) The amino acid sequence of the anti-PD-1 peptide SNTSESF with carboxy-terminal cysteine residue. B) Bioconjugation is formed first by attaching a bi-functional NHS-SM-PEG8 linker to a solvent-exposed amine group from lysine residues on CPMV, which provide maleimide groups for subsequent reaction with cysteine side chain of anti-PD1-peptides. Adapted from reference 112.....	20
Figure 1.7. Encapsulation of cargo — <i>e.g.</i> , protein, nucleic acid, and/or small molecules — into the interior of an icosahedral VLP via disassembly/reassembly method.	22
Figure 1.8. A) Disassembly of CCMV into coat proteins and subsequent reassembly in the presence of the siRNA to make CCMV-siRNA. B) FOXA1 expression levels in MCF-7 breast cancer cells following treatment with siRNA as determined by real time PCR. Reproduced with permission from reference 115. C) Encapsulation of MEG3 in MS2 by dual plasmid expression and subsequent modification with GE11 targeting peptide to make GE11-VLPs-MEG3. This formulation represses tumor growth by upregulating p53 expression and downregulating MDM2 expression. D) Proliferation of HepG2 hepatocellular carcinoma cells following treatment with GE11-VLPs-MEG3 as measured by CCK-8 viability assay. Reproduced with permission from reference 150.	27
Figure 1.9. A) Q β possesses 32 pores (1.5 or 3.0 nm) allowing for the diffusion of doxorubicin in or out of the VLP. Pores are then capped with 6 nm AuNPs. B) Cytotoxicity analysis after 4 h incubation of Q β /gold nanoparticle composites. C-E) Wide-field live cell images depicting doxorubicin release post irradiation, right side depicts laser treated: C) bright-field, D) nuclear stain, Hoechst 33342 nuclear dye, and E) doxorubicin (λ_{Ex} 470 nm, λ_{Em} 560 nm).....	30
Figure 2.1. A) The overall synthetic bioconjugation strategy involves synthesizing the croconium dye by arefluxing commercially available starting materials methyl isonipecotate and thiophene-2-thiol. bThe resulting ester was deprotected under alkaline conditions and cthe final dye, Croc (thiophene-croconaine dye), was produced in the condensation reaction with croconic acid. The free acids were dactivated as n-hydroxysuccinimide (NHS) esters and eadded under dilute conditions to a solution of Q β to prevent cross-linking. The functionalized Q β was incubated briefly in water to hydrolyze the remaining NHS esters back to the free acid. B) Elec-trophoresis mobility analysis of Q β before and after conjugation on SDS-PAGE (left) and agarose (center and right) gels show suc-cessful bioconjugation of dye to Q β . Non-reducing SDS-PAGE shows an increase in molecular weight of Q β after bioconjugation. The unstained agarose (center) shows a green band in bright light in the same spot in which a Coomassie-stained band (right) appears. The conjugate travels further toward the (+) electrode, which is anticipated from the replacement of lysines with carbox-yl functions. C) DLS and TEM (insert scale bar = 50 nm) of Q β and PTPhage demonstrate that the conjugation of croconium dye does not affect the size or polydispersity of the VLP.....	37

- Figure 2.2. UV-Vis Spectrographic analyses of equal molar concentrations of chromophores for Croc and PTPhage show A) a broadening of the NIR absorption of PTPhage (green line) compared to croconium dye (blue line). A photograph of PTPhage is shown in the insert. B) A linear relationship exists between PTPhage (30 $\mu\text{g. mL}^{-1}$) solution temperature increases and laser power after 3 mins of irradiation (laser power was set 0.0015, 0.18, 0.604, 1.02 $\text{W}\cdot\text{cm}^{-2}$). C) Photothermal heating profile of PTPhage and Croc at the same concentration (30 $\mu\text{g mL}^{-1}$) after 11 min of laser irradiation (808 nm, 0.18 $\text{W}\cdot\text{cm}^{-2}$) shows a significant difference in temperature increase (40.1°C for PTPhage and 29.1°C for Croc). D) Temperature variations of PTPhage and PBS under laser irradiation are mapped and quantified by a thermal camera. No noticeable temperature increase was observed in PBS under the 808 nm laser irradiation (0.18 $\text{W}\cdot\text{cm}^{-2}$) at different time points.38
- Figure 2.3. A) Photothermal stability of PTPhage after 10 min of laser irradiation (0.18 $\text{W}\cdot\text{cm}^{-2}$) is shown by intact HPLC profile of PTPhage before and after radiation. B) No significant change in absorption spectra of PTPhage after laser-induced heating for 10 min. C) DLS and D) TEM data (scale bar is 50 nm) prove thermal stability of PTPhage with no morphology change after 10 min of laser irradiation. E) Thermal cycling of PTPhage shows no change in heating profile after three cycles.40
- Figure 2.4. A) Experiment design of synergistic immunophotothermal therapy. B) Tumor growth curves of 4T1 tumor-bearing mice treated with PBS, Q β , Croc and PTPhage with and without laser radiation showing the most effective therapeutic approach is attributed to PTPhage which exhibited the greatest restriction to tumor growth. C) Tumor weight as a representative of tumor suppression verified high anti-tumor performance of PTPhage compared to Croc, Q β , and PBS groups D) Survival study of 4T1 tumor-bearing BALB/c mice (n = 5). E) Number of lung nodules after India ink staining. F) Representative images of India-ink-infused lungs of irradiated Croc, PTPhage and PBS mice with white spots clearly demonstrate number of metastatic nodules per each group. ** p < 0.05.....44
- Figure 2.5. In vivo immune responses after photothermal stimulation. A) DC maturation induced by various groups on mice bearing 4T1 tumors (gated on CD11c+ DC cells, Figure A24) after PTT treatment (Tmax = 54.2°C). Cells in the tumor-draining lymph node were assessed by flow cytometry after staining for CD80 and CD86 expressions. B) Quantification of CTLs (CD8+) in isolated lymph nodes. C-D) Percentage of activated TH-cells (CD4+CD44+CD62-) and CTLs in spleens. Single-cell suspensions were processed from the spleen and analyzed by flow cytometry after anti-CD3, -CD4, -CD8, -CD44, and -CD62L staining (Tmax = 54.2°C). E-F) Representative flow cytometry plots showing expression of CD86 and CD80 on DC of draining lymph node for different groups (gated on CD11c+, Figure A24) after PTT treatment (Tmax = 44.0 °C). G-H) Representative flow cytometry plots of effector CD4+ in spleen cells of different treatment groups analyzed by flow cytometry (stained with anti- CD3, -CD4, -CD44, and -CD62L) (Tmax = 44.0 °C). I- J) Representative flow cytometry plots showing percentages (gated on CD4+ cells, Figure A24) of CD4+FoxP3+ T cells in the spleen after various treatments.....51

Figure 3.1. A) Synthesis of dibromomaleimide-TPP (DB-TPP) linker followed by B) bioconjugation strategy on Q β . C) Electrophoretic mobility analyses of Q β before and after DB-TPP conjugation using SDS-PAGE (left) and agarose (right) gels showing successful bioconjugation of the maleimide linker to Q β , forming Q β -M-TPP. SDS-PAGE shows the successful reduction of the higher-order structures and their reappearance after conjugating DB-TPP. The fluorescence imaging of agarose (top right) shows the maleimide fluorescence at the same spot of the Coomassie-stained band. D) Fluorescence spectra of Q β -M-TPP and Q β before and after conjugation with DB-TPP (ex/em 400/540 nm) with a photograph showing the reaction mixtures of Q β -M-TPP under 365 nm UV lamp illumination. E) Size-exclusion chromatograph of Q β -M-TPP and Q β . After bioconjugation, F) DLS and G) TEM of Q β and Q β -M-TPP show no aggregation or structural change.58

Figure 3.2. A) Cell viability of A549 lung cancer cells after treating with Q β (GFP) and Q β (GFP)-M-TPP (2 mg/ml) for 4 h at 37 °C. B) Flow cytometry was used to assess the uptake of Q β (GFP)-M-TPP and Q β (GFP) (2 mg/ml) in fixed A549 cells after incubation at 37 °C for 4 h. C) Fluorescence microscopy images of fixed A549 cells treated with Q β (GFP) showing punctate dots coming from endocytic uptake and D) A549 cells treated with Q β (GFP)-M-TPP showing diffuse green fluorescence related to the cytosolic release of Q β (GFP). Color code: green: Q β (GFP). Scale bar = 50 μ m. E) Fluorescence micrograph of Q β (GFP) and F) Q β (GFP)-M-TPP in fixed A549 cells stained with MitoTracker showing no mitochondrial colocalization of Q β (GFP)-M-TPP. Color code: red: MitoTracker Deep Red FM and green: Q β (GFP). Scale bar = 50 μ m.....61

Figure 3.3. A) Conjugation scheme of Q β -PEG-TPP. Q β first is reduced with TCEP, followed by adding Dibromomaleimide-PEG (DB-PEG). Conjugation of TPP-NHS with surface amines is then performed using TPP-NHS. Characterization of Q β -PEG-TPP conjugation B) SDS gel C) 1% agarose gel D) TEM (scale bar: 100 nm). E) Fluorescence micrographs of H2073 cells treated with Q β (GFP) and Q β (GFP)-PEG-TPP. Q β (GFP)-PEG-TPP is driven into the mitochondria with greater colocalization efficiency (ρ), which is calculated using Pearson's coefficient, colocalization ($\rho = 0.56$) compared to non-targeted conjugates ($\rho = 0.28$). Color code: green: Q β (GFP), red: MitoTracker Deep Red FM.64

Figure 3.4. A) Scheme for disassembly of Q β virions to coat proteins, then the reassembly around siRNAs to make siRNA@Q β -M-TPP. B) Cell viability and relative levels of luciferase expression in HeLa luciferase cells after various treatments.66

Figure 4.1. Synthetic procedure, including the growth of ZIF over Anti-CTLA-4 (ipilimumab) to form a microcrystal. Formed ZIF has high affinity for the negatively charged PTPHage. These coated particles will generate heat upon 808 nm laser irradiation while ZIF begin degrades slowly, releasing ipilimumab.72

Figure 4.2. Characterization of biom mineralized anti-CTLA-4@ZIF using A) dynamic light scattering B) SEM micrograph. A monodispersed micron sized anti-CTLA-4@ZIF particle was form in a rhomb dodecahedral shape.73

Figure 4.3. Confocal micrograph of Cy7-anti-CTLA-4@ZIF. The outer shell fluoresces blue from trapped Cy7-anti-CTLA-4 while there is no fluorescence in Cy7 channel for ZIF. Scale bar = 50 μm74

Figure 4.4. A) Transmission electron microscopy image of PTPaheg coated on surface of ZIF. B) Photothermal heating profiles of ZIF, PTPhage and PTPhage- anti-CTLA4@ZIF at the same concentration ($50 \mu\text{g mL}^{-1}$) over 15 min of laser irradiation (808 nm , $0.18 \text{ W}\cdot\text{cm}^{-2}$) show strong PTPhage keeps its photothermal behavior after attaching to surface of ZIF and generates heat as effective as PTPhage, while ZIF did not show any significant difference in temperature increase.76

CHAPTER 1

VIRUS LIKE PARTICLES: A SELF-ASSEMBLED TOOLBOX FOR CANCER THERAPY

1.1 Introduction

Over the last few decades, nanotechnology has been used increasingly in biomedicine, including applications for disease diagnosis and treatment.^{1, 2} Tremendous effort has been devoted to designing a variety of organic and inorganic nanomaterials such as polymeric micelles,³ liposomes, dendrimers,⁴ carbon nanotubes,⁵ metal-organic frameworks,^{6, 7} and metal nanoparticles⁸ to achieve safe and protected cargo for targeted delivery.⁹⁻¹¹ The appeal of these artificially engineered materials is based particularly on their versatile synthetic strategies, which give them physical and chemical properties such as shape, size, charge, surface patterning, biocompatibility, and the ability to selectively interact with distinct cells and tissues.^{12, 13} These properties allow them to resolve the main obstacles encountered with existing pharmaceutical treatments — poor bioavailability, rapid clearance, and uncontrollable release of drugs.^{14, 15} However, despite advances, constructing simplistic and optimized synthetic nanostructures with low toxicity, multivalency, water solubility, functionalizability, and therapeutic loading capabilities, it challenging and complex process that limits the therapeutic application of these materials.^{13, 16, 17} In the past three decades, biomolecule-based nanostructures — such as supramolecular self-assembled proteins, peptides, lipids, and cellulose — have paved a new way toward the design of sophisticated multimodal nanomaterials.¹⁷⁻¹⁹ Supramolecular chemistry benefits from the nature of non-covalent interactions to integrate molecules such as proteins, small molecules, polysaccharides, and polymers in a dynamic and reversible state, which gives rise to

multifunctional platforms with high sensitivity to bioenvironmental changes such as pH, ionic strength, temperature, and oxidation.²⁰⁻²⁴ This bottom-up approach elaborates upon structural and functional diversity, which offers suitable shapes, inner structure, organized architectures, and high biocompatibility and bioavailability. However, one key problem that these systems face is low biostability under physiological conditions, arising from the non-covalent linkage that hold the building blocks.^{25, 26} Therefore, there is an effort to identify systems that not only overcome design barriers associated with synthetic materials, but also provide the desired features of self-assembled nanostructures with integrated stability. Virus-like particles (VLPs) have attracted significant attention as self-assembled supramolecular systems that imitate the highly symmetrical, polyvalent, and monodisperse conformation of real viruses while lacking a viral genome (DNA or RNA), which render them noninfectious.²⁷⁻²⁹ These proteinaceous materials offer advantages over the above-mentioned synthetic nanostructures by being biodegradable and biocompatible, as viruses are nature's tool to carry and deliver delicate genetic materials under adversarial physiological conditions.^{30, 31} Many VLPs follow suit by being exceptionally stable and robust against harsh conditions such as high pH and temperature.¹⁰

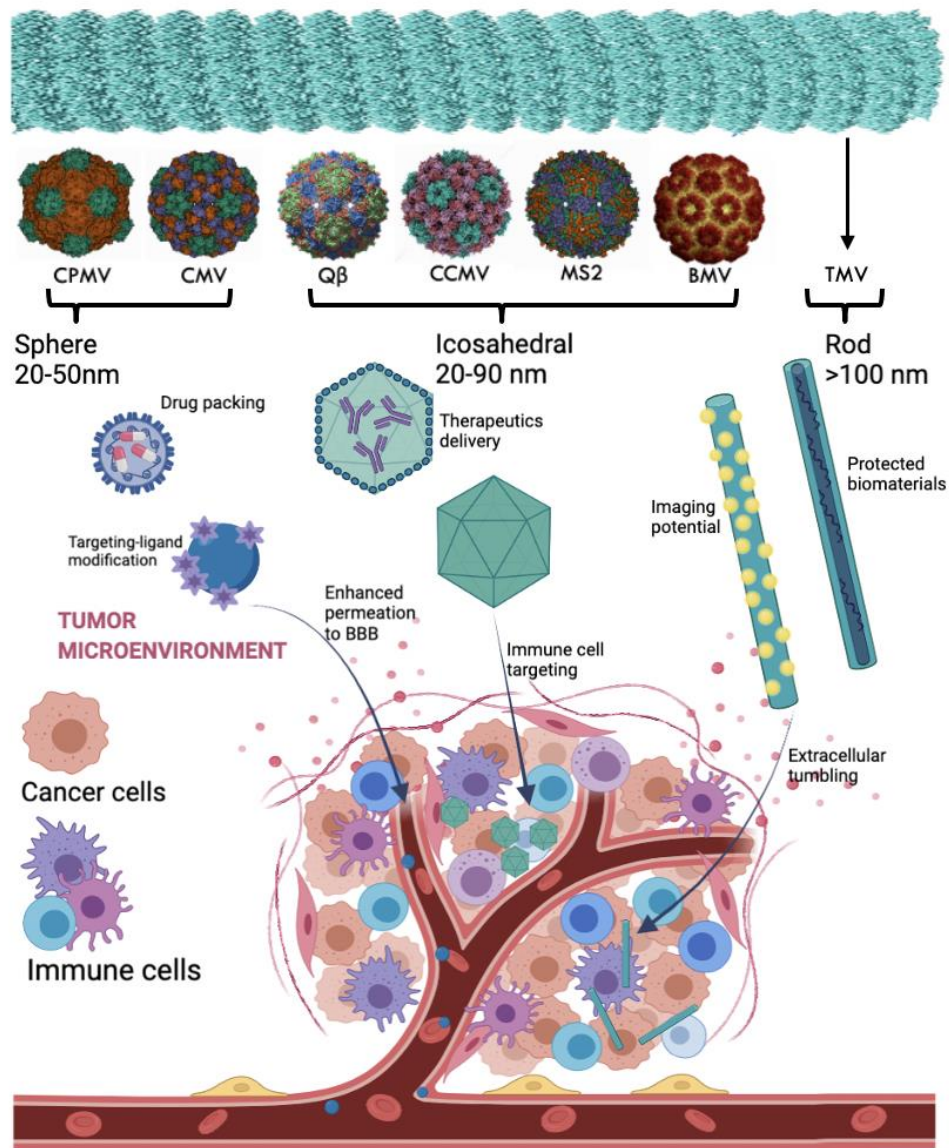


Figure 1.1. The structure function relationship of VLPs and their associated cellular uptake is innately related to their shape (noted by the arrows) while the chemical modification and loading capacities allows access to further targeted delivery of drugs, therapeutics, and biomaterials to specific cell types, such as cancer cells and immune cells, and regions, such as tumor microenvironments and passage to the blood brain barrier.

The synthesis and growth of VLPs has been reported in mammalian and insect cells,^{32, 33} bacteria, yeast,³⁴ and transgenic plants.³⁵ With many regenerable sources like plants and bacteria, the

harvesting of VLPs has ultimately led to the notion of VLP “farming” and large-scale production. The synthesis techniques for VLP generation have become quite sophisticated. Medicago, a Canada-based biotechnology company, has multiple plant-produced VLP-based vaccines under clinical investigation that are produced at a large scale.³⁶ The different sources of virus production result in the isolation of VLPs with different sizes (20–300 nm) and shapes (icosahedral, sphere, and rod).³⁷ The variety of shapes and sizes afforded from VLPs allow different cellular interactions, uptake, and immune system activation in various biological environments *e.g.*, tumor microenvironments, which provide various therapeutic applications such as imaging, immune cell targeting, and cargo delivery (Figure 1.1). For example, small-sized VLPs that range from 20–200 nm, are taken up by antigen presenting cells (APC) such as dendritic cells (DCs) and round VLP particles such as CCMV can reach secondary lymphoid organs better than rod like structures, resulting in a 100-fold increase in immune response in some cases.³⁸ However, even larger and rod-shaped viruses like the tobacco mosaic virus (TMV), have shown an order of magnitude increase in circulation time in the blood stream when coated with serum albumin, improving its therapeutic effect.³⁹ In all cases, the surface of these VLPs have a repetitive structure with solvent-exposed amino acids that allow for both genetic and chemical modification leading to a high density of functional groups. This unique and intrinsic feature of VLPs provides a large toolbox for chemists to construct bioconjugation schemes for adaptive functionality.⁴⁰ Many VLPs, including icosahedral Q β and MS2, allow access to their interior cavity through their pores or disassembly/self-assembly processes can be utilized to create a reaction environment, load cargo, and/or provide a protective shield. For example, the plant-based viruses cowpea chlorotic mottle virus (CCMV), cucumber mosaic virus (CMV), and cowpea mosaic virus (CPMV) provide

repeating functional handles for modification along both their interior and exterior surfaces for drug loading. The discrete “inner and outer” surfaces of VLPs provide a unique platform for concealing drug payloads within a VLP while modifying the outer surface for targeting. Therefore, VLPs offer a unique opportunity to combine benefits of the multiple surfaces and supramolecular self-assembly of liposomes with the polyvalency and robustness of polymers, while also coming in a variety of shapes and sizes that provide a unique versatility over most other materials.⁴¹ They are so diverse that their innate substructures have therapeutic applications for a multitude of cancer treatment such as chemotherapy, phototherapy,⁴² immunotherapy⁴³ and combinations with imaging. All these unique abilities of VLP nanoparticles to self-assemble, and for multifaceted functionalization, biocompatibility, immunogenicity, and high stability, create an ideal material for designing many therapeutic agents.^{27, 37, 40} In this chapter, we will discuss strategies involved in the surface modification, selective encapsulation of therapeutics, and exploitation of the versatility of VLPs to generate an effective cancer therapeutic platform in photothermal, immune, gene, and chemotherapies.^{44, 45}

1.2 Surface Modification

The intricate and repetitive design of virus-like particles allows for fabrication of highly tunable nanostructures for many therapeutic applications such as imaging, cancer therapy and drug delivery.⁴⁶⁻⁴⁸ The high-density presentation of tumor antigens/epitopes,⁴⁹ anti-cancer drugs,⁵⁰ and targeting ligands⁵¹ in a precise manner is possible by decorating the surface of VLPs using bioconjugation reactions. The surface of VLP capsids is typically populated with lysines,⁵² cysteines,⁵³ and glutamic acids that allow for chemical attachment via bioconjugation for surface decoration with proteins, epitopes, antigens, and small molecules. Further, certain amino acids like

methionine⁵⁴ can often be substituted for more nucleophilic or functionalizable amino acids by modifying the DNA used for capsid expression.⁵⁵ Active research in the field since the 1990s has helped develop an ever-expanding library of available chemical reactions that allow researchers to incorporate a larger repertoire of protein-VLP combinations to suit various cancer therapeutic needs.

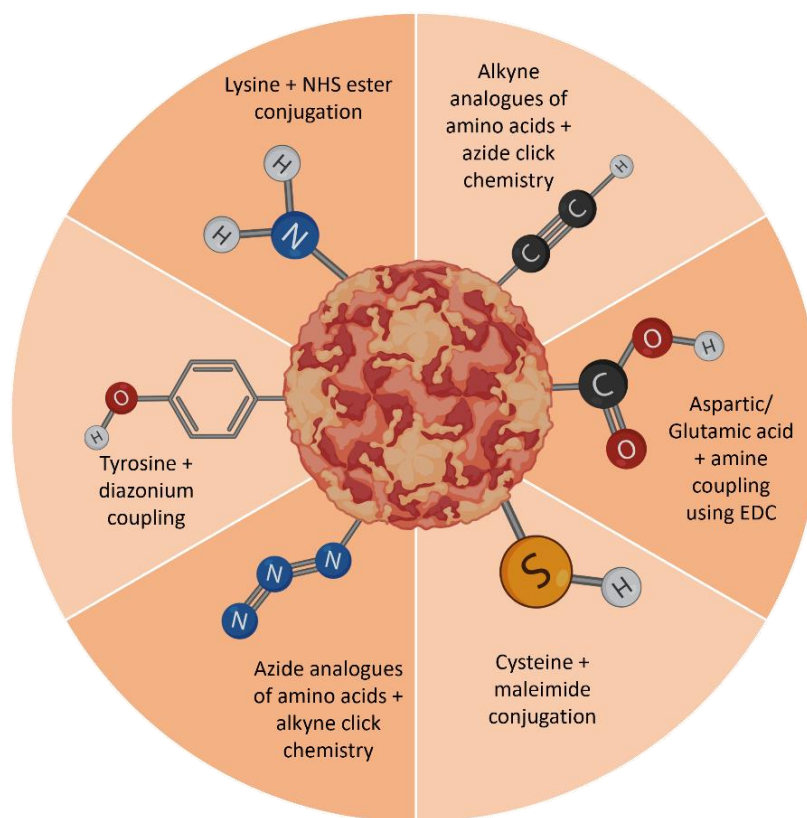


Figure 1.2. Common strategies employed for surface modification of VLPs associated with specific amino acid residues. The schematic represents an icosahedral VLP. Many methods for bioconjugations can be used in multiple ways such as the Lys and Asp for either ends of carbodiimide couplings as well as forming synthetic analogues of amino acids which are commonly used to attached azide or alkyne moieties for click reactions.

Exploiting the already-present amino acids on the surface of a VLP is a very direct and effective approach for conjugation of various ligands, peptides, and small molecules for functionalization

through several bioconjugation strategies (Figure 1.2). The VLPs CPMV, Q β , and MS2 have surface lysine groups that serve as reaction centers that can react through N-hydroxysuccinimide (NHS) ester chemistry for amide bond formation. This strategy is highly used for targeting many types of cancer cells known to overexpress folate receptors such as colorectal, ovarian, breast, and lung cancer. The decoration of drug-carrying VLPs with a dense folic acid exterior promote targeting and efficiency of particle delivery, useful for delivering drugs like doxorubicin and cisplatin.⁵⁶ Destito *et al.* attached⁵⁷ a high density of folic acids (FA) — about 100 FA moieties — on the surface of CPMV through the reaction of FA-NHS with solvent-exposed lysine groups to target cancer cells. Another example that further show cancer therapeutic applications of VLPs after lysine modification is reported by Aljabali *et al.*; in this work, the anticancer drug doxorubicin covalently attached⁵⁸ to the exterior of CPMV by EDC/NHS chemistry yields significant cytotoxicity to HeLa cells *in vitro* compared to free drug, owing to the concentrated presentation of drug into cancer cells. Cysteine groups on the VLP surface also offer a great platform for modification of various kinds, out of which the maleimide-thiol conjugations have been a popular approach and are hence extensively reported in literature.⁵⁹ However, free cystines are not common and instead are typically found as disulfide bonds, which are important for the structural stability of most proteins and VLPs.^{60, 61} The more recent development of disulfide-bridging maleimides — first described⁶² by Jones *et al.* — has allowed for disulfides to be used as bioconjugation handles without losing the covalent character. For example, Chen *et al.* synthesized⁶³ a library of dibromo maleimide derivatives and attached them by Michael addition to the 180 available cysteine residues on the surface of Q β (Figure 1.3A). The disulfide bridge first was reduced and

then crosslinked with dibromo functionalized maleimides to form Q β -maleimide conjugates. The developed modification was further used as a fluorescent probe for cell imaging.⁶⁴

Strable *et al.* demonstrated the Cu(I)-catalyzed, azide-alkyne cycloaddition (CuAAC) strategy on Hepatitis B virus-like particle (HBV) and Q β (Figure 1.3B) by conjugating 50% of the azide positions available on the VLP surface with fluorescein alkyne dye.^{65, 66} A very novel twist on click chemistry, which avoids the use of copper altogether, was demonstrated by Finbloom *et al.* who showed⁶⁵ that cucurbit[6]uril (CB6) — traditionally used in rotaxane synthesis — could catalyze triazole formation between two modified proteins. They demonstrate this by first using an NHS ester to install azide groups onto TMV, followed by the addition of propargylamine in the presence of CB6 to form a triazole product (Figure 1.3C). This reaction exploits the aqueous environment by entropically driving the hydrophobic azide and alkyne into the inner cavity of CB6, which is further stabilized by the protonated amines. Confined inside the macrocycle, the alkyne and azide undergo a traditional Huisgen 1,3-dipolar cycloaddition.

When the natural surface of a VLP lacks available functional handles, amino acid analogues prove to be useful as they can be swapped out for their native amino acid, populating the exterior with suitable groups allowing further conjugation. For example, by optimizing the concentrations of tyrosine analogues like p-propargyloxy-phenylalanine and p-azido-phenylalanine and methionine analogues like homopropargylglycine and azidohomoalanine respectively during protein expression, the native amino acid can be replaced by its analogue and providing the appropriate platform for suitable click chemistry conjugations.⁵⁴ Similar to the overexpression of folate receptors, prostate cancer cells are observed to have an overexpression of the membrane protease glutamate carboxypeptidase II (GPC II). Neburkova *et al.* demonstrated⁶⁷ how click chemistry

finds its application in prostate cancer therapeutics through conjugation of GPC II inhibitors onto several VLPs including Q β . Non-natural amino acids are often employed in the straightforward CuAAC strategy to achieve surface modifications of VLPs like Q β and MS2.⁵⁴ These residues are often azide or alkyne functionalized — or phosphines, but less popularly so — since they can undergo chemistry that works well in water and are orthogonal to bioconjugation strategies that depend on generating an electrophilic center.

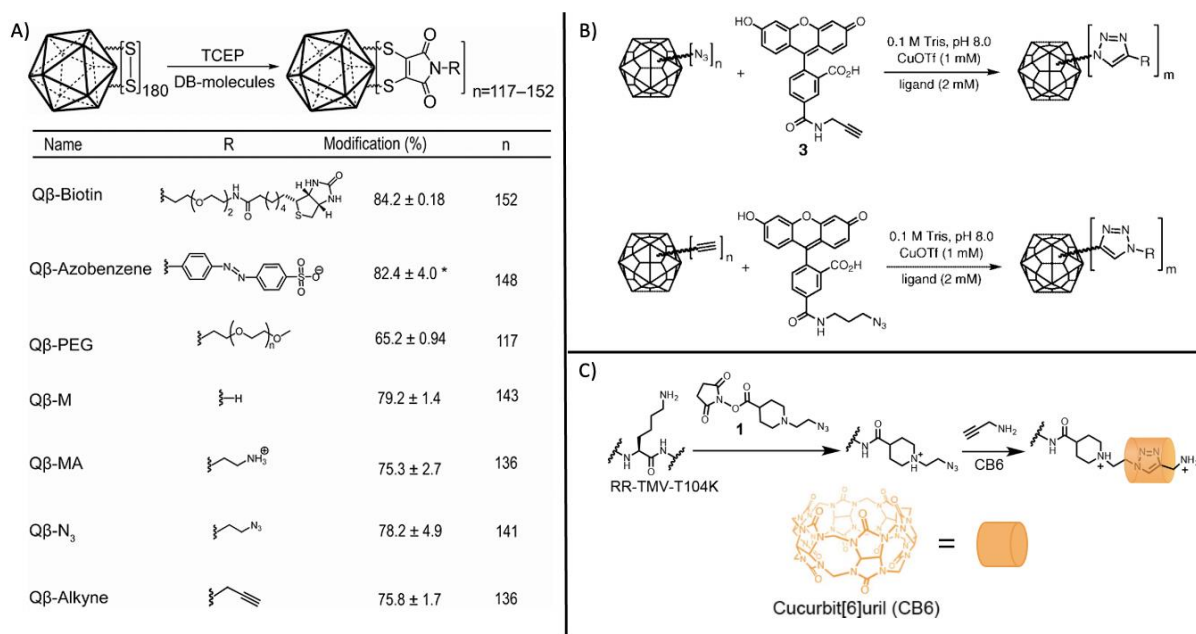


Figure 1.3. A) Reduction of disulfide bonds with TCEP and addition of dibromo maleimide to form maleimide conjugates demonstrated on icosahedral Q β .⁶³ B) Cu-catalyzed azide-alkyne click chemistry demonstrated in fluorescein alkyne dye conjugation to icosahedral Q β .⁶⁶ C) Functionalization of the rod-like VLP, TMV, with CB6 through reaction with formed triazole.⁶⁵

A relatively newer approach for conjugation is chemoenzymatic strategies, where the coat proteins of the VLPs are genetically engineered to incorporate amino acids that can act as recognition sequences; these recognition sequences selectively bind with peptides to incorporate in a

composite.^{68, 69} A special use case for this technique in therapeutic applications where the epitope/antigen to be delivered is a larger protein framework, and shorter peptide sequence derived from the antigen do not provide satisfactory amounts of antibody stimulation.⁷⁰ Several papers have used a sortase-mediated protein ligation strategies to achieve specific antigen binding.^{69, 71} This ligation technique — also known as sortagging — employs the sortase enzymes present in the cell wall of gram-positive bacteria, which is known for its function of facilitating the anchoring of surface proteins with an LPTEG recognition sequence. The sortagging ability of bacteriophages is used to employ this enzymatic pathway for conjugating sequences of choice, that we can modify with an LPTEG sequence prior to the reaction.⁷²

Addition of spacers to the VLP surface is a popular method for controlling the distance of attachment of peptides and epitopes to the surface, which can promote more efficient conjugation by eliminating steric congestion at the protein surface and allows more tunability in how dense the functionalization becomes. One end of these polar or non-polar flexible linkers are functionalized with azide or thiol groups depending on the chemistry required. Some of the more popular flexible linkers are found in the $-(\text{Gly})_n\text{-Ser-}$ form and are known for providing an added flexibility to the structure.⁷³ J. Park *et al.* showed⁴³ the use of GGGs linker to modify their peptide of choice with thiol and azide groups for conjugation via thiol-maleimide chemistry and azide-alkyne click chemistry respectively. Poly(ethylene)glycol (PEG) linkers are popular amongst several nanocarrier platforms for providing structural stability and improving circulation half-time.⁷⁴ PEGylation can help ensure the VLPs do not induce any unwanted immune responses and can promote extended circulation times. Bacteria-infecting viruses (phages), such as pseudo-spherical icosahedral structures Q β and MS2, can evade endosomal degradation through surface

modification with ligands such as poly(lysine)-DNA complexes and SP94 peptides, which protect the VLP from unwanted biological activity.^{75, 76}

VLPs allow for a high amount of precision in the practice of surface modification, giving one the ability to vary the epitope density on a virus-like particle by exercising control over the VLP-to-cargo ratio in the coupling reactions.⁷⁷ Apart from that, the hollow structure of VLPs offer excellent control towards functionalizing the exterior and interior surfaces selectively using some of the aforementioned orthogonal reaction methodologies for dual modification.^{63, 78} The advantages of using VLPs as a therapeutic platform are only further enhanced by their ability to be surface functionalized. We have discussed some popular approaches that have shown success in a variety of applications. With respect to cancer research, these surface functionalized VLPs serve as promising nanocarriers for non-invasive treatment strategies like phototherapy and immunotherapy. Their ability to deliver and present materials like chromophores and peptides is compounded by all the immunogenic benefits of using a non-synthetic biomaterial.

1.3 Phototherapy

Phototherapy, including photodynamic therapy (PDT) and photothermal therapy (PTT), has attracted extensive attention as a noninvasive, selective, and efficient cancer treatment strategy.⁷⁹⁻

⁸¹ This method works based on interaction of light with chromophores that can then undergo different photochemical reactions or transformations to exert a therapeutic effect. PTT, which converts light into heat, utilizes the thermal sensitivity of cells to destroy tumors through converting light in the near infrared (NIR) region (700–1100 nm). The NIR spectrum has low absorption/scattering in biological systems from water and biomolecules like hemoglobin and

melanin, giving it improved penetration depth through skin and tissues.^{82, 83} To date, the most efficient converters of NIR radiation into heat have been inorganic materials including metal nanoparticles, carbon nanotubes, sulfide nanomaterials, and metal oxides; however there are concerns over possible term toxicity and slow or absent biodegradability. This pushes the need for organic molecules such as indocyanine green (ICG) and heptamethine dyes as alternative PTT materials. Organic-based PTT agents permit photophysical tunability, higher safety, and cell targeting abilities, thus improving photothermal conversion efficiency and photostability. In contrast to PTT, PDT converts light into reactive oxygen species (ROS), which are toxic to cells, by using the interaction of specific wavelength (within 600–800 nm) of light with a photosensitizer (PS).^{84, 85} A photosensitizer at ground state (S_0) absorbs light energy and lifts an electron to an excited singlet state (S_1) where it undergoes an intersystem crossing by inverting the electron spin to the T_1 state. While in a T_1 state, the photosensitizer can abstract an electron from reducing molecules, such as tyrosine in a protein, to create a pair of radical anions ($PS^{\cdot-}$), which further donate their extra electrons to O_2 , producing superoxide anion radicals ($O_2^{\cdot-}$) or other small molecule radicals to produce potentially toxic cell-damaging products. Alternatively, it can transfer its energy directly to molecular oxygen in triplet ground state (3O_2), which converts ground state molecular oxygen into singlet oxygen (1O_2), which readily undergoes irreversible addition to nucleic acids.

PTT and PDT not only kill irradiated tumor cells but can also stimulate a series of immune responses by releasing damage-associated molecular patterns (DAMPs) related to apoptotic or necrotic tumor cells and inflammatory cells.^{86, 87} VLPs have been used in phototherapy — specifically PDT — for more than a decade. They have shown promising results thanks to their

multivalency allowing them to carry photosensitizers/photo-absorbers along with cancer targeting moieties.⁸⁸⁻⁹⁰ Generally, the efficiency of this strategy relies on the power of photoactive agents to trigger heat- or ROS-based cellular death, as well as initiating immunological cell death. One example of using VLPs to carry and locate high concentration of photosensitizer to the cells of interest for PDT is reported⁹¹ by Rhee *et al.*, where Q β was modified with a metalloporphyrin derivative for PDT and a glycan ligand that can specifically target CHO-CD22 receptor cells. The dual surface modification of Q β was performed through a CuAAC between azide-tailed zinc tetraaryl porphyrin (Figure 1.4A) ligand with alkyne-derivatized Q β (Figure 1.4B). The functionality of VLP-mediated PDT was tested by treating CHO-CD22 cells with different concentrations of modified Q β , followed by exposure to radiation (Figure 1.4C). The metabolic cell viability results showed modified Q β construction could specifically kill CHO-CD22 cells through a dose dependent manner after photoactivation, whereas, cells incubated with unmodified Q β remained viable after radiation. In addition, cytotoxicity was compared between CD22-positive and negative CHO cells after incubation with the same amount of conjugated Q β to show selectivity of attached ligands on cell surface receptors. Phase contrast and fluorescent microscope images show the selective nature of the modified Q β for CHO-CD22+ cells by comparison to CHO-CD22- cells (Figure 1.4E). Therefore, VLPs offer great potential for targeted delivery of photosensitizing compounds and provide a promising scaffold for photodynamic cancer treatment that results in an improved therapeutic index.

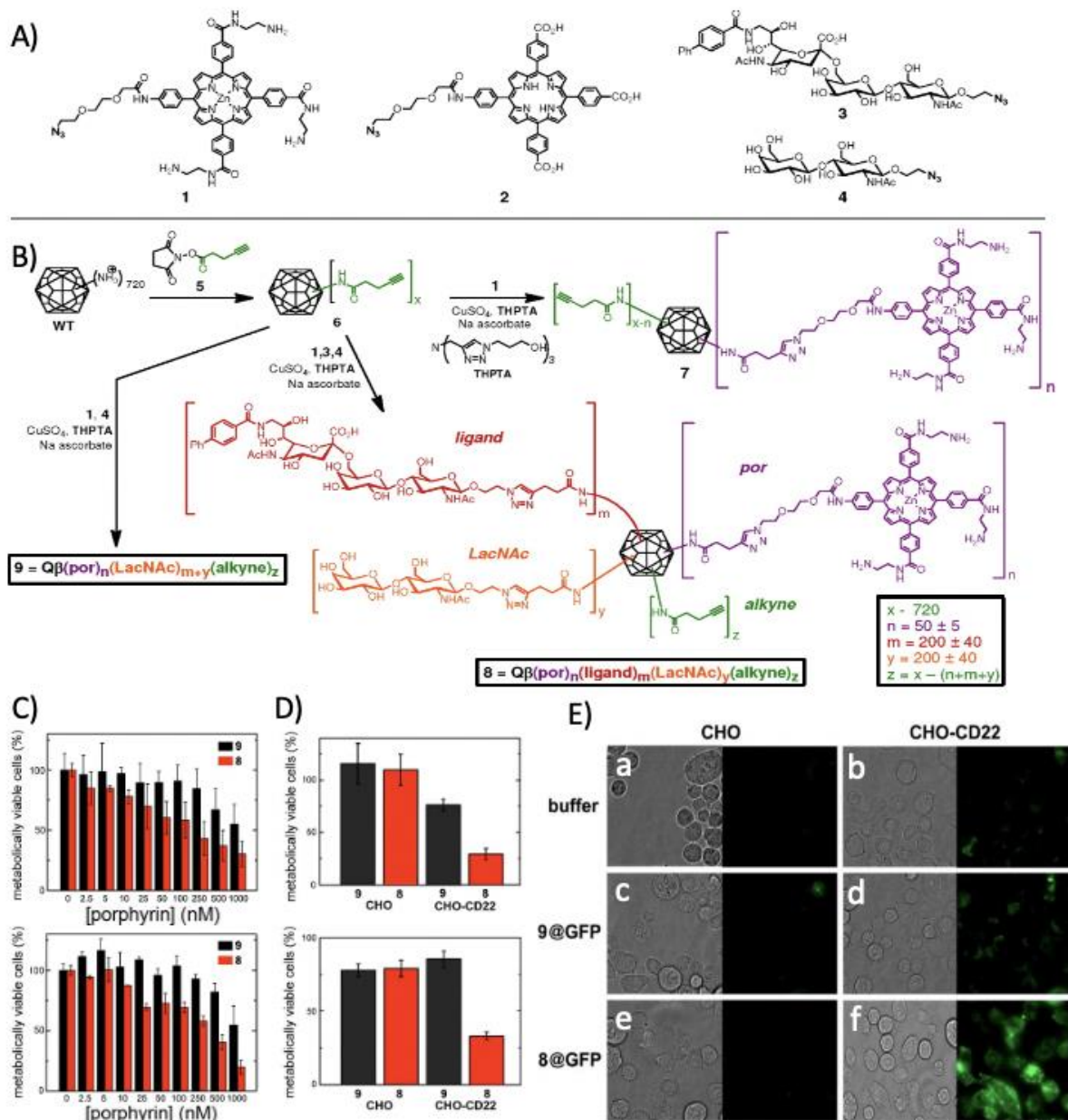


Figure 1.4. A) Azide-functionalized metalloporphyrin derivatives **1** and **2** and glycan ligands **3** and **4** for B) surface functionalization onto alkyne-modified Q β VLPs through CuAAC. C) Dose-response phototoxicity induced by zinc porphyrin-loaded Q β particles on CHO-CD22 cells, under full-spectrum irradiation (IC₅₀ ≈ 80 nM in porphyrin, 1.6 nM in particle) (top) and with filtered irradiation (430 ± 10 nm, IC₅₀ ≈ 230 nM in porphyrin, 4.6 nM in particle) (bottom). D) Comparison of CD22-negative and positive cells at 10 nM particle concentration (0.5 μM in porphyrin), under full-spectrum irradiation (top) and with 50 nM particles (2.5 μM in porphyrin), under irradiation

at 430 ± 10 nm (bottom). The MTT assay was performed 24 h after light exposure. E) Phase contrast and fluorescent microscope images of CHO (a, c and e) and CHO-CD22+ cells (b, d and f) incubated with PBS (a and b), 9@GFP16 (c and d), and 8@GFP16 (e and f) at 37 °C for 4 hours. Each particle was used at 1 nM (50 nM in porphyrin); the @ symbol denotes the encapsulation of multiple copies of GFP inside the particle. Reproduced with permission from reference 91.

VLPs also offer great potential for displaying photo absorbers such as organic based NIR molecules on their exterior surface. High density of photoabsorbers on surface of VLPs along with their high thermal stability turn them to a highly stable and efficient photothermal agent more powerful than most common inorganic and organic PTT agents. More recently, Shahrivarkevishahi *et al.* designed⁴² a photothermal and immunogenic VLP-based PTT agent called Photothermal Phage (PTPhage) through conjugation of hundreds of croconium dyes onto the solvent-exposed amine groups on the surface of Q β through EDC/NHS chemistry. The formulation showed significant enhancement in photothermal performance over free dye, and photothermal conversion efficiency, exceeding even gold nanorods. The cellular uptake and photothermal cytotoxicity of PTPhage was compared with free dye after incubating with identical concentrations of NIR dye with 4T1 breast cancer cells. High cellular uptake and 48% more cellular toxicity after 808 nm laser radiation was observed for PTPhage compared to the free dye. The *in vivo* photothermal antitumor response was also assessed after treating 4T1 tumor-bearing female BALB/c mice with the VLP formulation. As shown in Figure 1.5, the PTT-mediated VLP showed significant tumor volume suppression, longer survival time, and significant prevention of lung metastases. The study further tested immunological responses triggered by the PTPhage as an immuno-photothermal combinational treatment compared to a monotherapy design (VLP and Free dye) where the data clearly proved higher activation of CD8⁺ and CD4⁺ T cells and dendritic cells, along with a significant reduction in immunosuppressive T-regulatory response. The implicit immunogenicity

of Q β adds to the functionalization ability of VLPs and shows a great promise for designing highly effective immunotherapeutic agents that can promote therapeutic efficiency across the field of cancer immunotherapy.

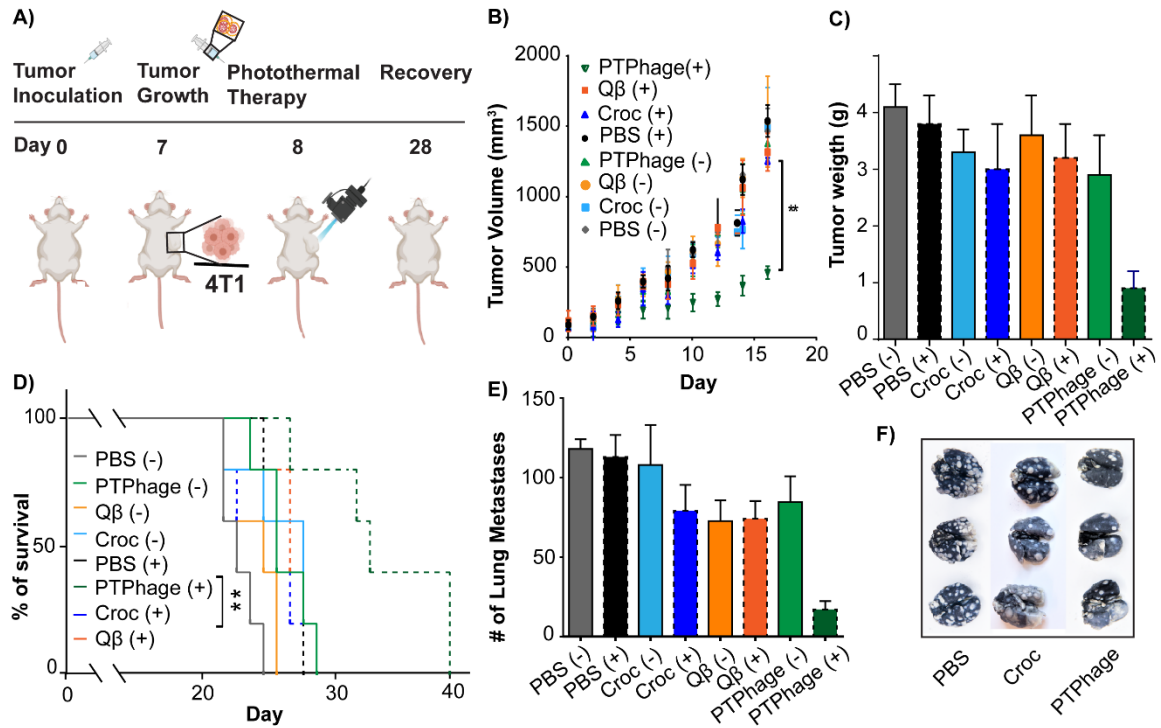


Figure 1.5. A) Experimental design of synergistic immunophotothermal therapy. B) Tumor growth curves of 4T1 tumor-bearing mice treated with PBS, Q β , Croc, and PTPhage with and without laser radiation showing the most effective therapeutic approach is attributed to PTPhage, which exhibited the greatest restriction to tumor growth. C) Tumor weight as a representation of tumor suppression verified high antitumor performance of PTPhage compared to Croc, Q β , and PBS groups. D) Survival study of 4T1 tumor-bearing BALB/c mice (n = 5). E) Number of lung nodules after India ink staining showed PTT modified VLP has significant effect in controlling metastasis. F) Representative images of India ink-infused lungs of irradiated Croc, PTPhage, and PBS mice with white spots clearly demonstrate number of metastatic nodules per each group. Reproduced with permission from reference 42.

1.4 Immunotherapy

Cancer immunotherapy works by stimulation of the immune system and is a strong method for inducing effective cellular and humoral immune responses, through vaccine and T cell infusion technologies, or through activating inhibitory antibodies on cancer cells.^{92,93} Virus like particles mimic the structure of viruses and their repetitive, highly-ordered antigenic structure can be recognized as a pathogen associated molecular patterns (PAMPs) by immune cells.⁹⁴ VLPs can directly interact with pathogen recognition receptors (PRRs), which are expressed on the cell surface and in endosomes of antigen presenting cells (APCs) — most notably dendritic cells (DCs) — and thus have been successfully used as adjuvants to elicit an immune response.⁹⁵ Activated DCs can process antigens into peptides for presenting on major histocompatibility complex class I/II (MHC-I/II) molecules that result in the creation of B7-1/CD80 and B7-2/CD86 costimulatory molecules and express pro-inflammatory cytokines that are necessary to prime the development of T cell and B cell immune responses.⁹⁶ The size distribution of VLPs is also within the optimal particle size range (20–200 nm) allows for drainage to lymph nodes for distribution throughout the lymphatic system to initiate a robust immune response by interaction with different cell types in the secondary lymphoid organs.^{95,97,98} Therefore, VLPs are able to induce T cell activation, which is related to antigen interaction of a T lymphocyte with APCs in secondary lymphatic tissue. T cells, including CD8⁺ cytotoxic T lymphocytes (CTLs) and CD4⁺ helper T cells, are key effector cells for anti-cancer immunity.⁹⁹ CTLs are able to kill tumor cells and activate APCs, following cytokine production, and creating a pro-inflammatory environment. CD4⁺ T cells, that are divided into different subtypes T_H1 and T_H2, induce cytokines that assist CTLs in killing tumor cells.¹⁰⁰ However, it is usually difficult to induce efficient CTL responses because of inefficient access of

exogenous antigens to the MHC class I pathway.^{94, 101} VLPs are capable of entering into both MHC I and MHC II presentation pathways and can therefore activate CD8⁺ T cells and direct them against cancer cells. VLPs with packed RNA during production can engage toll-like receptors (TLRs) including TLR7/8 and TLR3 and trigger innate immune responses.¹⁰² While the ability of VLPs to produce a cellular response has been confirmed by several clinical and preclinical studies, the power to amplify and provoke a specific type of immune response shows how VLPs are a powerful and flexible platform that can be chemically or genetically functionalized with innate stimuli such as antigens and epitopes of interest. Decorating surface of VLPs with different ligands including peptides, proteins, nucleic acids, and small molecules have shown promising results for applications in cancer immunotherapy and developing cancer vaccines.¹⁰³

The main strategy for the presentation of these targeting moieties is through bioconjugation with exposed amino acid residues on VLPs, addressed by various chemistries such as click chemistry, NHS ester acylation, and coupling reactions.¹⁰⁴ One interesting example of using VLPs for cancer immunotherapies is conjugation of PD-1 peptide SNTSESF, known as AUR7, to the 30 nm icosahedral, plant-based CPMV.¹⁰⁵ It is reported that CPMV itself can be recognized by TLR2 and TLR4 to activate the innate immune system while the RNA inside CPMV can activate TLR7.^{106, 107} As shown in Figure 1.6, a two-step bioconjugation strategy is used to couple the PD-1 peptide to CPMV, by first attaching a bi-functional (NHS)-PEG8-maleimide (SM-PEG8) linker to the lysine groups on the surface of CPMV through NHS-amine chemistry for amide formation. The second reaction is between the cysteine-terminated peptide and the maleimide on the linker, which resulted in the decoration of the surface of CPMV with 25 peptides. Therefore, the multivalent display and high concentration delivery of SNTSESF combined with the intrinsic immunogenicity

of CPMV showed a promising synergistic effect in the treatment of mice bearing serous ovarian tumors. Data showed mice treated with several doses of peptide decorated CPMV had prolonged survival time significantly compared to free peptide and to a physical mixture of CPMV and peptide, demonstrating the enhanced effect of multivalent presentation combined with the immunogenicity of the formulation. Another example of using a VLP in cancer immunotherapy combined with their functionalizability was reported¹⁰⁸ by Wu *et al.* They generated a library of 20 peptides of mucin-1 (MUC1), which is highly expressed by many types of cancer cells. The peptides were fused to the surface of Q β through an alkyl amide linker. They immunized mice with three different tumor models: B16 melanoma cells, MCF-7 breast cancer cells, and a metastasis model. Results showed the Q β -immunized mice had a significant reduction in the number of metastases in the lung.

VLPs have also demonstrated increased humoral or antibody-mediated immunity by displaying foreign antigens on their surface. Humoral immunity begins with antigen engulfment by naïve B cells followed by transportation of the antigen to the lymph nodes. Through the production of cytokines, B cells differentiate into antibody secreting plasma cells, some of which are deemed as long-living plasma cells or memory B cells.¹⁰⁹ VLP-based humoral immunity such as cellular response is attributed to the size, repetitive geometric shape, and their TLR-agonizing ability. They are taken up by DCs or pass directly through lymphatic tissue, allowing for their downstream interaction with B cells. The highly ordered and repetitive structure of VLPs is recognized by B cell receptors (BCRs) and leads to a Th-dependent humoral immune response.¹¹⁰ The use of a VLP as an epitope scaffold has shown to produce a higher antibody titer response. Literature has reported covalently attaching epitopes to the surface of VLPs can enhance antibody response

significantly.¹¹¹ However, self-immunity — specifically in cases of cancer-related neoantigens — remains a large challenge in immunotherapy. The use of highly repetitive structure, which can be decorated with a multitude of neoantigens, overcomes the self-immunity associated with many previous vaccination strategies. For example, Palladini *et al.* demonstrated¹¹² with membrane protein HER-2 (Figure 1.6A) that is overexpressed in breast cancer cells, displayed on a VLP (Figure 1.6B) was able to induce a specific antibody response. The HER-2 VLP vaccination prophylactically reduced spontaneous tumor occurrence in HER-2 transgenic mice by 50-100%. Also, the HER-2 VLP vaccination significantly reduced tumor growth and survival in wild-type mice injected with HER-2 expressing carcinoma.

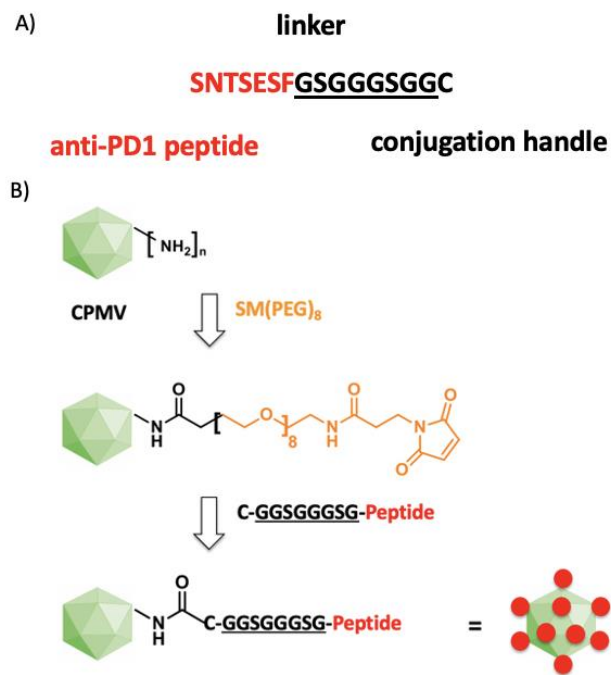


Figure 1.6. A) The amino acid sequence of the anti-PD-1 peptide SNTSESF with carboxy-terminal cysteine residue. B) Bioconjugation is formed first by attaching a bi-functional NHS-SM-PEG8 linker to a solvent-exposed amine group from lysine residues on CPMV, which provide maleimide groups for subsequent reaction with cysteine side chain of anti-PD1-peptides. Adapted from reference 112.

VLPs, such as Q β and MS2, are also often employed as cargo-loaded scaffolds for various immunological agents such as CpG or anti-cancer drugs, like doxorubicin, or modified with antigens/targeting linkers, such as macrolide antibiotics¹¹³ for lung cancer targeting or peptide p33¹¹⁴ for melanoma tumor cells. The functional properties of VLPs can be further developed by not only antigens and targeting ligands but also encapsulating genetic materials, such as mRNA and siRNA. VLP capsids protect these materials from enzymatic degradation and detection by the body's immune system, resulting in sufficient delivery and therapeutic response.¹¹⁵

1.5 Encapsulation

In addition to modifying the exterior surface of VLPs, the interior of icosahedral capsids can also be exploited for the delivery of various cargo. Three main methods exist for loading cargo into icosahedral VLPs. The first is to disassemble the VLP into its subunit proteins and reassemble the capsid in the presence of the cargo (Figure 1.7).¹¹⁶⁻¹¹⁹ During disassembly, the VLP is incubated with a chelating agent, such as egtazic acid (EGTA) or ethylenediaminetetraacetic acid (EDTA), to destabilize the capsid and a reducing agent, such as dithiothreitol (DTT), to break the disulfide bonds that bridge the pores. A denaturing agent, such as urea or glacial acetic acid, can also be used to help break down the capsid into individual coat proteins. This disassembly is done in a high salt solution to precipitate the RNA, which can be aided by the addition of nucleases and metal salts. The precipitated RNA is pelleted, and the coat protein solution is dialyzed and purified by size exclusion chromatography — usually Sephadex gel filtration — to remove excess salts and provide a pristine solution of VLP coat proteins. The coat proteins are then combined with the cargo of interest and dialyzed against a stabilizing high salt solution for reassembly. If needed, hydrogen peroxide can be added to help promote reformation of the disulfide bonds. It should be

noted that the ratio of coat protein to cargo should be optimized to achieve maximal loading efficiency.^{120, 121}

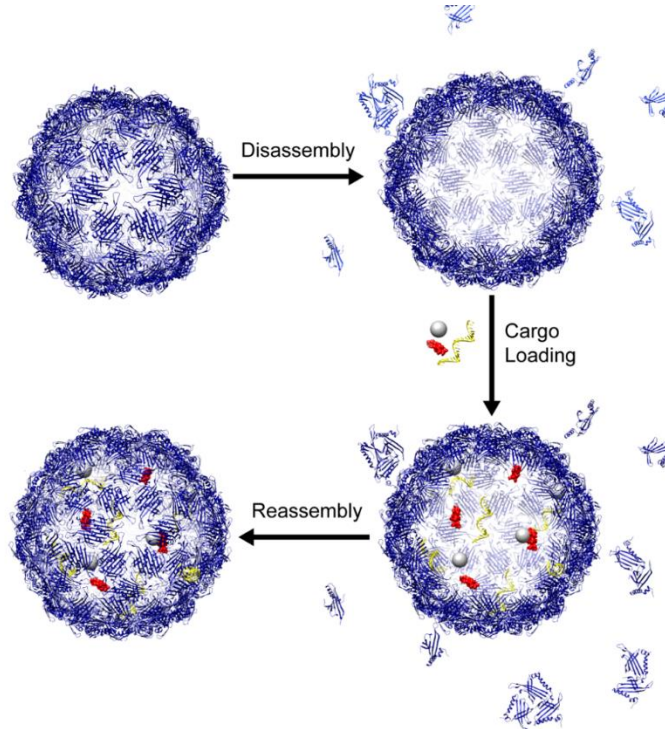


Figure 1.7. Encapsulation of cargo — *e.g.*, protein, nucleic acid, and/or small molecules — into the interior of an icosahedral VLP via disassembly/reassembly method.

This method was inspired by the inherent action of VLPs to spontaneously assemble around nucleic acids and is driven by favorable interactions between coat protein-coat protein, coat protein-cargo, and cargo-cargo. Two proposed methods exist to detail the VLP assembly around a negatively charged cargo; (1) coat proteins assemble as a group in a disordered fashion and cooperatively arrange themselves to form an ordered capsid or (2) the coat protein-coat protein interactions are stabilized by the nucleic acid and instigate a nucleation growth mechanism with the sequential addition of coat proteins.¹²² The preferred method of assembly is determined by the ionic strength of the solution; the former occurs primarily at low ionic strength whereas the latter

occurs at higher ionic strength. Furthermore, individual coat proteins may electrostatically interact with an RNA motif that signals packaging of the viral genome during VLP expression.¹²³⁻¹²⁶ Ashley *et al.* exploited⁷⁶ this trait by conjugating *pac* site RNA to quantum dots, drugs, and ricin toxin A-chain to mediate encapsulation of these cargo in the interior of the MS2 capsid during reassembly.

A second method to introduce cargo inside of a VLP — also possibly the simplest — is via diffusion through surface pores. VLPs often have small pores and if the cargo of interest is a small molecule, it can simply enter the interior of the capsid through these pores. For the icosahedral viruses, the surface pores are ~2 nm in size.⁷⁷ Small molecules can diffuse into the interior of the capsid where they weakly bind to the charged coat protein or RNA, forming a low leakage drug carrier. For example, Franke *et al.* electrostatically immobilized the cationic anticancer drug (cisplatin) on the anionic inner surface of TMV.¹²⁷ Similarly, RNA-free capsids can be produced and then loaded with foreign genetic material via a “soaking” method that allows DNA to enter the interior of the capsid through the pores of the VLP, followed by binding of the stem loop to interior residues for oligodeoxynucleotide (ODN) retention.¹²⁸ In order to generate RNA-free capsids, the VLP is dialyzed against a high salt solution of physiological pH which causes the capsid to swell and become susceptible to nuclease action.^{129, 130} Treatment with nucleases results in degradation of the RNA, and after purification by density gradient centrifugation, RNA-free VLPs are obtained.¹¹⁶

The third method is to design a recombinant plasmid containing the coding sequence of the VLP coat protein, the mRNA sequence of interest, and the RNA motif sequence that binds the interior residues of the capsid. When this plasmid is expressed in a host system, the mRNA is encapsulated

in the VLP during capsid formation by exploiting the interaction between the interior residues of the capsid and the RNA motif.¹³¹⁻¹³⁶ A dual plasmid expression system can be used if the promoters are compatible. This method has also been adapted to encapsulate proteins in the VLP capsid during expression. Fielder *et al.* used¹²⁶ a dual plasmid expression system to co-express the VLP Q β coat protein, a Rev-tagged cargo enzyme, and a bifunctional mRNA aptamer. The α -Rev tagged aptamer binds to the Rev-tagged protein and the interior residues of the capsid through a hairpin loop resulting in enzyme encapsulation during *in vivo* assembly. These methodologies can be employed for the delivery of various cancer therapeutics including nucleic acids for gene therapy and small drug molecules for chemotherapy.

1.6 Gene Therapy

Gene therapy is a new technology being developed for the treatment of a wide variety of diseases, including cancer. This treatment method focuses on the delivery of foreign genetic material into cells to produce a therapeutic effect through the replacement or inactivation of a disease-causing gene.¹³⁷ For example, the p53 tumor suppressor gene that regulates cell division and cell death is mutated in over 50% of human cancers.¹³⁸ If this gene was replaced in cancer cells, the growth and spread of the cancer could be slowed. The first gene therapy product was actually a recombinant human p53 adenovirus for the treatment of head and neck cancer that was approved by the China Food and Drug Administration (CFDA) in 2003 and hit the market in 2004.¹³⁹ In 2017, the first gene therapies were FDA approved and as of now, there are ~20 FDA approved gene therapies, with thousands in clinical trials.¹⁴⁰⁻¹⁴² With this exploding technology, there is a significant amount of ongoing research dedicated to developing new and improved gene therapies.

The main obstacles facing gene therapies center around the fact that genetic material (DNA/RNA) is easily degraded by nucleases, is not targeted or efficiently taken up by cells, and can be degraded by lysosomes upon endocytosis.^{143, 144} As a result, several methods have been developed to improve the efficiency of intracellular gene delivery including cell stressing (electroporation, heat shock), physical methods (injection, biolistic), nanoparticle-mediated delivery (liposomes, polymers, and nanoparticles), and viral vector delivery.¹⁴⁵ Of these methods, viral vector delivery is most commonly employed with adenovirus vectors used to deliver DNA and lentivirus vectors to deliver RNA.¹⁴⁶ However, these vectors lack a targeting mechanism and sometimes result in side effects.^{147, 148} As compared to other nanoparticle delivery systems, VLPs are more robust, biocompatible, monodisperse, and functionalizable and better suited for this task.

Icosahedral VLPs (CCMV, MS2, and Q β) have been favored for gene therapy applications because of their small size (~28 nm) as they can carry genetic material in their internal cavity, providing protection against nucleases. The positive surface charge of these VLPs means they can be readily taken up by cells and have the potential to shield the strong negative charge of the nucleic acid cargo. Furthermore, the surface of these VLPs can be functionalized with ligands for targeted delivery of genes to reduce off-target effects, and for endosomal escape to protect cargo from lysosomal degradation. The chemical modifiability of VLPs have made them strong candidates for gene delivery formulations with the means to overcome the current challenges facing the field today.

Each of the above methods have been used to efficiently encapsulate genetic cargo in VLPs for gene therapy,¹⁴⁹ however dual plasmid¹³² and disassembly/reassembly¹²¹ are most commonly employed. For example, Lam *et al.* used¹¹⁵ a disassembly/reassembly method (Figure 1.8A) to

encapsulate siRNA targeting FOXA1 in the cowpea chlorotic mottle virus (CCMV) for the treatment of breast cancer. Initially it was found that the CCMV-siRNA was unable to silence the expression of FOXA1 in the breast cancer cell line MCF-7. However, after modifying the surface with the cell penetrating peptide, M-lycotoxin peptide L17E, the formulation was able to escape the endolysosomal compartment and achieve silencing that was comparable to lipofectamine delivery (Figure 1.8B). On the other hand, Chang *et al.* packaged¹⁵⁰ the long non-coding RNA tumor suppressor gene, maternally expressed gene 3 (MEG3), in MS2 via a dual-plasmid expression system. After purifying the VLPs-MEG3, the surface was crosslinked with the dodecapeptide YHWYGYTPQNVI (GE11) to target the epidermal growth factor receptor (EGFR) that is overexpressed on many carcinoma cells (Figure 1.8C). With this targeted formulation, the authors were able to demonstrate hepatocellular carcinoma (HCC) tumor suppression *in vitro* and *in vivo* (Figure 1.8D). With the help of VLPs, researchers have been able to overcome the main challenges facing gene therapy today by providing a multivalent system that can both protect genetic cargo from nuclease degradation and offer targeted, efficient delivery. In addition to encapsulating genetic materials, VLPs can carry a high dose of various anti-cancer drugs and improve chemotherapy treatments by targeting delivery to cancer cells and minimizing the side effects on healthy cells.

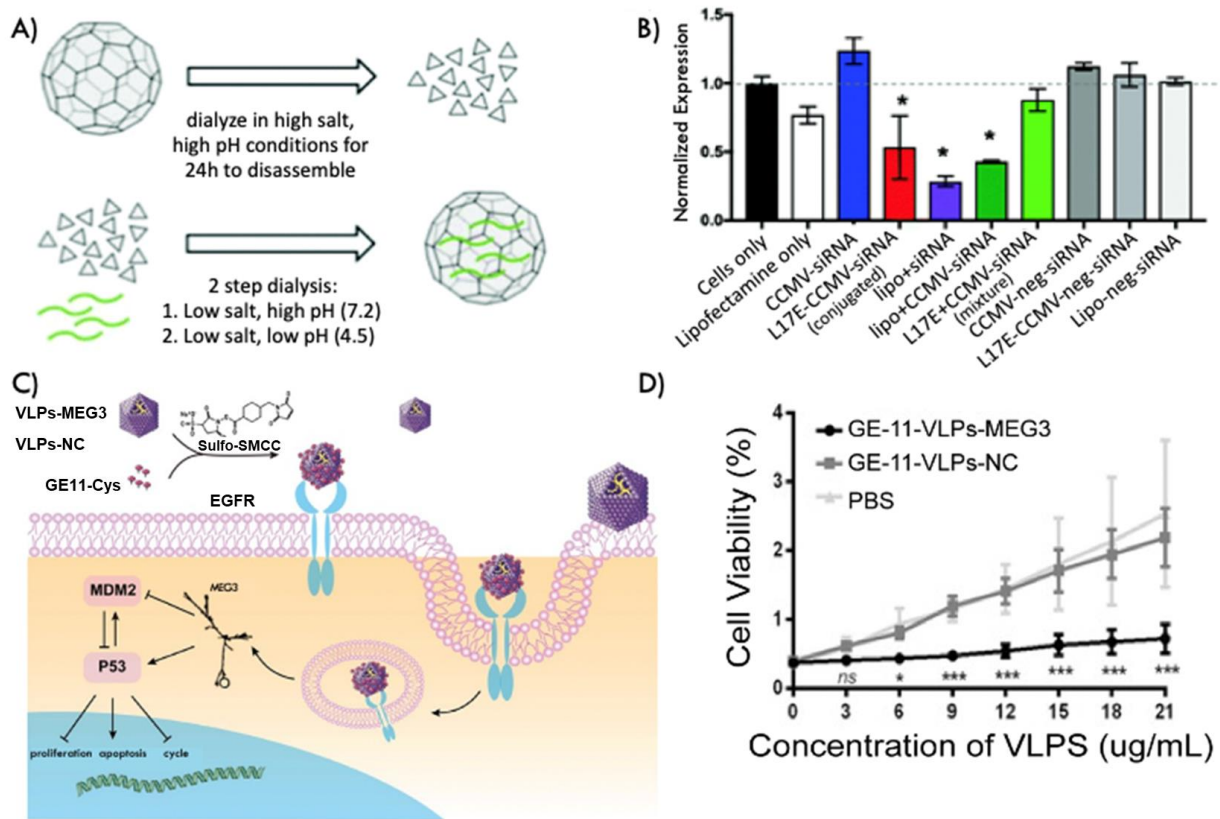


Figure 1.8. A) Disassembly of CCMV into coat proteins and subsequent reassembly in the presence of the siRNA to make CCMV-siRNA. B) FOXA1 expression levels in MCF-7 breast cancer cells following treatment with siRNA as determined by real time PCR. Reproduced with permission from reference 115. C) Encapsulation of MEG3 in MS2 by dual plasmid expression and subsequent modification with GE11 targeting peptide to make GE11-VLPs-MEG3. This formulation represses tumor growth by upregulating p53 expression and downregulating MDM2 expression. D) Proliferation of HepG2 hepatocellular carcinoma cells following treatment with GE11-VLPs-MEG3 as measured by CCK-8 viability assay. Reproduced with permission from reference 150.

1.7 Chemotherapy

Chemotherapy is the most common anti-cancer treatment. Chemotherapeutic agents are small molecules that kill and inhibit the growth and spread of cancer cells, typically by targeting fast growing cells. Common therapeutic agents such as doxorubicin, cisplatin, and 5-fluorouracil tend to be broadly cytotoxic, and when introduced systemically, they cause harsh side effects.¹⁵¹ The

use of chemotherapeutics to effectively fight cancer while minimizing the systemic side effects remains an issue in anti-cancer research.¹⁵² The use of nanocarriers such as VLPs is one way to effectively target tumors while minimizing toxicity in healthy tissues.¹⁵³ Some advantages of VLPs over traditional nanoparticles as drug vehicles include their biocompatible and biodegradable nature, straight-forward production, and enhanced cellular uptake.¹⁵⁴ Importantly, the ability of VLPs to effectively deliver therapeutic agents is attributed to the enhanced endocytic uptake of the capsid over the free drug. Once endocytosed and trafficked into the lysosome, the capsid is degraded, releasing the anti-cancer drug.

As previously discussed, there are multiple methods to encapsulate cargo inside VLPs. VLPs possess a natural affinity for encapsulating anionic moieties, which mimic their native viral genome, making them well-suited for RNA delivery.¹⁵⁵⁻¹⁵⁷ Similarly, encapsulation of therapeutics can be achieved through the denaturation of the coat protein followed by the renaturation of the capsid around the negative charge of new cargo or by taking advantage of the RNA stem loop (*pac* site) that mediates coat protein self-assembly.^{123, 132} Many VLP capsids are porous in nature to protect their encapsulated genome while allowing the diffusion of water and ions. These porous capsids allow for the infusion or diffusion of small molecules such as chemotherapeutic agents across the VLP.¹⁵⁸ Yildiz *et al.* loaded¹⁵⁹ CPMV with proflavine by utilizing the affinity of the drug towards the interior, negatively charged RNA. It was demonstrated the CPMV lacking RNA was not able to load the drug cargo. This method resulted in anti-cancer activity across several cancer cell lines. Introducing “smart” behavior into VLPs to control drug release has also been developed. Benjamin *et al.* loaded⁹⁰ doxorubicin non-covalently into Q β through infusion of the drug. Doxorubicin — which is positively charged and hydrophobic — weakly binds to the single-

stranded RNA inside Q β . Following drug loading, photolytically active gold nanoparticles were grown onto the pores, guided by disulfide residues, effectively capping the pores of the VLP (Figure 1.9A). Using nanosecond laser irradiation, the group was able to target drug release in specific locations resulting in cell death. Upon irradiation, AuNPs converted the light energy to heat, causing the breakdown of the capsid. Doxorubicin was then released from the capsid and shows cytotoxic effects in cells only in the laser pathway. This specificity is attributed to the nanosecond irradiation, which prevented the heating of the bulk of the solution. Upon incubation alone, AuNP@Q β (Dox) showed high cell viability after 4 h incubation with RAW macrophages, whereas free Dox showed a significantly lower cell viability (Figure 1.9B). The *in vitro* release of Dox in A549 lung cancer cells was observed only after irradiation, as demonstrated below through live cell fluorescent imaging (Figure 1.9C-E).

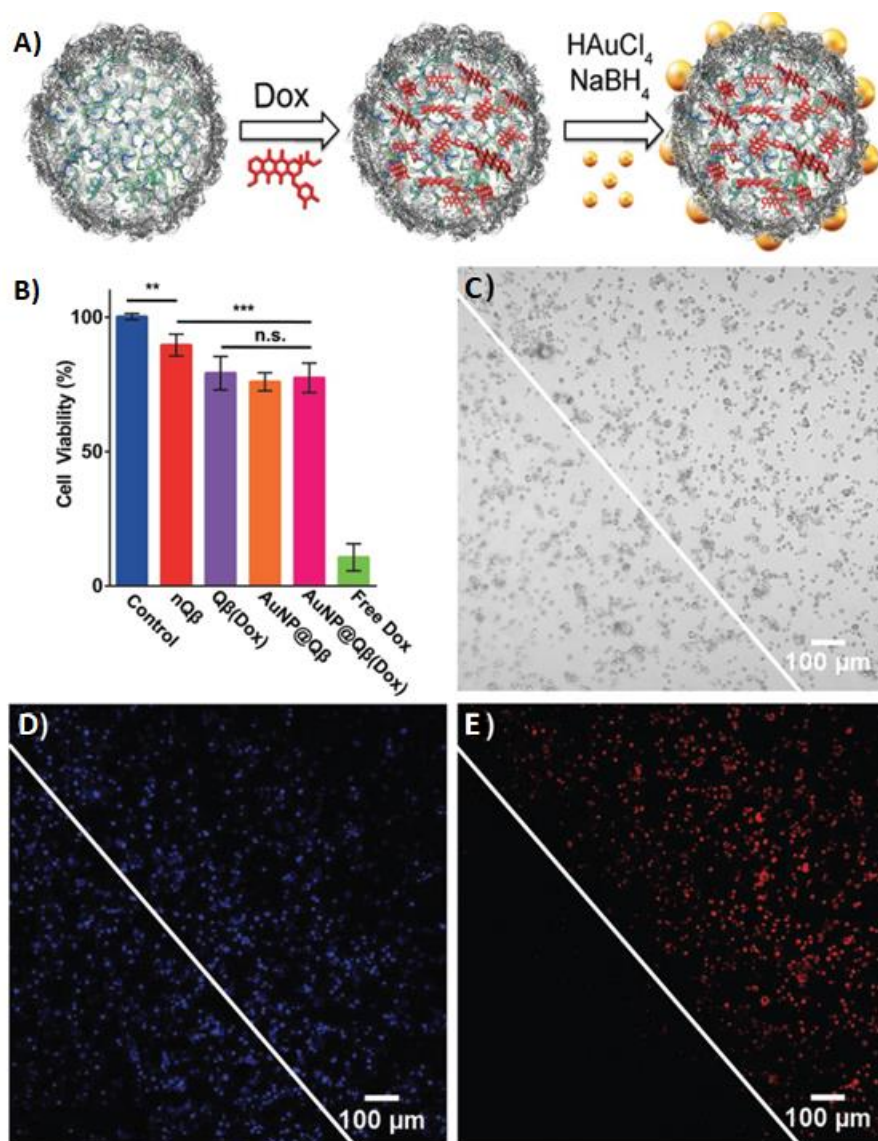


Figure 1.9. A) Qβ possesses 32 pores (1.5 or 3.0 nm) allowing for the diffusion of doxorubicin in or out of the VLP. Pores are then capped with 6 nm AuNPs. B) Cytotoxicity analysis after 4 h incubation of Qβ /gold nanoparticle composites. C-E) Wide-field live cell images depicting doxorubicin release post irradiation, right side depicts laser treated: C) bright-field, D) nuclear stain, Hoechst 33342 nuclear dye, and E) doxorubicin (λ_{Ex} 470 nm, λ_{Em} 560 nm). Reproduced with permission from reference 90.

1.8 Conclusion

Virus-like particles are self-assembled from viral structural proteins with incredibly organized scaffolds. These biocompatible and nontoxic particles are widely used in nanomedicine and show special promise for cancer therapies. Their capabilities to be modified genetically and chemically on their outer surface and inner cavities through amino acid chemistries and self-assembly processes offer specific targeting, stability, and solubility. They are considered not only as excellent packaging and delivery tools for anti-cancer drugs and genetic materials, but also a powerful platform to display antigens, epitopes, PT agents, surfactants, polymer coatings, and ligands in a dense repeating array to improve therapeutic efficiency. Moreover, VLPs can engage both the innate and adaptive immune systems even without any adjuvants in a similar way to pathogens. These smart multifunctional nanocarriers can act as potential combinational therapeutics with existing strategies such as phototherapy, immunotherapy, gene therapy, and chemotherapy. The success of these protein-based nanoparticles with well-designed structures offers a more powerful toolbox for clinical cancer treatment in the near future.

CHAPTER 2
PHOTOTHERMALPHAGE: A VIRUS-BASED PHOTOTHERMAL
THERAPEUTIC AGENT

Authors – Arezoo Shahrivarkevishahi*, Michael A. Luzuriaga, Fabian C. Herbert, Alisia C. Tumac, Olivia R. Brohlin, Yalini H. Wijesundara, Abhinay V. Adlooru, Candace Benjamin, Hamilton Lee, Perouza Parsamian, Jashkaran Gadhvi, Nicole J. De Nisco, and Jeremiah J. Gassensmith

The Department of Chemistry and Biochemistry, BSB13.102

The University of Texas at Dallas

800 West Campbell Road

Richardson, Texas 75080-3021

Reprinted with permission from Shahrivarkevishahi, A.; Luzuriaga, M. A.; Herbert, F. C.; Tumac, A. C.; Brohlin, O. R.; Wijesundara, Y. H.; Adlooru, A., V.; Benjamin, C. E.; Hamilton, L.; Parsamian, P.; Gadhvi, J.; De Nisco, N., J.; Gassensmith, J. J., PhotothermalPhage: A Virus-Based Photothermal Therapeutic Agent. *J. Am. Chem. Soc.*, **2021**, *143* (40), 16428-16438. Copyright 2021 American Chemical Society.

2.1 Introduction

Photothermal therapy (PTT) has emerged as a localized, noninvasive, and highly specific cancer treatment strategy that takes advantage of the heat sensitivity of cells to induce cellular death in tumors.¹⁶⁰⁻¹⁶² The cellular death and injury promote the formation of damage associated molecular patterns (DAMPs) that aid in generating a systemic immune response against tumor sites.¹⁶³⁻¹⁶⁵ Typically, to achieve an efficient thermal ablation in the tumor microenvironment (TME), heating over 50 °C is required.¹⁶⁶ The induced inflammation kills cancer cells by impairing protein and DNA function in addition to turning “cold” immune-dysfunctional TMEs into “hot” immunological environments by stimulating the production and release of DAMPs that prime the formation of activated dendritic cells and promote the production of cancer killing CD8⁺ T-cells.^{167, 168} An important factor to induce an effective immunological response in PTT treatment is using efficient photoabsorbers, particularly those that absorb light in the near-infrared (NIR) region (700–1100 nm), where biological molecules like hemoglobin and melanin are the most transparent.¹⁶⁹ Organic-based photoabsorbing molecules and inorganic nanomaterials are the most commonly employed preclinical photothermal agents (PTAs) that absorb light in the NIR region and facilitate efficient heat production.^{170, 171} The NIR region allows for deeper light penetration through skin and several photothermally active NIR organic molecules, such as heptamethine^{172, 173} and phthalocyanine^{174, 175} represent an ongoing area of research. Problematically, many of these dyes, including the clinically approved indocyanine green (ICG), degrade rapidly from a self-inflicted generation of reactive oxygen species (ROS), which necessitates repeated dosing for effective PTT treatment.^{176, 177} One approach to overcome these issues is with the use of inorganic PTA-like nanostructures,¹⁷⁸ carbon nanomaterials,¹⁷⁹ and iron oxide nanoparticles,¹⁸⁰ which have

shown strong absorption cross-sections and high photothermal stability; however, metal-nanoparticles, particularly those made from gold, are generally not biodegradable and remain inside the body for long periods.¹⁸¹ Finding a balance between high photothermal stability and pharmacokinetics is a key challenge in selecting suitable photothermal materials to simultaneously improve the therapeutic effect of PTT and fulfill its clinical efficiency. Recently, croconium dyes have shown promise as they possess high NIR extinction coefficients, low fluorescence quantum yields, and high photostability making them promising candidates for photothermal therapy.^{182, 183} Indeed, recent work has shown they have photothermal efficiencies comparable or even surpassing those of gold nanostructures and ICG.¹⁸⁴ However, their *in vivo* performance is restricted by poor aqueous solubility, self-aggregation, short circulation half time, quick diffusion from tumor tissue, and rapid clearance from the body.^{185, 186} We wondered if by combining the superior photophysical properties of the croconium system with a biodegradable nanoparticle platform, we could circumvent this problem and produce a next-generation PTT agent that induces effective thermal ablation while also adjuvanting PTT's immune-activating properties.

Virus-like particles (VLPs) are noninfectious self-assembled protein-based nanoparticles derived from the self-assembled coat proteins of viral capsids and are promising candidates for next-generation bioorganic-based photothermal agents. VLPs are biocompatible, biodegradable, thermally stable, monodisperse, and show polyvalent chemical modifiability, which all provide unique opportunities to design bespoke compositions with programmed function.¹⁸⁷⁻¹⁹⁴ Their highly organized and symmetric nature and nanometer size (20–200 nm) allow them to be taken up by toll-like receptors (TLRs) on antigen-presenting cells (APCs) as pathogen-associated molecular patterns (PAMPs) and drained to local lymph nodes to interact with immune cells. These

properties have made VLPs attractive in a broad range of systems such as, drug delivery, photodynamic therapy, vaccination, gene therapy, and imaging.¹⁹⁵⁻²⁰⁷ VLPs expressed in bacteria (i.e., *E. coli*), including bacteriophage Q β , incorporate nucleic acids (RNA) during the assembly process in host cells (*E. coli*) that can alter the adaptive immune response through the engagement of the packed RNA with different pattern recognition receptors (PRRs). Nevertheless, most VLPs are inefficient in inducing a robust cytotoxic T lymphocyte and T helper cell response by themselves. Thus, we wondered if the mild immunogenicity of Q β would synergistically work with NIR light-activated hyperthermia to promote a more robust anti-cancer immune response that combines all the positive features of gold nanostructures (efficient thermal conversion) with free croc dyes (biodegradability).

In this work, we take advantage of the self-adjuvanting and site-specific functionalizability of bacteriophage Q β to engineer a photothermal and the mildly immunogenic phage (or VLP) we call PhotothemaPhage (PTPhage). The formulation is an effective photo-immunotherapy system in a triple-negative breast cancer tumor model in BALB/c mice with lung metastasis. Specifically, we show that VLP Q β (Figure 2.1A), a 30 nm icosahedral nanoparticle that can be expressed in high yields, possesses exceptional thermostability, and has multiple functional handles for bioconjugation,²⁰⁸⁻²¹² serves as a powerful photothermal agent following functionalization with hundreds of croconium dyes. Not only can PTPhage sustain significant bulk photothermal heating *in vitro* and *in vivo* without denaturing, but the nanoparticle formulation also shows a significant enhancement in photothermal performance over free dye and considerable improvements in solubility. Moreover, PTPhage is taken into cells better than free croconium dye and achieves significantly greater heating *in vivo* than equimolar concentrations of free dye. Finally, in proof-

of-principle immunological studies, we find that this contribution not only causes higher *in vitro* and *in vivo* thermal cytotoxicity but also improves T-cell and dendritic cell activation over the well-known mildly immunomodulatory features of VLP Q β .²¹³⁻²¹⁶

2.2 Results and Discussion

Photothermal Phage Synthesis and Characterization

As shown in Figure 2.1A, our approach for the covalent modification of bacteriophage Q β begins with synthesizing a symmetric croconium dye. Q β VLP is composed of 180 identical capsid proteins, each with four reactive primary amine groups (three lysines and N-terminus) exposed to the outer surface, presenting a total of 720 potential sites for Croc dye labeling. Bioconjugation was employed using N-hydroxysuccinimidyl (NHS) ester activated Croc (Croc-NHS) as a site-specific and amine-reactive reagent. The resulting symmetric dye can potentially crosslink two VLPs, which produces aggregates that precipitate out of solution. To avoid this, the ratio and concentration of dye to Q β , incubation time, and purification procedures needed optimization. We found that 1:4 mole ratio of Q β to dye and 12 h incubation time produced the best colloidal stability, particle size, and dye loading for our final product, PTPhage. Denaturing polyacrylamide gel electrophoresis (Figure 2B left) shows an upward shift of the subunit bands of PTPhage, indicating an increase in the molecular weight compared to Q β . Native agarose electrophoresis of the conjugate, which is visually seen as the blue band in the bright field image in Figure 2.1B center, shows greater migration toward the positive electrode compared to unfunctionalized Q β (Figure 2.1B, right), in line with the expected greater negative charge from the free carboxylates. Product morphology was confirmed by transmission electron microscopy (TEM) and dynamic light scattering (DLS) analysis (Figure 2.1C) at 25 °C, which shows a nearly unchanged

hydrodynamic radius from unfunctionalized Q β (32.95 ± 0.12 nm) following attachment of the Croc dye (33.10 ± 0.15 nm). The total number of dyes per capsid was determined to be approximately 1.2 by UV-Vis analyses, giving an average of 212 dyes per VLP.

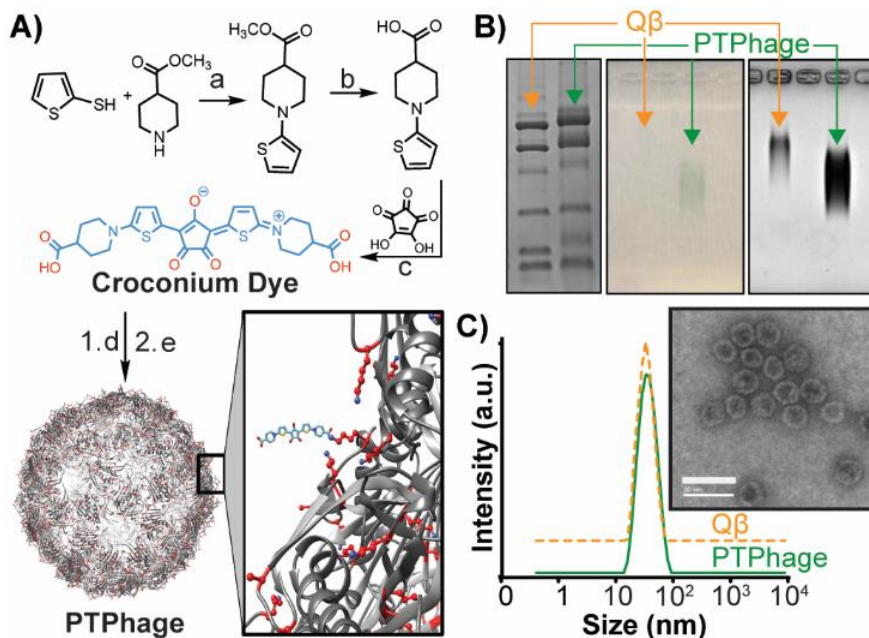


Figure 2.1. A) The overall synthetic bioconjugation strategy involves synthesizing the croconium dye by arefluxing commercially available starting materials methyl isonipecotatate and thiophene-2-thiol. b) The resulting ester was deprotected under alkaline conditions and c) the final dye, Croc (thiophene-croconaine dye), was produced in the condensation reaction with croconic acid. The free acids were deactivated as n-hydroxysuccinimide (NHS) esters and added under dilute conditions to a solution of Q β to prevent cross-linking. The functionalized Q β was incubated briefly in water to hydrolyze the remaining NHS esters back to the free acid. B) Electrophoresis mobility analysis of Q β before and after conjugation on SDS-PAGE (left) and agarose (center and right) gels show successful bioconjugation of dye to Q β . Non-reducing SDS-PAGE shows an increase in molecular weight of Q β after bioconjugation. The unstained agarose (center) shows a green band in bright light in the same spot in which a Coomassie-stained band (right) appears. The conjugate travels further toward the (+) electrode, which is anticipated from the replacement of lysines with carboxyl functions. C) DLS and TEM (insert scale bar = 50 nm) of Q β and PTPhage demonstrate that the conjugation of croconium dye does not affect the size or polydispersity of the VLP.

Dyes used in PTT are most efficient when they are intensely colored and cannot dissipate energy through radiative relaxation pathways, *e.g.*, fluorescence, or electron transfer, or intersystem crossing. Croc is well suited for this as it has strong NIR absorption ($\lambda_{\max} = 783 \text{ nm}$, $\epsilon_{\max} = 2.0 \times 10^5 \text{ mol}^{-1} \text{ cm}^{-1}$ in water),²¹⁷ negligible fluorescence, and low oxygen photosensitization — which also improves its photostability — a known issue with ICG and the extensively investigated heptamethine dyes. We were pleased to find that PTPhage exhibits a strong NIR absorption maximum ($\lambda_{\max} = 783 \text{ nm}$) identical to that of free croconium dye, yet the absorption spectrum is significantly broadened (Figure 2.2A). This broadening is pronounced in the NIR region, which promotes more efficient conversion of clinically used lasers (emissions centered at 808 nm).

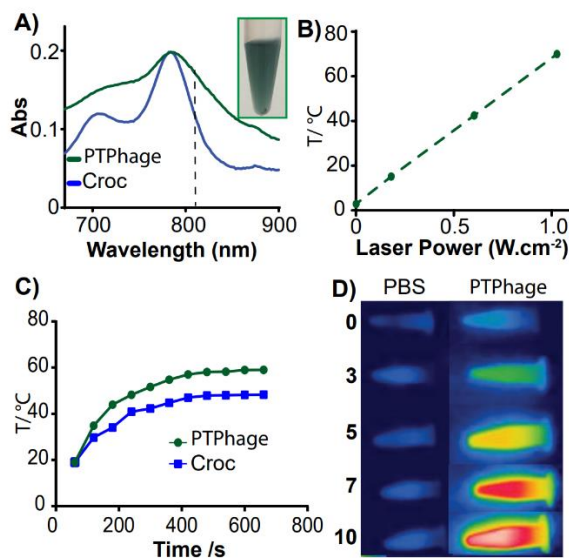


Figure 2.2. UV-Vis Spectrographic analyses of equal molar concentrations of chromophores for Croc and PTPhage show A) a broadening of the NIR absorption of PTPhage (green line) compared to croconium dye (blue line). A photograph of PTPhage is shown in the insert. B) A linear relationship exists between PTPhage (30 $\mu\text{g} \cdot \text{mL}^{-1}$) solution temperature increases and laser power after 3 mins of irradiation (laser power was set 0.0015, 0.18, 0.604, 1.02 $\text{W} \cdot \text{cm}^{-2}$). C) Photothermal heating profile of PTPhage and Croc at the same concentration (30 $\mu\text{g} \cdot \text{mL}^{-1}$) after 11 min of laser irradiation (808 nm, 0.18 $\text{W} \cdot \text{cm}^{-2}$) shows a significant difference in temperature

increase (40.1°C for PTPhage and 29.1°C for Croc). D) Temperature variations of PTPhage and PBS under laser irradiation are mapped and quantified by a thermal camera. No noticeable temperature increase was observed in PBS under the 808 nm laser irradiation (0.18 W·cm⁻²) at different time points.

This effect was made apparent when we compared the bulk solution photothermal response of PTPhage and free dye. Both solutions containing an identical concentration of chromophore (30 µg·mL⁻¹) were fitted with a thermocouple and placed in front of a thermal camera. Temperature change in each solution was monitored over 11 min of laser irradiation at 808 nm and 0.18 W·cm⁻². As seen in Figure 2.2C, the solutions showed a marked difference in heating rates and maximum temperature with PTPhage showing a ΔT of 40.1°C and a T_{max} of 59.1°C compared to free dye (ΔT : 29.9°C T_{max} = 48.5 °C). Additional laser irradiation experiments have been done to investigate photothermal properties of PTPhage at different laser powers (0.0015, 0.18, 0.604 and 1.02 W·cm⁻²), times of radiation (1–10 min), and various concentrations (0.1–1 mg· mL⁻¹) of PTPhage. For instance, we found an increase in the bulk temperature of the solution that is linear with laser power (Figure 2.2B and Figure A10). Collectively, the PTPhage appears to have superior photothermal properties compared to free dye, which allows for lower laser power density and dye concentration, potentially reducing side effects on normal tissue. To show that the 808 nm laser does not change the temperature of the water itself, we irradiated a solution of buffer and PTPhage (Figure 2.2D and A10) and observed no temperature change in the PBS solution, whereas we could heat a solution of PTPhage from room temperature to 61 °C with an 808 nm laser at 0.18 W·cm⁻².

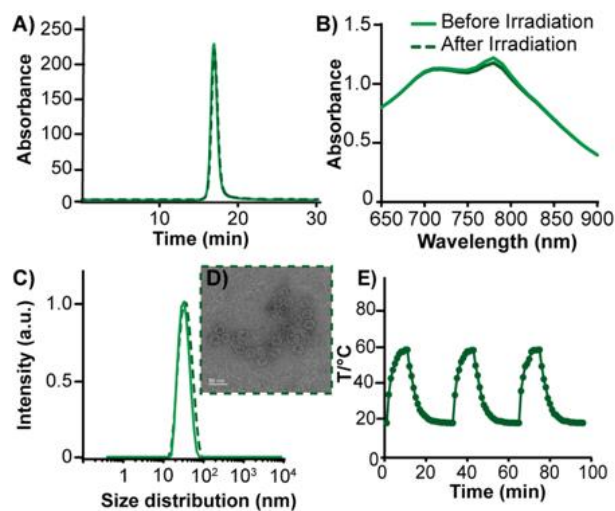


Figure 2.3. A) Photothermal stability of PTPhage after 10 min of laser irradiation ($0.18 \text{ W}\cdot\text{cm}^{-2}$) is shown by intact HPLC profile of PTPhage before and after radiation. B) No significant change in absorption spectra of PTPhage after laser-induced heating for 10 min. C) DLS and D) TEM data (scale bar is 50 nm) prove thermal stability of PTPhage with no morphology change after 10 min of laser irradiation. E) Thermal cycling of PTPhage shows no change in heating profile after three cycles.

The photothermal stability of the PTPhage complex was proven by comparing size distribution, absorption, and size exclusion chromatography before and after 10 min of continuous laser irradiation ($0.18 \text{ W}\cdot\text{cm}^{-2}$) as shown in Figure 2.3A-D. The results showed no photobleaching, aggregation, or structural change, indicating high photostability of the system. To demonstrate the remarkable stability of the PTPhage, we performed a thermal cycling experiment. A PTPhage solution ($30 \mu\text{g}\cdot\text{mL}^{-1}$ of Croc concentration) was irradiated repeatedly (808 nm , $0.18 \text{ W}\cdot\text{cm}^{-2}$), and the temperature was monitored over the heating and cooling cycles, as shown in Figure 2.3E. The PTPhage showed impressive photothermal durability—we tested its photothermal behavior by radiating a single sample for 10 min intervals over 10 days and monitored the heating and cooling curve (Figure A.11) and found no obvious change in the maximum temperature or cooling curve. In line with strong absorbance in the NIR region and high photostability, we further determined

the photothermal efficiency of the PTPhage and compared it with existing photothermal materials — free Croc dye and gold nanorod (AuNR).²¹⁸ We found that the PTPhage has higher photothermal conversion efficiency (77%) compared to Croc alone (70%) and AuNR (68%), which is in line with the literature (Figure A12). From these results, we believe that the high photostability, durability, and remarkable photothermal conversion efficiency of PTPhage make it a good candidate for PTT.

PhotothermalPhage *In Vitro* Cytotoxicity

Cellular uptake of both PTPhage and free Croc was assessed on 4T1 (murine breast cancer) cells. Because Croc lacks fluorescence, we determined uptake by measuring the amount of remaining dye in the supernatant after a 4 h incubation period. In a typical experiment, PTPhage and Croc were added to cell media in equal chromophore concentrations, and after 4 h, the cells were removed, the media filtered, and the total absorption at the λ_{\max} was compared before and after. All concentrations were within the linear range of Beer's law, allowing direct calculation of before and after concentrations. As shown in Figure A.13, cellular uptake of PTPhage is about twice that of croconium dye. Croc, being negatively charged, is very unlikely to partition into the cell, and so these results were not surprising. Next, for the *in vitro* phototoxicity in 4T1 cells, the photoablation efficiency of PTPhage and Croc was determined by incubating identical concentrations ($3.1 \mu\text{g} \cdot \text{mL}^{-1}$) in cell culture. After 4 h incubation at $37 \text{ }^\circ\text{C}$, cells were washed with PBS and fresh phenol red-free media to remove any remaining dye. Before laser irradiation, the microwell plate was equilibrated to $37 \text{ }^\circ\text{C}$, as it has been shown in previous studies that initial temperature (RT vs $37 \text{ }^\circ\text{C}$) has a significant effect on the *in vitro* PTT efficiency. All four experimental groups were exposed to an 808 nm laser for 10 min ($0.18 \text{ W} \cdot \text{cm}^{-2}$). The next day, cell

viability in each well was determined by MTT assay. As shown in Figure A.14, all formulations before laser radiation showed low toxicity, whereas the cell viability of PTPhage dropped dramatically to 17% while free Croc dropped to only 65% after laser radiation. We attribute this greater cell killing to the improved cellular uptake and therefore greater intracellular heating. These results were qualitatively confirmed through visual analyses of cell viability via a live/dead cell assay (Figure A.14). With these results in hand, we conducted *in vivo* anti-tumor studies to see if we would observe similarly improved response with PTPhage. To further check the biocompatibility of the formulation, we tested cell viability in two different cancer cell lines, 4T1 breast cancer and T42 epithelial bladder cancer cells, after treatment with PTPhage, Croc and Q β using LDH cytotoxicity assay. As shown in Figure A15 and Figure A16 there was no sign of toxicity in the PTPhage group.

Photothermal Anti-tumor Response *In Vivo*

We assessed the anti-tumor effect of our system in the same murine mouse cancer model discussed above. 4T1 cells (1×10^6) were implanted into the abdominal mammary gland of 4–6-week-old female BALB/c mice. One day before injection, the fur was removed from the spot of injection (tumor site) for better monitoring of tumor growth and tumor volume measurement using calipers. Tumor development was allowed to proceed until the average tumor size reached 5–6 mm, after which mice were randomly divided into four groups with radiation and four groups without radiation for various treatment: PBS (negative control), Q β , and identical concentrations (by chromophore) of Croc and PTPhage. Following randomization, mice from each group (n=5) were injected intratumorally²²⁰ (50 μ l) in a single location in the tumor site using an insulin syringe. We allowed two hours for the injections to diffuse through the tumor microenvironment and then

laser treatment was performed (808 nm, 0.18 W·cm⁻², 10 min) as schematically shown in Figure 2.4A and the tumor temperature was monitored using a thermal camera (Figure A.18-and A.19). Intratumoral injections with photoactive therapeutics make sense since the tumor must be accessible for irradiation. The effect of treatment was evaluated by monitoring the body weight of the mice and measuring tumor volume over 16 d. Tumor volumes were measured using calipers every other day after treatment and calculated according to the equation: $Vol = (tumor\ length) \times (tumor\ width) \cdot 2/2$. The tumors treated with PTPhage plus laser irradiation developed a sizeable black scab on the tumor site and showed slower tumor growth compared to all other experimental groups. The bodyweight of each group was monitored over 16 d, and we found no significant change, which suggests PTPhage, Q β , and Croc did not induce toxicity (Figure A20). Furthermore, to observe pathological toxicity, H&E staining of the major organs of the mice including heart, liver, lung, and kidney were performed after treatment of the mice with PTPhage, Croc, Q β , and PBS. As shown in Figure A17 neither adverse effects nor significant histological abnormality in the treatment group was found, suggesting high biocompatibility of our formulation. The irradiated Croc dye and Q β by itself slightly delayed the growth of the primary tumor though nowhere near as much as the PTPhage formulation, which caused obvious tumor ablation after NIR laser exposure. The degree of tumor ablation and resection induced by different groups was further confirmed through tumor volume and tumor weight Figure 2.4B and 2.4C. As shown in Figure 2.4D, PTPhage again produced significant suppression on tumor growth compared to Q β and Croc alone. H&E and TUNEL staining of the tumor showed lower nuclei count and cell density as well as the highest apoptosis of tumor cells in PTPhage compared to other groups (Figure A22). Survival of the different groups of treated tumor-bearing mice was studied

over 38 d following the initial tumor inoculation. As shown in the Kaplan–Meier survival curve, illustrated in Figure 2.4E, only PTPhage prolonged survival time compared to other groups. Metastatic burden was evaluated at day 16 post-treatment by removing the lungs and staining them with India ink, which preferentially blackens healthy tissue making the metastasis stand out. Control groups (PBS) and unirradiated free Croc show statistically identical tumor burdens, as illustrated in Figure 2.4E, Figure 2.4F and Figure A.21. The unaltered Q β and irradiated free Croc groups all produced a modest and statistically significant decrease in metastatic burden. Summarily, the anti-tumor activity of PTPhage appears to be improved over free croc.

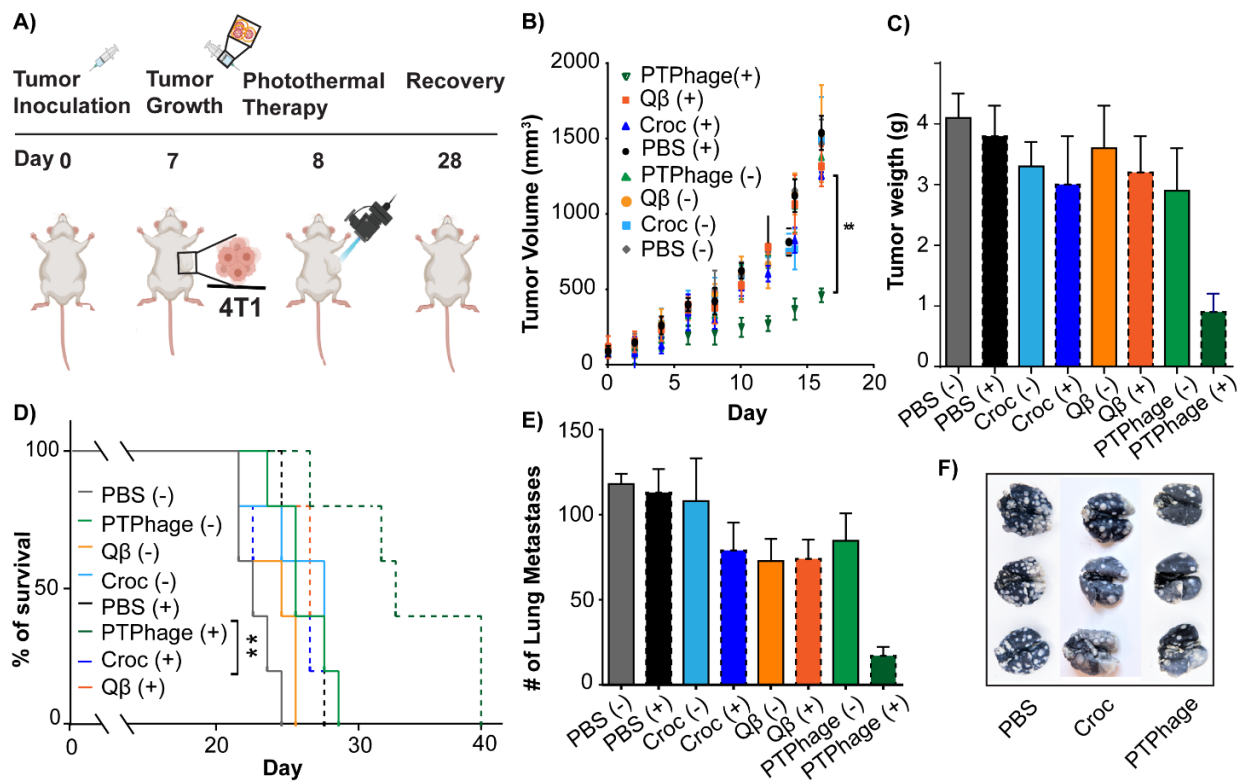


Figure 2.4. A) Experiment design of synergistic immunophotothermal therapy. B) Tumor growth curves of 4T1 tumor-bearing mice treated with PBS, Q β , Croc and PTPhage with and without laser radiation showing the most effective therapeutic approach is attributed to PTPhage which exhibited the greatest restriction to tumor growth. C) Tumor weight as a representative of tumor suppression verified high anti-tumor performance of PTPhage compared to Croc, Q β , and PBS groups D) Survival study of 4T1 tumor-bearing BALB/c mice (n = 5). E) Number of lung nodules

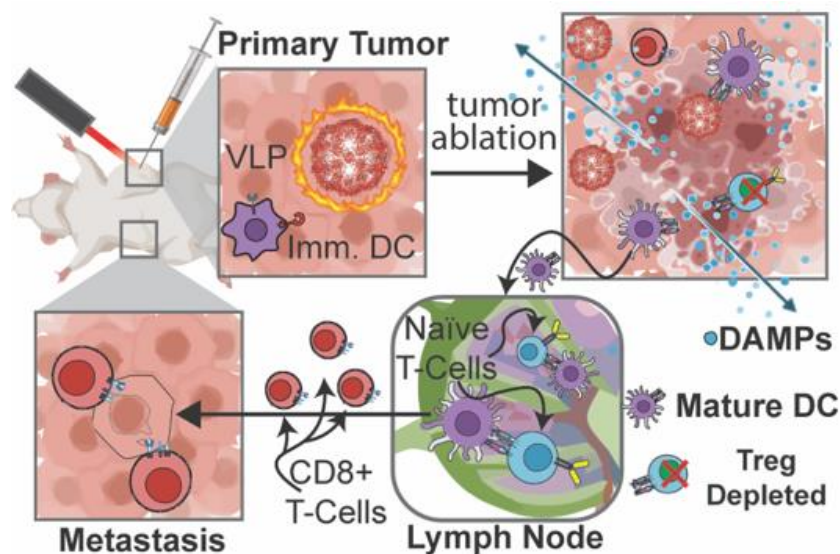
after India ink staining. F) Representative images of India-ink-infused lungs of irradiated Croc, PTPhage and PBS mice with white spots clearly demonstrate number of metastatic nodules per each group. ** $p < 0.05$.

Immunological Studies

While the scope of this work is primarily the synthesis and anti-tumor response of PTPhage, we wondered if the VLP was enhancing the immunological response initiated by the PTT. Detailed anti-tumor immunological studies will be addressed in subsequent work. Our initial focus in this part of the study was the assessment of dendritic and T-cell activation and an assessment of any downregulation of protective T-cell (Treg) response. In anti-tumor immunity, dendritic cells (DCs) are an important and effective class of APCs that plays a pivotal role in initiating and regulating innate and adaptive immunities.²²¹ Generally, immature DCs ingest foreign materials through different surface receptors, including pattern recognition receptors that trigger their maturation.^{222,}²²³ PRRs detect PAMPs (derived from microorganisms) and DAMPs (produced by the body's dying cells). Mature DCs can process antigens into peptides for presenting on major histocompatibility complex class I/II (MHC-I/II) molecules that coincide with increased expression of B7-1/CD80 and B7-2/CD86 costimulatory molecules. Following maturation and antigen exposure, DCs migrate into the draining lymph node—where contact is mediated between DCs and T-cells—and promote the differentiation and proliferation of naïve T-cells into cytotoxic T lymphocytes (CTLs), which are key effector cells for anti-cancer immunity.^{168, 224-226} Only mature DCs can elicit anti-tumor effector T-cell responses, which can be determined by assessing DC maturation *in vitro* following exposure to an antigen. It is well-known that VLPs mimic viruses in their size, structure, and antigenic epitopes.^{227, 228} Their 20–200 nm size is in the optimal diameter range that can directly drain to the lymph node. In addition, because of their regular

polyhedron structure and highly repetitive surface feature, VLPs are sensed as PAMPs by PRRs on the surface of DCs. Furthermore, the encapsulated nucleic acids also can be recognized by PRRs and promote DC maturation for priming CD4⁺ T helper lymphocytes and CD8⁺ cytotoxic T lymphocytes.²¹⁵ These cytotoxic T-cells can then fight systemic cancer at metastatic sites.

We first investigated whether Q β stimulates the maturation of DCs by using cultured bone marrow derived DCs (BMDCs) separated from BALB/c mice and incubating them with different concentrations of Q β for 24 h. The expression of DCs maturation markers — proteins called CD80 and CD86 — were determined by staining them with anti-CD80 and anti-CD86 fluorescent antibodies and quantifying them using flow cytometry (FCM). We found that Q β upregulates the expression of CD86 & CD80 and enhances the percentage of matured DCs (CD11c⁺CD80⁺CD86⁺) in BMDCs at all concentrations tested compared to PBS (Figure A23). Next, we focused on evaluating the adaptive immunity triggered by Q β at cellular levels after incubation with splenocytes harvested from a naïve mouse. Again, Q β was mildly able to promote the effector CD4⁺ T helper lymphocytes (CD4⁺CD3⁺CD44⁺CD62L⁻) and CD8⁺ cytotoxic T lymphocytes (CD8⁺CD3⁺CD44⁺CD62L⁻), which show possible immunoadjuvant potential of Q β in the PTPhage system to stimulate anti-tumor immune responses (Figure A.23).



Scheme 2.1. Schematic illustration of PTPhage-initiated photothermally-triggered anti-tumor immune response. An initial photothermal excitation of the VLP causes an increase in temperature, which results in local tissue ablation. This causes local apoptosis/necrosis and the release of immune-stimulating DAMPs. The presence of intact VLP in the ablated tumor environment simulates a potential infection, which causes downregulation of the immunosuppressive response by suppressing Treg cell formation. These responses can be measured in the draining lymph node. In this lymph node, cancer anti-gens collected by activated dendritic cells can present to naïve T-cells, which mature to cytotoxic CD8⁺ cells. These cells can then attack metastatic lesions.

PTT induces apoptosis and necrosis, efficiently destroys tumor cells, subsequently releasing debris containing tumor-associated antigens and chemokines.^{229, 230} These antigens are subsequently taken up by DCs and trafficked to the lymph node, triggering anti-tumor immune responses. Furthermore, DAMPs released from necrotic cancer cells, such as heat shock proteins, calreticulin, and ATP, can also promote DC maturation and assist in activating effector CD8⁺ T-cells that enter circulation to fight against primary and metastatic sites systemically (**Scheme 1**).^{165, 231} Our data shows that Q β can simultaneously act as an immunological agent to promote DC activation and enhance infiltration of CTLs. As shown in Figure 2.2C, PTPhage and Croc both show favorable photothermal effects in a wide temperature range (40–60 °C); thus, we set up our *in vivo* experiment to evaluate immunostimulatory activities of the combinational formulation

compared to PTT alone. BALB/c mice were inoculated with 4T1 cells and grown until they had a primary tumor size of 100 mm³. The mice were separated into four groups ($n=5$) and injected with PBS, Q β , Croc, or PTPhage (same dye concentration as free Croc). Two hours post-injection, they were irradiated with 808 nm laser for 10 min (0.18 W·cm⁻²). We conducted our experiment initially by assessing identical concentrations (the same number of NIR dyes) of PTPhage and free Croc as measured by UV-Vis. The temperature at the tumor surface ends up being higher for PTPhage (54±2 °C) compared to free Croc (40±1 °C) (Figure A18 and A19), which can be ascribed to a more rapid clearance of free Croc from the tumor and greater photothermal efficiency of PTPhage at 808 nm. Three days post-treatment, the mice were sacrificed, and the spleen and draining lymph node were collected to analyze the T lymphocytes and mature DCs by flow cytometry after co-staining with various markers. It is worth noting that post-PTT the populations of immune cells within the tumors were all very low, likely from the photoablation, and getting useful data from the tumors was difficult. Since our interest is in studying how PTPhage adjuvants the effects of ablative PTT, this was anticipated. We were able to get statistically meaningful data from the draining lymph and spleen; however, and these populations are generally useful in measuring local and systemic immune response in cancers.^{232,233} The percentage of matured DCs (CD11c⁺ CD80⁺ CD86⁺) in the draining lymph node from PTPhage was 24% greater than the Croc group, as shown by higher expression of costimulatory molecules CD80 and CD86 (Figure 2.5A), validating PTPhage 's *in vitro* behavior, and showing it can enhance the activation of APCs better than each formulation alone. We also determined how PTPhage affects CD8⁺ T-lymphocyte cells in the draining lymph node and found a significant number of activated (CD44⁺ CD62L⁻) CD8⁺ T-cells in the PTPhage group compared to other treated groups (Figure 2.5B). Number of activated CD4+

and CD8⁺ were also determined in spleen (Figure 2.5C and 2.5D) and found a significant increase in group treated with PTPhage. To exclude the effect of the more efficient photothermal and tumor residency of PTPhage, we analyzed DCs maturation in the draining lymph node when tumor tissue temperature for both PTPhage and croc group reached the same temperature after laser irradiation (this required different amounts of dye in each formulation). Multiple studies show that heating tumor cells at low temperature (39.5–44 °C) enhances blood flow in the tumor and improves the permeability of tumor vasculature and may promote better migration of DCs between tumor and lymphoid organs even if it is not as efficient as a higher temperature range (> 45°C) in destroying the primary tumor. Therefore, we utilized 1.5 µg. mL⁻¹ PTPhage and four times the amount of Croc (6.0 µg. mL⁻¹) to produce a final tumor temperature of approximately 44 °C and maintained this temperature for 10 min by 808 nm laser irradiation. Intriguingly, as shown in Figure 2.5E and 2.5F, we observed the same general trends where PTPhage outperforms free dye significantly in stimulating DC and T-cells. Consequently, we do not think that temperature alone explains the anti-tumor results reported above.

We next assessed T-cell responses to PTPhage. The population of activated effector CD8⁺ cytotoxic T-cell (CTL—CD8⁺CD44⁺CD62L⁻) and activated CD4⁺ T-helper cells (T_H—CD4⁺CD44⁺CD62⁻) were quantified in spleens by FCM after various treatments. Compared to either Croc or Qβ alone, the combination treatment resulted in 2.10-fold increase in helper CD4⁺ T-cell and 2.12-fold increase in CTL CD8⁺ T-cells compared to Croc. (p < 0.05). Figure 2.5E, 2.5F, 5G and 2.5H. These results collectively demonstrate that PTPhage can act as a powerful photothermal agent along with potentiating PTT's immunological response. The single-cell suspensions of spleens from four different groups of mice were stained with anti-CD11c, -CD4, -

CD44, and -CD62L antibodies to measure how much effector T-cells were expressed after each treatment. As displayed in Figure 2.5G and 2.5H, significant CD4⁺CD44⁺CD62⁻ cells appeared for mice treated with PTPhage. One limitation in most of radiotherapy systems is that, following tissue damage, the tumor microenvironment can develop immunosuppressive cells, which creates an immunological "cold" tumor that restricts the therapeutic performance.^{167, 234, 235} Several studies have reported^{8, 52} that the efficiency of PTT inversely correlates with Treg cells, an immunosuppressive subset of CD4⁺ T cells characterized by the expression of factor forkhead box protein P3 (FoxP3).

Necrotic cell death induced by PTT causes an inflammatory response that promotes the expression of Treg immunosuppressive molecules to prevent the initiation of a strong systemic immune response. We expected that Q β may amplify the immune response, and its presence as a foreign viral protein might "trick" the immune system into turning off this immunosuppressive response. Therefore, we assessed the presence of CD4⁺FoxP3⁺ after different treatments by flow cytometry to investigate the ratio of the effector CD4⁺ T-cells vs. Treg in the spleen—an organ that serves as a systemic repository for the immune system. As expected, and shown in Figure 2.5I and 2.5J, PTT alone produces a suppressive environment while PTPhage—a combination of PTT and the immunoadjuvanting agent Q β —decreased the percentage of Tregs (lower CD4⁺FoxP3⁺). This is significant because cancer therapeutic therapy efficacy is associated with tumor suppression and higher survival time correlates with lower Tregs and higher effector T-cells.

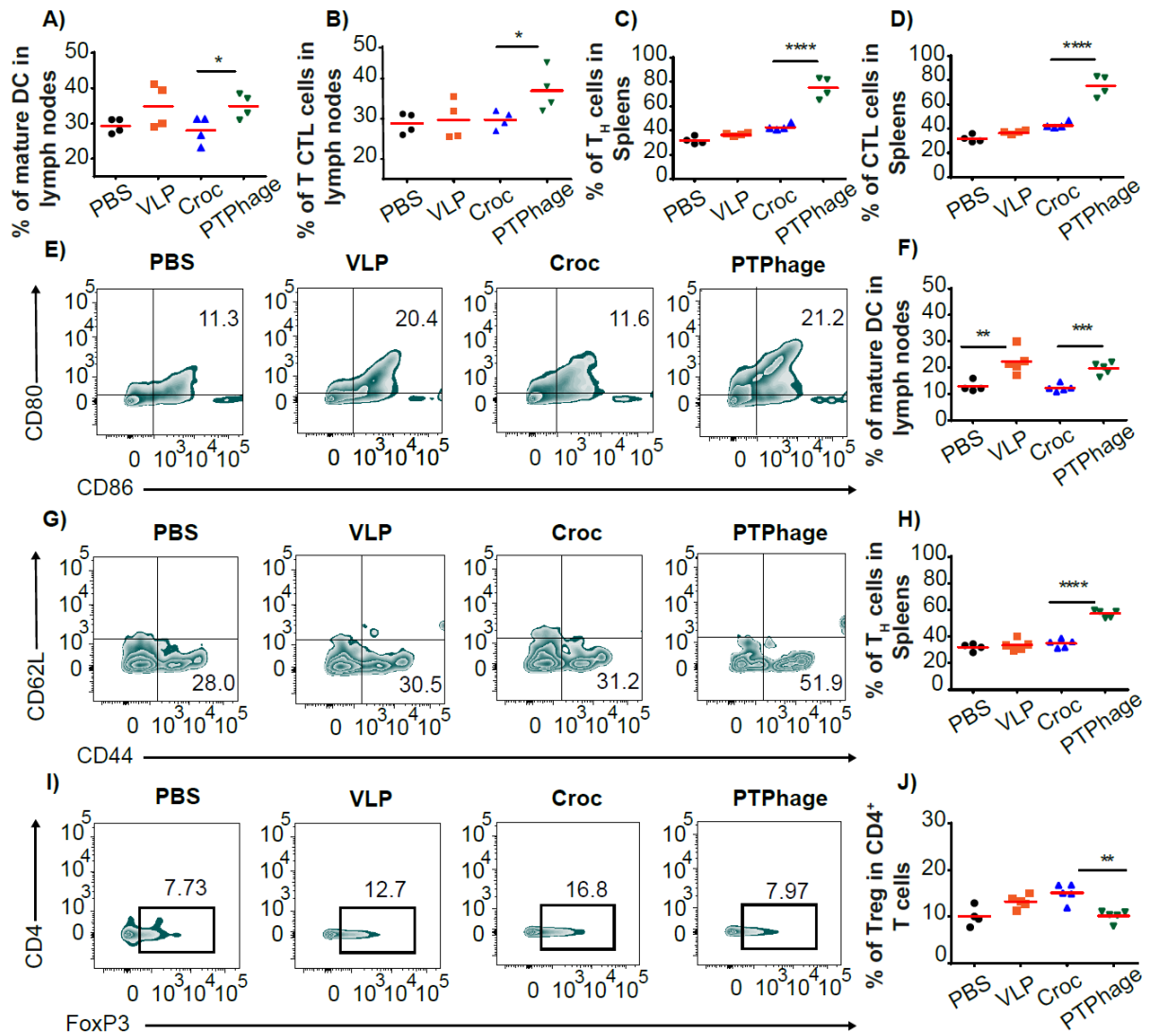


Figure 2.5. In vivo immune responses after photothermal stimulation. A) DC maturation induced by various groups on mice bearing 4T1 tumors (gated on CD11c⁺ DC cells, Figure A24) after PTT treatment (T_{max} = 54.2°C). Cells in the tumor-draining lymph node were assessed by flow cytometry after staining for CD80 and CD86 expressions. B) Quantification of CTLs (CD8⁺) in isolated lymph nodes. C-D) Percentage of activated TH-cells (CD4⁺CD44⁺CD62⁻) and CTLs in spleens. Single-cell suspensions were processed from the spleen and analyzed by flow cytometry after anti-CD3, -CD4, -CD8, -CD44, and -CD62L staining (T_{max} = 54.2°C). E-F) Representative flow cytometry plots showing expression of CD86 and CD80 on DC of draining lymph node for different groups (gated on CD11c⁺, Figure A24) after PTT treatment (T_{max} = 44.0 °C). G-H) Representative flow cytometry plots of effector CD4⁺ in spleen cells of different treatment groups analyzed by flow cytometry (stained with anti- CD3, -CD4, -CD44, and -CD62L) (T_{max} = 44.0 °C). I-J) Representative flow cytometry plots showing percentages (gated on CD4⁺ cells, Figure A24) of CD4⁺FoxP3⁺ T cells in the spleen after various treatments.

2.3 Conclusions

In this work, we took advantage of VLP Q β 's biocompatibility, functionalizability, and modest immunogenicity to produce a new synthetic-biomaterial hybrid PTT "PTPhage". This formulation significantly improved the photophysical properties of Croc, including photothermal conversion efficiency and water solubility, as shown by an enhancement of cellular death upon 808 nm laser exposure than free dye. In addition, this synergistic combination showed excellent NIR light-induced tumor ablation by suppressing 70% of the primary breast cancer tumor in BALB/c mice bearing a highly metastatic 4T1 tumor compared to 18% for Croc alone. PTPhage also prolonged survival time and reduced lung metastasis by 85% compared to control. Our initial immunological screening strongly suggests that the VLP may adjuvant PTT by promoting greater DC, T-helper and Cytotoxic T-cell responses while lowering immunosuppressive Treg cells. These results are intriguing and studies that combine effective Th1 promoting adjuvants, lower intra-tumoral temperatures, and checkpoint inhibitors to promote these effects even more are underway.

All Supplementary Information can be found in Appendix A.

CHAPTER 3

INTRACELLULAR DELIVERY OF VIRUS-LIKE PARTICLES USING A SHEDDABLE LINKER

3.1 Introduction

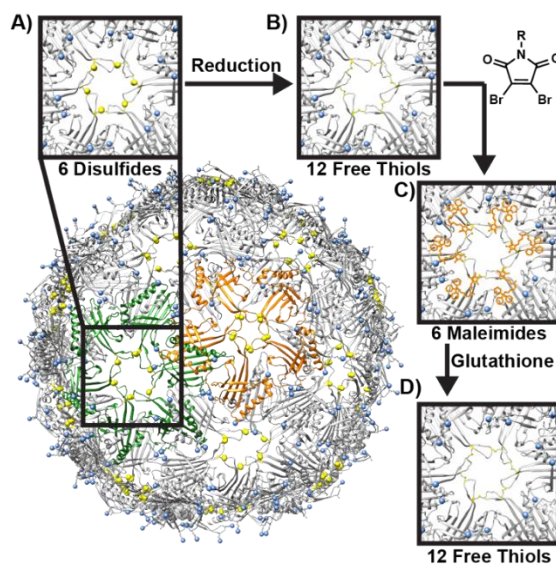
Effective medicine for diagnosing and treating diseases including cancer, genetic disorders, Alzheimer's, and Parkinson's requires access to the cell cytoplasm.²³⁶⁻²³⁹ Cytosolic delivery of nanomaterials and biomacromolecules is fraught with biological barriers—the largest being endosomal escape.²⁴⁰ There are few routes of entry for large or charged macromolecules aside from endocytosis, and once inside the cell endosome, the most likely outcome is eventual lysosomal degradation resulting in low dose of delivery, poor bioavailability, and limited therapeutic efficiency. This limitation has presented itself as a significant challenge, specifically in cytosolic delivery of large and charged therapeutic cargos and targeted delivery of drugs into the intracellular compartment. Therefore, a delivery system capable of escaping the endosome before lysosomal degradation is needed. Some available delivery systems, including hydrogels,²⁴¹ lipid nanoparticles,²⁴² cell-penetrating peptides,²⁴³ and metal-organic frameworks,²⁴⁴ have shown potential in promoting cellular uptake, protecting cargo from enzymatic hydrolysis, and enhancing site-specific delivery. However, these systems suffer from various limitations including, leakage of encapsulated cargo, toxicity, and inefficient delivery that results in low bioavailability.

The small lipophilic cationic molecule, triphenylphosphonium (TPP), has been long exploited as a mitochondrial targeting moiety for small and medium-sized molecules.^{245, 246} Cargo tagged with a TPP moiety can escape the endosome and preferentially bind to the negatively charged

mitochondrial matrix.²⁴⁷⁻²⁴⁹ We wondered if we could promote endosomal escape yet avoid mitochondrial targeting by installing a linker between the nanoparticle and the TPP moiety that degrades once the nanoparticle enters the cytoplasm. TPP is an easily synthesized small molecule with low toxicity and can be chemically functionalized to a wide range of nanoparticle platforms. This provides our approach with a distinct advantage over peptides, which are more costly, more complicated to attach to surfaces, and susceptible to enzymatic degradation.

To demonstrate our approach, we employed a proteinaceous nanoparticle called a virus-like particle (VLP). VLPs have emerged as a promising platform for various therapeutic applications ranging from imaging, gene delivery, and drug delivery.²⁵⁰⁻²⁵³ They are non-infectious, biocompatible, biodegradable, monodisperse, and robust platforms that can carry small molecules,^{254, 255} polymers,²⁵⁶ and/or intact proteins either by supramolecular entrapment within their interior or by chemical conjugation to their surface.²⁵⁷ The bacteriophage Q β is a 28 nm icosahedral engineered VLP with 180 identical coat proteins that self-assembles around random mRNA during expression in *E. coli*.²⁵⁸⁻²⁶¹ We, and others, have shown that the coat proteins of Q β can be disassembled, the random mRNA discarded, and then reassembled around new cargo or genetic material.^{116, 259, 260} Furthermore, Q β possesses functionalizable primary amine groups on three surface-exposed lysine residues (K2, K13, and K16) and the N-terminus (Scheme 3.1) as well as 180 solvent-exposed disulfide groups that crosslink either six or five proteins to form hexameric (Scheme 3.1A) and pentameric subunits, respectively. These disulfides can be reduced (Scheme 3.1B), and the free sulfhydryl groups are effectively “rebridged” in quantitative yields using a maleimide crosslinker (Scheme 3.1C).^{64, 254}

This work demonstrates a “shedtable” cytosolic delivery approach by attaching a TPP containing moiety through a disulfide-bridging maleimide that forms a stable two-carbon bridge between the sulfurs. The maleimide on the VLP readily undergoes retro-Michael additions in the presence of glutathione (Scheme 1D), which is present in millimolar concentrations (10^{-3} M) in the cytosol but micromolar concentrations (10^{-6} M) outside the cell.^{262, 263} *In vitro*, the TPP-functionalized virus undergoes endocytosis, escapes the endosome, and then sheds the TPP-functionalized maleimide linker through a thiol exchange with glutathione in the cytosol. Moreover, we have developed a single-pot approach that allows us to simultaneously reassemble the virus around genetic cargo with a functionalized dibromomaleimide serving to ‘sew up’ the capsid. Finally, as proof of principle, we demonstrate the cytosolic delivery of Q β loaded with Green Fluorescent Protein (GFP) and, in a second example, the cytosolic delivery of siRNA that stops expression of luciferase.



Scheme 3.1. Structure of Q β VLP (exposed nitrogens are labeled in blue, and cysteines are labeled yellow). Hexameric and pentameric structures are colored green and orange, respectively. A) Close-up of one of the hexameric disulfide-lined pores. B) The disulfides can be reduced quantitatively to produce free sulfhydryl groups. C) These can be crosslinked using a

dibromomaleimide reagent. D) The maleimide crosslinkers come off in the presence of glutathione to produce 12 free thiols.

3.2 Results and Discussion

Synthesis and characterization of Q β -M-TPP

TPP has a delocalized positive charge over large hydrophobic phenyl rings, which is known to permeate lipid bilayers and cross into the mitochondrial matrix through non-carrier-mediated transport because of the significant mitochondrial membrane potential.^{246, 264-266} Our approach involves chemically modifying the surface of the engineered VLP Q β using a synthetic linker that separates the TPP from the viral surface once the capsid enters the cytosol. We prepared a dibromomaleimide-triphenylphosphonium (DB-TPP) linker (Figure 3.1A and B) via direct EDC coupling. The dibromomaleimide moiety reacts with thiol groups in a two-step reaction,²⁶⁷ each step having a half-life of seconds.^{64, 268} Q β contains 180 disulfide bonds, each of which can be a potential site for functionalization via this approach. The attachment of DB-TPP to Q β forms a covalent two-carbon “bridge” between the free thiol groups in reduced Q β (Figure 3.1B).^{268, 269} First, Q β is reduced using tris(2-carboxyethyl) phosphine (TCEP), which is confirmed by electrophoretic mobility in non-reducing sodium dodecyl sulfate polyacrylamide gel electrophoresis (SDS-PAGE). The starting Q β pentameric and hexameric subunit bands are shown in Figure 3.1C, which are converted almost exclusively into monomer bands following reduction. Ellman’s assay further confirms reduction against a cysteine standard curve (Figure B1), where approximately 95% of the disulfides on Q β were found to be reduced into free thiols. The bioconjugation was then completed following the addition of the DB-TPP molecule, and within a few minutes, conjugation was confirmed by a significant visible increase in yellow-green

fluorescence under UV light. Electrophoretic mobility using non-reducing SDS-PAGE (Figure 3.1C) shows the reformation of the hexameric and pentameric subunits and a slight upward migration of these bands compared to unreduced Q β . These bands are also fluorescent under UV light, providing further evidence for the successful conjugation of the M-TPP linker to Q β . Native agarose electrophoresis of the conjugate, which is visualized by UV and Coomassie staining, shows less migration toward the positive electrode than unfunctionalized Q β , which is attributed to the additional positive charge from the TPP moiety. Intensity from the newly formed Q β maleimide-TPP conjugate (Q β -M-TPP) can be measured by fluorescence spectroscopy at 540 nm (excitation 400 nm) (Figure 3.1D).⁶⁴ This emergence of yellow fluorescence following the successful displacement of the bromides and formation of the dithiolated conjugate has been attributed to lower self-quenching and a decrease in the frequency of emission-decreasing collisional events with solvent molecules following conjugation.^{64,270} We found no changes in the size of Q β -M-TPP compared to Q β as determined by size exclusion chromatography (SEC) and dynamic light scattering (DLS) analyses (Figures 3.1E and 3.1F) – Q β and Q β -M-TPP have hydrodynamic radii (R_h) of 31.92 ± 10.76 and 31.22 ± 10.36 nm respectively. Transmission electron microscopy (TEM) confirms that the morphology of conjugated Q β -M-TPP is unchanged (Figure 3.1G). ζ -potential measurements show an increase in positive charge on Q β after conjugation, which arises from the cationic nature of TPP (Figure B.2). Lastly, the total number of conjugated linkers per capsid was determined to be approximately 140 linkers (78% of surface disulfide bonds) per Q β by Ellman's assay (Figure B.1)

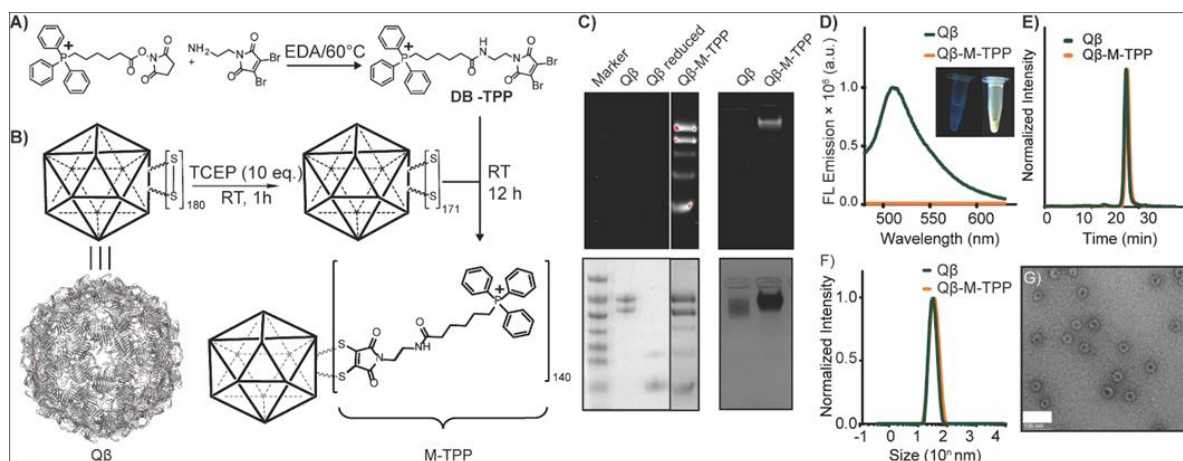


Figure 3.1. A) Synthesis of dibromomaleimide-TTP (DB-TTP) linker followed by B) bioconjugation strategy on Q β . C) Electrophoretic mobility analyses of Q β before and after DB-TTP conjugation using SDS-PAGE (left) and agarose (right) gels showing successful bioconjugation of the maleimide linker to Q β , forming Q β -M-TTP. SDS-PAGE shows the successful reduction of the higher-order structures and their reappearance after conjugating DB-TTP. The fluorescence imaging of agarose (top right) shows the maleimide fluorescence at the same spot of the Coomassie-stained band. D) Fluorescence spectra of Q β -M-TTP and Q β before and after conjugation with DB-TTP (ex/em 400/540 nm) with a photograph showing the reaction mixtures of Q β -M-TTP under 365 nm UV lamp illumination. E) Size-exclusion chromatograph of Q β -M-TTP and Q β . After bioconjugation, F) DLS and G) TEM of Q β and Q β -M-TTP show no aggregation or structural change.

Glutathione (GSH) tripeptide is the most abundant thiol species in the cytoplasm of living cells and acts as a biological reducing agent. The intracellular concentration of GSH is (1–10 mM), whereas the concentration drops to about 1–10 μ M in extracellular matrices.^{271,272} Therefore, the cytoplasm of mammalian cells contains 100–1000 times the amount of GSH compared to the extracellular compartment creating a thiol-rich environment. This environment presents a unique opportunity for the specific and selective cytosolic release of cargo via a thiol exchange reaction with our disulfide-linker on Q β . We hypothesized that the Q β -M-TTP formulation, with its thiol-maleimide bonds, will undergo retro-Michael additions with the abundant GSH, separating most of the TPP from the VLP surface, and forming GSH-M-TTP. To verify this supposition, we labeled dibromomaleimide with the small fluorescent molecule FITC (Figure B.3) and did an *ex-vitro*

thiol-exchange experiment by subjecting the Q β -M-FITC conjugate to conditions that would approximate the cytoplasm (20 mM HEPES, 100 mM KCl, 1 mM MgCl₂, 1 mM EDTA, 1 mM glutathione, pH 7.4, 37 °C).^{36,273} Scrambling of M-FITC linker from Q β onto GSH was analyzed using SEC. As expected, data shown in Figure B.4 indicates cleavage of the M-FITC linker from Q β and attachment to GSH. The starting retention time of Q β -M-FITC is 16.8 min in the SEC trace. After 24 h, however, we observed the formation of new FITC-labeled oligomers of GSH with lower MW compared to Q β , having retention times of 21.3 and 27.9 min. We note that there is still Q β -M-FITC after 24 h, though the peak height decreased about 61% over the course of 24 h. This observation suggests such conjugates have the potential to cleave in the cytoplasm of cells; however, to determine if the amount of cleavage was sufficient, we moved to *invitro* experiments.

Cellular Uptake, Cytotoxicity, and Cytosolic Delivery of Q β -M-TPP

We next moved to *in vitro* studies of the conjugates. A549 human lung cancer cells were employed to evaluate the cell viability, cellular uptake, and cytosolic delivery following treatment with the designed formulation. To visualize the protein trafficking into and throughout the cell, we used fluorescently engineered Q β that contains Green Fluorescent Protein within the viral capsid—Q β (GFP).¹²⁴ The viability of A549 cells following different treatments with Q β (GFP) and Q β (GFP)-M-TPP was measured by 3-(4,5-dimethylthiazol-2-yl)-2,5-diphenyltetrazolium bromide (MTT) assay and compared to that of untreated controls. As shown in Figure 3.2A, we found exceptionally low toxicity even at high concentrations, with cell viabilities greater than 97% following exposure to each formulation at a 2 mg/ml concentration after a 4 h incubation. These results indicate that the Q β particles decorated with M-TPP should have high biocompatibility and low toxicity. Next, we treated cells with Q β (GFP) or Q β (GFP)-M-TPP and quantified cellular

uptake with flow cytometry after fixing the cells. We observed a slight increase in uptake in cells treated with Q β (GFP)-M-TPP, as compared to Q β (GFP), which suggests modifying Q β with the linker does not significantly affect particle uptake (Figure 3.2B). We next used fluorescence microscopy to visualize uptake and cytosolic delivery of Q β (GFP)-M-TPP in fixed A549 cells. The obtained images revealed that the delivered Q β (GFP)-M-TPP was evenly distributed as green fluorescence throughout the cytoplasm (Figure 3.2D) while Q β (GFP) shows punctate fluorescence dots that indicate endosomal entrapment (Figure 3.2C). We also tested the cytosolic delivery of Q β (GFP)-M-TPP vs Q β (GFP) in live A549 cells as shown in Figure B.15A. In the live-cell imaging studies, we observed the same results as in fixed cells. The Q β (GFP)-M-TPP green fluorescence was diffuse in the cells, proving the ability of Q β (GFP)-M-TPP to escape the endosome and reach the cytoplasm; however, we saw very little green fluorescence in live cells treated with Q β (GFP) because it was quenched from the acidic environment of the endosome.¹¹⁶

²⁷⁴ The live cells were also stained with LysoTracker and nuclear stain Hoescht dye as shown in Figure B.16 and B.17. Furthermore, to emphasize that TPP does not deliver Q β (GFP) to the mitochondria because of cytosolic cleavage, the treated and fixed cells were stained with MitoTracker™ Deep Red FM. As shown in Figure 3.2E and 3.2F, there is no overlap between the red fluorescence of MitoTracker and the green fluorescence of Q β (GFP).

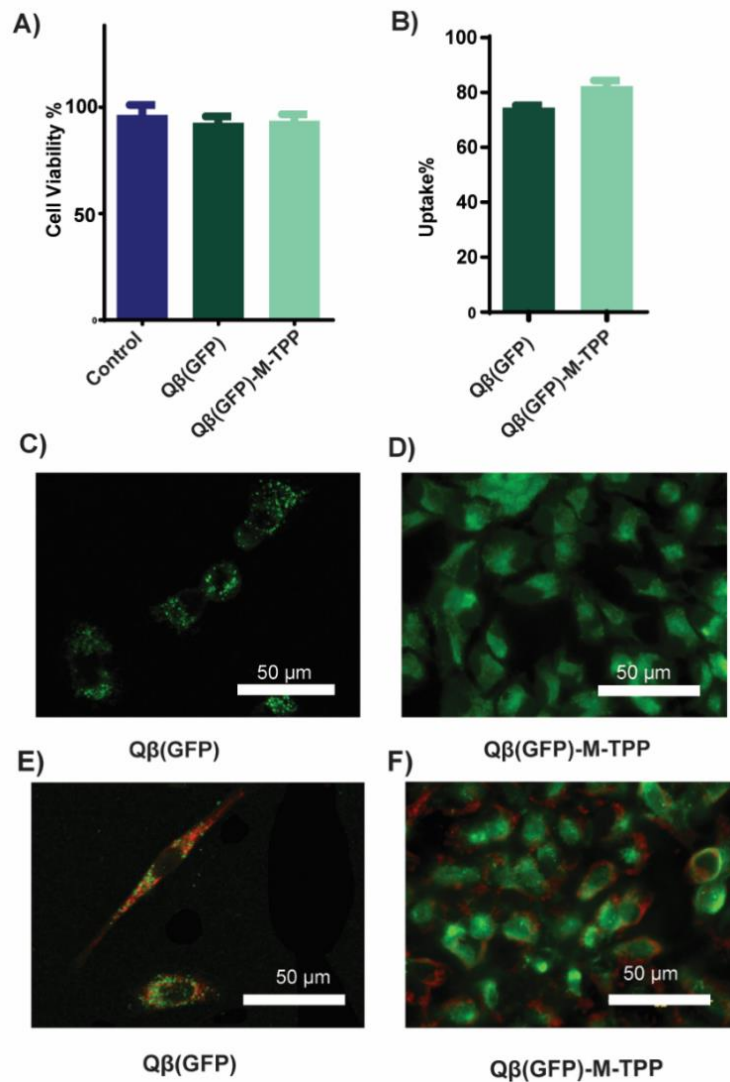


Figure 3.2. A) Cell viability of A549 lung cancer cells after treating with Qβ(GFP) and Qβ(GFP)-M-TPP (2 mg/ml) for 4 h at 37 °C. B) Flow cytometry was used to assess the uptake of Qβ(GFP)-M-TPP and Qβ(GFP) (2 mg/ml) in fixed A549 cells after incubation at 37 °C for 4 h. C) Fluorescence microscopy images of fixed A549 cells treated with Qβ(GFP) showing punctate dots coming from endocytic uptake and D) A549 cells treated with Qβ(GFP)-M-TPP showing diffuse green fluorescence related to the cytosolic release of Qβ(GFP). Color code: green: Qβ(GFP). Scale bar = 50 μm. E) Fluorescence micrograph of Qβ(GFP) and F) Qβ(GFP)-M-TPP in fixed A549 cells stained with MitoTracker showing no mitochondrial colocalization of Qβ(GFP)-M-TPP. Color code: red: MitoTracker Deep Red FM and green: Qβ(GFP). Scale bar = 50 μm.

To further prove the role of the intermediate linker in thiol exchange cleavage and cytosolic delivery, we labeled the lysine residues of Q β with TPP using a non-cleavable linker.²⁷⁵ We expected that functionalizing the Q β surface with TPP without a cleavable linkage would traffic our carrier, Q β , to the mitochondria. To test this, we covalently attached the TPP to the free amine groups on the surface of Q β through NHS ester chemistry (Figure 3.3A). Curiously, unlike the attachment at the disulfides, this functionalization resulted in a sensitivity of the Q β towards ions in the buffer and resulted in poor colloidal stability and precipitation when preparing the sample in cell media (DMEM) for *in vitro* studies. Efforts to control this by reducing the number of TPP molecules to a relative minimum were only modestly successful. We previously found that attaching lipophilic drug molecules to the Q β lysines creates problems for colloidal stability, and by attaching polyethylene glycol (PEG) linkers across the disulfides, we could significantly increase the solubility and stability of the Q β .²⁷⁶ Here, we applied the same strategy and first decorated Q β with dibromomaleimide-PEG at the reduced disulfide bonds followed by attachment of TPP moieties to the free lysines. Bioconjugation conditions were optimized, and particle size, surface charge, and morphology before and after conjugation were characterized, as shown in Figure 3.3B-D. The mitochondria-targeting of Q β -M-TPP was assessed *in vitro* by confocal fluorescence microscopy. Cells treated with Q β (GFP)-M-TPP and stained with MitoTracker Deep Red FM were used to determine the colocalization of the green fluorescence of Q β (GFP) conjugates with the mitochondria (Figure 3.3E). Colocalization was calculated using Pearson's coefficient (ρ) and NIH ImageJ. From the results, the targeted conjugates show greater colocalization with MitoTracker ($\rho = 0.56$) than the non-targeted conjugates ($\rho = 0.28$), suggesting modest colocalization within the mitochondria. Notably, a significant number of particles were

still observed in the endosome/lysosome (punctate dots), but there was no diffuse fluorescence indicative of cytosolic delivery.

Cytoplasmic Delivery of siRNA to Efficiently Silence Luciferase in vitro.

To further verify cytosolic entry and check the applicability of our delivery system, we used Q β -M-TPP to deliver siLuc, a siRNA (small-interfering RNA) probe capable of silencing luciferase expression in HeLa luciferase cells.²⁷⁷ siRNA is a powerful therapeutic tool that inhibits specific messenger RNA (mRNA) expression in the cytosol and effectively downregulates the gene expression processes.²⁷⁸ However, siRNA is highly anionic, has a relatively large molecular weight, and quickly degrades in cell media. Naked siRNA cannot readily penetrate cell membranes and reach the cytoplasm; therefore, we hypothesized that encapsulation of siRNA in Q β -M-TPP could enhance cytosolic delivery and improve gene silencing compared to free siRNA or Q β that lacked cleavable TPP groups.

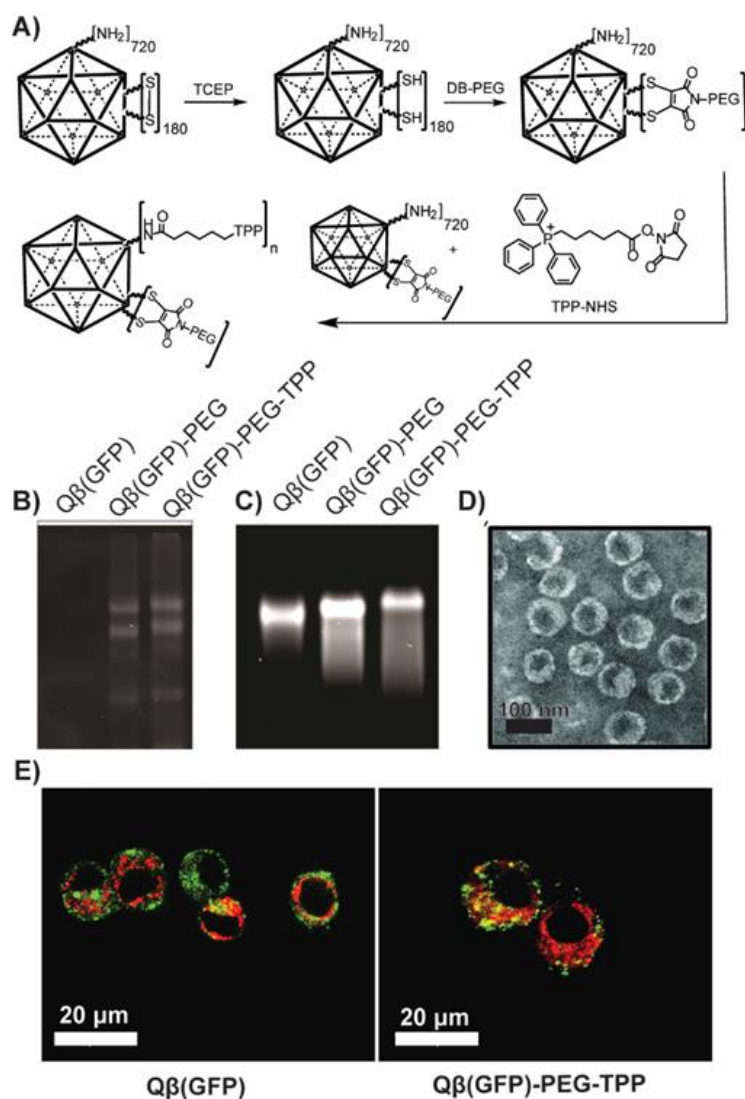


Figure 3.3. A) Conjugation scheme of Q β -PEG-TTP. Q β first is reduced with TCEP, followed by adding Dibromomaleimide-PEG (DB-PEG). Conjugation of TPP-NHS with surface amines is then performed using TPP-NHS. Characterization of Q β -PEG-TTP conjugation B) SDS gel C) 1% agarose gel D) TEM (scale bar: 100 nm). E) Fluorescence micrographs of H2073 cells treated with Q β (GFP) and Q β (GFP)-PEG-TTP. Q β (GFP)-PEG-TTP is driven into the mitochondria with greater colocalization efficiency (ρ), which is calculated using Pearson's coefficient, colocalization ($\rho = 0.56$) compared to non-targeted conjugates ($\rho = 0.28$). Color code: green: Q β (GFP), red: MitoTracker Deep Red FM.

Q β capsid formation occurs in the recombinant *E. coli* expression system through charge-mediated interactions between the negatively charged random *E. coli* RNA and positively charged Q β coat

protein subunits.^{116, 279} Disulfide formation in the biological synthesis of Q β is occurring after the capsid has self-assembled likely following exposure to molecular oxygen in the bacteria or following cell lysis. Given the highly negative charge of siRNA,²⁸⁰ we hypothesized siLuc could promote assembly of Q β capsids and addition of the DB-TPP could “sew” the capsid up in a one-pot process. Specifically, we anticipated that we could reduce the Q β with DTT and disassemble the capsid in a salt solution. The addition of siLuc could then promote capsid reassembly, and DB-TPP could seal the capsid *in situ* as the last step (Figure 3.4A).

First, purified Q β VLPs were disassembled into coat proteins through a salt-controlled disassembly method^{116, 250} by adding the reducing agent 1,4-dithioerithrol (DTT) and magnesium chloride (MgCl₂), which facilitates the recovery and precipitation of packed RNA. Next, the obtained coat protein (CP) was purified using dialysis and centrifugation. SEC, agarose, and SDS gel electrophoresis were used to verify the *E. Coli* RNA was removed and the Q β disassembled into CPs (Figure B18). Data show the presence of CPs through a single band in SDS-PAGE and positive charge migration through agarose gel electrophoresis with a change in capsid retention time by SEC. Reassembly proceeded in the presence of siRNA under DTT reducing conditions. We found that a siRNA to CP ratio of 1:4 was sufficient to promote complete capsid formation.

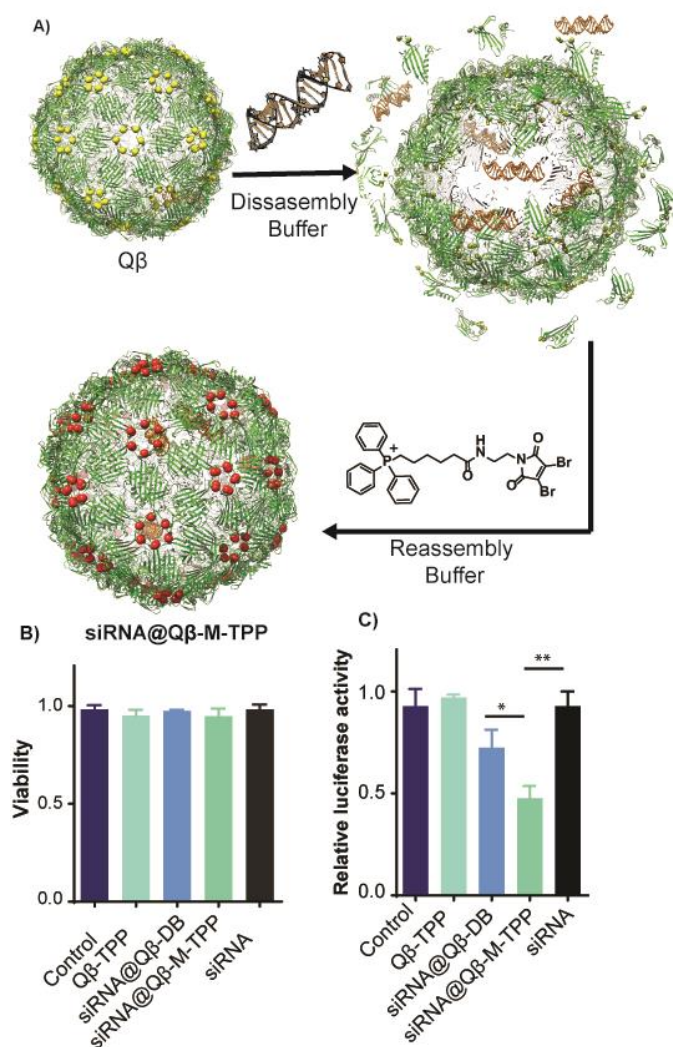


Figure 3.4. A) Scheme for disassembly of Q β virions to coat proteins, then the reassembly around siRNAs to make siRNA@Q β -M-TPP. B) Cell viability and relative levels of luciferase expression in HeLa luciferase cells after various treatments.

Finally, we proceeded with the surface installation of TPP directly in the reassembly buffer by adding 50 eq of DB-TPP to the solution. Absorbance at A260/280 ratio was used to confirm complete siLuc packing. We were happy to find that the A260/280 ratio increased from 0.87 (pre-siLuc packing) to 2.0 (post-siLuc packing). Direct observation of the VLP assemblies was done by TEM. Figure B.19 shows well formed VLPs after the encapsulation of the siRNA, which is

further confirmed by agarose and SDS gel electrophoresis with the hexameric and pentameric subunits of siRNA@Q β -M-TPP exhibiting similar integrity to native Q β (Figure B9). To assess the *in vitro* cytosolic delivery of siRNA using siRNA@Q β -M-TPP, we compared the silencing ability of naked siRNA, siRNA loaded in Q β without the M-TPP linker, and siRNA loaded in Q β -M-TPP in luciferase-expressing HeLa cells. The cell viability and luciferase expression were measured using standard One-Glo Tox luciferase and cell viability assay. It was found that after 24 h, all treatment groups had high cell viability (Figure 3.4B) but the siRNA@Q β -M-TPP treated cells showed a significantly lower luciferase expression (47%) as compared to free siRNA treated cells (93%) (Figure 3.4C). Considering uptake of Q β and Q β -M-TPP are comparable, this result further proves the cytosolic delivery of our formulation and demonstrates – as a proof-of-principle – that we can enhance cytosolic siRNA delivery via this approach.

3.3 Conclusions

Most nanoparticle-based delivery systems must escape the endosome and lysosome to reach the cytosol for efficient therapeutic and diagnostic action. In this work, we chemically modify the surface of an engineered protein model, Q β , using a glutathione-sensitive linker attached to a lipophilic cation to overcome endosomal entrapment and achieved cytosolic delivery. As proof-of-principle, we successfully demonstrate the applicability of our synthetic bioconjugation strategy in the cytosolic delivery of a VLP carrying GFP and siRNA *in vitro*. Our “shedddable linker” strategy is further confirmed because no cytosolic delivery is observed without a GSH cleavable linker. We believe our synthetic strategy addresses critical challenges for the intracellular delivery of macromolecular therapeutics.

CHAPTER 4

MULTIFUNCTIONAL PHOTO-IMMUNO METAL-ORGANIC FRAMEWORK: COMBINATIONAL STRATEGY TOWARD CANCER TREATMENT

4.1 Introduction

Cancer immunotherapy (CI) is considered as one of the most promising and efficacious therapeutic approaches to treat wide range of malignant cancers through activating immune system,^{281, 282} modulation of the tumor microenvironment²⁸³ and overcoming the immunosuppressive mechanisms that cancer cells employ to avoid immune recognition.²⁸⁴ This type of therapy encompasses several forms from cytokine to chimeric antigen receptor (CAR) T-cell²⁸⁵ that combat cancer by stimulation of immune system or attenuating anticancer immune response whose effect long-lasting cancer remission or even complete eradication of primary tumor and metastasis lesions. Despite this clinical promise severe toxicity, immunorelevant side effects and low response rate on fraction of patients are associated with these methods.²⁸⁶ An exciting breakthrough in cancer immunotherapy that are receiving notable attention to break down these limitations is the clinical use of FDA approved immune checkpoint inhibitors including ipilimumab (anti-CTLA-4) and nivolumab (anti-PD-1), which function through boosting the adaptive immune system. In general, T cell activation involves receptor-ligand interactions between CD28 a T-cell receptor and the B7 ligands (B7.1 and B7.2) on surface of antigen presenting cells (APC). This interaction firmly regulated by inhibitory checkpoints such as cytotoxic T-lymphocyte-associated antigen 4 (CTLA4) on T cells and B7 ligands to prevent aberrant immune function. Several studies showed CTLA-4 bind to B7 with higher affinity than CD28 which exploit the inhibitory pathway to block T cells activation and cause high suppression

of antitumor immune response. Indeed, blockade of this signaling pathway using anti-CTLA4 antibodies can rescue the interaction of the costimulatory T-cell receptor CD28 with the B7 ligand and stimulate proliferation and activation of T cells so that immune cells can recognize and eliminate tumor cells.²⁸⁷ The efficacy and use of checkpoint inhibitors as systemic therapies is however limited by cold immunological phenotype, dose-limiting toxicities concern, biodegradation and nonspecific cellular interaction.^{288, 289} Hence, many research is going on developing approaches to administrate checkpoint inhibitors in a safe and controlled manner to targeting lesion. One of the promising approaches is integrating these therapeutic agents with inorganic, organic and biological based delivery platforms including nanoparticles, implants, biomaterials and cell-based nanocarriers. These formulations offering a safe and effective platform for encapsulating these immunostimulatory agents that protect them from surrounding biological environment, prolong circulation half-time and effectively deliver high dose of immunostimulants to the tumor site whereby greatly promote the potency of immunotherapeutic payloads by boosting tumor immunogenicity and minimizing toxicities. Another advantage of the delivery platforms such as protein, polymer-based nanoparticles and liposomal systems is their ability to co-administrate different antigens and immunostimulants together/simultaneously to maximize the immune response.^{290, 291} The tumor microenvironment can greatly benefit from the synergistic effect of the multiple immunotherapies strategy in harnessing different immune-resistant pathways compared to use of free compounds. For instance, the sustained release of cytokine in combination with an inhibitory molecule induce significant improvement in antitumor effect by secreting inflammatory response while simultaneously overcome the immunosuppressive mechanisms in tumor microenvironment.²⁹² Developing the co-delivering system for immune checkpoint

inhibitors (e.g., PDL-1, CTLA-4) combined with other immunotherapeutic modalities (immunoadjuvant and cytokines) in a sustained release manner through a safe, biodegradable, site selective and functionalize nanocarrier (hydrogel, polymers, and liposome) can provide an opportunity to combine different therapeutic approaches and further enhance their antitumor effect compare to monotherapy. However, many of these formulations such as hydrogel, liposomal and polymeric delivery systems, metal nanoparticles and carbon nanotubes suffer from limited stability, low drug loading capacity, degradability, and possible cytotoxicity which drastically influence their sustained release and ability to amplify activated immune response.

Over the past two decades, metal-organic frameworks (MOFs) have emerged as a solution to these problems as a unique class of inorganic–organic hybrid nanomaterial. These crystalline-shaped nanomaterials built from coordination of metal cluster to organic ligands form well defined structure with large surface area and highly order porosities. Diverse synthetic strategies have been explored in their formulation that led to various morphologies, compositions, sizes, and chemical properties. These unique features endow them with ability to encapsulate different therapeutic hosts with high loading capacity, multifunctionality for targeting ability and codelivery of several cargos including antigens and immunomodulators which along with their intrinsic biodegradability enable them to perform as a promising combinational platform in on demand drug delivery and cancer immunotherapy. Although, cancer immunotherapy drug such as ICIs loaded onto a metal-organic framework may exhibits improved targeting delivery as well as a steady release, still there is concern about many cancer patients with low tumor antigen and immunosuppressive tumor microenvironments who would not respond to this therapy. Therefore, combining MOFs as a safe and sustained release ICIs nanocarrier combined with another therapeutic strategy such fever like

photothermal therapy (PTT) (temperature 44 °C) that sensitize tumors to ICIs by upregulating checkpoint proteins and promoting antigen presenting cells and T cell priming into TME can be an effective approach to turn “cold” immunosuppressive tumor microenvironments to “hot” tumors. Our lab has previously shown that MOF platform has ability to prolong the release of protein antigens and enhance the immune response while having high thermal and biological stability. (Michael papers). We also have developed a new phototherapeutic system based on VLPs (PhotothemralPhage, which is introduced in chapter 2) that effectively convert NIR light to heat and initiate an immune response by activating DC and T cells. In this account, we took advantage of both mentioned strategies to present an effective immunophotothermal system that work based on combination of mild PTT and slow release of ICIs.

Our design strategy is based on metal-organic frameworks subset zeolitic imidazolate frameworks (ZIFs) that is loaded with an anti-CTLA-4 checkpoint inhibitor (FDA approved ipilimumab) and coated with a photothermal agent based on non-infectious virus-like particles (VLPs) that induces both tumor thermal ablation as well as promotes anti-tumor immunity through the release of toll-like receptor stimulating antigen. This synergistic formulation is made first by encapsulating anti-CTLA-4 within ZIF via a biomimetic crystal growth process then coating its surface with bacteriophage Q β decorated with croconium dye a system called PhotothermalPhage through electrostatic interaction between negatively charged PTPhage and positively charged zinc. Figure 4.1 Q β in PTPhage itself is an immunoadjuvant, owing to its encapsulated bacterial RNA and its highly organized structure also can be recognized as a pathogen associated molecular pattern by toll like receptors (TLRs) on antigen presenting cells (APCs).^{202, 214, 293} Through these immunoactivation pathways, this strategy can address the main obstacle in CBI therapy—the lack

of activated APCs (dendritic cells, macrophages, etc) and insufficient tumor associated antigen in tumor microenvironment.²⁸⁹ ZIF will protect the encapsulated anti-CTLA-4 from the temperatures induced by the photothermal treatment and promote the slow and local release of anti-CTLA-4 directly into TME.

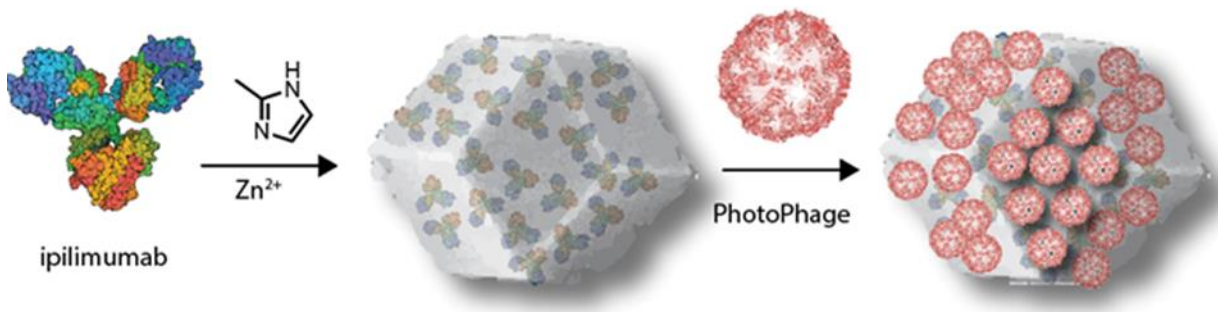


Figure 4.1. Synthetic procedure, including the growth of ZIF over Anti-CTLA-4 (ipilimumab) to form a microcrystal. Formed ZIF has high affinity for the negatively charged PTPHage. These coated particles will generate heat upon 808 nm laser irradiation while ZIF begin degrades slowly, releasing ipilimumab.

4.2 Results and Discussion

Design and Characterization of Anti-CTLA4 @ZIF

ZIF formation is dominated by a coordination reaction between zinc metals and methylimidazole ligands and has been shown by our group and others that can encapsulate a variety of biomacromolecules including soluble proteins, viruses, and whole cells through biomimetic mineralization processes which the cargo influenced forming pre-nucleated clusters with ligands and metal.

Here, we encapsulated 0.5 mg/mL of ipilimumab (the anti-CTLA-4 drug) into ZIF-8 crystals under mild aqueous conditions by mixing ipilimumab solution with aqueous solutions of 2-methylimidazole (1600 mM) and zinc acetate (20 mM). Upon mixing the reagents, the reaction

begins immediately, and the mixture went from colorless to cloudy. Solution was placed on a laboratory rotisserie to ensure proper mixing. After 3h incubation at RT, ipilimumab embedded ZIF-8 crystals were formed and could be easily collected by centrifugation ($2071 \times g$ for 10 min). The resulting pellet was washed two times with water and pellet was dried under high pressure overnight. The resulting biomineralized anti-CTLA-4@ZIF-8 particles were characterized using scanning electron microscopy (SEM) and dynamic light scattering (DLS). A monodisperse anti-CTLA-4@ZIF-8 particles with an average size of 1254 ± 8.9 nm were obtained in the biomimetic mineralization synthesis (Figure 4.2). SEM micrographs of the resulting micro crystals show the typical rhombic dodecahedral shape of ZIF.

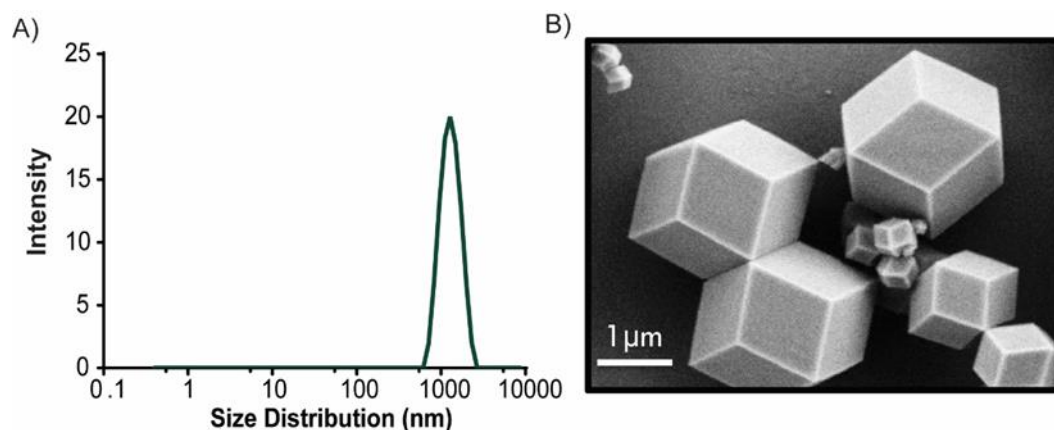


Figure 4.2. Characterization of biomineralized anti-CTLA-4@ZIF using A) dynamic light scattering B) SEM micrograph. A monodispersed micron sized anti-CTLA-4@ZIF particle was form in a rhomb dodecahedral shape.

Fluorescence labeling of anti-CTLA4 and measuring encapsulation efficiency

To calculate the encapsulation efficiency and be able to track the *in vitro* uptake and *in vivo* release profile of antibody for future works anti-CTLA-4 need to be labeled with a fluorophore. For this purpose, Cy7-NHS (Thermo Fisher) dye were incubated with 1 mg/mL ipilimumab (YERVOY)

in 0.1 M sodium bicarbonate solution (pH 8.3) at 4°C, overnight. The unreacted dye was removed by washing with 5.0 mL of buffer 5 times using 50 kDa cutoff centrifugation filters (4,000 × g, 10 min). The conjugation was characterized using 1% agarose gel. As shown in Figure C1 Cy7 fluorescence in the labeled antibody was appeared in the agarose gel at same spot as unlabeled anti-CTLA-4 which prove the successful attachment of dye to the antibody. Fluorophore-labeled ipilimumab was subsequently used to make Cy7-anti-CTLA-4@ZIF and the encapsulation efficiency was quantified by measuring the amount of unencapsulated Cy7-anti-CTLA-4 in the supernatant during synthesis. Cy7 ($\lambda_{Ex} = 750$ nm and $\lambda_{Em} = 773$ nm) fluorescence was determined using fluorescence spectroscopy before and after encapsulation to measure amount of entrapped Cy7-anti-CTLA-4 within ZIF. An encapsulation efficiency of 95% was obtained. The encapsulation of Cy7-anti-CTLA-4 also were visualized by confocal microscopy, Cy7-anti-CTLA-4 showed a strong fluorescence in Cy7 channel while there is not any obvious Cy7 fluorescence for ZIF alone. (Figure 4.3)

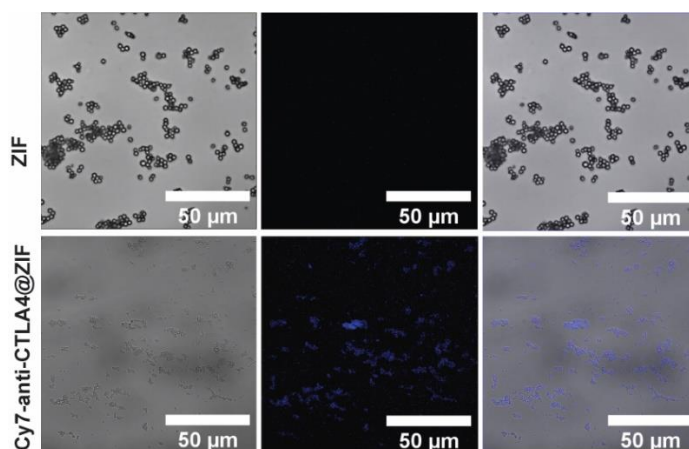


Figure 4.3. Confocal micrograph of Cy7-anti-CTLA-4@ZIF. The outer shell fluoresces blue from trapped Cy7-anti-CTLA-4 while there is no fluorescence in Cy7 channel for ZIF. Scale bar = 50 μm.

Next to confirm Ipilimumab was not damaged during encapsulation in the ZIF crystals, ZIF-shell was dissolved by treatment with 0.5 M EDTA—a process called exfoliation. A size exclusion chromatography (SEC) was run before and after exfoliation as shown in Figure C2. Ipilimumab remained intact after encapsulating the protein in ZIF-8.

Decorating surface of anti-CTLA4@ZIF with PhotothermalPhage

The goal of this project is developing a near infrared light triggered photoimmunotherapy platform by dual labeling of metal organic framework to ablate tumor by heat and simultaneously boost the immune response against cancer cells through slow delivery of an immune check point inhibitor. Hence, we modified surface of anti-CTLA4-@ZIF by a croconium dye-Q β virus like particle hybrid (PhotothermalPhage) both as a photothermal agent and immunoadjuvant. For this purpose, anti-CTLA4@ZIF were incubated with 0.5 mg/mL of PhotothermalPhage (PTPhage) for 4h, then washed twice with water. The pellet was collected after centrifugation ($2071 \times g$ for 10 min) and were characterized by transmission electron microscopy. As shown in Figure 4.4A PTPhage was observed on the surface of rhombododecahedral shape anti-CTLA4@ZIF as dark small particles that show successful decoration of ZIF surface with a photothermal agent. Next, we tested thermal behavior of particle compared to ZIF and PTPhage solution by radiation with 808 nm laser for different times (2, 5, 10 and 15 min), at constant laser power 0.18 w/cm^2 . Temperature change was monitored using a thermal camera in each solution. As seen in Figure 4.4B, the solutions of PTPhage- anti-CTLA4@ZIF showed a significant heating rate as PTPhage while no temperature increase was observed in ZIF solution.

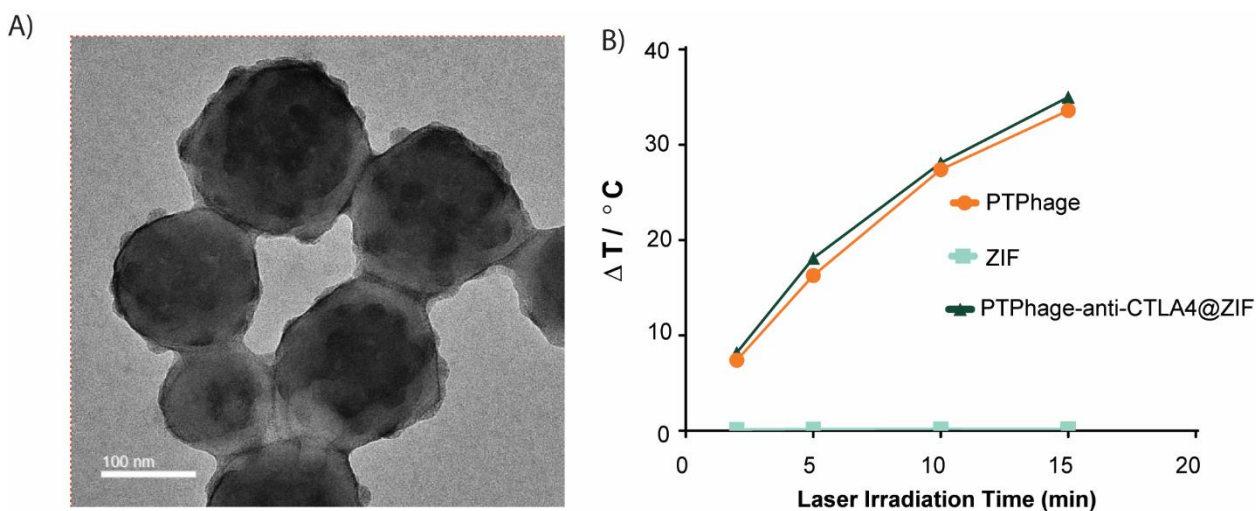


Figure 4.4. A) Transmission electron microscopy image of PTPaheg coated on surface of ZIF. B) Photothermal heating profiles of ZIF, PTPhage and PTPhage- anti-CTLA4@ZIF at the same concentration ($50 \mu\text{g mL}^{-1}$) over 15 min of laser irradiation (808 nm, $0.18 \text{ W}\cdot\text{cm}^{-2}$) show strong PTPhage keeps its photothermal behavior after attaching to surface of ZIF and generates heat as effective as PTPhage, while ZIF did not show any significant difference in temperature increase.

4.3 Conclusions

We next will explore whether produced heat by our functionalized MOF after irradiation with a safe and low power near infrared laser would be able to locally kill cancer cells and enhance *in vitro* cytotoxicity induced by photothermal agent. We will also evaluate the efficiency of the MOF-based photoimmunotherapy formulation on eradicating primary tumor and controlling metastasis in an orthotopic mice models bearing melanoma tumor model (B6F10 tumor). It is expected that the co delivery of multiple immunological agents synergized with thermal ablation suppress tumor progression and prolong the survival time. We will compare activated immune responses between mice treated with PTPhage-anti-CTLA4@ZIF and PTPhage, ZIF, anti-CTLA4 and PBS. We expected to observe a significant increase in antitumor immune response in mice treated with

PTPhage-anti-CTLA4@ZIF because of synergist effect between thermal ablation, sustained release of anti-CTLA4 and presence of virus like particle.

CHAPTER 5

CONCLUSION AND FUTURE WORK

5.1 Conclusions

The development of therapeutic nanomaterials for efficient disease diagnosis, prevention and treatment is gaining momentum. Several nanoparticles such as polymeric, metallic, and lipid-based nanoparticles being utilized within the clinical setting and offered multiple benefits such as cell and tissue site specific targeting, high solubility and extended half-life which resulted improving therapeutic index in many diseases such as cancer, diabetes, and etc. However, there is continued demand for developing biomaterials with quality of being safe, biodegradable, biocompatible and most importantly being easily synthesized and functionalized to create particles with all desired features. Virus like particles (VLPs) a self-assembled protein-based nanomaterials have emerged as a solution to design an multifunctional and effective therapeutic agent which offer several therapeutic advantages compared to other nanomaterials. VLP mimic structure of viruses thus have an empty cavity to carry genetic materials/cargos which is being used as a nanocarrier for drug delivery and gene therapy. They also have a repetitive and symmetric structure that can be recognized by immune system which increase the enrichment of immunotherapies within the lesion and most importantly have solvent exposed amino acids on the surface that provide functionalization ability through various chemistries. As a chemist in this dissertation, we have first considered VLPs as an organic compound/folded polymers that contain several nucleophilic functional groups on their surfaces such as amine (from lysine residue), thiol (from cysteine) and etc. These functional groups then were modified with high density of powerful synthetic linker and near infrared dye through several bioconjugation strategies that in complement with VLP's

intrinsic immunogenicity and structural properties turned to powerful means for immunophothermal therapy and cytosolic nucleic acid delivery. Therefore, by combining chemistry, biology, and immunology we have elucidated the potential and power of virus like particle platform both for in vitro and in vivo therapeutic application.

5.2 Future Directions

Virus like particles acquire a great potential in wide variety of therapeutic applications including cancer treatment. Understanding the characteristics of these biomaterials and their behavior in different biological environments will enable scientists to establish novel strategies for targeting the desired area for treatment, prevention, and diagnosis in many diseases. Their multi functionalization ability will allow to construct next generation of multi-therapeutic particles that can combine various therapeutic molecules or even various type of particles for treating several diseases all at one. All these potentials combined with intrinsic properties of VLPs such as size, immunogenicity, high stability, biocompatibility yield more effective therapies and preventive properties.

APPENDIX A

EXTENDED DATA FOR CHAPTER 2

MATERIALS

Chemicals

Potassium chloride, FB Essence, potassium phosphate monobasic, potassium phosphate dibasic, Dulbecco's Modified Eagle's Medium (6429), Tris base, sodium phosphate monobasic, tryptone, sodium phosphate dibasic, yeast extract, sodium dodecyl sulfate, sodium chloride, glycine, and Coomassie Brilliant Blue reagent were used without further purification. Reagents were purchased from Research Product International (Mt Prospect, IL, USA), VWR (Radnor, PA, USA), Chem-Impex Int'l (Wood Dale, IL, USA), Thermo Fisher Scientific (Waltham, MA, USA), and Sigma-Aldrich (St. Louis, MO, USA).

Characterization of Photothermal Phage

TEM. Transmission electron micrographs were taken on a JEOL JEM-1400+ (JEOL, Tokyo, Japan) at 120 kV with a Gatan 4k × 4k CCD camera. 5 μL of the ~ 0.1 mg. mL⁻¹ de-salted sample was placed on a 300 mesh Formvar/carbon-coated copper grid (Electron Microscopy Sciences, Hatfield, PA, USA), allowed to stand for 30 seconds, and wicked off with Whatman #1 filter paper. 5 μL of 2% uranyl acetate (SPI Supplies, West Chester, PA, USA) was placed on the grid, allowed to stand for 30 seconds, wicked off as before, and the grid allowed to dry completely in air.

Dynamic-light scattering. Analysis was done with a Malvern analytical Zetasizer Nano ZS. A disposable microcuvette was used throughout the measurements. Experimental parameters

included the following: 25 °C, a 175° scattering angle, medium refractive index of 1.33, a 633 nm laser, and material refractive index of 1.51.

Gel Electrophoresis. 1% agarose gels used throughout the experiments. Experimental parameters for running the gel include the following: 100 V, 30 mins, and a running solution consisting of 1×TBE buffer. Samples were prepared in either 100% glycerol or mixed with ethidium bromide (5 µL). 10% SDS PAGE gels were used throughout all the studies. Experimental parameters for running SDS gels consist of the following: 100 V and a running time of 75 min. Samples were mixed with SDS dye. Protein ladder used consists of EZ-Run pre-stained protein marker. All gels were stained with Coomassie brilliant blue overnight and imaged the next day.

Bradford Assay. The amount of Q β before and after bioconjugation was measured using the Bradford method with bovine serum albumin as standard. All protein determination values were based on the average of three separate measurements.

Laser Setup.

All NIR laser irradiations were performed using a continuous 808 nm Newport/Spectra-Physics Integra-MP (model 140-8S-30KS) diode laser controlled by Integra Soft Version 3.0.4 software. The laser power density was measured using a Newport power meter (model 1928-C) **Figure A1.**



Figure A.1. Experimental setup consisting of a continuous 808 nm diode laser and a FLIR E6-XT thermal camera

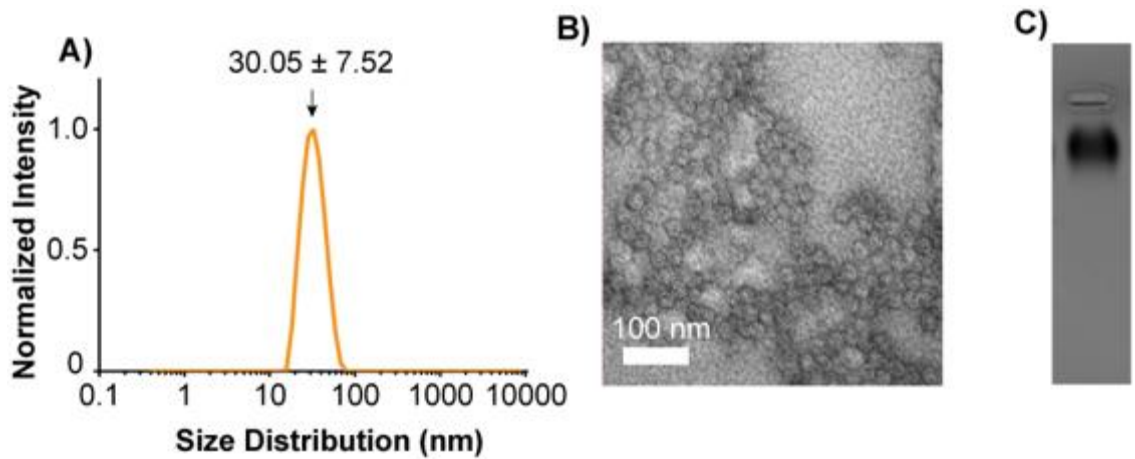


Figure A.2. Q β Characterization by A) DLS, B) TEM and C) 1% Agarose gel, Coomassie stained.

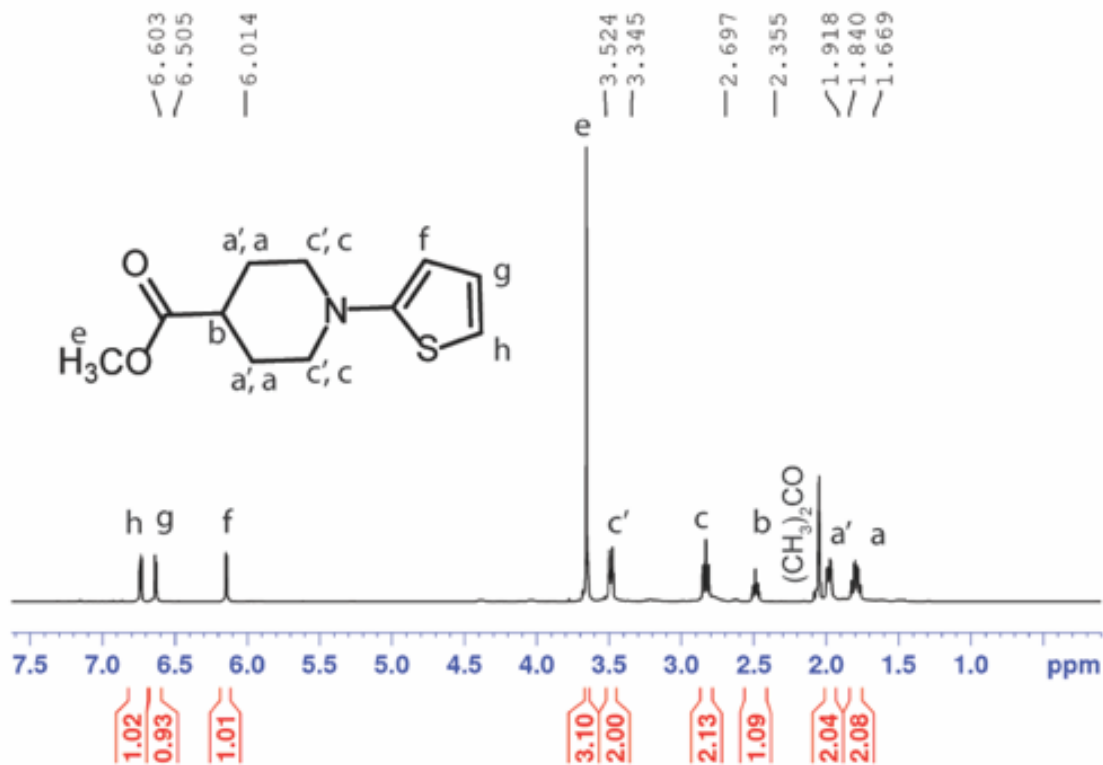


Figure A.3. ¹H NMR of methyl 1-(thiophen-2-yl) piperidine-4-carboxylate]

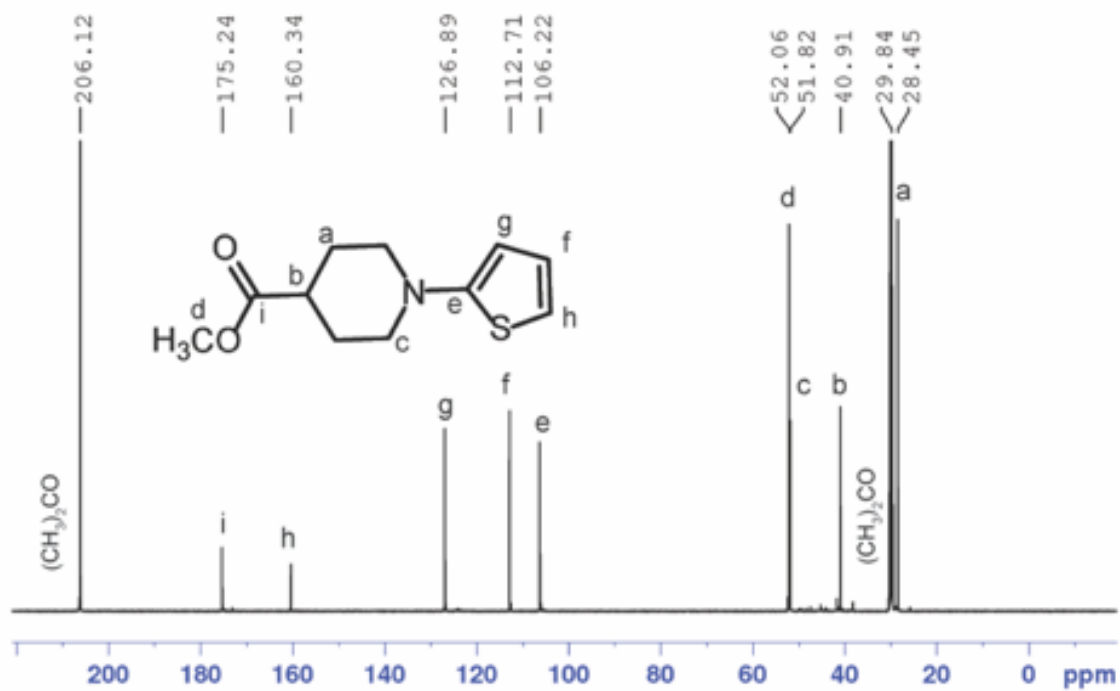


Figure A.4. ^{13}C NMR of methyl 1-(thiophen-2-yl) piperidine-4-carboxylate]

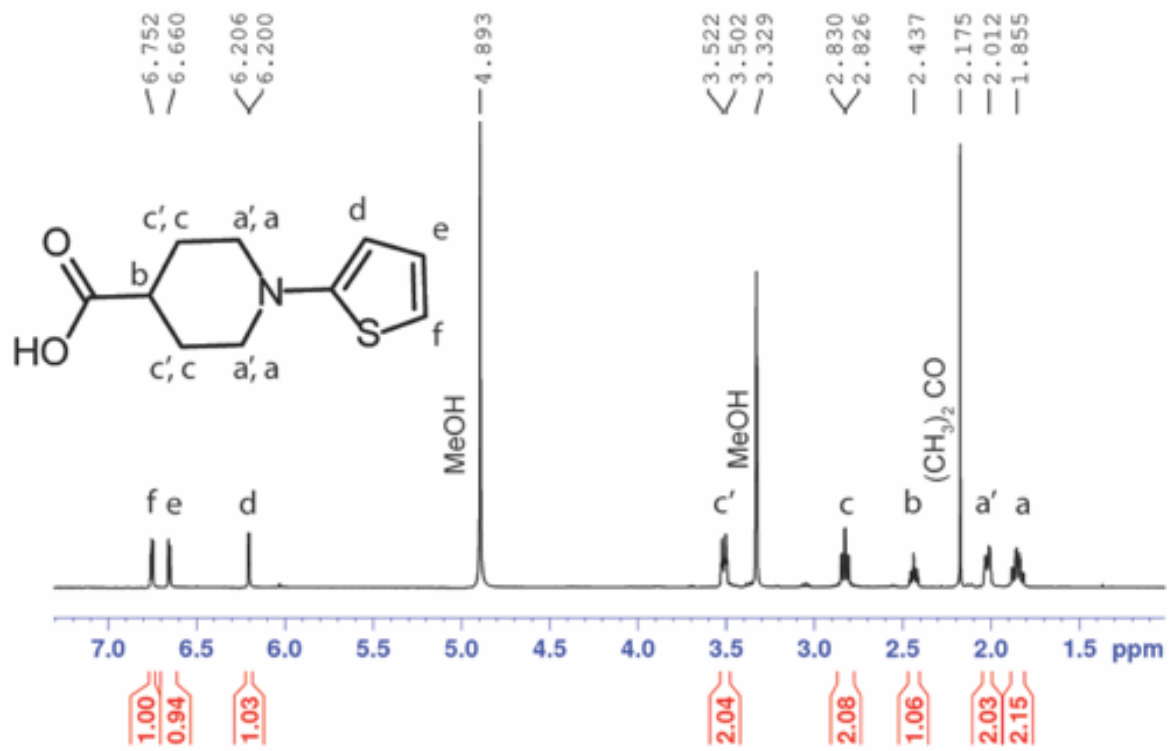


Figure A.5. ¹H NMR of [2,5-bis[(4-carboxylic-piperidylamino) thiophenyl]-croconium]

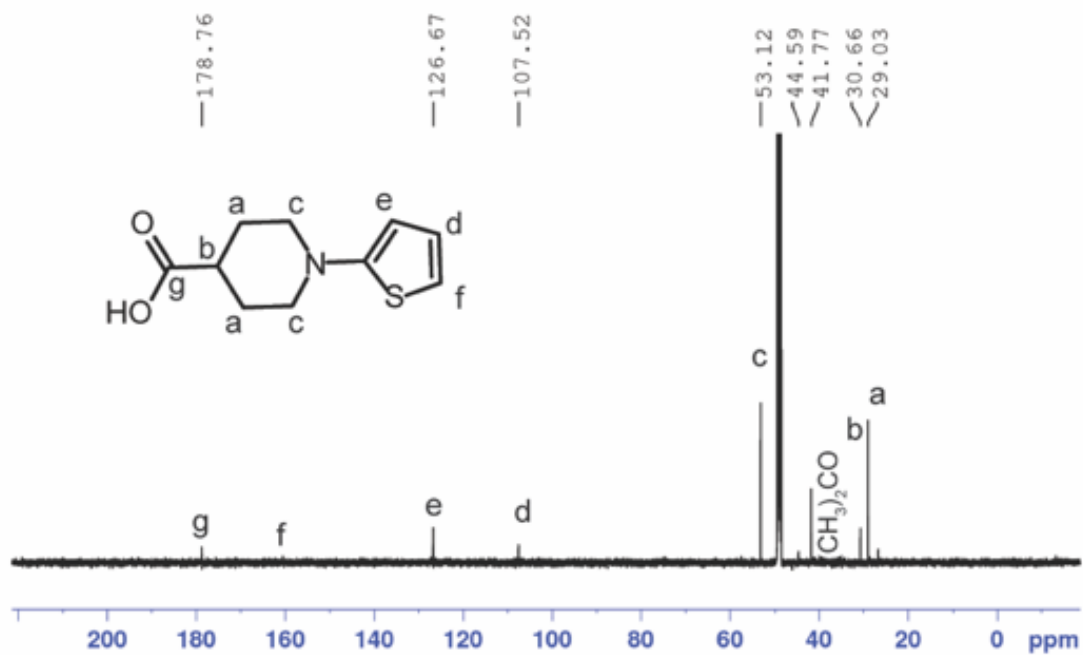


Figure A.6. ¹³C NMR of [2,5-bis[(4-carboxylic-piperidylamino) thiophenyl]-croconium]



Figure A.7. ¹H NMR of synthesized croconium dye

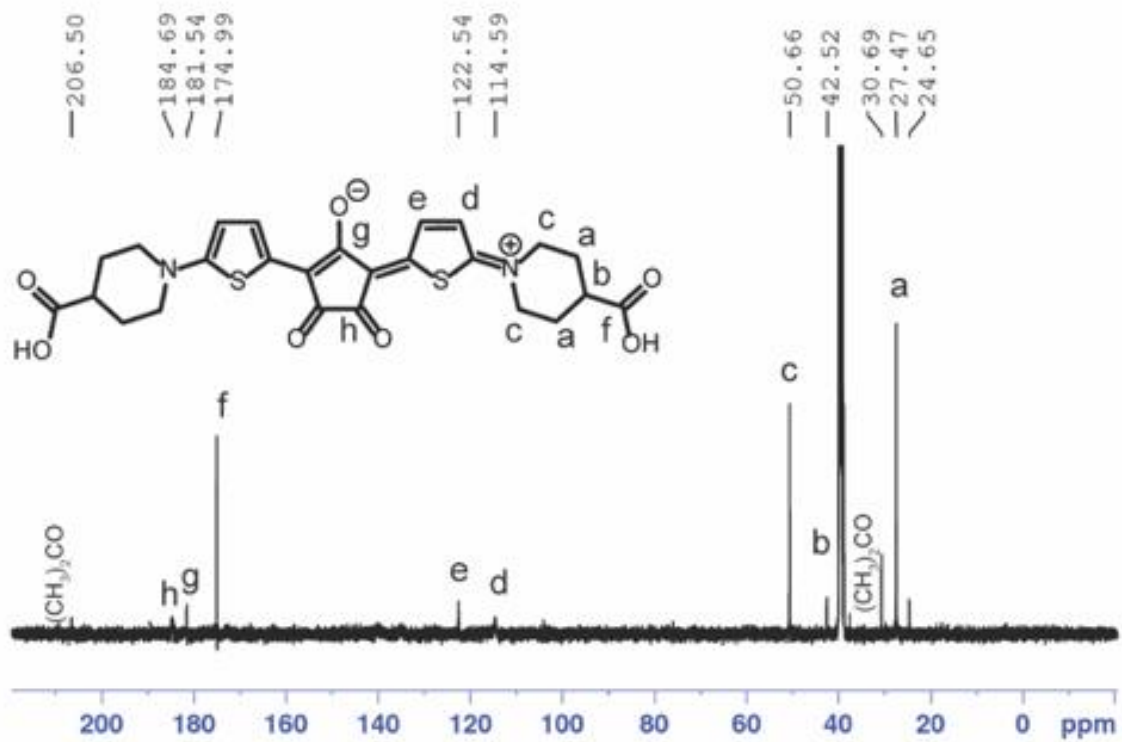


Figure A.8. ^{13}C NMR of synthesized croconium dye.

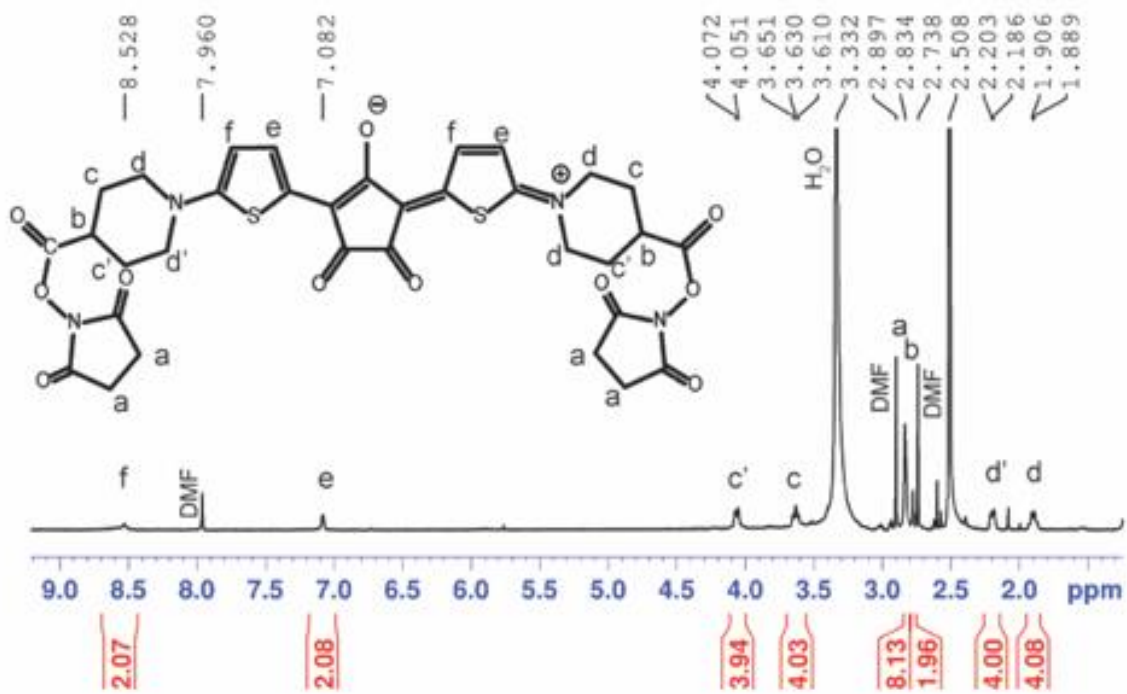


Figure A.9. ^1H NMR of synthesized croconium NHS ester

Photothermal Analysis of PTPhage

To check the photothermal behavior of PTPhage, various concentrations of PTPhage (0.1–1 mg·mL⁻¹ calculated with Bradford assay) were irradiated with 808 nm laser (0.18 W·cm⁻²) for 10 min and solutions temperature were measured using a thermocouple. As shown in **Figure A10A** there is a linear relationship between temperature increase and PTPhage concentration. To show that the temperature of Q β lacking croconium dye and the buffer solution does increase with laser irradiation, temperature was monitored in control solutions and after 10 min radiation, as shown in **Figure A10B**, no change in temperature of either Q β and PBS buffer was observed while PTPhage showed a significant temperature increase.

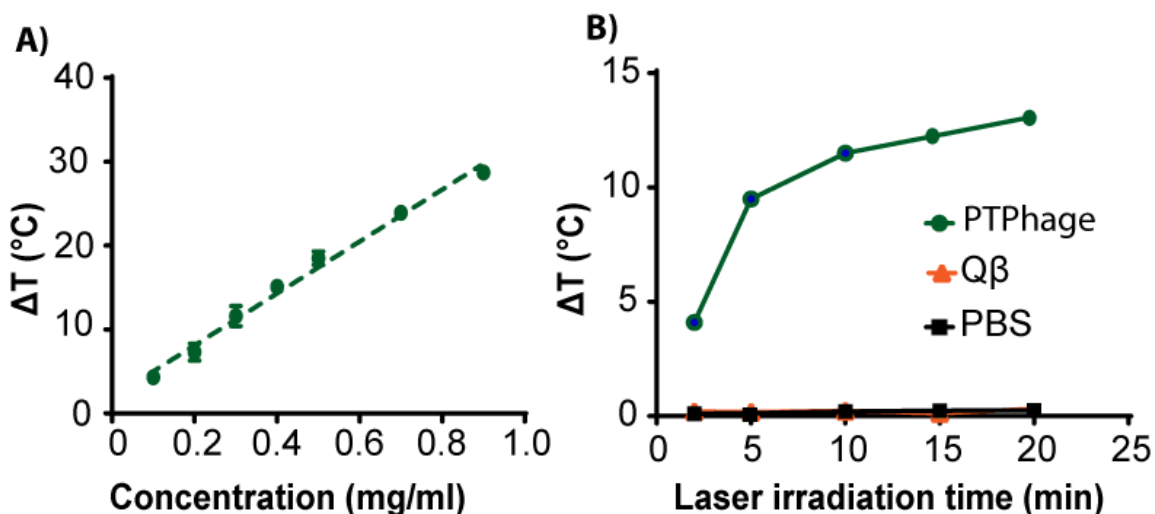


Figure A.10. Linear response of PTPhage as a function of concentration (A) and time (B) under 808 nm laser irradiation (0.18 W·cm⁻²).

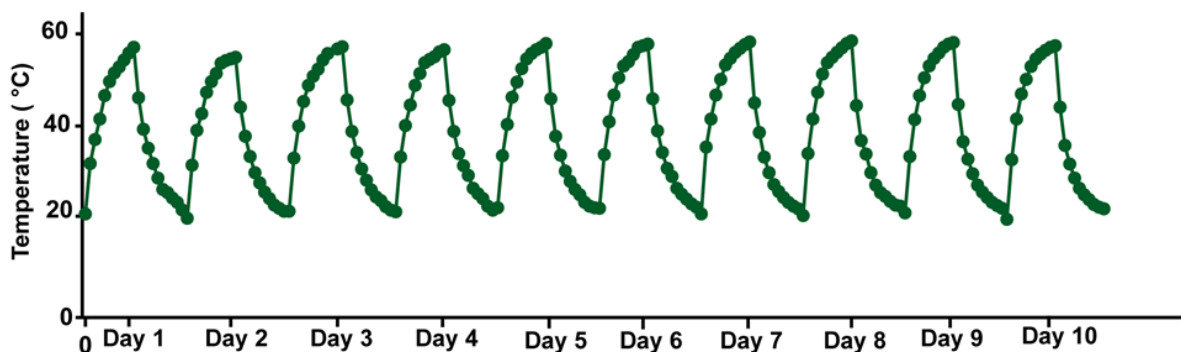


Figure A.11. Thermal cycling of PTPhage shows no change in heating profile of same sample over 10 days after 10 min 808 nm laser irradiation ($0.18 \text{ W}\cdot\text{cm}^{-2}$).

Photothermal Conversion Efficiency

The photothermal conversion efficiency (η) was calculated based on a previously reported method¹⁻² following Equation 1, where h is the heat transfer coefficient, s is the surface area of the solution, T_{max} is the maximum system temperature, T_{amb} is the surrounding temperature, I refers to the laser power, A_λ refers to the absorbance of solution, Q_s is the heat associated with the light absorbance of the solvent and container, and η is the photothermal conversion efficiency. To obtain hs , based on Equation 2, where m is 0.15 g and C is $4.2 \text{ J/g}\cdot^\circ\text{C}$, first we calculated τ using Equation 3 with a value for θ as defined in Equation 4. Equal concentrations of PTPhage Croc, and AuNR ($15\text{nm}\times 50\text{nm}$) ($41\mu\text{g}\cdot\text{mL}^{-1}$) were irradiated for 10 min with 808 nm laser ($0.18 \text{ W}\cdot\text{cm}^{-2}$) and a cooling curve was plotted based on time versus $\ln(\theta)$ (based on Equation 4 for each temperature).

$$\eta = \frac{hs(T_{max} - T_{amb}) - Q_s}{I(1 - 10^{-A_\lambda})} \quad (\text{Equation 1})$$

$$hs = \frac{mC}{\tau_s} \quad (\text{Equation 2})$$

$$t = -\tau_s \ln(\theta) \quad (\text{Equation 3})$$

$$\theta = \frac{T - T_{sur}}{T_{max} - T_{sur}} \quad (\text{Equation 4})$$

According to **Figure A12**, τ_s values were obtained as follows: 154.51 for PTPhage, 179.46 for Croc, and 196.73 for AuNR (15nm×50nm). These values were further substituted in to calculate h_s from Equation 2 and photothermal conversion efficiency (η) from Equation 1.

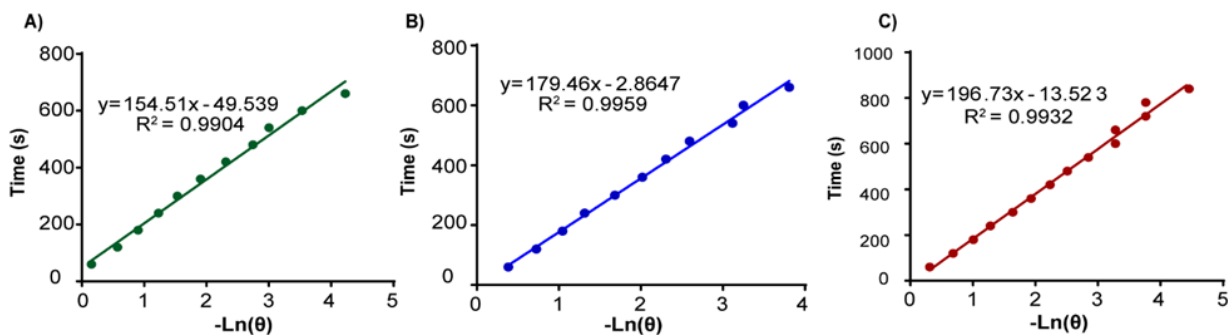


Figure A.12. Linear time data versus $-\ln(\theta)$ obtained from the cooling curve after 10 min 808 nm laser irradiation ($0.18 \text{ W}\cdot\text{cm}^{-2}$) to equal concentration ($41 \mu\text{g}\cdot\text{mL}$) of A) PTPhage, B) Croc and C) AuNR.

Cell Studies

4T1 cells were seeded and grown to a density of 1×10^5 cells/mL in a 24 well culture plate a day before experimentation in RPMI media supplemented with 10 % FBS and 2% penicillin-streptomycin at 37°C in 5 % CO_2 humidified environment (grown to 70% confluency). The cells were then treated with PTPhage and Croc ($3.1 \mu\text{g}/\text{ml}$ croc concentration in media) for 4 h. After 4 h, the supernatant was removed and centrifuged at $500 \times g$ for 5 min to remove any cellular debris and absorbance of collected supernatant was measured over 650–900 nm before and after incubation. Cellular uptake was obtained from changes in absorbance at 789 nm before and after incubation. The decrease in absorbance used to calculate a cellular uptake of 30% of the PTPhage (0.42 nmol) and 17% of Croc (0.23 nmol).

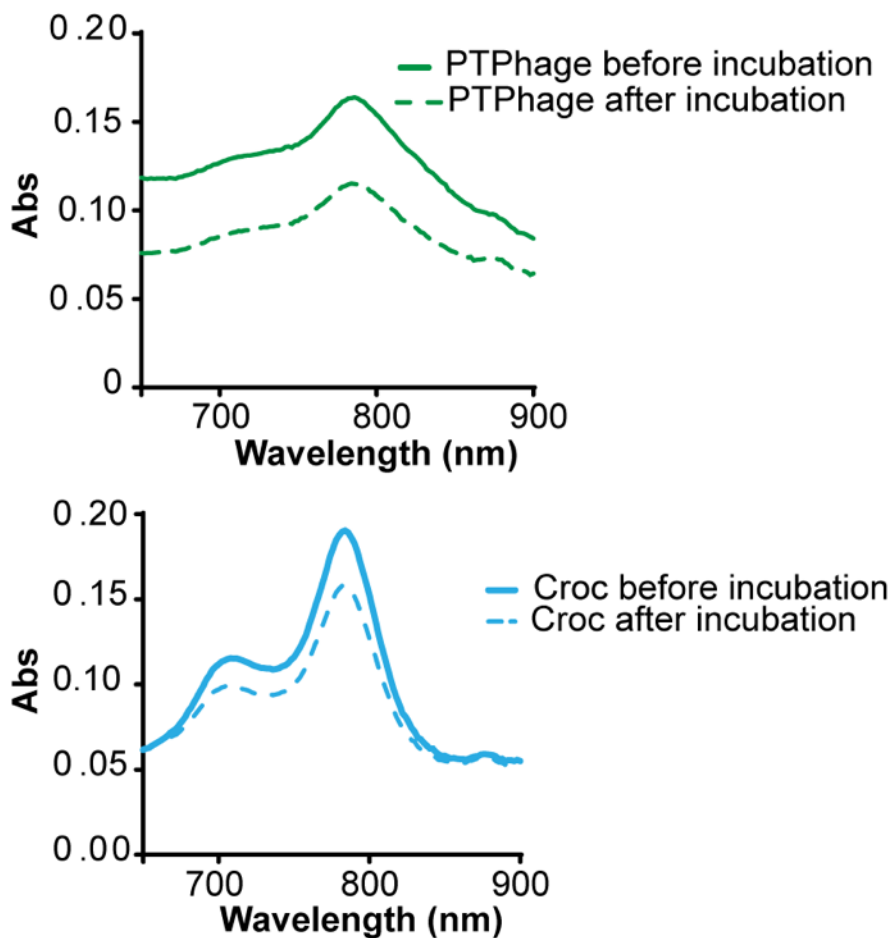


Figure A.13. Cellular uptake of PTPhage and Croc. Absorption profile of PTPhage and Croc before and after 4h incubation with 4T1 cells.

In Vitro Cell Viability and Photothermal Cytotoxicity.

4T1 breast cancer cells cultured in RPMI 1640 medium supplemented with 10% Fetal Bovine Serum and 1% penicillin-streptomycin were seeded in a 96 well plate at a concentration of $\sim 1.0 \times 10^5$ cells/mL. The next day, PTPhage, Croc and PBS samples were added to the cells at a concentration of $1 \text{ mg}\cdot\text{mL}^{-1}$ (Q β concentration) and incubated for 4 h. After incubation, to check cell viability, $0.5 \text{ mg}\cdot\text{mL}^{-1}$ MTT reagent was added to the cells and incubated for another 2 h. Then,

the media was removed from the wells and the cells resuspended in DMSO. The absorbance of the plate was read at 570 nm. Further, to determine photothermal induced cell death, wells containing equal numbers of cells were treated with PTPhage, Croc, and PBS samples at the concentration of $1 \text{ mg}\cdot\text{mL}^{-1}$ ($\text{Q}\beta$ concentration) and incubated for 4 h. After incubation, samples were removed, and cells were washed with phenol red free media ($3\times$) and replaced with fresh media. The microwell plate was placed in an incubator thermally equilibrated to 37°C . Each of the wells were irradiated for 10 min from above the plate with a continuous 808 nm laser ($0.18 \text{ W}\cdot\text{cm}^{-2}$). The supernatant was replaced with fresh media and the wells incubated overnight at 37°C . The photothermal cytotoxicity was evaluated by MTT cell viability assay described above.

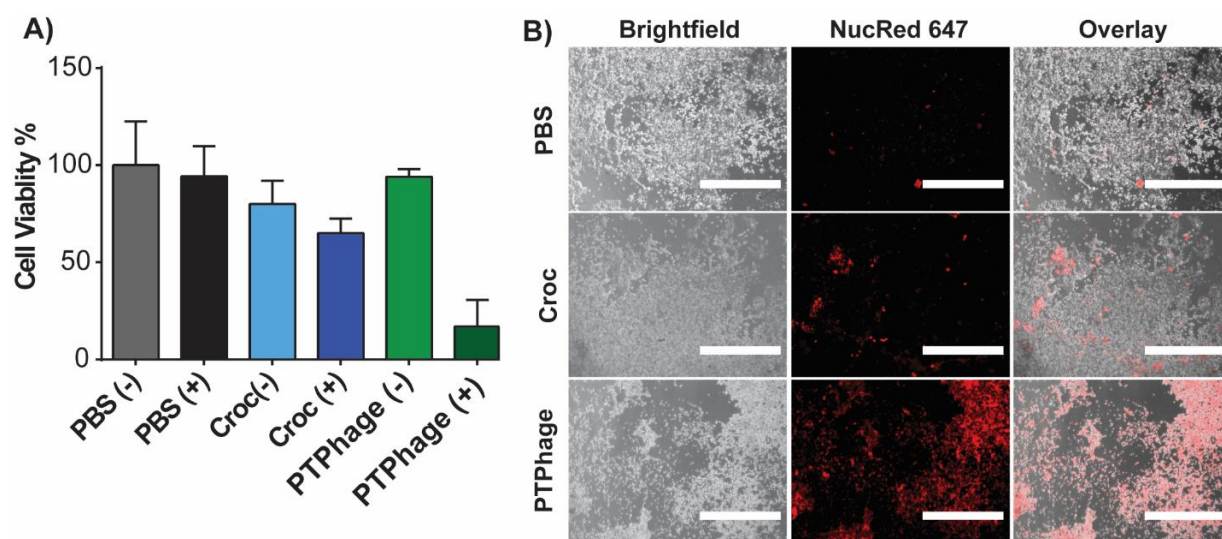


Figure A.14. Photocytotoxicity of PTPhage and Croc in cancer cells A) Cell viability of 4T1 after treatment with PTPhage and Croc and PBS with and without radiation (808 nm , 10 min , $0.18 \text{ W}\cdot\text{cm}^{-2}$). B) Fluorescence images of Nuc Red 467-stained 4T1 cells after incubation with PTPhage and Croc for 4 h and being exposed to 808 nm laser for 10 min ($0.18 \text{ W}\cdot\text{cm}^{-2}$). Scale bar : $1000 \mu\text{m}$.

In vitro LDH cytotoxicity assay

T24 and 4T1 cells were seeded in a 96 well plate (100 μ L/well) at a concentration of 1×10^5 cells/mL a night before the experiment. PTPhage Q β at concentration of 2 mg/mL and same dye concentration as Croc in triplicate were incubated for 4 h. 10 μ L lysis buffer was added to the negative control cells for 30 mins. Added 100 μ L working solution to each well and incubated the plate in the dark at room temperature for 30 mins. Follow by adding 50 μ L of stop solution to all wells and read the plate at 490 nm.

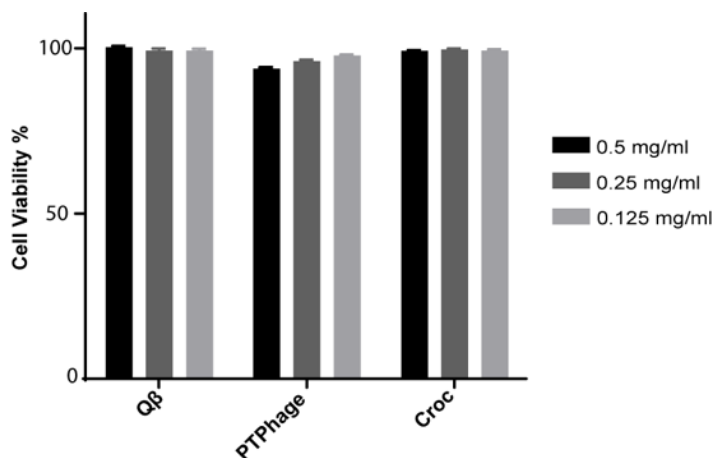


Figure A.15. Cell viability of T24 after 4h treatment with PTPhage , Croc and Q β with and without radiation (808 nm,10 min, $0.18 \text{ W} \cdot \text{cm}^{-2}$).

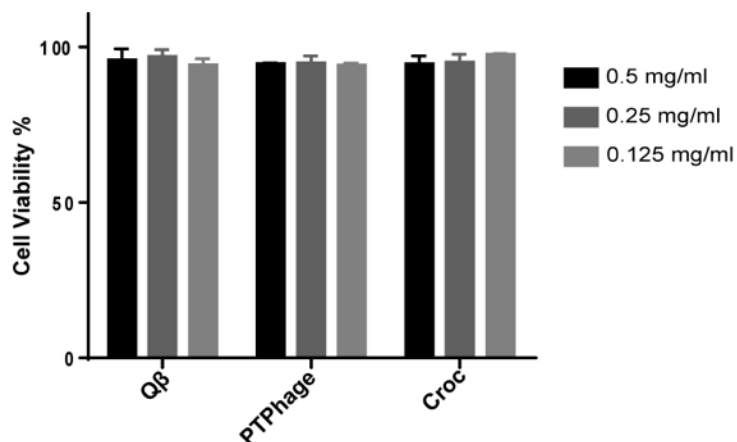


Figure A.16. Cell viability of 4T1 after 4h treatment with PTPhage, Croc and Qβ with and without radiation (808 nm, 10 min, 0.18 W·cm⁻²).

H&E Staining of main organs and tumor tissue

Mice treated with PBS, Croc, PTPhage and Qβ were sacrificed, and the lungs, heart, kidney, liver, and tumor were collected for histological study. The mouse organs were fixed in 4% formaldehyde solution, processed, and embedded in paraffin wax. Organs were sectioned at 4 μm using a Leica rotary microtome. The sections were then collected and stained with hematoxylin and eosin (H&E) for pathological analysis.

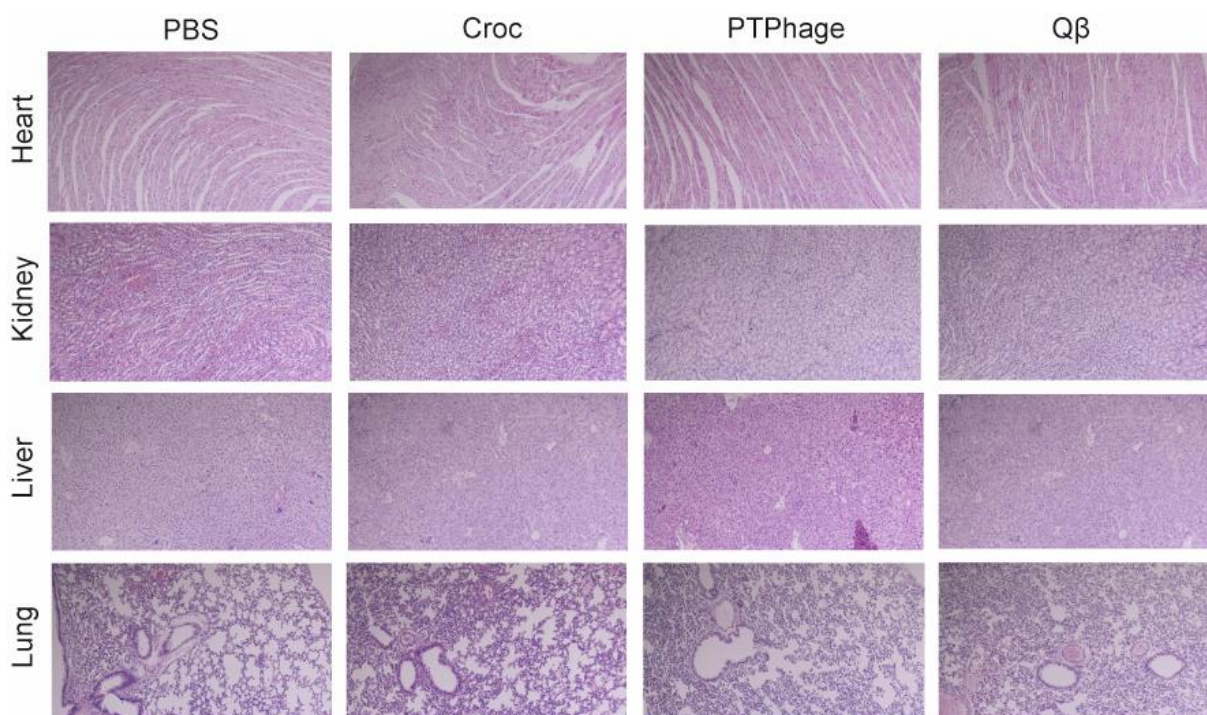


Figure A.17. The representative H&E staining images of major tissues.

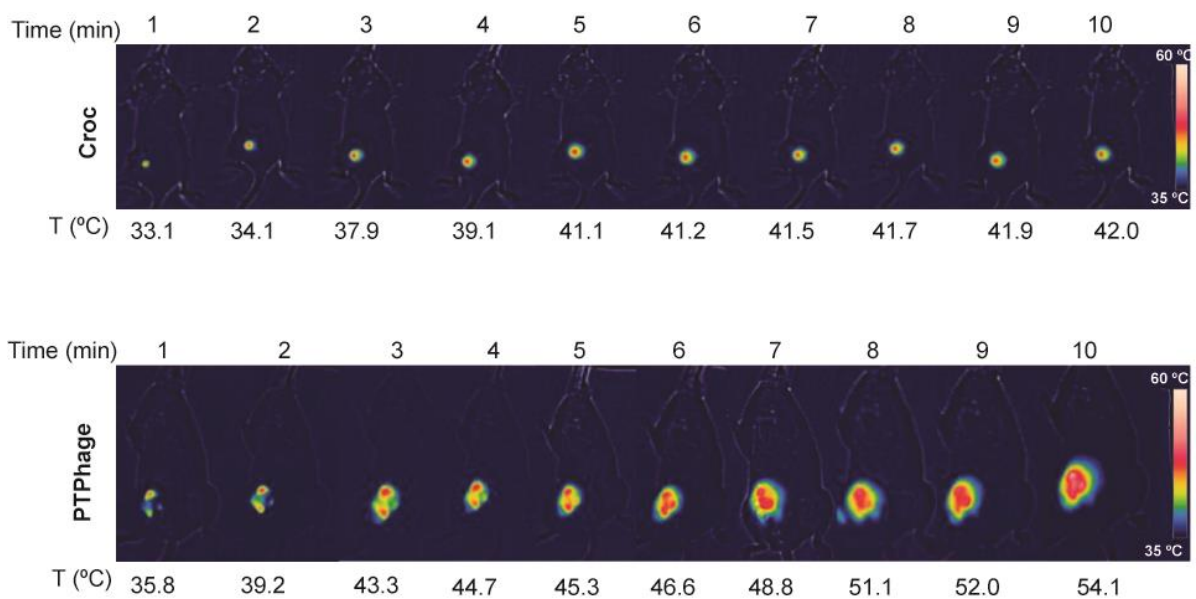


Figure A.18. Representative IR thermal images of tumor-bearing mice treated with PTPhage and Croc at different NIR radiation times (808 nm, $0.18 \text{ W}\cdot\text{cm}^{-2}$, 10 min) after intratumoral (i.t.) injection.

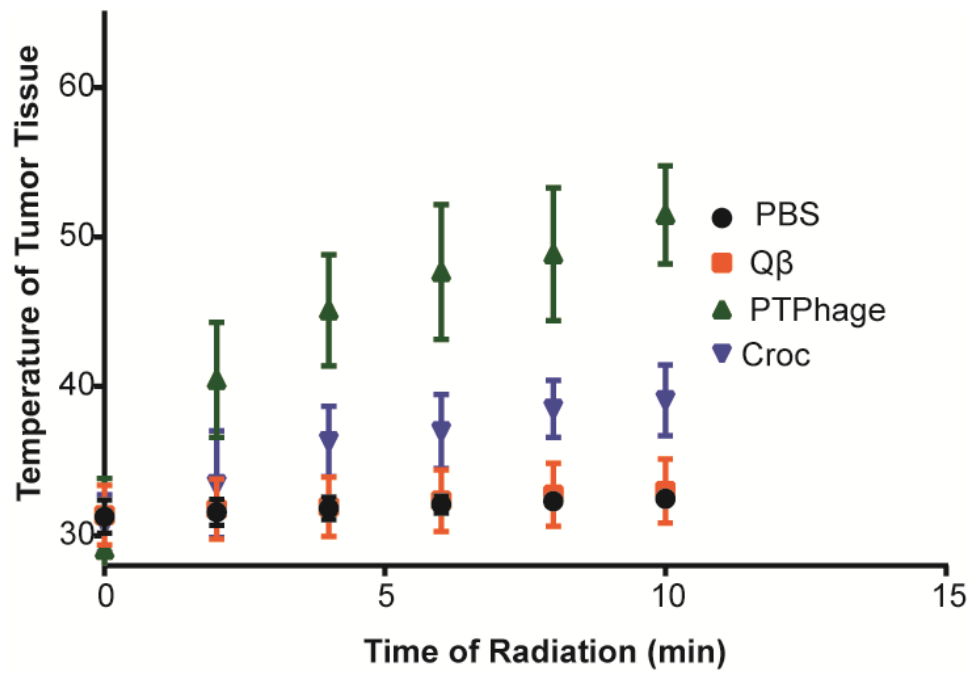


Figure A.19. Tumor tissue temperature monitored by thermal imaging camera of mice treated with PTPhage, Croc, Qβ and PBS during 10 min 808 nm laser irradiation ($0.18 \text{ W}\cdot\text{cm}^{-2}$).

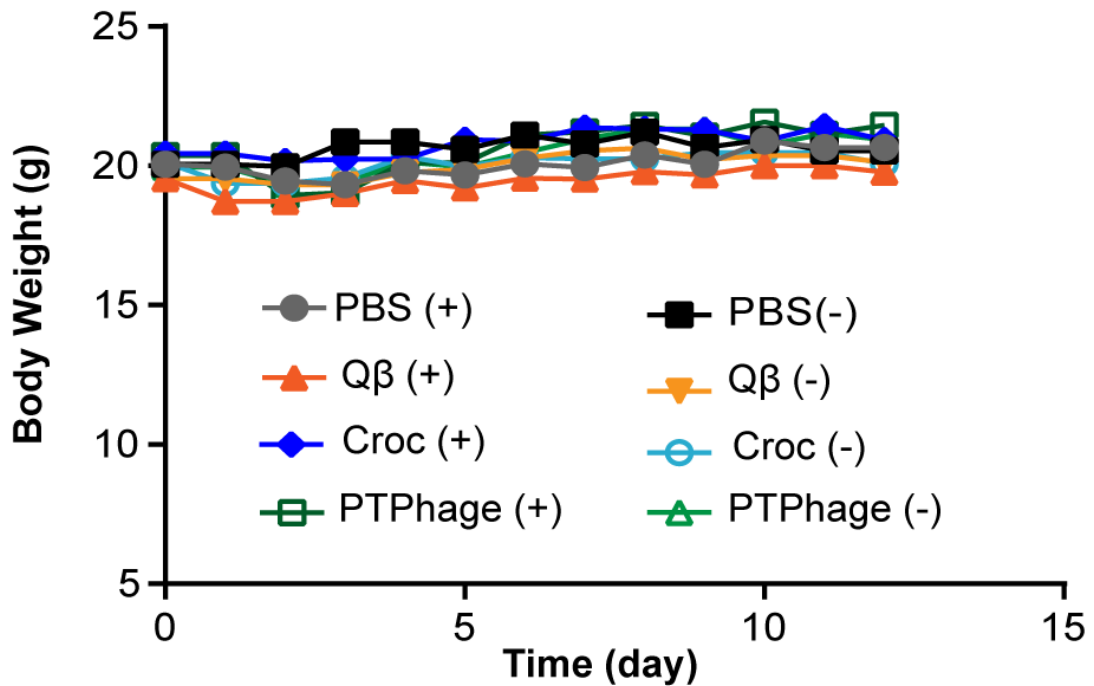


Figure A.20. Treatment-induced toxicity was monitored by recording mouse body weight every day. (Note: body weight should not change more than 20% of initial weight during treatment time).



Figure A.21. Representative images of India-ink-infused lungs of Croc, PTPhage and PBS mice that white spot clearly demonstrate number of metastatic nodules per each group.

Tissue TUNEL apoptosis assay.

Tumor tissues were fixed and were then stained with Cell Meter™ TUNEL apoptosis assay kit.

The signal was acquired with fluorescence microscope using a FITC and DAPI filter set.

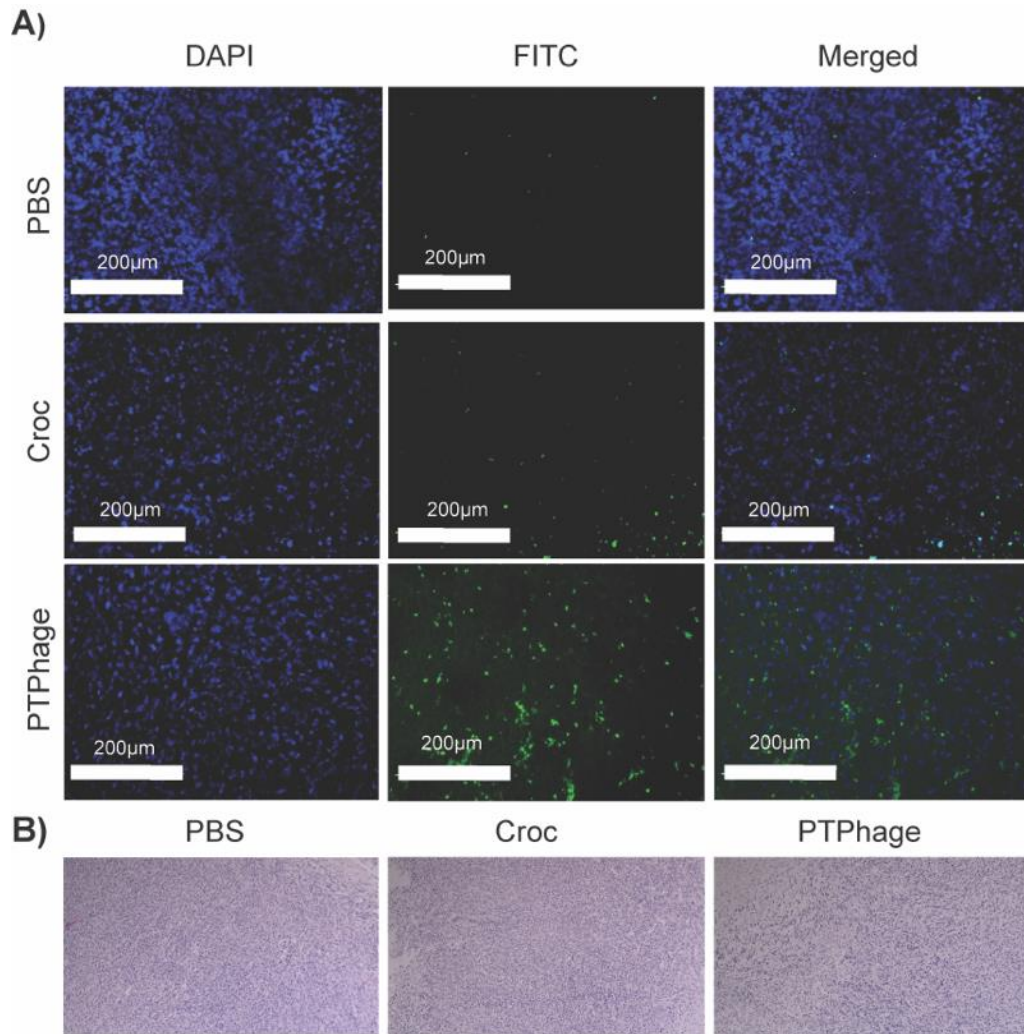


Figure A.22. Evaluation of tumor cell apoptosis in vivo by TUNEL assay. representative images (at 100× magnification) of tumor sections from mice treated with PBS, Croc and PTPhage (green fluorescence of apoptotic cells and blue fluorescence of cell nuclei were detected using fluorescence microscope. B) H&E-stained tumor slices (at 40× magnification) collected from mice post different treatment, indicating lower nuclei count and cell density in PhotoPahge compared to other groups.

Bone Marrow-Derived Dendritic Cells (BMDCs) Isolation.

BMDCs were isolated from 6-week-old BALB/c mice based on protocol described ^[3] by Lutz *et al* with some modification. Mice were euthanized, and the femurs and tibiae were collected. The intact bones were soaked in 75 % (v/v) ethanol for disinfection and then washed with RPMI 1640

medium in a petri dish. Next, the femurs and tibiae were separated, and both ends of the femur bone were cut off with a sterile pair of sharp scissors. The bone marrow was flushed with Hanks' Balanced Salt Solution (HBSS) using a 1 mL syringe with a 29 G needle and passed through a 70- μm nylon cell strainer until the bone turned from bright red to white. The collected cells were centrifuged $250 \times g$ for 8 min and the resulting pellet was resuspended in 3 mL of Red Blood Cell (RBC) Lysis Buffer, washed 3 times with RPMI 1640, and the cells were counted and plated with density of 1×10^6 cells in 9.8 mL culture medium (RPMI-1640 + 10% FBS + 20 mM penicillin/streptomycin). 0.2 mL of mouse recombinant granulocyte macrophage colony-stimulating factor (rmGM-CSF) from stocks ($1000 \text{ ng}\cdot\text{mL}^{-1}$) was added and cells were incubated at 37°C with 5% CO_2 . After three days, another 10 mL of the culture medium were added to the plate without removing any previous media and cells were incubated with a total of 20 mL culture medium for three more days. At day six and eight, half of the media (10 mL) was gently removed and centrifuged at $250 \times g$ for 5 min, then collected cells were resuspended in 10 mL fresh media (RPMI-1640 + 10% FBS + 20 mM penicillin/streptomycin) containing $200 \text{ ng}\cdot\text{mL}^{-1}$ rmGM-CSF and then added back into the original plate. At day 10, cells were fed the same way as day six and eight (10 mL RPMI-1640 + 10% FBS + 20 mM penicillin/streptomycin) but this time, the amount of rmGM-CSF in the medium contained only $100 \text{ ng}\cdot\text{mL}^{-1}$. For complete maturation, the day 10 non-adherent cells were collected by gentle pipetting, centrifuged at $300 \times g$ for 5 min at RT, and resuspended in 10 mL media containing $100 \text{ ng}\cdot\text{mL}^{-1}$ rmGM-CSF and then cultured for 24–48 hours. At day 12, nonadherent cells were collected and centrifuged for $300 \times g$, 5 min and counted by hemocytometer to culture 400,000 cells in 24 a well plate. DCs were treated with different concentrations of Q β (50, 100 and 200 μg) and PBS as control and incubated for 24 h. The effect

of Q β on bone marrow-derived dendritic cell maturation was evaluated by flow cytometry after staining with anti-CD11c, anti-CD80, and anti-CD86. The flow cytometry data were analyzed by FlowJo software and are illustrated in Figure A.23A. For evaluating the adaptive immunity triggered by Q β , spleens were removed from 6-week old BALB/c mice and immediately shredded with tweezers and passed through a 70- μ m nylon cell strainer using RPMI 1640 medium supplemented with 10% FB Essence, 1% penicillin-streptomycin, and 50 μ m β -mercaptoethanol. The cells were centrifuged at 1,000 $\times g$ for 5 mins. The red blood cells were then lysed with Red Blood Cell (RBC) Lysis Buffer for 5 mins at RT. The cells were centrifuged at 1,000 $\times g$ for 5 mins. The splenocytes were washed 3 \times with clean media and counted by hemocytometer. After counting, 1 $\times 10^6$ cells were cultured in a 24 well plate and incubated with different concentration of Q β (50, 100 and 200 μ g) for 24 h. Cells stained with anti-CD3, -CD4, -CD8, -CD44 and -CD62L and data analysis was carried out using FlowJo software with gating strategy shown in Figure A.24.

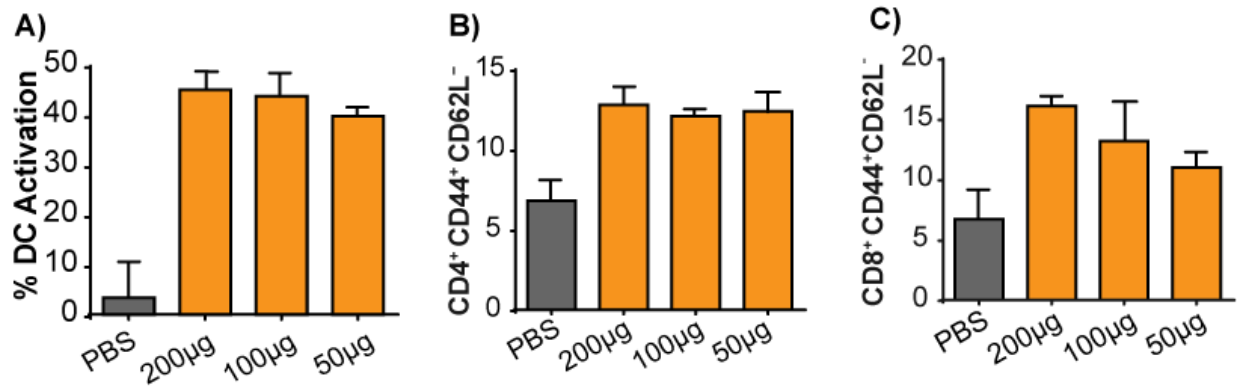


Figure A.23. *In vitro* immunostimulatory response of Qβ at different concentrations against BMDC and splenocyte isolates from BALB/c mice by flow cytometry (n=3). A) Bone marrow-derived DCs were analyzed for expression of CD80, CD86, CD11c by flow cytometry after stimulated with different concentration of Qβ for 24h. B) Flow cytometric analysis of CD3⁺CD4⁺CD44⁺CD62L⁻ splenocyte harvested from naïve mice and stimulated with different concentration of Qβ. C) Flow cytometric analysis of CD3⁺CD8⁺CD44⁺CD62L⁻ splenocyte harvested from naïve mice and stimulated with different concentration of Qβ.

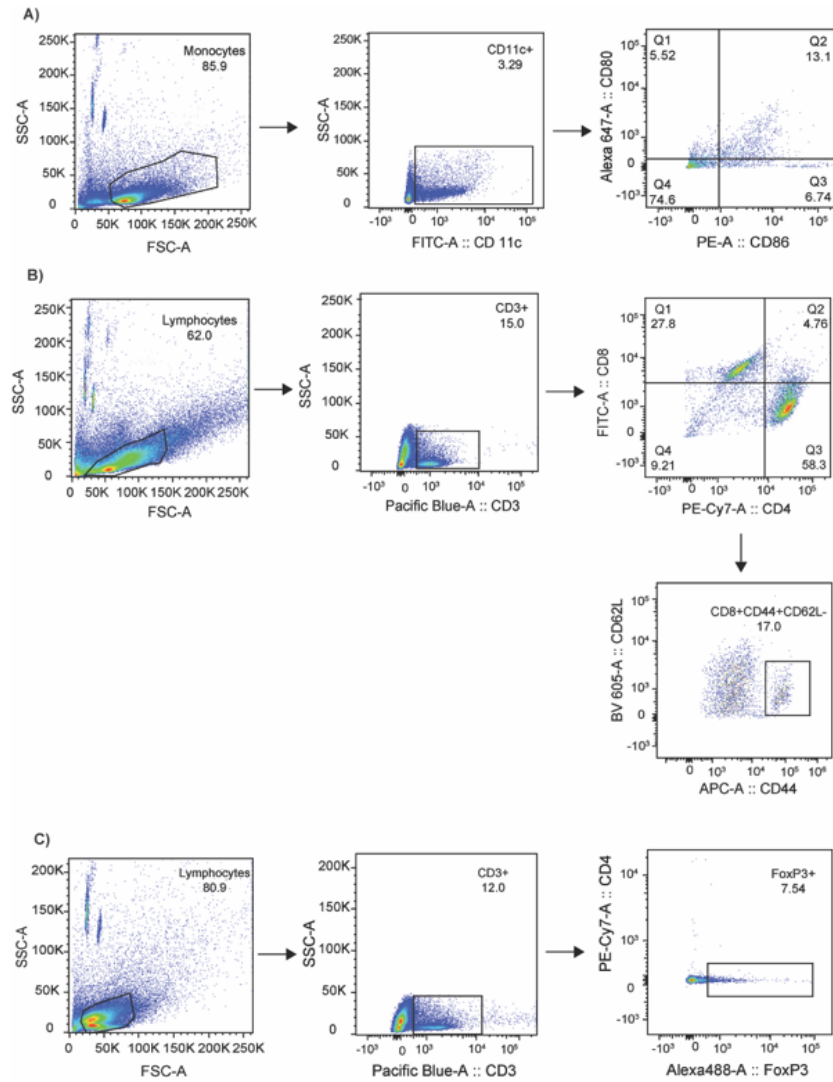


Figure A.24. Dot plot demonstrating gating strategies used to define A) CD11c⁺, CD80⁺ and CD86⁺ in tumor draining lymph node. B) CD3⁺, CD4⁺, CD8⁺ and CD8⁺CD4⁺CD62L⁻ in splenocyte obtained from BALB/c mice bearing 4T1 tumor. C) CD4⁺ producing Foxp3 in splenocyte isolated from BALB/c mice bearing 4T1 tumor.

APPENDIX B

EXTENDED DATA FOR CHAPTER 3

MATERIALS

(3,4-dibromomaleimide, N-methylmorpholine, methylchloroformate, Di-tert-butyl dicarbonate ((Boc)₂O), ethylenediamine, 6-bromohexanoic acid, triphenylphosphine, N-hydroxysuccinimide (NHS), and triethylamine were purchased from Sigma-Aldrich, Alfa Aesar, and Chem Impex. Potassium chloride, FBEssence, potassium phosphate monobasic, potassium phosphate dibasic, Dulbecco's Modified Eagle's Medium (6429), Tris base, sodium phosphate monobasic, tryptone, sodium phosphate dibasic, yeast extract, sodium dodecyl sulfate, sodium chloride, peptone, glycine, and Coomassie Brilliant Blue reagent were used without further purification. Reagents were purchased from Research Product International (Mt Prospect, IL, USA), VWR (Radnor, PA, USA), Chem-Impex Int'l (Wood Dale, IL, USA), Thermo Fisher Scientific (Waltham, MA, USA), and Sigma-Aldrich (St. Louis, MO, USA). siRNA HPLC purified siRNA luciferase(5'-GAUUAUGUCCGGUUAUGUA[dT][dT]-3'antisense:3'

UACAUAACCGGACAUAUAUC[dT][dT]-5') was purchased from Sigma Aldrich.

Size exclusion chromatography. Size exclusion chromatography was accomplished on an Agilent 1100 series HPLC system on a GS400SWXL (7.8 mm × 300 cm) column (flow rate 0.5 mL/min) using an aqueous mobile phase (0.1M Sodium Phosphate buffer, pH 7.4).

Gel analyses. 10% Sodium dodecyl sulfate-polyacrylamide gel electrophoresis (SDS-PAGE) was conducted on a BioRad Mini-PROTEAN Tetra Cell system. All electrophoresis protein samples were mixed with SDS loading buffer and heated to 95 °C for 5 min to ensure complete

denaturation. Molecular mass markers from Fisher Scientific were applied for approximation of the apparent molecular masses. Gels were run at 200V for 60 mins using SDS running buffer. Gels were imaged using a BioRad ChemiDoc Touch Imaging System. 1% agarose gels were used throughout the experiments. Experimental parameters for running the gel include the following: 100 V, 30 mins, and a running solution consisting of 1× TBE buffer. Samples were prepared in 50% glycerol.

Fast protein liquid chromatography (FPLC). VLP purification was performed using a BIO-RAD NGC Chromatography System. We used a size-exclusion Superose-6 Increase 10/300 GL column for all purification purposes. All trials used potassium phosphate buffer (1 M, pH 7.4) as eluting solution, a flow rate of 0.3 mL/min, and sample collection done at RT. All particles eluted between 12-14 mL.

Transmission electron microscopy (TEM). Transmission electron micrographs were taken on a JEOL JEM-1400+ (JEOL, Tokyo, Japan) at 120 kV with a Gatan 4k × 4k CCD camera. 5 μL of the ~0.1 mg/mL desalted sample was placed on a 300 mesh Formvar/carbon-coated copper grid (Electron Microscopy Sciences, Hatfield, PA, USA), allowed to stand for 30 seconds, and wicked off with Whatman #1 filter paper. 5 μL of 2% uranyl acetate (SPI Supplies, West Chester, PA, USA) was placed on the grid, allowed to stand for 30 seconds, wicked off as before, and the grid allowed to dry completely in air.

Dynamic-light scattering. Analysis was done with a UV-Vis Malvern Panalytical Zetasizer Nano ZS. A disposable microcuvette was used throughout the measurements. Experimental parameters included the following: 25 °C, a 175 ° scattering angle, a medium refractive index of 1.33, a 633 nm laser and material refractive index of 1.51.

Centrifugations and purification: Centrifugations were conducted using a Fiberlite F10 rotor at 19,510 \times g and a Sorvall Legend Micro 17 tabletop centrifuge at 17,000 \times g. General desalting and removal of other small molecules of biological samples were achieved using Amicon Ultra-15, either 10 kDa or 100 kDa molecular weight cut off (MWCO) centrifugal filter units. Dialysis was performed using Fisherbrand™ Regenerated Cellulose Dialysis with a 3.5 kDa MWCO.

Bradford assay: The amount of Q β before and after bioconjugation was measured using the Bradford method with bovine serum albumin as the standard. All protein determination values were based on the average of triplicate measurements.

Expression and purification of Q β and Q β (GFP). The expression and purification of Q β VLPs was done by using a published procedure, which is reproduced here in brief. The plasmids were gifts from Prof. M.G. Finn of the Georgia Institute of Technology. In a 10 mL of starter culture of E. coli BL21 cells with the plasmid were amplified to 500 mL of SOB media (100 μ g/mL kanamycin) at 37 °C until the OD₆₀₀ was 0.9-1.0. To that, 1 mM (final concentration) of isopropyl β -D-1-thiogalactopyranoside (IPTG) was added to induce the expression at 37 °C overnight. Cells were harvested by centrifuging using a Fiberlite F10 rotor at 10,500 rpm (19,510 \times g) for one hour at 4 °C, followed by re-suspending into 70 mL of 0.1 M potassium phosphate buffer (pH 7.00). Cells were lysed by in a cell homogenizer and the lysate was centrifuged in a Fiberlite F10 rotor at 10,500 rpm (19,510 \times g) for one hour at 4 °C. The pellet was discarded, ammonium sulfate was added to the supernatant to produce a final concentration of 2 mM, and the solution was incubated with rotation for at least 1 h at 4 °C. The suspension was centrifuged using Fiberlite F10 rotor at 10,500 rpm (19,510 \times g) for one hour at 4 °C. The pellet was re-suspended in 10 mL of 0.1 potassium phosphate buffer (pH 7.00), and an equal volume solution of n-butanol and chloroform

(1:1) was added. The solution was vortexed and pelleted by centrifuge in a Fiberlite F10 rotor at 10,500 rpm ($19,510 \times g$) for 30 min at 4 °C. The top aqueous layer was carefully recovered and further purified by 10-40% sucrose gradient in a SW-28 rotor at 23,500 rpm ($73,078 \times g$) for 16 hours at 4 °C. The band containing Q β particles was visualized by white light—typically from the flash of a cell phone—from the bottom of the tube and extracted using a long needle. This extract was pelleted using a Ti-70 rotor at 60,000 rpm ($264,902 \times g$) for 2.5 hours. The pellet was re-suspended into the desired buffer.

Bioconjugation of TPP-DB to Q β . Q β solution was prepared in a 10 mM sodium phosphate solution (pH 5.00) and the disulfide bonds were reduced by addition of tris(2-carboxyethyl) phosphine (TCEP) (10 eq per disulfide) at RT for one hour (each Q β has 180 disulfide bonds). 20 eq of TPP-DB compound dissolved in 10% DMF was added to the reduced Q β solution (1 mg/mL). The reaction was incubated at RT overnight. The conjugated product was purified by centrifuge filter ($4300 \times g$, 20 mins \times 3, 10,000 MWCO) using 10 mM sodium phosphate solution (pH 5.00).

Bioconjugation of TPP-NHS to Q β . Q β -TPP conjugates are not soluble and precipitate in phosphate buffer, so the reaction was done in HEPES buffer. TPP-NHS ester in DMF (20 eq) was added to Q β in HEPES and incubated at room temperature for 6 h on a rotisserie. The conjugates were purified by centrifugal filter ($4300 \times g$, 20 mins \times 3, 10,000 MWCO) or PD10 desalting column to get rid of excess small molecules using HEPES.

Bioconjugation of DB-PEG to Q β . Q β was prepared in 10 mM sodium phosphate solution (pH 5.00) and first reduced with 10 equivalents of TCEP, followed by the addition of dibromomaleimide-PEG (DB-PEG). The reaction was then left on a rotisserie overnight at RT

before purifying using centrifugal filter (4300 ×g, 20 mins ×3, 10,000 MWCO) or a PD10 desalting column with HEPES buffer. Conjugation of TPP-NHS with surface amines was then performed using the same method as bioconjugation of TPP-NHS to Q β .

Cytoplasm mimicking cleavage experiment. To evaluate the cytoplasm GSH-triggered release mechanism of the maleimide linker, we first labeled dibromaleimide with Fluorescein Isothiocyanate (FITC). To investigate the cleavage behavior of Q β -M-FITC using an artificial cytoplasm environment, a solution of Q β -M-FITC (2 mg/ml) was incubated in a solution of 20 mM HEPES, 100 mM KCl, 1 mM MgCl₂, 1 mM EDTA, pH 7.4 and 1 mM glutathione, which mimics cytoplasm conditions. The mixture was vortexed for 10 s, then incubated at 37 °C for 24 h, and the DB-FITC release was monitored by size exclusion chromatography over 24 h.

Cytotoxicity of Q β (GFP)-DB-TPP. To investigate the cytotoxicity of Q β (GFP)-DB-TPP on A549 cells, 100 μ L of 2 mg/ml of the conjugated of Q β (GFP)-DB-TPP and Q β (GFP) was incubated in a 96 well plate with 10⁵ cells for 4 h and the viability was compared to control cells by a standard colorimetric 3-(4,5-Dimethylthiazol-2-yl)-2,5-diphenyltetrazolium bromide (MTT) assay. Cellular viability was determined based on the conversion of the water-soluble yellow MTT dye to an insoluble purple formazan over the course of 2 h. Formazan was then solubilized with 100 μ L of DMSO before reading the absorbance of each well at 570 nm (n = 3).

Uptake of Q β (GFP)-DB-TPP. To measure the uptake of Q β (GFP)-DB-TPP on A549 cells, 500 μ L of 2 mg/ml of the conjugated of Q β (GFP)-DB-TPP and Q β (GFP) was incubated in a 24 well plate with 10⁶ cells for 4 h. The cells were trypsinized with 1× trypsin-EDTA, moved to Eppendorf tubes, washed 3× with 1× PBS, fixed with 4% PFA for 15 mins at RT, washed 3× with 1× PBS, and transferred into cell culture tubes for analysis by flow cytometry. GFP fluorescence was

measured on a BD Bioscience LSRFortessa and the fluorescence intensity value of Q β (GFP)-DB-TPP and Q β (GFP) were compared using FlowJo v10 software.

Cytosolic delivery of Q β (GFP)-M-TPP. To study the *in vitro* GSH sensitive behavior of Q β (GFP)-DB-TPP, A549 cancer cells (10^5 cells) were seeded one night before experiment in 24 well plate in serum free media DMEM, supplemented with 1% Pen-Strep cell culture media, and incubated at 37 °C, 5% CO $_2$. Cells treated with either Q β (GFP) and Q β (GFP)-DB-TPP in 2 mg/ml concentration for 2 h before being washed 3 \times with serum free media and 3 \times with PBS. The cells were stained with DAPI for nucleus staining, or lysotracker blue DND imaged by epi fluorescence microscopy.

Disassembly of Q β Bacteriophages. To harvest coat proteins (CPs), 45 mg Q β (2.5 mg/mL) in PBS was disassembled directly into monomers under denaturing conditions when treated with 10 mM DTT for 15 min at RT. The solution was then centrifuged at 650 rpm (87 \times g) for 10 min and treated with 0.7 M MgCl $_2$ for 1h to precipitate the RNA. The disassembled CP/RNA mixture was then centrifuged at 4,000 rpm (3,283 \times g) (Allegra X-14R) for 10 min at 4 °C and the supernatant was collected for purification using a 100,000 MWCO spin column to remove capsids from CPs.

Encapsulation of siRNA inside Q β capsid. To assemble Q β around siRNA, we modified a procedure reported by the Bachmann group.²⁵⁰ Coat proteins (1 mg/ml) were mixed with 0.24 mg/ml siRNA in the presence of 1.0 M urea, 250 mM NaCl, and 2.5 mM DTT. The mixture was dialyzed at RT with 300 mL of 20 mM sodium phosphate and 250 mM NaCl (pH 7.2) using a 3.5 kDa cut off cartridge. After 4 h of dialysis, DB-TPP (50 eq to CP) was added to the mixture and allowed to react for 1 h at RT, followed by dialysis with a 300 kDa cut off cartridge against 500 mL of PBS.

Evaluation of in vitro RNA delivery using One Glo +Tox assay: HeLa cells expressing firefly luciferase (HeLa-Luc) were seeded (10,000 cells/well in opaque white 96-well plate) a day before the experiment and allowed to attach to the plate overnight in phenol red-free Dulbecco's modified Eagle's medium (DMEM). Then 100 μ l of 2mg/ml Q β -M-TPP encapsulated anti-luciferase siRNA, naked siRNA, Q β -M without TPP moiety encapsulated anti-luciferase siRNA, and Q β -M-TPP was added to each well and incubated for 24 h. Firefly luciferase activity and viability were analyzed using One Glo + Tox assay kits. Briefly, this assay is a two-step procedure with an "add-mix-read" format that checks luciferase gene expression in viable cells. The first step is checking viability based on an AFC fluorophore that measures live-cell-protease activity. To test this, 20 μ l of CellTiter-Fluor™ Reagent (prepared as 5 \times solution using 10 μ l of GF-AFC Substrate in 2ml of Assay Buffer) was added to all wells, and mixed briefly with an orbital shaker at 500 rpm and incubated for 1h at 37°C. Then fluorescence was read using a fluorometer at 380–400nmEx/505nmEm. The second part of the assay uses the ONE-Glo™ Luciferase Assay system to quantify the firefly luciferase reporter gene expression by measuring luminescence. For this purpose, 100 μ l of ONE-Glo™ Reagent was added to each well and incubated for 3 minutes, then luminescence was measured using a luminometer.

Synthesis of DB-amine

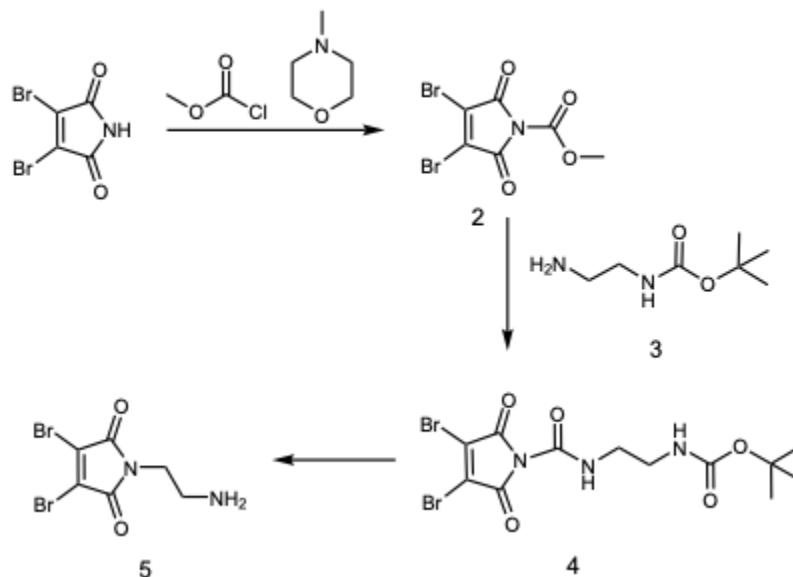


Figure B.1. Synthetic pathway of Dibromomaleimide-triphenyl phosphonium linker.

Synthesis of Methyl 3,4-dibromo-2,5-dioxo-2,5-dihydro-1H-pyrrole-1-carboxylate (Compound 2): 3,4-dibromomaleimide (1.0 g, 3.9 mmol) and N-methylmorpholine (0.43 ml, 3.9 mmol) were dissolved in 35 mL of THF and methylchloroformate (0.30 ml, 3.9 mmol) was added to the mixture. The reaction was stirred at room temperature (RT) for 20 min. After stirring, 40 mL of dichloromethane (DCM) was added, and the organic phase was washed with water (liquid-liquid extraction). The organic phase was dried over anhydrous MgSO_4 , filtered, and solvent was evaporated under reduced pressure to yield a pink solid. Yield: (1.15g, 3.70 mmol, 94%) ^1H NMR (600 MHz, CDCl_3) δ ppm 4.00 (s, 3 H). ^{13}C NMR (600 MHz, CDCl_3) δ ppm 54.85, 131.48, 146.99, 159.30.

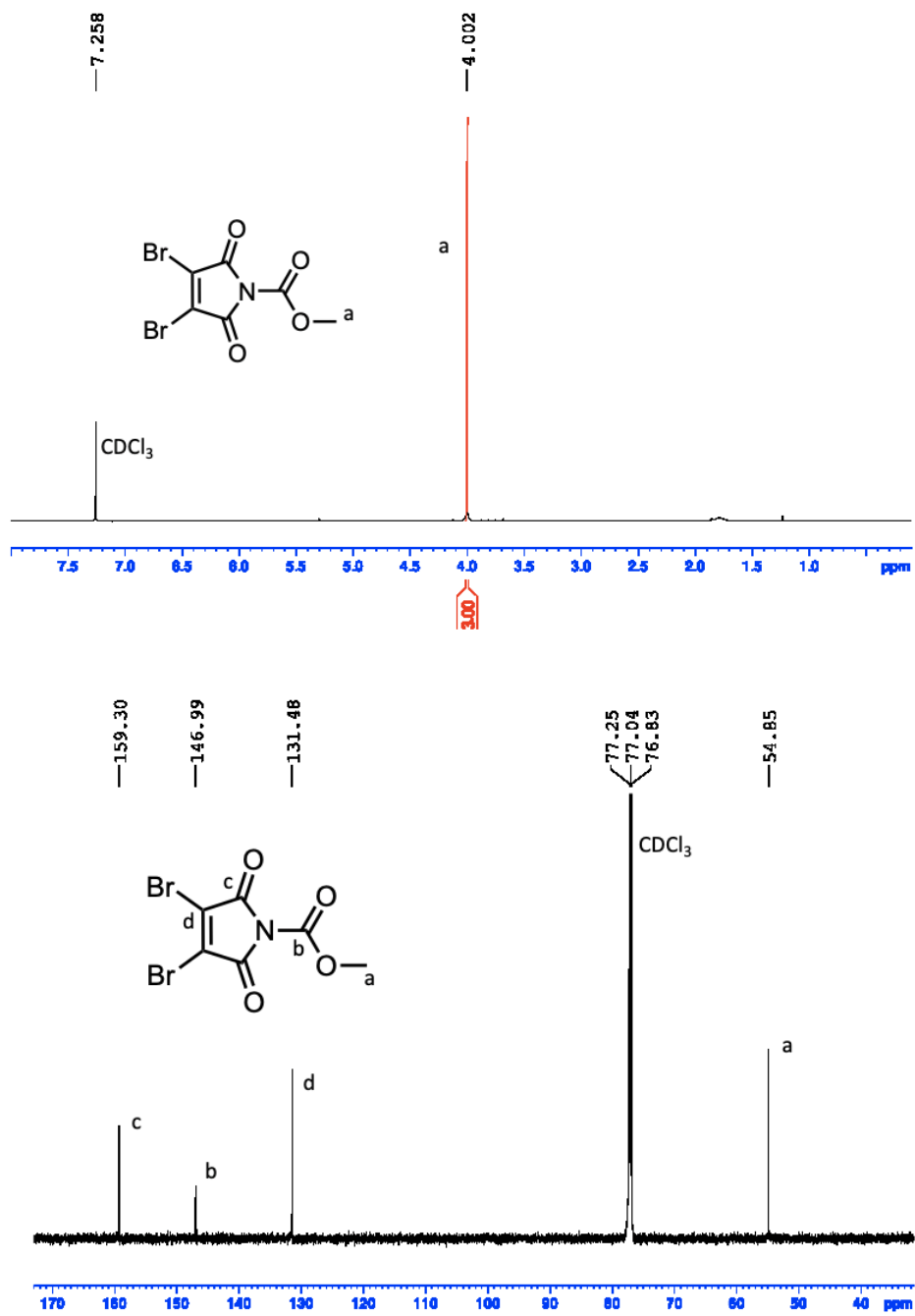


Figure B.2. ^1H and ^{13}C NMR of compound 2.

Synthesis of tert-butyl N-(2-aminoethyl) carbamate (Compound 3): To a solution of (Boc)₂O (5.0 g, 23 mmol) dissolved in DCM (10 mL) was added a solution of ethylenediamine (30.63 mL, 458.2 mmol) in DCM (50 mL) at 0°C. After addition, the mixture was allowed to reach RT for and stirred for 2 h. The organic phase was washed with water and dried over anhydrous MgSO₄. The organic layer was separated and concentrated under reduced pressure. The residue was again dissolved in 20 mL of diethyl ether and 20 mL brine. The mixture was acidified to a pH of 5.00 using a 4 M solution of HCl. The di-protected ethylenediamine was extracted in diethyl ether and discarded. The pH of the aqueous phase was again adjusted to 10.50 with a 2 M solution of NaOH and extracted with ethyl acetate. The organic phase was dried over anhydrous MgSO₄, filtered, and the solvent was evaporated under reduced pressure to yield the product as a yellow oil (2.24g, 14.0 mmol, 60%). ¹H NMR (600 MHz, CDCl₃) δ ppm 1.44 (9H, s), 2.79 (2H, t, *J*=5.89 Hz), 3.16 (2H, d, *J*=5.18 Hz), 5.46 (1H, bs). ¹³C NMR (600 MHz, CDCl₃) δ ppm 28.33, 41.79, 43.36, 78.88, 156.27.

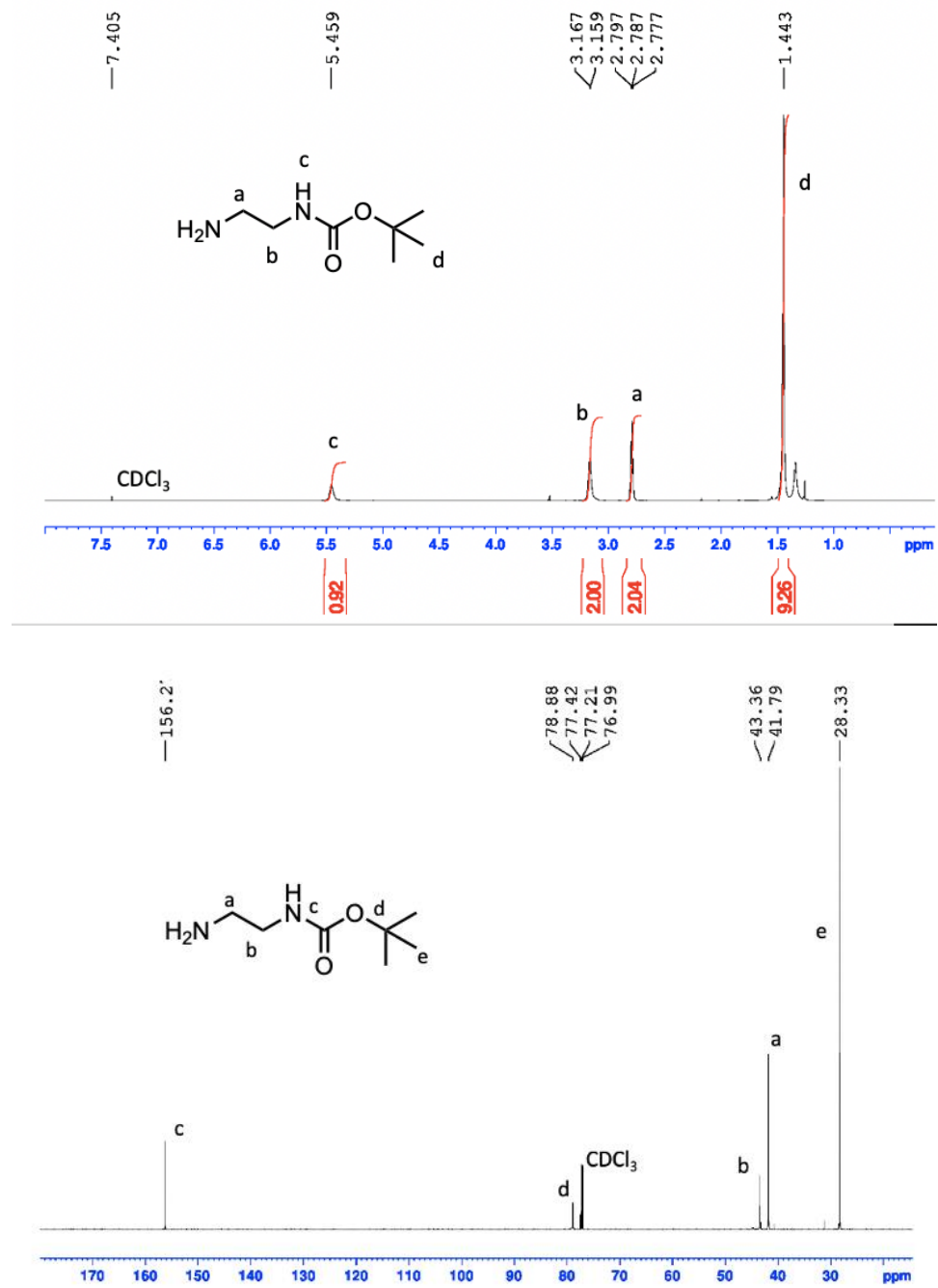


Figure B.3. ^1H and ^{13}C NMR of compound 3.

Synthesis of tert-butyl N-[2-(3,4-dibromo-2,5-dioxo-2,5-dihydro-1H-pyrrol-1-yl) ethyl] carbamate (Compound 4): To synthesize compound 4, compound 2 (1.050 g, 3.360 mmol) and compound 3 (0.5400 g, 3.360 mmol) were each dissolved in DCM (10 mL). The compound 3 solution was slowly added to the compound 2 solution and allowed to stir for 2 h. The reaction was then washed, and the organic phase was separated, dried with anhydrous MgSO₄, filtered, and then removed under reduced pressure. (0.60 g, 1.4 mmol, 51%) ¹H NMR (600 MHz, CDCl₃) δ ppm 1.39 (9H, s), 3.35 (2H, d), 3.74 (2H, d, *J*=2.27 Hz). ¹³C NMR (600 MHz, CDCl₃) δ ppm 28.29, 39.56, 79.84, 129.48, 156.07, 164.07.

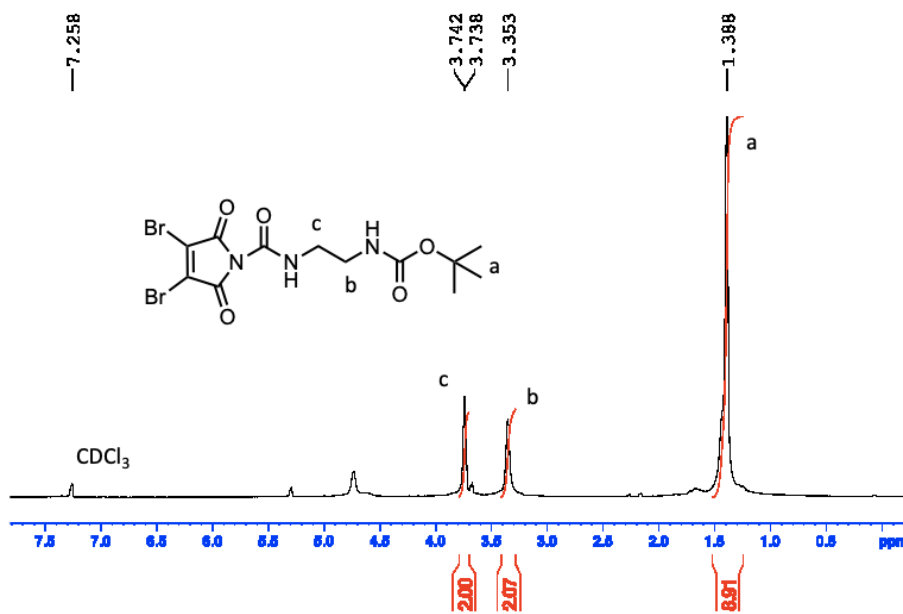


Figure B.4. ¹H and ¹³C NMR of compound 4

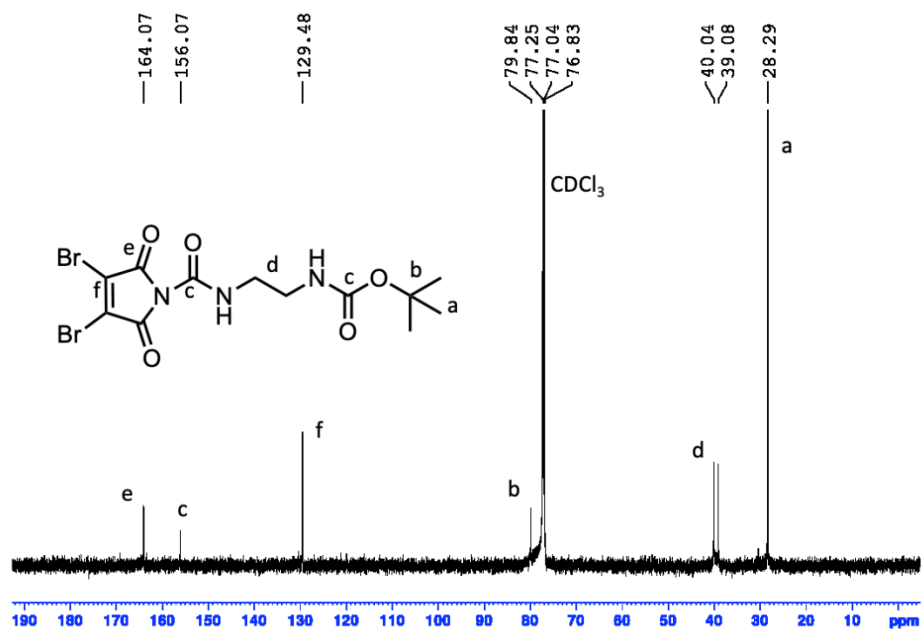


Figure B.5. ¹H and ¹³C NMR of compound 4.

Synthesis of 2-(3,4-dibromo-2,5-dioxo-2,5-dihydro-1H-pyrrol-1-yl) ethan-1-aminium trifluoroacetate (Compound 5):

To remove the Boc protecting group, compound 4 (1.0 g, 2.5 mmol) was dissolved in 20 mL of DCM/trifluoroacetic acid (TFA) (1:1), and the solution was stirred at RT for 1 h. Solvent was evaporated under reduced pressure to yield white crystals (0.90 g, 3.1 mmol, 81%). ¹H NMR (600 MHz, D₂O) δ ppm 3.12 (2H, t, *J*=5.79 Hz), 3.81 (2H, t, *J*=5.83 Hz). ¹³C NMR (600 MHz, (CD₃)₂SO) δ ppm 37.21, 37.80, 129.86, 164.67.

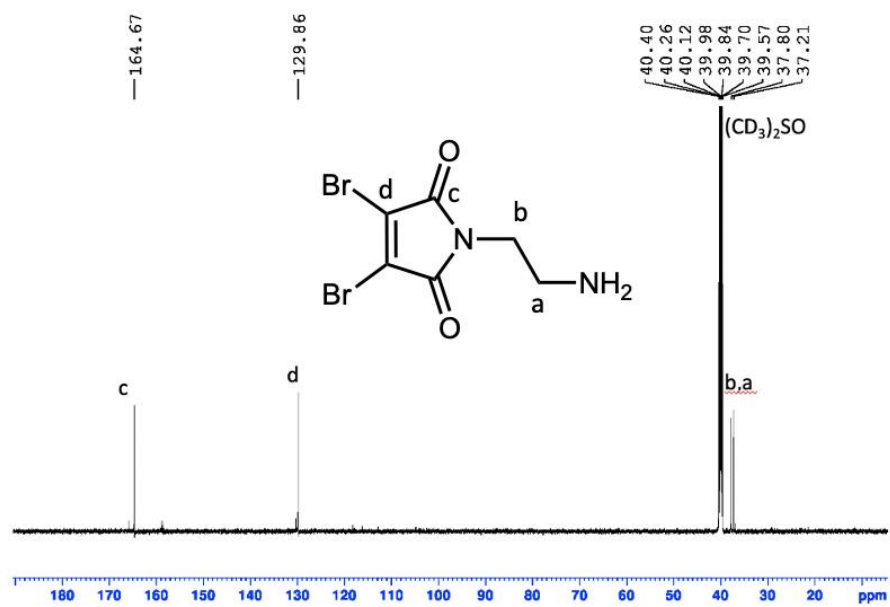
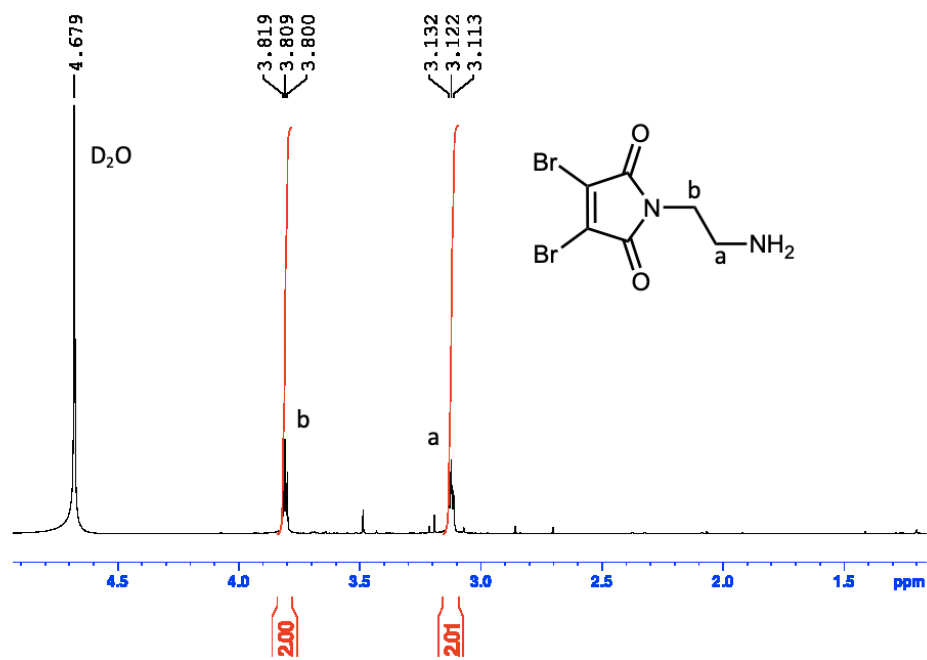
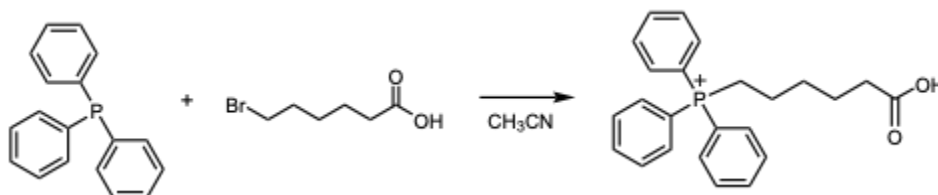


Figure B.6. ¹H and ¹³C NMR of compound 5.

Synthesis of (5-carboxypentyl)triphenylphosphonium (TPP-acid):



A solution of 6-bromohexanoic acid (8.0 g, 41 mmol) and triphenylphosphine (11.3 g, 43.2 mmol) in 50 mL acetonitrile was refluxed under N₂ nitrogen for 16 h. Upon cooling to room temperature, the product began to crystallize. The crystal product was filtered and washed with Et₂O (4 × 30 mL) to afford a white powder (14.4 g, 38.1 mmol, 93%). ¹H NMR (600 MHz, CDCl₃) δ ppm 1.69 (6H, s), 2.43 (2H, t, *J*=3.15 Hz), 3.62 (2H, t, *J*=6.74 Hz), 7.75 (15H, m, *J*=6.29 Hz). ¹³CNMR (600 MHz, CDCl₃) δ ppm 21.81, 22.43, 22.77, 23.99, 29.49, 29.60, 34.32, 117.90, 118.47, 130.62, 133.67, 135.16, 175.75

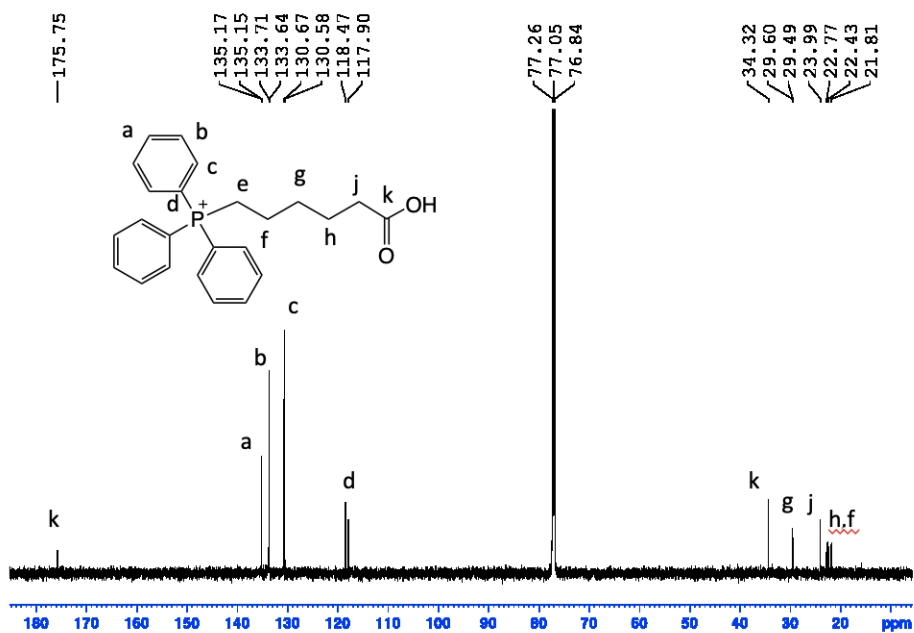
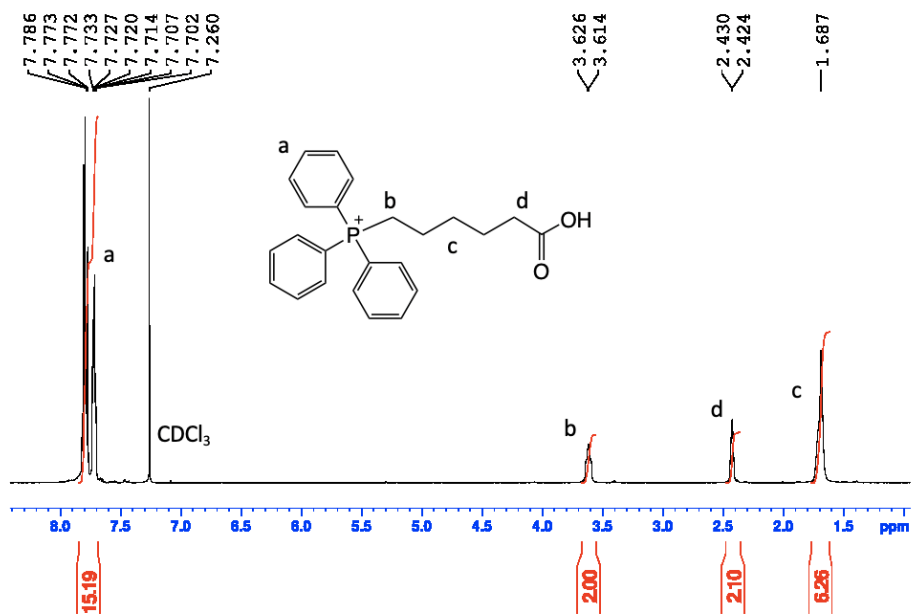
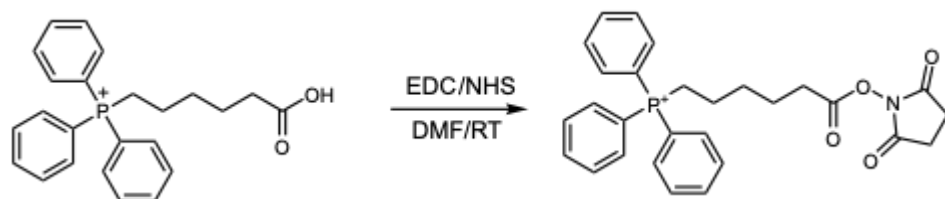


Figure B.7. ¹H and ¹³C NMR of TPP-acid.

Synthesis of (6-((2,5-dioxopyrrolidin-1-yl)oxy)-6-oxohexyl) triphenylphosphonium (TPP-NHS):



To a flask with (5-carboxypentyl) triphenylphosphonium (0.64g, 1.4 mmol dissolved in 10 ml of DMF) was added 1-ethyl-3-(3-dimethylaminopropyl)carbodiimide (EDC) (0.60 g, 3.8 mmol) and N-hydroxysuccinimide (NHS) (0.49 g, 4.2 mmol). The reaction was stirred at RT overnight. The solvent was evaporated under reduced pressure and the residue was further purified by silica chromatography (gradient 0–20% MeOH in DCM) to yield a white solid (0.25 g, 0.10 mmol, 37%). ^1H NMR (600 MHz, DMSO) δ ppm 1.62 (6H, m, $J=14.90$ Hz), 2.09 (2H, t), 2.66 (2H, t, $J=7.26$ Hz), 2.82 (4H, d), 7.84 (15H, m, $J=7.13$ Hz). ^{13}C NMR (600 MHz, DMSO) 20.40, 20.73, 21.79, 23.79, 25.91, 30.26, 118.73, 119.29, 130.70, 134.09, 135.37, 170.71

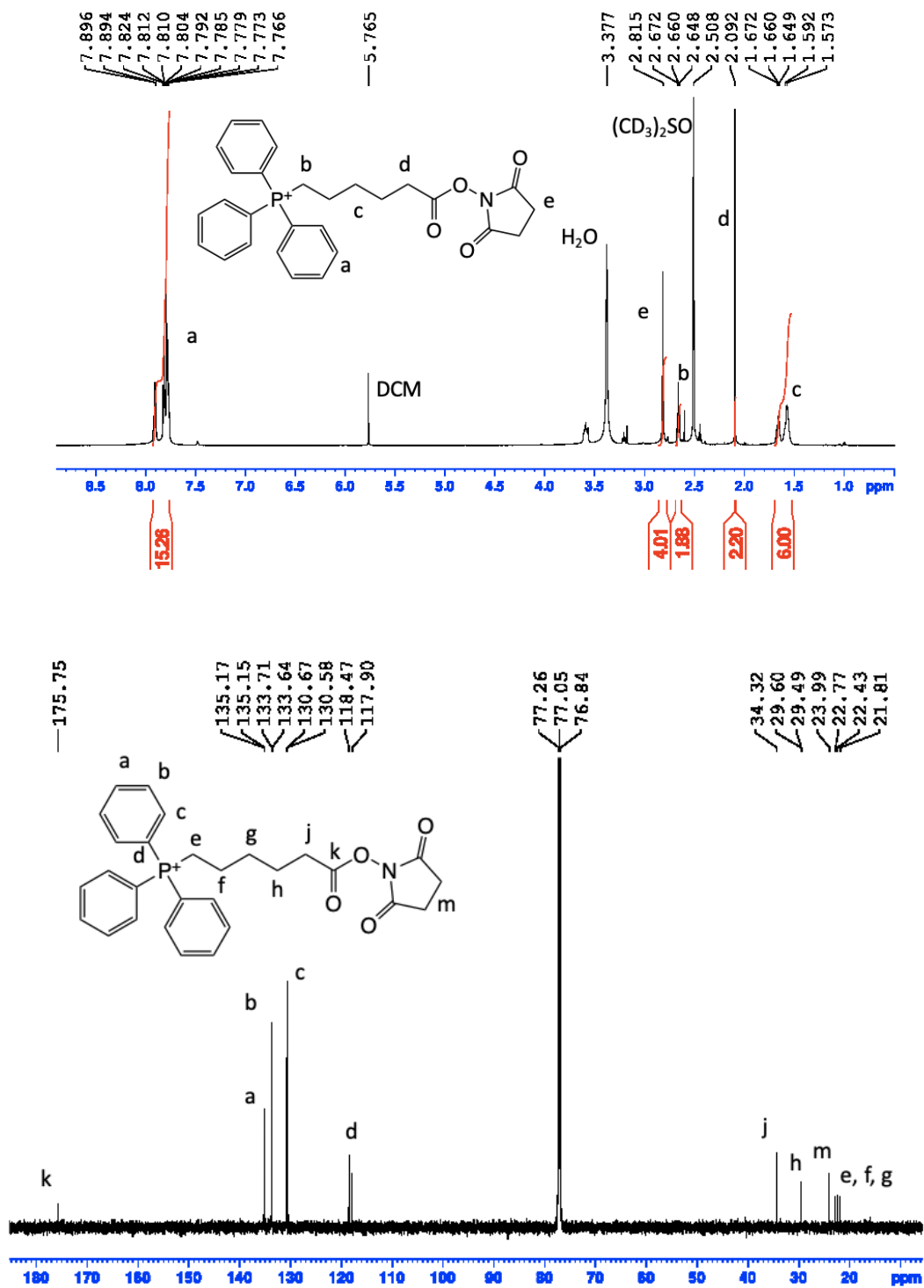
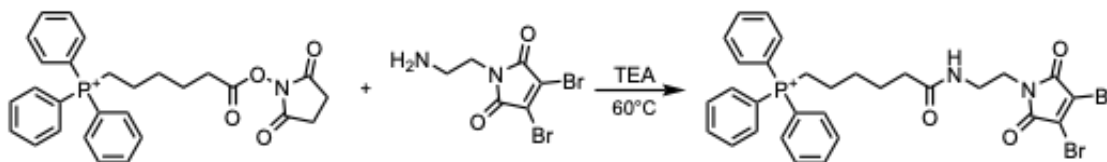


Figure B.8. ¹H and ¹³C NMR of TPP-NHS.

Synthesis of (6-((2-(3,4-dibromo-2,5-dioxo-2,5-dihydro-1H-pyrrol-1-yl) ethyl) amino)-6-oxohexyl)triphenylphosphonium. (TPP-DB):



Compound 5 (0.18 g, 0.44 mmol) was dissolved in DMF (10mL), and triethylamine (TEA) (0.06 mL) was added to solution and stirred for 0.5 h. TPP-NHS (0.23 g, 0.49 mmol) was dissolved in DMF (5 mL) and added to the stirred solution of compound 5 at 60 °C for 72h. The reaction mixture was cooled down to RT, solvent was removed, and crude were purified with basic alumina column under gradient of 0–10% MeOH:DCM. The solvent was removed and the product was collected (0.116 g, 0.177 mmol, 37%). ¹H NMR (600 MHz, DMSO) δ ppm 1.45 (6H, m, *J*=21.89 Hz), 2.73 (2H, t, *J*=3.86 Hz), 2.78 (2H, t), 2.90 (2H, t, *J*=3.54 Hz), 3.56 (2H, t), 7.87 (15H, m, *J*=10.10 Hz), 8.22 (1H, bs). ¹³C NMR (600 MHz, DMSO) δ ppm 22.17, 24.23, 29.99, 31.24, 32.33, 35.24, 37.15, 118.77, 119.33, 130.70, 134.07, 135.36, 162.78, 172.09. ESI) *m/z*: [M -Br] calculated for C₃₀H₃₀Br₂N₂O₃P⁺ 657.40; found, 657.14.

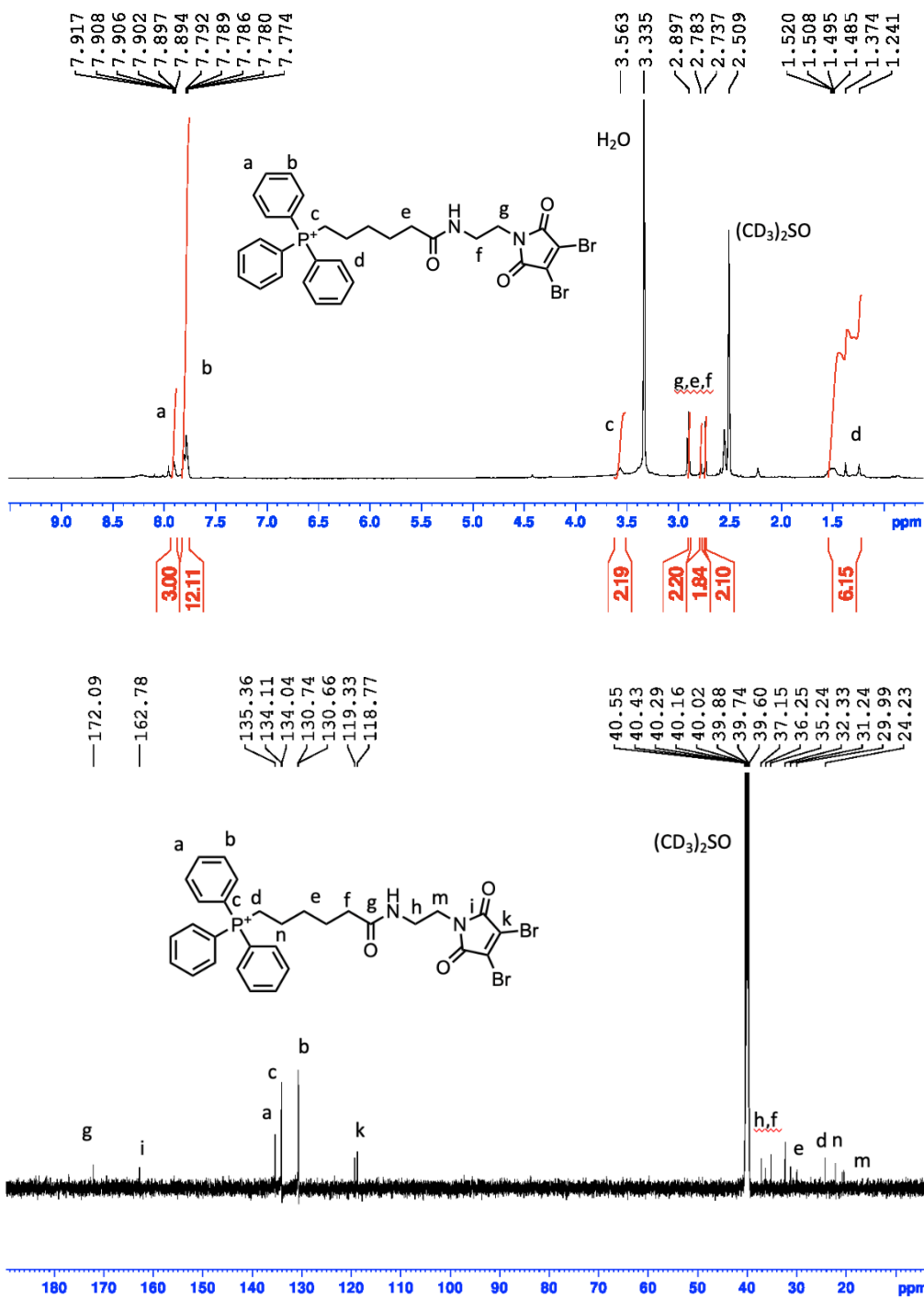
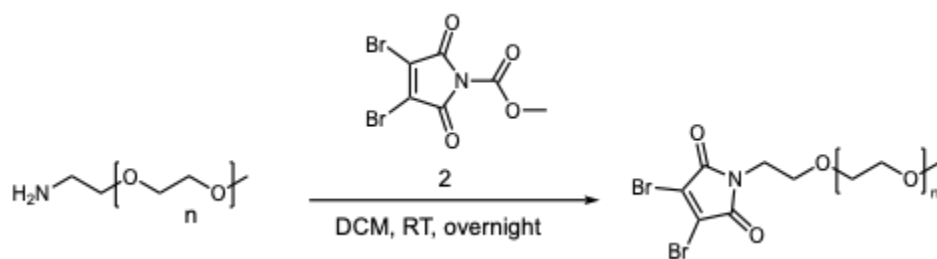
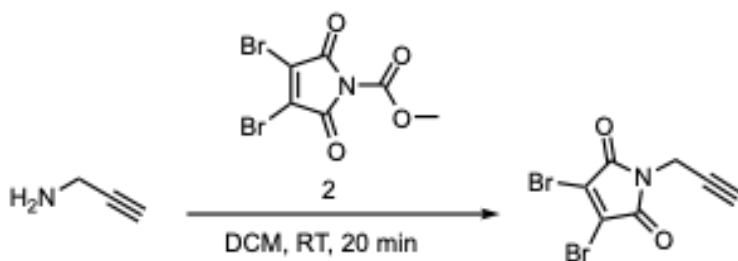


Figure B.9. ¹H and ¹³C NMR of TPP-DB.



Synthesis of dibromomaleimide-PEG: To a solution of compound **2** (0.1 g, 0.4 mmol) in 50 mL of DCM, methoxypolyethylene glycol amine 1000 (0.5 g, 0.5 mmol) was added, and the reaction mixture was stirred overnight. The solvent was removed under reduced pressure and purified using silica chromatography (gradient 0-30% MeOH in DCM) to yield a yellow oil (0.4 g, 0.3 mmol, 64%). $^1\text{H NMR}$ (500 MHz, CDCl_3) δ ppm 3.31 (s, 3 H) 3.47-3.49 (t, $J=5.00$, 2H) 3.50 - 3.62 (m, 88 H) 3.75 (t, $J=5.00$, 2H). $^{13}\text{C NMR}$ (126 MHz, CDCl_3) δ ppm 38.94, 52.19, 59.05, 67.54, 70.08, 70.58, 71.94, 129.43, 163.81. HRMS: Mass calculated for $[\text{M}+\text{H}]^+$ 1236.4376, observed 1236.4414.



Synthesis of 3,4-dibromo-1-(prop-2-yn-1-yl)-2,5-dihydro-1H-pyrrole-2,5-dione: DB-Alk was synthesized using a published procedure.⁶⁴ Propargylamine (0.025 mL, 0.381 mmol) was added to a solution of compound **2** (0.100 g, 0.432 mmol) in 5 mL of DCM and stirred for 30

min. After stirring, 40 mL of DCM was added and the organic phase was dried over anhydrous MgSO_4 , filtered and solvent was removed under reduced pressure. Yield (0.097g, 0.331 mmol, 0.387%) ^1H NMR (600 MHz, CDCl_3) δ ppm 2.27 (1H, s, $J=2.43$ Hz), 4.38 (2H, d, $J=2.46$ Hz). ^{13}C NMR (600 MHz, CDCl_3) δ ppm 28.61, 72.58, 76.06, 77.15, 129.83, 162.66. HRMS: Mass calculated for $[\text{M}+\text{H}]^+$. 291.8609, observed 291.8604.

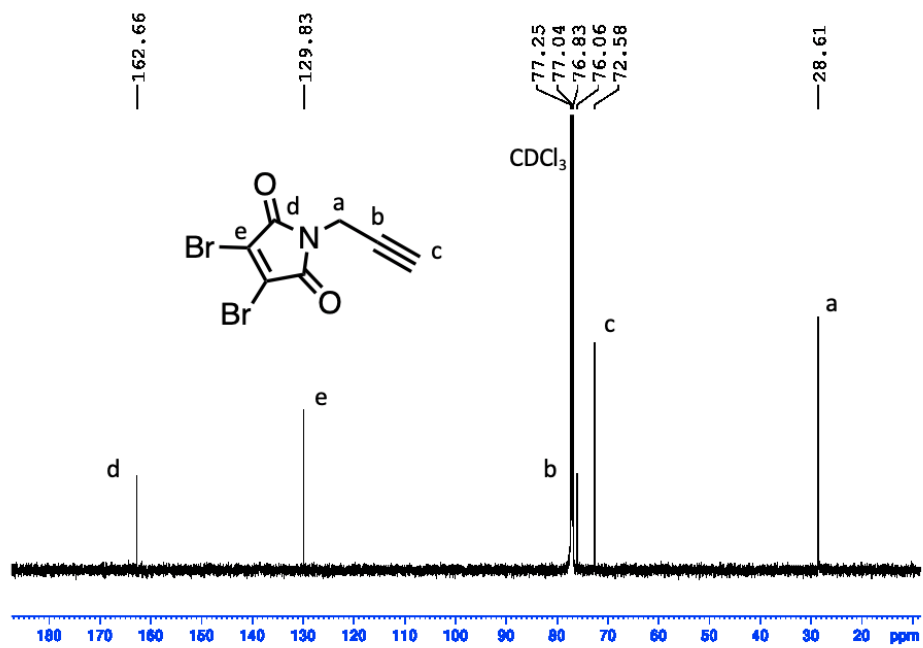
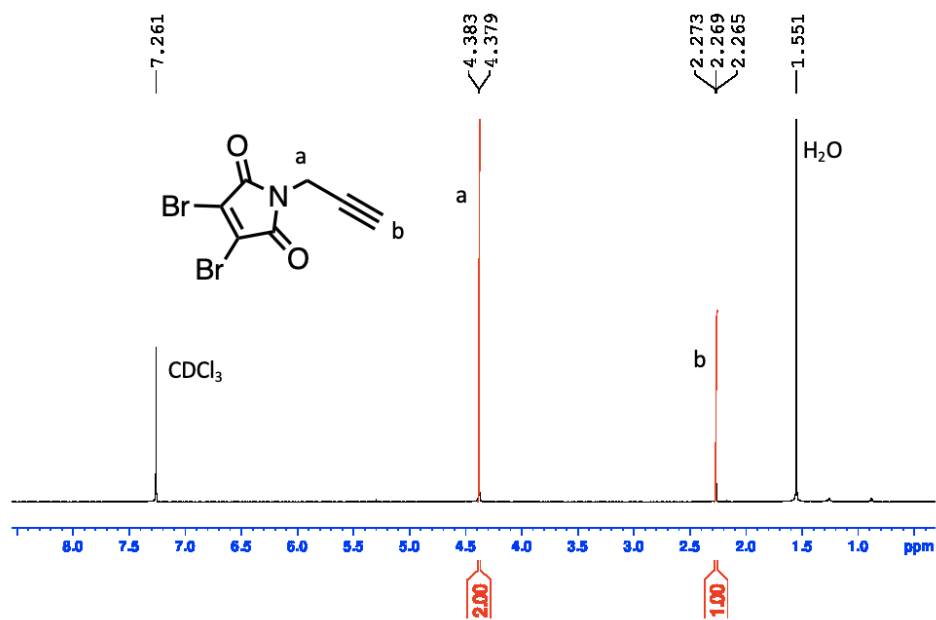


Figure B.10. ¹H and ¹³C NMR of DB-Alk.

Synthesis of 2-azido-ethylamine: A solution of sodium azide (3.1 g, 47 mmol) in 13 ml of water was mixed with 2-Bromoethylamine hydrobromide (3.1 g, 15 mmol) and heated up to 80 °C for 24 h. Then the mixture was cooled down to 0 °C in an ice bath and kept for 15 minutes to make the temperature homogenous in all parts of the mixture. Then, KOH (4.0 g, 71 mmol) was added to the stirred solution at 0° C. The mixture was then extracted with diethyl ether (4 ×16 mL). The organic phase was collected and dried over MgSO₄ and filtered. The solvent was removed under reduced pressure at 35 °C to yield 1.18 g (13.7 mmol, 71%) of 2-azido-ethylamine. ¹H-NMR (CDCl₃, 600 MHz) δ: 3.35– 3.55 (t, 2 H), 2.84 – 2.86 (t, 2 H). ¹³C-NMR (CDCl₃, 600 MHz) δ: 54.73, 41.43.

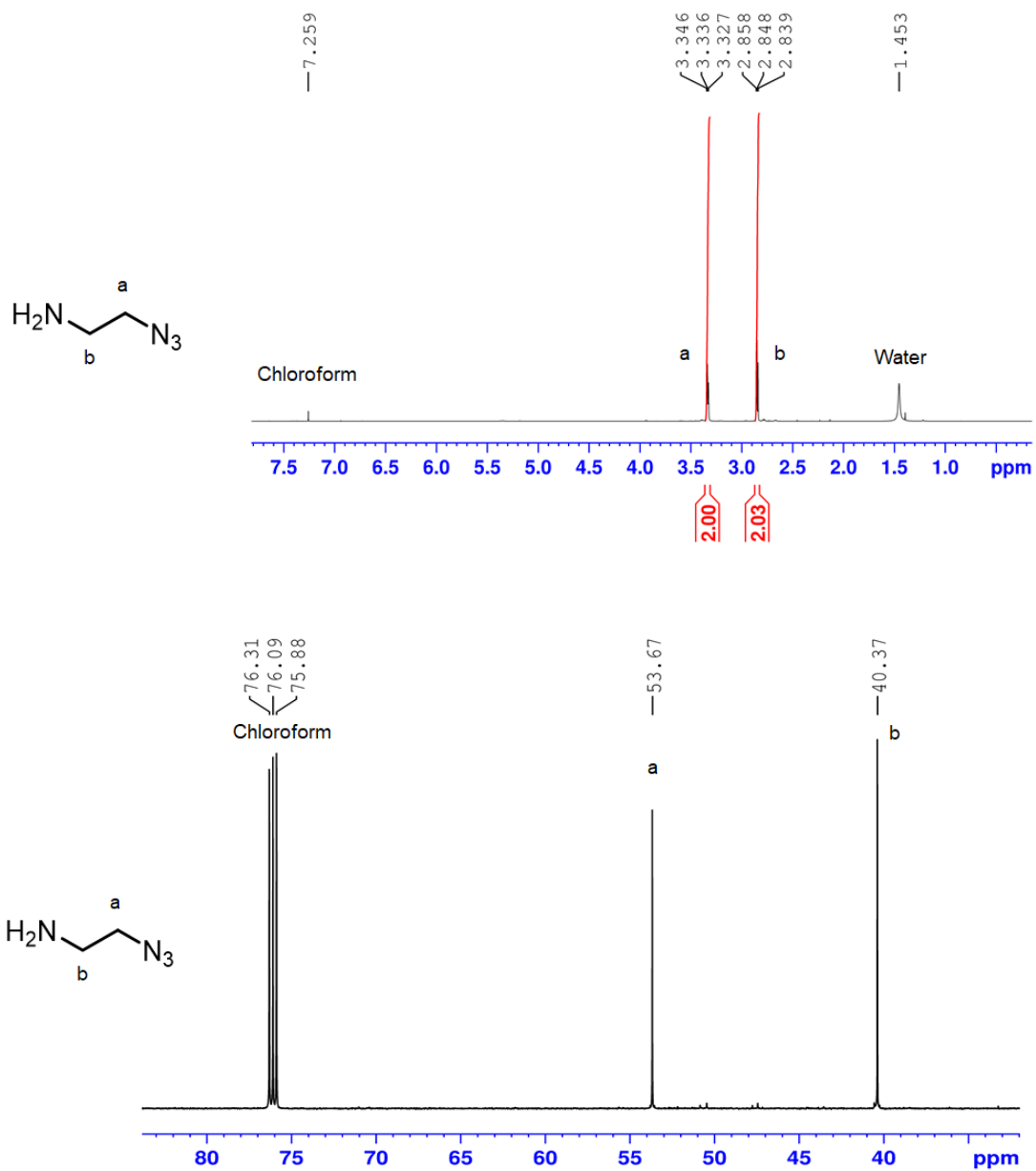


Figure B.11. ¹H and ¹³C NMR 2-azido-ethylamine.

Synthesis of fluorescein-azide: 5-(3-(2-Azidoethyl)thioureido)-2-(6-hydroxy-3-oxo-3H-xanthen-9-yl)-benzoic acid [FITC-Azide] was synthesized as reported in the literature.²⁹⁴ A 15 mL MeOH solution of fluorescein isothiocyanate (150 mg, 0.77 mmol) was mixed with 500 μ L of TEA and 2-azidoethyl amine (65.0 mg, 0.535 mmol). The mixture was then stirred overnight at room temperature. The solvent was evaporated under vacuum and the dark orange powder was collected (0.115 g, 0.242 mmol, 81% yield). ¹H-NMR (CD₃OD, 600 MHz) δ : 7.93 (s, 1 H), 7.71 – 7.72 (d, 1 H), 7.24 – 7.25 (d, 1 H), 7.17 – 7.19 (d, 2 H), 6.62 (s, 4 H), 3.86 (s, 2 H), 3.62 (s, 2 H). ¹³C-NMR (CD₃OD, 500MHz) δ : 9.14, 47.58, 51.15, 103.76, 113.87, 128.62, 131.64 , 141.63, 156.88, 172.13, 183.17.

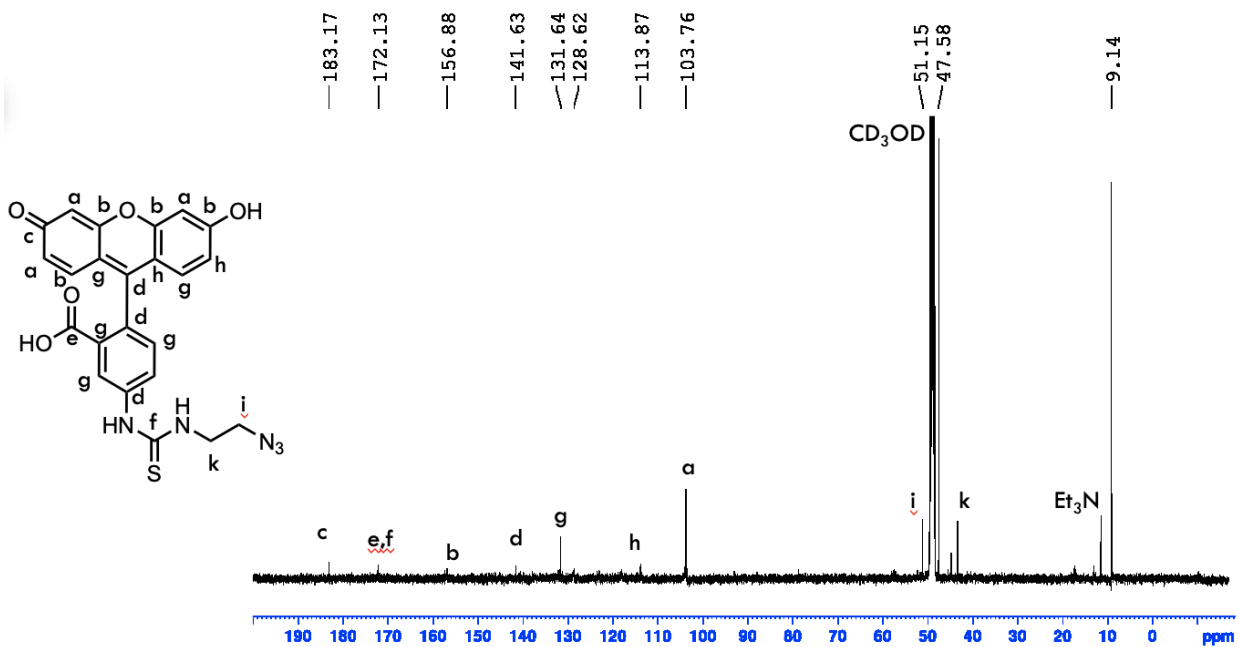
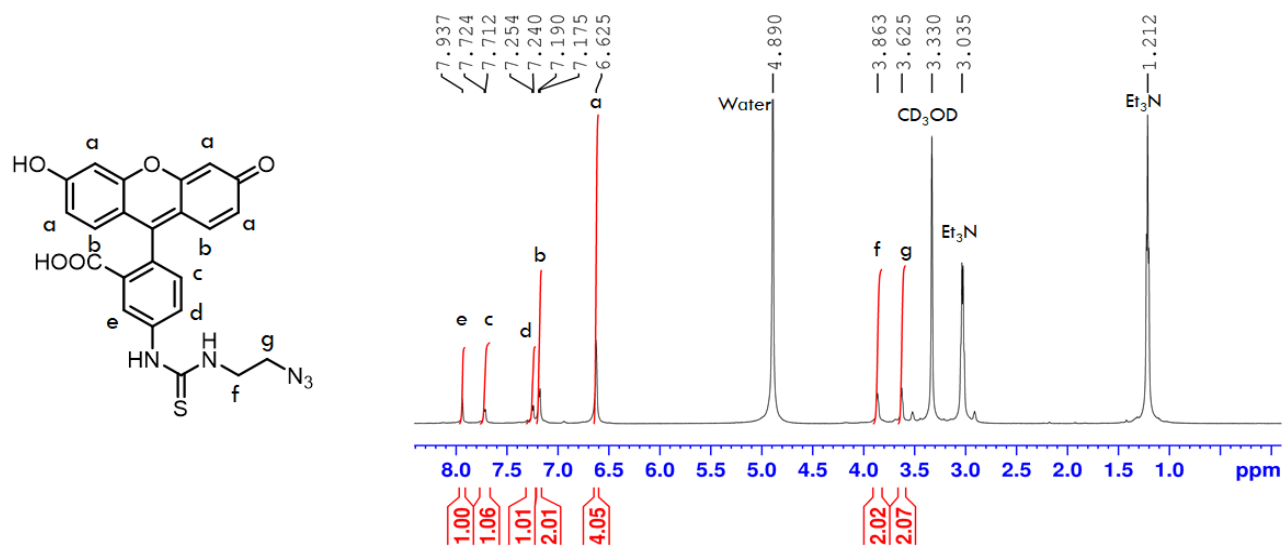


Figure B.12. ^1H and ^{13}C NMR of fluorescein-azide.

Determination of conjugation yield using Ellman's assay: Ellman's reagent solution was prepared by dissolving 4 mg of Ellman's reagent in 1 mL of reagent buffer (0.1 M sodium phosphate buffer, pH 8.00 with 1 mM EDTA). To make working solution, 125 μ L of prepared Ellman's reagent was added into 6.25 mL of reagent buffer. 25 μ L of cysteine standards (0 mM, 0.25 mM, 0.5 mM, 0.75 mM, 1.0 mM, 1.25 mM, 1.5 mM) was added into 255 μ L of Ellman's working solution, followed by incubation at RT for 15 min before reading the absorbance at 500 nm. A standard curve was plotted (**Figure B11**). The unfunctionalized cysteine concentrations of Q β conjugates were obtained from the standard curve. The reaction yield was calculated using:

$$Yield\% = \left(1 - \frac{c_1}{c_2}\right) * 100\%$$

c_1 : cysteine concentration of Q β conjugates

c_2 : cysteine concentration of Q β before reaction

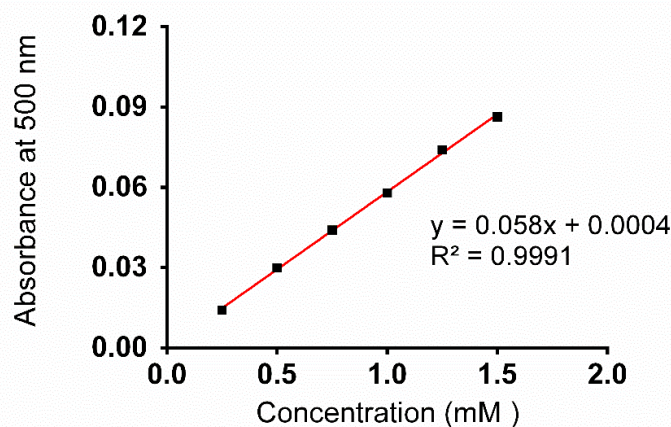


Figure B.13. Ellman's assay calibration curve. The standards cysteine concentrations are 1.5 mM, 1.25 mM, 1.0 mM, 0.75 mM, 0.5 mM, 0.25 mM, and 0 mM in Ellman's assay reagent buffer (0.1 M sodium phosphate buffer, pH 8.0 with 1 mM EDTA)

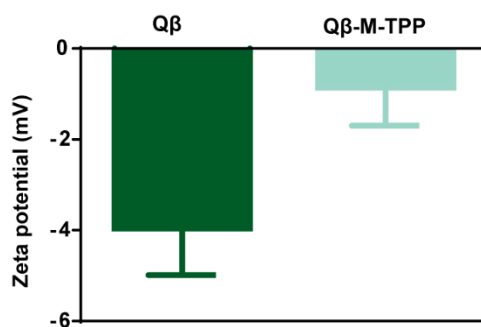


Figure B.14. ζ potential variation of Q β before and after M-TPP conjugation

Labeling Q β -Maleimide with FITC (Q β -M-FITC): To label Q β -Maleimide with FITC to test cytoplasm mimicking experiment by monitoring FITC fluorescence, first Q β is decorated with dibromomaleimide-alkyne (DB-Alk). 3 mg stock of purified Q β was reduced using 10 eq. of TCEP HCl (1h, RT). To the solution of reduced Q β , 2 mL of 0.1 M NaP buffer (pH 5) along with 20 eq. of DB-Alk in DMF (20 μ L) was added that appeared as a bright yellow fluorescent, the solution incubated at RT, overnight. The resulting solution was washed (3 \times) in a 10 K MWCO centrifugal spin column with 0.1 M NaP buffer (pH 5) three times. Next FITC-azide was conjugated to the alkyne group on the Q β surface through copper catalyzed azide-alkyne cycloaddition (CuAAC) click chemistry. To do that, 10 μ L of FITC-N3 in DMF (16.2 mM) was added to 1 ml of 1 mg/ml Q β -M-alkyne then 15 μ L of CuSO $_4$ ·5H $_2$ O (5 mg, 4 mM) was premixed with 30 μ L THPTA (22.0 mg, 41.5 mM) and added to the reaction mixture. Lastly 150 μ L of aminoguanidine HCl (11.0 mg, 99.5 mM) was added followed by 150 μ L of sodium ascorbate (2.00 mg, 13.3 mM). The solution was mixed for 4 h on a rotisserie. The resulting solution was washed (3 \times) in a 10 K MWCO centrifugal spin column with 0.1 M potassium phosphate buffer (pH 7).

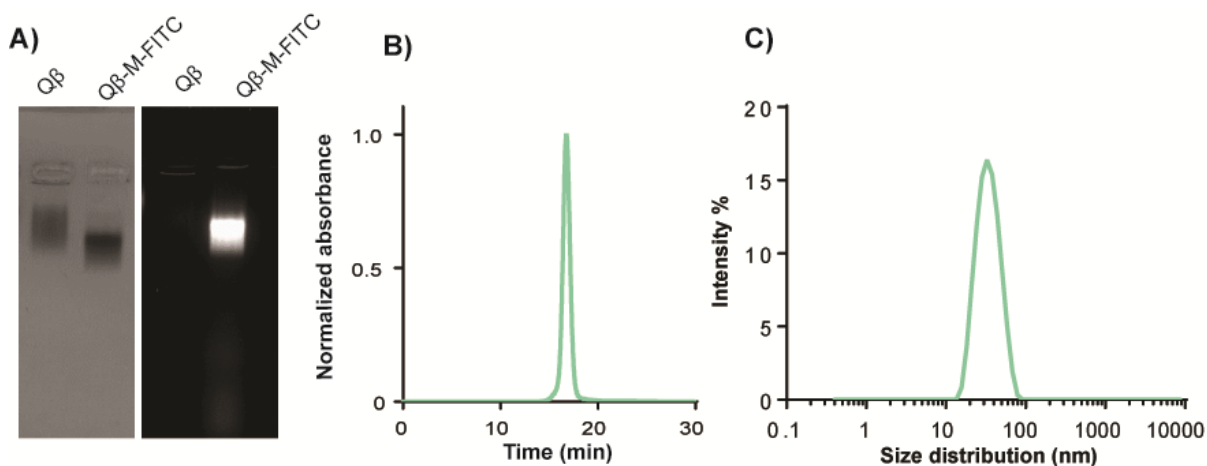


Figure B.15. Characterization of Q β -M-FITC conjugate using A) 1% agarose gel electrophoresis, showing a shift toward positive electrode due to negative charge of FITC B) SEC and C) DLS shows unchanged size distribution of 31.70 nm \pm 11.7 with PDI: 0.103.

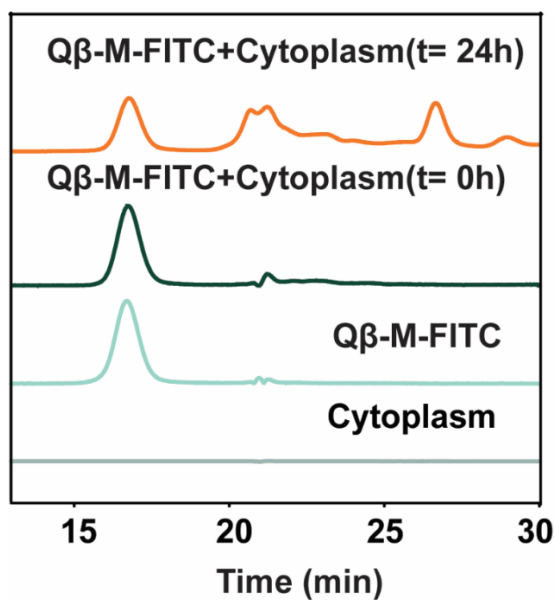


Figure B.16. Mimicking the cytoplasm cleavage by subjecting Q β -M-FITC to a solution of 20 mM HEPES, 100 mM KCl, 1 mM MgCl₂, 1 mM EDTA, pH 7.4 and 1 mM glutathione. The mixture was vortexed for 10 s then maintained at 37 °C for 24 h. M-FITC release was monitored by size exclusion chromatography.

Artificial cytoplasm cleavage: After a successful conjugation of maleimide-FITC linker to Q β , the cytosolic cleavage ability of Q β -M-FITC system was checked *ex vitro*. A solution that would approximate the of cytoplasm (20 mM HEPES, 100 mM KCl, 1 mM MgCl₂, 1 mM EDTA, pH 7.4, 1 mM, glutathione, 37 °C) was prepared. Cytoplasm solution (20 μ l) was added to a solution of Q β -M-FITC (380 μ l of 0.2 mg/ml) and incubated at 37 °C for 24 h. Cleavage of MA-FITC from Q β was monitored by size exclusion chromatography at 490 nm.

Fluorescence microscopy studies: 1×10^5 A549 cells were seeded on 35 mm glass bottom petri dish (MatTek) in DMEM (Sigma-Aldrich, supplemented with 10% FBS, 4500 mg/L glucose and 1% Pen-Strep) cell culture media, and incubated at 37 °C, 5% CO₂ one day before experiments. 2 mg/ml of Q β (GFP) and conjugate formulations were prepared in serum-free cell media and incubated with cells at 37 °C, 5% CO₂ for 4 hours. Cells were washed three times with serum-free cell media three times and three times with 1 \times DPBS, followed by nucleus staining (DAPI Thermo Fisher Scientific) or LysoTracker at 37 °C for 30 min. Cells were then washed with 1 \times DPBS three times before imaging. All the samples were imaged using an epi fluorescence EVOS fl microscope. Filter setting: GFP-UV (laser: 405 nm, filter: 500 nm to 540 nm) (Q β (GFP) and Q β GFP conjugates), Cy5 (nucleus). Images were processed using ImageJ.

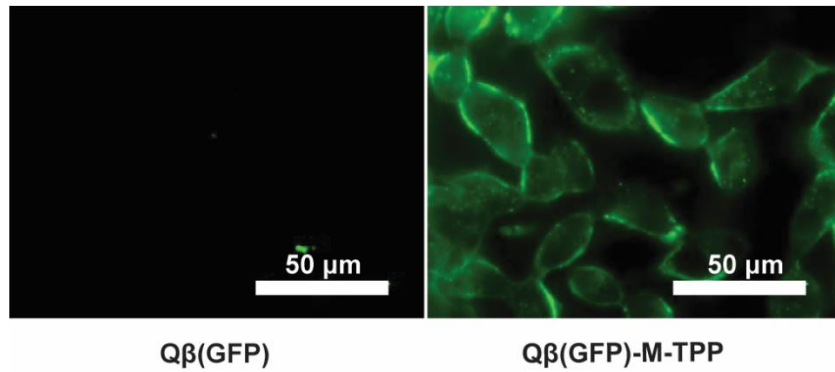


Figure B.17. Fluorescence micrographs of $Q\beta(GFP)$ and $Q\beta(GFP)-M-TPP$ in live A549 cells where the $Q\beta(GFP)-M-TPP$ shows entry into the cytosol, while the green fluorescence in $Q\beta(GFP)$ is quenched by acidic environment of endosome. Color code: green: $Q\beta(GFP)$. Scale bar = 50 μm .

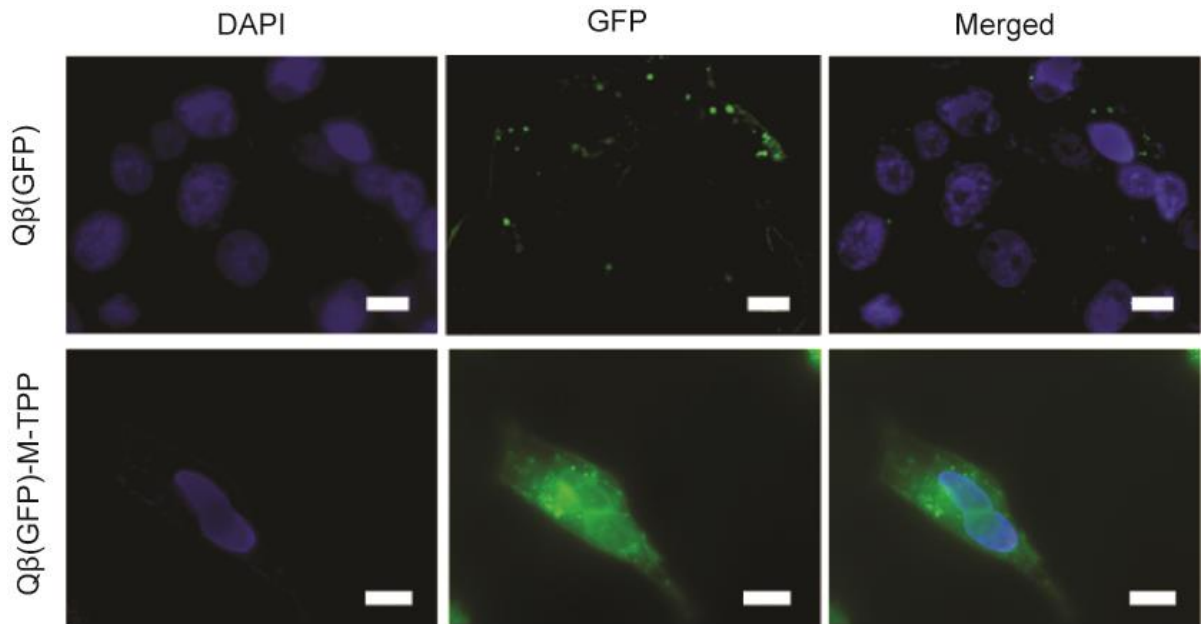


Figure B.18. Nuclei staining of A549 cells treated with $Q\beta(GFP)-DB-TPP$ and $Q\beta(GFP)$. Fluorescence micrograph showing cytosolic delivery of $Q\beta(GFP)-DB-TPP$. Scale bar: 10 μm .

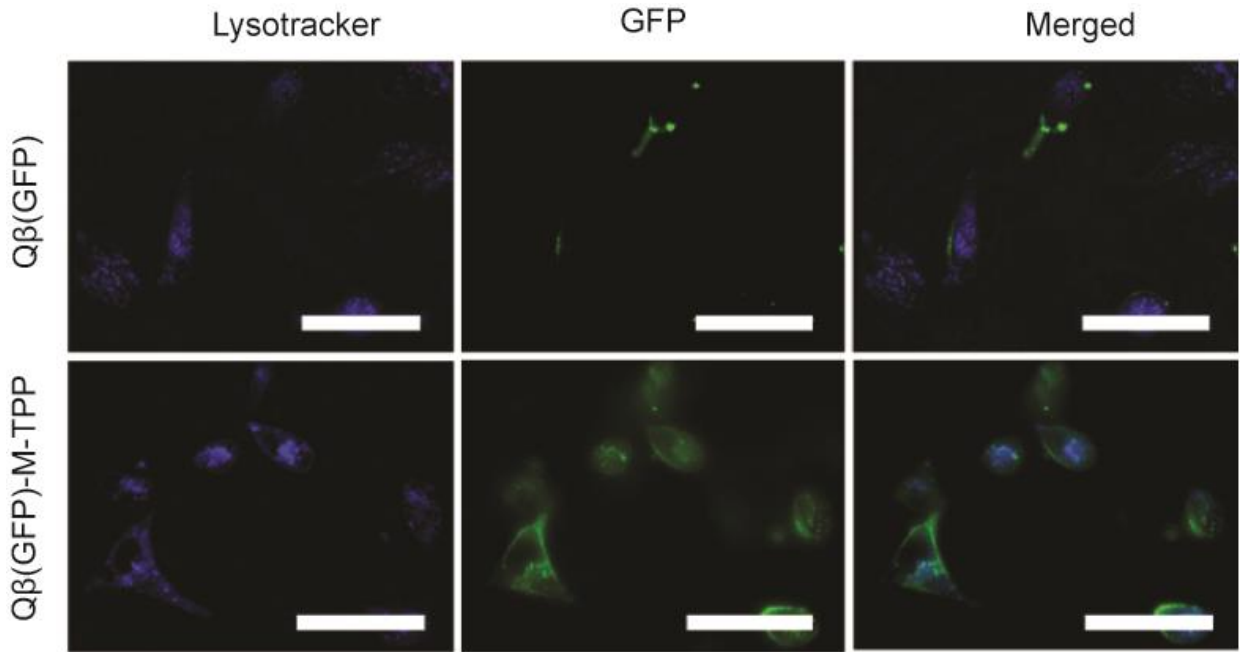


Figure B.19. Fluorescence micrograph of A549 cells with Q β (GFP)-TPP and Q β (GFP). Lysotracker in blue; particles in green. Scale bar = 50 μ m.

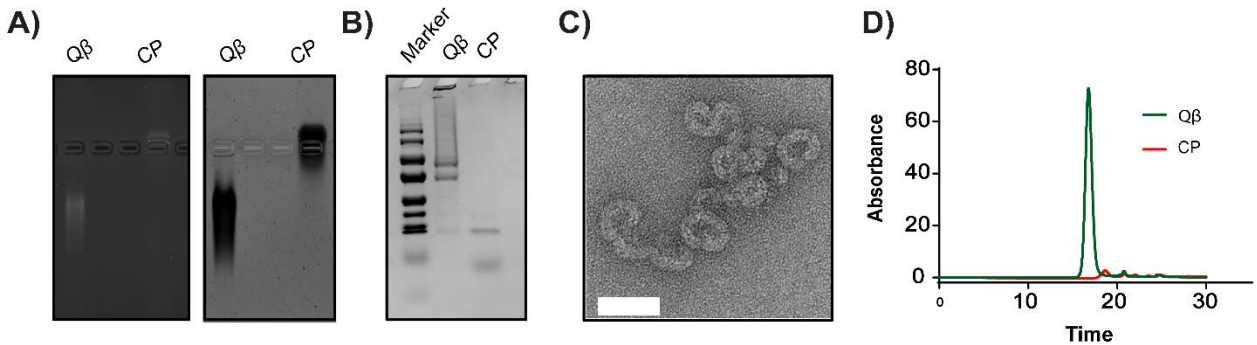


Figure B.20. Characterization of disassembled Q β . A) Native agarose gel electrophoresis SYBRGold stained showing removing *E. coli* RNA in Q β , (Right) Protein-stained bands show a positive nature for CP by moving toward negative electrode vs Q β B) Coomassie stained SDS-PAGE of Q β and coat protein showing reduction of crosslinked hexameric and pentameric subunit after disassembly. C) TEM micrographs of disassembled Q β display denatured capsid. D) Size exclusion chromatography profile of Q β and CP analyzed by absorbance at 280 nm.

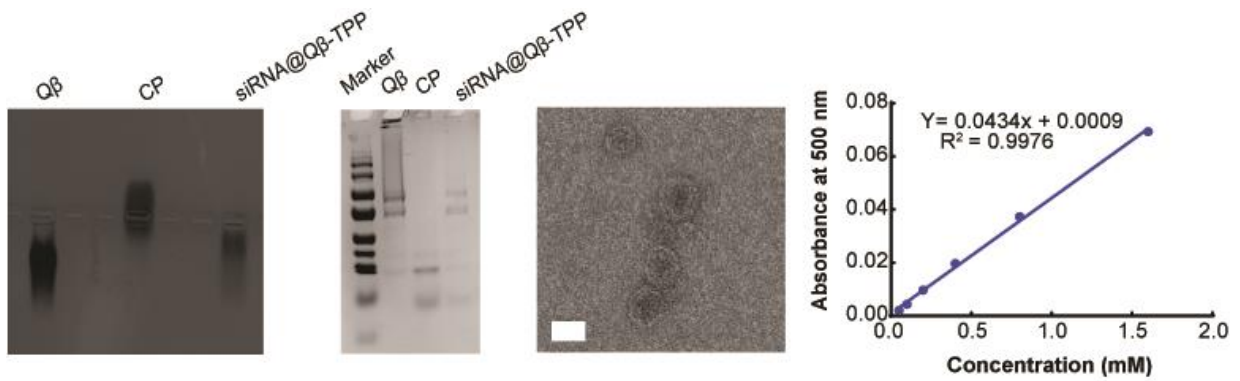


Figure B.21. A) protein-stained native agarose (1%) analysis of reassembled, disassembled, and intact Q β showing clear reformation of VLP band after reassembly. Through the protein band integrity and moving toward positive electrode C) Transmission electron microscopy imaging revealed that reconstituted Q β -M-TPP carrying siRNAs structurally forming unchanged icosahedral particles. D) Cysteine standard curve related to Ellman assay 78% conjugation efficiency is calculated.

APPENDIX C

EXTENDED DATA FOR CHAPTER 4

Material and Methods:

Ethylenediaminetetraacetic acid (EDTA), 2-methylimidazole, potassium phosphate dibasic, potassium phosphate monobasic, sodium bicarbonate, sodium carbonate, sodium chloride, sodium hydroxide, sodium phosphate dibasic, sodium phosphate monobasic and zinc acetate dihydrate were purchased from Sigma-Aldrich (St. Louis, MO, USA), Thermo Fisher Scientific (Waltham, MA, USA), or VWR (Radnor, PA, USA), and used without further modification.

Fluorescence

Fluorescence measurements were taken using a Tecan Spark 20M plate reader.

Scanning Electron Microscopy

SEM was performed on a ZEISS Supra 40 Scanning Electron Microscope (Zeiss, Oberkochen, Germany) with an accelerating voltage of 2.5 kV and a working distance of 6.7 to 15.3 mm. Samples were sputtered with a 37 Å layer of gold.

Transmission Electron Microscopy

Transmission electron micrographs were taken on a JEOL JEM-1400+ (JEOL, Tokyo, Japan) at 120 kV with a Gatan 4k × 4k CCD camera. 5 µL of the ~0.1 mg/mL desalted sample was placed on a 300 mesh Formvar/carbon-coated copper grid (Electron Microscopy Sciences, Hatfield, PA, USA), allowed to stand for 30 seconds, and wicked off with Whatman #1 filter paper. 5 µL of 2% uranyl acetate (SPI Supplies, West Chester, PA, USA) was placed on the grid, allowed to stand for 30 seconds, wicked off as before, and the grid allowed to dry completely in air.

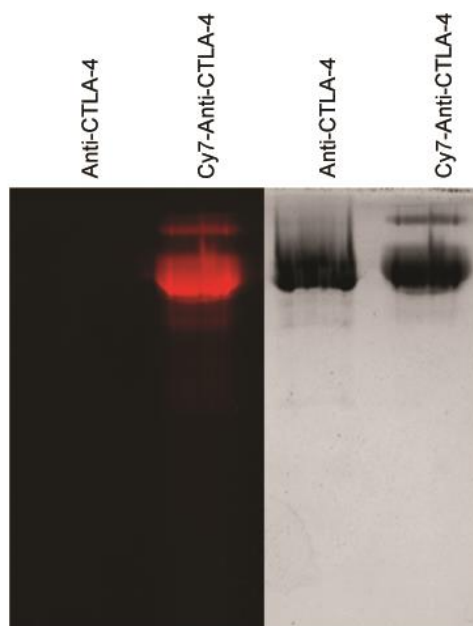


Figure C.1. 1% Agarose gel characterizing conjugation of Cy7 to anti-CTLA4 . Left) Unstained agarose show a bright fluorescence in Cy 7 infrared fluorescent detection channel imaged by Typhoon Right) Coomassie stained band of Cy7-anti-CTLA4 in same spot with fluorescent band.

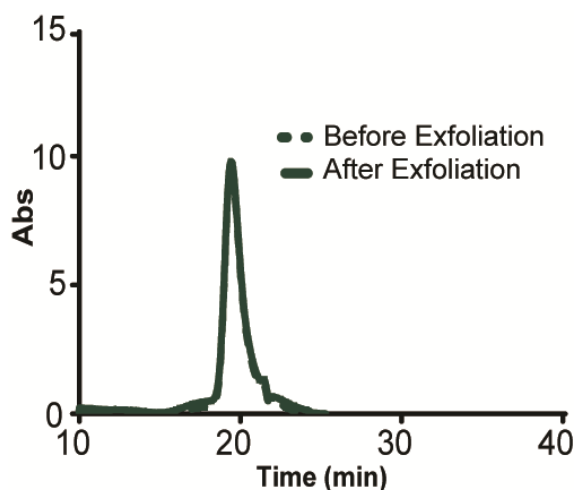


Figure C.2. 1% Agarose gel characterizing conjugation of Cy7 to anti-CTLA4 . Left) Unstained agarose show a bright fluorescence in Cy 7 infrared fluorescent detection channel imaged by Typhoon Right) Coomassie stained band of Cy7-anti-CTLA4 in same spot with fluorescent band.

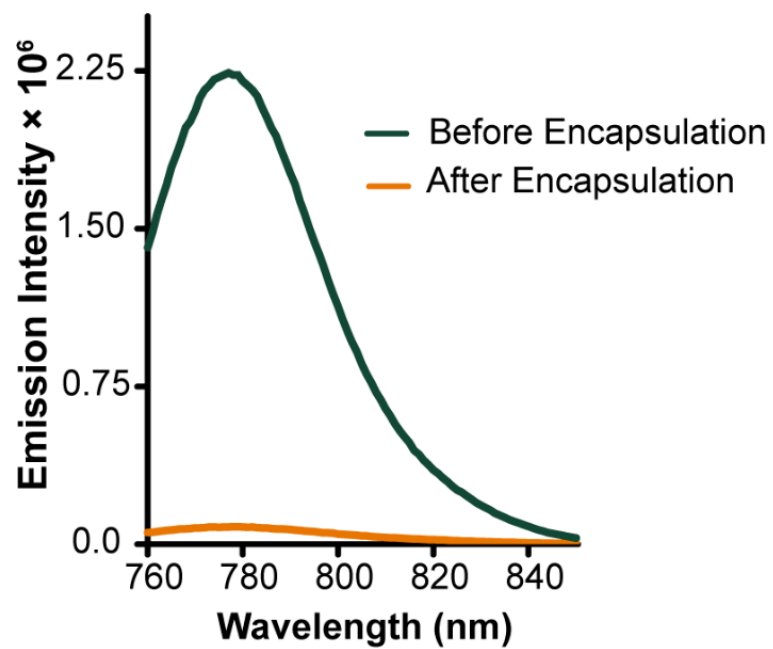


Figure C.3. Encapsulation efficiency of Cy7-anti-CTLA4 in ZIF measured by fluorescence of the supernatant ($\lambda_{\text{ex}} = 730 \text{ nm}$).

REFERENCES

1. Razieh Rezaei, M.S., Hamid Reza Mozaffari, Hedaiat Moradpoor, Sara Karami, Amin Golshah, Behroz Salimi, and Hossein Karami The Role of Nanomaterials in the Treatment of Diseases and Their Effects on the Immune System. *Open Access Maced J Med Sci.* **7**, 1884-1890 (2019).
2. Mallanagouda Patil, D.S.M., and Sowjanya Guvva Future impact of nanotechnology on medicine and dentistry. *J Indian Soc Periodontol.* **12**, 34-40 (2008).
3. Jian Gong, M.C., Ying Zheng, Shengpeng Wang, Yitao Wang Polymeric micelles drug delivery system in oncology. *Journal of Controlled Release* **159**, 312-323 (2012).
4. Evelyn Roopngam, P. Liposome and polymer-based nanomaterials for vaccine applications. *Nanomedicine Journal* **6**, 1-10 (2019).
5. Gregory G. Wildgoose, C.E.B., Richard G. Compton Metal Nanoparticles and Related Materials Supported on Carbon Nanotubes: Methods and Applications. *Small* **2**, 182-193 (2006).
6. Ming-Xue Wu, Y.-W.Y. Metal–Organic Framework (MOF)-Based Drug/Cargo Delivery and Cancer Therapy. *Advanced Materials* **29** (2017).
7. Sun, Y., Zheng, L., Yang, Y. et al. Metal–Organic Framework Nanocarriers for Drug Delivery in Biomedical Applications. *Nano-Micro Lett.* **12** (2020).
8. *al., I.M.T.e.* Metallic Nanoparticles for Targeted Drug Delivery. *Nanomat. Che Tech* **1**, 1-3 (2017).
9. Ranjita Misra, S.A., Sanjeeb K.Sahoo Cancer nanotechnology: application of nanotechnology in cancer therapy. *Drug Discovery Today* **15**, 842-850 (2010).
10. Choi, H., Liu, W., Liu, F. et al. Design considerations for tumour-targeted nanoparticles. *Nature Nanotech* **5**, 42-47 (2010).
11. Fakhar ud Din, W.A., Izhar Ullah, Omer Salman Qureshi, Omer Mustapha, Shumaila Shafique, and Alam Zeb Effective use of nanocarriers as drug delivery systems for the treatment of selected tumors. *Int J Nanomedicine* **12**, 7291-7309 (2017).
12. Ibrahim Khana, K.S., Idrees Khan Nanoparticles: Properties, applications and toxicities. *Arabian Journal of Chemistry* **12**, 908-931 (2019).
13. Jayanta Kumar Patra, G.D., Leonardo Fernandes Fraceto, Estefania Vangelie Ramos Campos, Maria del Pilar Rodriguez-Torres, Laura Susana Acosta-Torres, Luis Armando

- Diaz-Torres, Renato Grillo, Mallappa Kumara Swamy, Shivesh Sharma, Solomon Habtemariam, and Han-Seung Shin Nano based drug delivery systems: recent developments and future prospects. *J Nanobiotechnology* **16** (2018).
14. Scotti N, R.E.V.-l.p.p.i.p.a.p.v.E.R.V. Virus-like particles produced in plants as potential vaccines. . *Expert Rev Vaccines*. **12**, 211-224 (2013).
 15. Shizhu Chen, Q.Z., Yingjian Hou, Jinchao Zhang and Xing-Jie Liang Nanomaterials in medicine and pharmaceuticals: nanoscale materials developed with less toxicity and more efficacy. *European Journal of Nanomedicine* **5**, 61-79 (2013).
 16. Richard Song, M.M., Chenshuang Li, Kang Ting, Chia Soo, and Zhong Zheng Current development of biodegradable polymeric materials for biomedical applications. *Drug Des Devel Ther.* **12**, 3117-3145 (2018).
 17. Santosh Yadav, A.K.S.a.P.K. Nanoscale Self-Assembly for Therapeutic Delivery. *Front. Bioeng. Biotechnol.* (2020).
 18. Lin Y, M.C. Bio-inspired supramolecular self-assembly towards soft nanomaterials. . *Front Mater Sci.* **5**, 247-265 (2011).
 19. Habibi N, K.N., Memic A, Shafiee H. Self-assembled peptide-based nanostructures: Smart nanomaterials toward targeted drug delivery. *Nano Today* **11**, 41-60 (2016).
 20. Lu R, Z.X., Cheng X, Zhang Y, Zan X, Zhang L. Medical Applications Based on Supramolecular Self-Assembled Materials From Tannic Acid. . *Front Chem.* **8** (2020).
 21. M. Malkoch, E.M., A.M. Nyström, 6.04 - Dendrimers: Properties and Applications., *Polymer Science: A Comprehensive Reference* **6**, 113-176 (2012).
 22. Matthew J. Webber, E.A.A., E. W. Meijer & Robert Langer Supramolecular biomaterials. *Nature Materials* **15**, 13-26 (2016).
 23. Stoddart, M.C.T.F.a.J.F. Synthetic Supramolecular Chemistry. *Acc. Chem. Res.* **30**, 393-401 (1997).
 24. Jovica D. Badjić, A.N., Stuart J. Cantrill, W. Bruce Turnbull, and J. Fraser Stoddart Multivalency and Cooperativity in Supramolecular Chemistry. *Acc. Chem. Res.* **38**, 723-732 (2005).
 25. Xin Jin, L.Z., Bai Xue, Xinyuan Zhu, Deyue Yan Supramolecular nanoscale drug-delivery system with ordered structure. *National Science Review* **6**, 1128-1137 (2019).
 26. Zhou J, L.J., Du X, Xu B. Supramolecular biofunctional materials. *Biomaterials* **129**, 1-27 (2017).

27. Xuanwei Ding, D.L., George Booth, Wei Gao, Yuan Lu, Virus-Like Particle Engineering: From Rational Design to Versatile Applications. *Biotechnol. J.* **13** (2018).
28. Schwarz B, U.M., Douglas T. Biomedical and Catalytic Opportunities of Virus-Like Particles in Nanotechnology. . *Adv Virus Res.* **97**, 1-60 (2017).
29. Donaldson B, A.-B.F., Young V, Scullion S, Ward V, Young S. Virus-like particles, a versatile subunit vaccine platform. . *Subunit Vaccine Delivery. Berlin: Springer*, p. 159-180 (2015).
30. Pushko P., P.P., Grens E. Development of Virus-Like Particle Technology from Small Highly Symmetric to Large Complex Virus-Like Particle Structures. *Intervirology* **56**, 141-165 (2013).
31. Michael A. Luzuriaga, R.P.W., Madushani Dharmarwardana, Candace E. Benjamin, Shaobo Li, Arezoo Shahrivarkevishahi, Sarah Popal, Lana H. Tuong, Chayton T. Creswell, and Jeremiah J. Gassensmith Enhanced Stability and Controlled Delivery of MOF-Encapsulated Vaccines and Their Immunogenic Response In Vivo. *ACS Appl. Mater. Interfaces* **11**, 9740-9746 (2019).
32. Laura Cervera, A.A.K. Large-Scale Transient Transfection of Suspension Mammalian Cells for VLP Production. *Methods Mol Biol.* **1674**, 117-127 (2018).
33. Geen Dong -hang, C.-J.C., Chih-Yin Lin, Hsei-Chorn Chen, Hungwen Chen Improvement of glycosylation in insect cells with mammalian glycosyltransferases. *J Biotechnol.* **102**, 61-71 (2003).
34. Anette Schneemann, M.J.Y. Viral Assembly Using Heterologous Expression Systems And Cell Extracts. *Advances in Protein Chemistry* **64**, 1036 (2003).
35. Rybicki, E.P. Plant molecular farming of virus-like nanoparticles as vaccines and reagents. *WIREs Nanomed Nanobiotechnol.* **12**, 1587 (2020).
36. D'Aoust MA, C.M., Charland N, et al. D'Aoust MA, Couture MM, Charland N, et al. The production of hemagglutinin-based virus-like particles in plants: a rapid, efficient and safe response to pandemic influenza. *Plant Biotechnology Journal.* 2010 Jun;8(5):607-619. . *Plant Biotechnology* **8**, 607-619 (2010).
37. Dennis Diaz, A.C., Anwar Sunna Bioengineering Strategies for Protein-Based Nanoparticles. *Genes (Basel)* **9**, 370 (2018).
38. Simon Zinkhan, A.O., Ina Balke, Gunta Reseviča, Andris Zeltins, Simone de Brot, Cyrill Lipp, Xinyue Chang, Lisha Zha, Monique Vogel, Martin F. Bachmann, Mona O. Mohsen

- The impact of size on particle drainage dynamics and antibody response. *Journal of Controlled Release* **331**, 296-308 (2021).
39. Andrzej S.Pitek, S.A.J., Frank A.Veliz, Sourabh Shukla, Nicole F.Steinmetz Serum albumin ‘camouflage’ of plant virus based nanoparticles prevents their antibody recognition and enhances pharmacokinetics. *Biomaterials* **89**, 89-97 (2016).
 40. H E van Kan-Davelaar, J.C.M.v.H., J J L M Cornelissen, M. S. T Koay Using viruses as nanomedicines. *Br J Pharmacol.* **171**, 4001-4009 (2014).
 41. Dinh To Le, K.M.M. In Vitro Assembly of Virus-Like Particles and Their Applications. *Life* **11**, 334 (2021).
 42. Arezoo Shahrivarkevishahi, M.A.L., Fabian C. Herbert, Alisia C. Tumac, Olivia R. Brohlin, Yalini H. Wijesundara, Abhinay V. Adlooru, Candace Benjamin, Hamilton Lee, Perouza Parsamian, Jashkaran Gadhvi, Nicole J. De Nisco, and Jeremiah J. Gassensmith PhotothermalPhage: A Virus-Based Photothermal Therapeutic Agent. *J. Am. Chem. Soc.* **143**, 16428-16438 (2021).
 43. Young Hun Chung, J.P., Hui Cai, Nicole F. Steinmetz, S100A9-Targeted Cowpea Mosaic Virus as a Prophylactic and Therapeutic Immunotherapy against Metastatic Breast Cancer and Melanoma. *Adv. Sci.*, 2102796 (2021).
 44. Young Hun Chung, H.C., Nicole F. Steinmetz Viral nanoparticles for drug delivery, imaging, immunotherapy, and theranostic applications. *Advanced Drug Delivery Reviews* **156**, 214-335 (2020).
 45. Pokorski JK, S.N. The art of engineering viral nanoparticles. . *Mol Pharm.* **8**, 29-43 (2011).
 46. Saghi Nooraei, H.B., Zakieh Sadat Hoseini, Camellia Katalani, Abbas Hajizade, Andrew J. Easton & Gholamreza Ahmadian Virus-like Particles: preparation, immunogenicity and their roles as nanovaccines and drug carriers. *Journal of Nanobiotechnology* **19**, 59 (2021).
 47. Roldão A, M.M., Castilho LR, Carrondo MJ, Alves PM. Virus-like particles in vaccine development. *Expert Rev Vaccines.* 2010 Oct;9(10):1149-76. . *Expert Rev Vaccines.* **9**, 1149-1176. (2010).
 48. Isabel Junie Hildebrandt, S.S.G. Molecular imaging applications for immunology. *Clin Immunol.* **111**, 210-224 (2004).
 49. Braeden Donaldson, F.A.-B., Simon J. Pelham, Katie Young, Vernon K. Ward & Sarah L. Young Multi-target chimaeric VLP as a therapeutic vaccine in a model of colorectal cancer. *Journal for ImmunoTherapy of Cancer* **5**, 69 (2017).

50. Emily J. Hartzell, R.M.L., Millicent O. Sullivan, and Wilfred Chen Modular Hepatitis B Virus-like Particle Platform for Biosensing and Drug Delivery. *ACS Nano* **14**, 12642-122651 (2020).
51. Chun-Chieh Chen, L.X., Marie Stark, Tingwei Ou, Prasida Holla, Kai Xiao, Shizuo G Kamita, Bruce D Hammock, Kit Lam & R Holland Cheng Chemically activatable viral capsid functionalized for cancer targeting. *Nanomedicine* **11** (2016).
52. Pratik Singh, G.D., Anette Schneemann & Marianne Manchester Canine parvovirus-like particles, a novel nanomaterial for tumor targeting. *Journal of Nanobiotechnology* **4** (2006).
53. Hema Masarapu, B.K.P., Paul L. Chariou, He Hu, Neetu M. Gulati, Bradley L. Carpenter, Reza A. Ghiladi, Sourabh Shukla, and Nicole F. Steinmetz Physalis Mottle Virus-Like Particles as Nanocarriers for Imaging Reagents and Drugs. *Biomacromolecules* **18**, 4141-4153 (2017).
54. Swartz, K.G.P.a.J.R. Surface Functionalization of Virus-Like Particles by Direct Conjugation Using Azide–Alkyne Click Chemistry. *Bioconjugate Chem* **22**, 376-387 (2011).
55. Hamilton Lee, C.E.B., Chance M. Nowak, Lana H. Tuong, Raymond P. Welch, Zhuo Chen, Madushani Dharmawardana, Kyle W. Murray, Leonidas Bleris, Sheena D’Arcy, and Jeremiah J. Gassensmith Regulating the Uptake of Viral Nanoparticles in Macrophage and Cancer Cells via a pH Switch. *Mol. Pharmaceutics* **15**, 2984-2990 (2018).
56. Qiu Xian Thong, R.B., Kok Lian Ho, Noorjahan Banu Alitheen & Wen Siang Tan Thermally-responsive Virus-like Particle for Targeted Delivery of Cancer Drug. *Scientific Reports* **9**, 3945 (2019).
57. Giuseppe Destito, R.Y., Chris S. Rae, M.G. Finn, Marianne Manchester Folic Acid-Mediated Targeting of Cowpea Mosaic Virus Particles to Tumor Cells. *Chemistry & Biology* **14**, 1152-1162 (2007).
58. Aljabali AA, S.S., Lomonosoff GP, Steinmetz NF, Evans DJ. CPMV-DOX delivers. *Mol Pharm.* **10**, 3-10.
59. Rebekah A. Miller, A.D.P., and Matthew B. Francis Self-Assembling Light-Harvesting Systems from Synthetically Modified Tobacco Mosaic Virus Coat Proteins. *J. Am. Chem. Soc.* **129**, 3104-3109 (2007).
60. Simon C, K.T., Herbst S, et al. Disulfide linkage and structure of highly stable yeast-derived virus-like particles of murine polyomavirus. *J Biol. Chem.* **289**, 10411-10418 (2014).

61. Kobayashi S, S.T., Igarashi M, Orba Y, Ohtake N, Nagakawa K, et al. Cysteine Residues in the Major Capsid Protein, Vp1, of the JC Virus Are Important for Protein Stability and Oligomer Formation. *PLoS ONE* **8**, e76668 (2013).
62. Mathew W. Jones, R.A.S., Felix F. Schumacher, Stephen Caddick, James. R. Baker, Matthew I. Gibson, and David M. Haddleton Polymeric Dibromomaleimides As Extremely Efficient Disulfide Bridging Bioconjugation and Pegylation Agents. *JACS* **134**, 1847-1852 (2012).
63. Zhuo Chen, N.L., Shaobo Li, Madushani Dharmarwardana, Anna Schlimme, Jeremiah J Gassensmith Viral chemistry: the chemical functionalization of viral architectures to create new technology. *Wiley Interdiscipl Rev. Nanomed. Nanobiotechnol.* **8**, 512-534 (2016).
64. Zhuo Chen, S.D.B., Jenifer S. Calvo, Kyle W. Murray, Galo L. Mejia, Candace E. Benjamin, Raymond P. Welch, Duane D. Winkler, Gabriele Meloni, Sheena D'Arcy, and Jeremiah J. Gassensmith Fluorescent Functionalization across Quaternary Structure in a Virus-like Particle. *Bioconjugate Chem* **28**, 2277–2283 (2017).
65. Joel A. Finbloom, K.H., Clancy C. Slack, Ariel L. Furst, and Matthew B. Francis Cucurbit[6]uril-Promoted Click Chemistry for Protein Modification. *J. Am. Chem. Soc.* **139**, 9691-9697 (2017).
66. Erica Strable, D.E.P., Jr., Andrew K. Udit, Steven Brown, A. James Link, John T. Ngo, Gabriel Lander, Joel Quispe, Clinton S. Potter, Bridget Carragher, David A. Tirrell, and M. G. Finn Unnatural Amino Acid Incorporation into Virus-Like Particles. *Bioconjugate Chem* **19**, 866-875 (2008).
67. Jitka Neburkova, F.S., Jirina Zackova Suchanova, Libor Kostka, Pavel Sacha, Vladimir Subr, Tomas Etrych, Petr Simon, Jitka Barinkova, Robin Krystufek, Hana Spanielova, Jitka Forstova, Jan Konvalinka, and Petr Cigler Inhibitor–GCPII Interaction: Selective and Robust System for Targeting Cancer Cells with Structurally Diverse Nanoparticles. *Mol. Pharmaceutics* **15**, 2932-2945 (2018).
68. Xuanjun Wu, J.Y., Andrew T. DeLaitsch ,Zahra Rashidijahanabad ,Shuyao Lang, Tayeb Kakeshpour, Yuetao Zhao, Sherif Ramadan, Paulo Vilar Saavedra, Vilma Yuzbasiyan-Gurkan, Herbert Kavunja, Hongzhi Cao, Jeffrey C. Gildersleeve, Xuefei Huang Chemoenzymatic Synthesis of 9NHAc-GD2 Antigen to Overcome the Hydrolytic Instability of O-Acetylated-GD2 for Anticancer Conjugate Vaccine Development. *Angew. Chem.* **133**, 2-12 (2021).
69. Shubing Tang, B.X., Xiaohua Ye, Zhong Huang, Zhikang Qian A Modular Vaccine Development Platform Based on Sortase-Mediated Site-Specific Tagging of Antigens onto Virus-Like Particles. *Sci. Rep.* **6**, 25741 (2016).

70. Dustin Patterson, B.S., John Avera, Brian Western, Matthew Hicks, Paul Krugler, Matthew Terra, Masaki Uchida, Kimberly McCoy, and Trevor Douglas Sortase-Mediated Ligation as a Modular Approach for the Covalent Attachment of Proteins to the Exterior of the Bacteriophage P22 Virus-like Particle. *J. Am. Chem. Soc.* **139**, 9691-9697 (2017).
71. Patterson D, S.B., Avera J, et al. Sortase-Mediated Ligation as a Modular Approach for the Covalent Attachment of Proteins to the Exterior of the Bacteriophage P22 Virus-like Particle. *Bioconjug Chem.* **28**, 2114-2124 (2017).
72. Xiaolin Dai, A.B.a.U.G. Broadening the scope of sortagging. *RSC Adv.* **9**, 4700-4721 (2019).
73. Xiaoying Chen, J.Z., and Wei-Chiang Shen Fusion Protein Linkers: Property, Design and Functionality. *Adv. Drug Deliv. Rev.* **65**, 1357-1369 (2012).
74. Alberto Gabizon, H.S., Aviva T. Horowitz, Samuel Zalipsky Tumor cell targeting of liposome-entrapped drugs with phospholipid-anchored folic acid-PEG conjugates. *Adv. Drug Deliv. Rev.* **56**, 1177-1192 (2004).
75. Cotten M, W.E., Zatloukal K, Birnstiel ML. Chicken adenovirus(CELO virus) particles augment receptor-mediated DNA delivery tomammalian cells and yield exceptional levels of stable transformants. *J. Virol.* **67**, 3777-3785 (1993).
76. Carlee E. Ashley, E.C.C., Genevieve K. Phillips, Paul N. Durfee, Mekensey D. Buley, Christopher A. Lino, David P. Padilla, Brandy Phillips, Mark B. Carter, Cheryl L. Willman, C. Jeffrey Brinker, Jerri do Carmo Caldeira, Bryce Chackerian, Walker Wharton, and David S. Peabody Cell-Specific Delivery of Diverse Cargos by Bacteriophage MS2 Virus-like Particles. *ACS Nano* **5**, 5729-5745 (2011).
77. Andrea Jegerlehner, T.S., Gerd Lipowsky, Markus Schmid, Paul Pumpens, Martin F. Bachmann Regulation of IgG antibody responses by epitope density and CD21-mediated costimulation. *European Journal of Immunology* **32**, 3305-3314 (2002).
78. Madushani Dharmawardana, A.F.M., Zhuo Chen, Philip M. Palacios, Chance M. Nowak, Raymond P. Welch, Shaobo Li, Michael A. Luzuriaga, Leonidas Bleris, Brad S. Pierce, A. Dean Sherry, and Jeremiah J. Gassensmith Nitroxyl Modified Tobacco Mosaic Virus as a Metal-Free High-Relaxivity MRI and EPR Active Superoxide Sensor. *Mol. Pharmaceutics* **15**, 2973-2983 (2018).
79. Behzad Mansoori, A.M., Mohammad Amin Doustvandi, Fatemeh Mohammadnejad, Farzin Kamari, Morten F. Gjerstorff, Behzad Baradaran, Michael R. Hamblin Photodynamic therapy for cancer: Role of natural products. *Photodiagnosis and Photodynamic Therapy* **26**, 395-404 (2019).
80. Han, H.S.C., K.Y. Advances in Nanomaterial-Mediated Photothermal Cancer Therapies: Toward Clinical Applications. *Biomedicines* **9** (2021).

81. Chitgupi U, Q.Y., Lovell JF Targeted Nanomaterials for Phototherapy. . *Nanotheranostics* **1**, 38-58 (2017).
82. Kim HS, L.D. Near-Infrared-Responsive Cancer Photothermal and Photodynamic Therapy Using Gold Nanoparticles. *Polymers (Basel)* **10**, 961 (2018).
83. Jie Li, W.Z., Wenhui Ji, Jiqing Wang, Nanxiang Wang, Wanxia Wu, Qiong Wu, Xiyan Hou, Wenbo Hu and Lin Li Near infrared photothermal conversion materials: mechanism, preparation, and photothermal cancer therapy applications. *Journal of Materials Chemistry B* **9**, 7909-7926 (2021).
84. Correia, J.H.R., J.A.; Pimenta, S.; Dong, T.; Yang, Z. Photodynamic Therapy Review: Principles, Photosensitizers, Applications, and Future Directions. *Pharmaceutics* **13**, 1332 (2021).
85. Abrahamse H, H.M. New photosensitizers for photodynamic therapy. *Biochem J.* **473**, 347-364 (2016).
86. Xu X, L.H., Lee R Near Infrared Light Triggered Photo/Immuno-Therapy Toward Cancers. *Front. Bioeng. Biotechnol.* **8** (2020).
87. Feifan Zhou, J.Y., Yuqing Zhang, Mingyang Liu, Mark L. Lang, Min Li and Wei R. Chen Local Phototherapy Synergizes with Immuno-Adjuvant for Treatment of Pancreatic Cancer through Induced Immunogenic Tumor Vaccine. *Clinical Cancer Research* **24** (2018).
88. Sourabh Shukla, H.H., Hui Cai, Soo-Khim Chan, Christine E. Boone, Veronique Beiss, Paul L. Chariou, and Nicole F. Steinmetz Plant Viruses and Bacteriophage-Based Reagents for Diagnosis and Therapy. *Annual Review of Virology* **7**, 559-587 (2020).
89. Lin S, L.C., Han X, Zhong H, Cheng C. Viral Nanoparticle System: An Effective Platform for Photodynamic Therapy. *Int J Mol Sci* **22**, 1728 (2021).
90. Candace E. Benjamin, Z.C., Peiyuan Kang, Blake A. Wilson, Na Li, Steven O. Nielsen, Zhenpeng Qin, and Jeremiah J. Gassensmith Site-Selective Nucleation and Size Control of Gold Nanoparticle Photothermal Antennae on the Pore Structures of a Virus. *J. Am. Chem. Soc.* **140**, 17226-17233 (2018).
91. Rhee JK, B.M., Nycholat C, Paulson JC, Kitagishi H, Finn MG. Glycan-targeted virus-like nanoparticles for photodynamic therapy. . *Biomacromolecules* **13**, 2333-2338 (2012).
92. Waldman, A.D., Fritz, J.M. & Lenardo, M.J. A guide to cancer immunotherapy: from T cell basic science to clinical practice. . *Nat Rev Immunol* **20**, 651-668 (2020).

93. Zhang, Y., Zhang, Z. The history and advances in cancer immunotherapy: understanding the characteristics of tumor-infiltrating immune cells and their therapeutic implications. *Cell Mol Immunol* **17**, 807-821 (2020).
94. Zepeda-Cervantes J, R.-J.J., Vaca L. Interaction Between Virus-Like Particles (VLPs) and Pattern Recognition Receptors (PRRs) From Dendritic Cells (DCs): Toward Better Engineering of VLPs. . *Front Immunol.* **11**, 1100 (2020).
95. Mohsen MO, G.A., Vogel M, Bachmann MF. Interaction of Viral Capsid-Derived Virus-Like Particles (VLPs) with the Innate Immune System. . *Vaccines (Basal)* **6**, 37 (2018).
96. Mbongue JC, N.H., Torrez TW and Langridge WHR The Role of Dendritic Cell Maturation in the Induction of Insulin-Dependent Diabetes Mellitus. *Front. Immunol* **8** (2017).
97. Bachmann, M., Jennings, G. Vaccine delivery: a matter of size, geometry, kinetics and molecular patterns. *Nat Rev Immunol* **10**, 787-796 (2010).
98. Wenhua Liao, Z.H., Can Liu, Lin Lin, Rui Chen, Baidong Hou Characterization of T-Dependent and T-Independent B Cell Responses to a Virus-like Particle. *The Journal of Immunology* **198**, 3846-3856 (2017).
99. Cubas R, Z.S., Kwon S, et al. Virus-like particle (VLP) lymphatic trafficking and immune response generation after immunization by different routes. *J Immunother.* **32**, 118-128 (2009).
100. Knutson KL, D.M. Tumor antigen-specific T helper cells in cancer immunity and immunotherapy. . *Cancer Immunol Immunother.* **54**, 721-728 (2005).
101. Lélia Delamarre, H.H., Ira Mellman Presentation of Exogenous Antigens on Major Histocompatibility Complex (MHC) Class I and MHC Class II Molecules Is Differentially Regulated during Dendritic Cell Maturation. *J Exp Med* **198**, 111-122 (2003).
102. Datta SK, R.E. Induction of antigen cross-presentation by Toll-like receptors. *Springer Semin Immunopathol.* **26**, 247-255 (2004).
103. Wang, J., Li, Y. & Nie, G. Multifunctional biomolecule nanostructures for cancer therapy. *Nat Rev Mater* **6**, 766-783 (2021).
104. Chunxi Hou, H.X., Xiaojia Jiang, Yijia Li, Shengchao Deng, Mingsong Zang, Jiayun Xu, and Junqiu Liu Virus-Based Supramolecular Structure and Materials: Concept and Prospects. *ACS Appl. Bio Mater.* **4**, 5961-5974 (2021).
105. Gautam, A.B., V.; Wang, C.; Wang, L.; Steinmetz, N.F. Plant Viral Nanoparticle Conjugated with Anti-PD-1 Peptide for Ovarian Cancer Immunotherapy. . *Int. J. Mol. Sci.* **22**, 9733 (2021).

106. Lizotte, P., Wen, A., Sheen, M. et al. In situ vaccination with cowpea mosaic virus nanoparticles suppresses metastatic cancer. *Nature nanotech* **11**, 295-303 (2016).
107. Murray AA, W.C., Fiering S, Steinmetz NF. In Situ Vaccination with Cowpea vs Tobacco Mosaic Virus against Melanoma. *Mol. Pharm.* **15**, 3700-3716 (2018).
108. Xuanjun Wu, C.M., Christian Pett, Jin Yu, Manuel Schorlemer, Sherif Ramadan, Shuyao Lang, Sandra Behren, Ulrika Westerlind, M G Finn, Xuefei Huang Synthesis and Immunological Evaluation of Disaccharide Bearing MUC-1 Glycopeptide Conjugates with Virus-like Particles. *ACS Chem. Biol.* **14**, 2176-2184 (2019).
109. Zabel F, K.T., Bachmann MF. Virus-induced humoral immunity: on how B cell responses are initiated. . *Curr Opin Virol.* **3**, 357-362 (2013).
110. Zepeda-Cervantes J, R.-J.J.a.V.L. Interaction Between Virus-Like Particles (VLPs) and Pattern Recognition Receptors (PRRs) From Dendritic Cells (DCs): Toward Better Engineering of VLPs. *Front. Immunol* **11** (2020).
111. Qian, C.L., X.; Xu, Q.; Wang, Z.; Chen, J.; Li, T.; Zheng, Q.; Yu, H.; Gu, Y.; Li, S.; Xia, N. Recent Progress on the Versatility of Virus-Like Particles. *Vaccines* **8** (2020).
112. Palladini A, T.S., Janitzek CM, et al. Virus-like particle display of HER2 induces potent anti-cancer responses. *Oncoimmunology* **7** (2018).
113. Stephen N. Crooke, J.S., Idris Raji, Bocheng Wu, Adegboyega K. Oyelere, & Finn, a.M.G. Lung Tissue Delivery of Virus-Like Particles Mediated by Macrolide Antibiotics. *Mol. Pharmaceutics* **16**, 2947-2955 (2019).
114. Mona O.Mohsen, A.C.G., Gustavo Cabral-Miranda, Caroline C.Krueger. Fabiana MSLeoratti, Jens V.Stein, Martin F.Bachmanna Delivering adjuvants and antigens in separate nanoparticles eliminates the need of physical linkage for effective vaccination. *Journal of Controlled Release* **251**, 92-100 (2017).
115. Lam, P. & Steinmetz, N.F. Delivery of siRNA therapeutics using cowpea chlorotic mottle virus-like particles. *Biomaterials Science* **7**, 3138-3142 (2019).
116. Fabian C. Herbert, O.R.B., Tyler Galbraith, Candace Benjamin, Cesar A. Reyes, Michael A. Luzuriaga, Arezoo Shahrivarkevishahi, and Jeremiah J. Gassensmith Supramolecular Encapsulation of Small-Ultrared Fluorescent Proteins in Virus-Like Nanoparticles for Noninvasive In Vivo Imaging Agents. *Bioconjugate Chem.* **31**, 1529-1536 (2020).
117. Laurence Lavelle, J.-P.M., Mari Gingery The disassembly, reassembly and stability of CCMV protein capsids. *Journal of Virology* **146**, 311-316 (2007).
118. María V. Villagrana-Escareño, E.R.-H., Othir G. Galicia-Cruz, Ana L. Durán-Meza, Viridiana De la Cruz-González, Carmen Y. Hernández-Carballo, and Jaime Ruíz-García

- VLPs Derived from the CCMV Plant Virus Can Directly Transfect and Deliver Heterologous Genes for Translation into Mammalian Cells. *BioMed Research International* (2019).
119. Odisse Azizgolshani, R.F.G., Ruben Cadena-Nava, Charles M.Knobler, William M.Gelbart Reconstituted plant viral capsids can release genes to mammalian cells. *Virology* **441**, 12-17 (2013).
 120. Ruben D. Cadena-Nava, M.C.-G., Rees F. Garmann, A. L. N. Rao, Charles M. Knobler, and William M. Gelbart Self-Assembly of Viral Capsid Protein and RNA Molecules of Different Sizes: Requirement for a Specific High Protein/RNA Mass Ratio. *J. Virol.* **86**, 3318-3326 (2012).
 121. Stockley, F.A.G.a.P.G. MS2 Viruslike Particles: A Robust, Semisynthetic Targeted Drug Delivery Platform. *Mol. Pharmaceutics* **10**, 59-68 (2013).
 122. William M. Aumiller, J., Masaki Uchida, and Trevor Douglas Protein cage assembly across multiple length scales. *Chem. Soc. Rev.* **47**, 3433-3469 (2018).
 123. Jeff E. Glasgow, S.L.C., Matthew B. Francis, and Danielle Tullman-Ercek Osmolyte-Mediated Encapsulation of Proteins inside MS2 Viral Capsids. *ACS Nano.* **6**, 8658-8664 (2012).
 124. Jin-Kyu Rhee, M.H., Jason D. Fiedler, Steven D. Brown, Florian Manzenrieder, Hiroaki Kitagishi, Corwin Nycholat, James C. Paulson, and M.G. Finn Colorful Virus-Like Particles: Fluorescent Protein Packaging by the Q β Capsid. *Biomacromolecules* **12**, 3977-3981 (2011).
 125. Min Wu, W.L.B., and Peter G. Stockley Cell-Specific Delivery of Bacteriophage-Encapsidated Ricin A Chain. *Bioconjugate Chem* **6**, 587-595 (1995).
 126. Jason D. Fiedler, S.D.B., Jolene L. Lau, M. G. Finn RNA-Directed Packaging of Enzymes within Virus-like Particles. *Angew. Chem. Int. Ed.* **49**, 9648-9651 (2010).
 127. Christina E. Franke, A.E.C., Ravi B. Patel, and Nicole F. Steinmetz Tobacco Mosaic Virus-Delivered Cisplatin Restores Efficacy in Platinum-Resistant Ovarian Cancer Cells. *Mol Pharm.* **15**, 2922-2931 (2018).
 128. Min Wu, T.S., William L.Brown, Peter G.Stockley Delivery of antisense oligonucleotides to leukemia cells by RNA bacteriophage capsids. *Nanomedicine: Nanotechnology, Biology and Medicine* **1**, 67-76 (2005).
 129. J.B.Bancroft, G.J.H., Rou Markham A study of the self-assembly process in a small spherical virus formation of organized structures from protein subunits in vitro. *Virology* **31**, 354-379 (1967).

130. Young, T.D.M. Host–guest encapsulation of materials by assembled virus protein cages. *Nature* **393**, 152-155 (1998).
131. Anne Prel, V.C., Régis Gayon, Philippe Ravassard, Christine Duthoit, Emmanuel Payen, Leila Maouche-Chretien, Alison Creneguy, Tuan Huy, Nguyen, Nicolas Martin, Eric Piver, Raphaël Sevrain, Lucille Lamouroux, Philippe Leboulch, Frédéric Deschaseaux, Pascale Bouillé, Luc Sensébé Jean-Christophe Pagès Highly efficient in vitro and in vivo delivery of functional RNAs using new versatile MS2-chimeric retrovirus-like particles. *Molecular Therapy - Methods & Clinical Development* **2**, 15039 (2015).
132. Jinming Li, Y.S., Tingting Jia, Rui Zhang, Kuo Zhang, Lunan Wang Messenger RNA vaccine based on recombinant MS2 virus-like particles against prostate cancer. *International Journal of Cancer* **134**, 1683-1694 (2013).
133. Yang Pan, Y.Z., Tingting Jia, Kuo Zhang, Jinming Li, Lunan Wang, Development of a microRNA delivery system based on bacteriophage MS2 virus-like particles. *FEBS Journal* **279**, 1198-1208 (2012).
134. Yang Pan, T.J., Yuan Zhang, Kuo Zhang, Rui Zhang, Jinming Li, and Lunan Wang MS2 VLP-based delivery of microRNA-146a inhibits autoantibody production in lupus-prone mice. *Int J Nanomedicine* **7**, 5957-5967 (2012).
135. Yanlan Yao, T.J., Yang Pan, Hongna Gou, Yulong Li, Yu Sun, Rui Zhang, Kuo Zhang, Guigao Lin, Jiehong Xie, Jinming Li, and Lunan Wang Using a Novel MicroRNA Delivery System to Inhibit Osteoclastogenesis. *Int J Mol Sci* **16**, 8337-8350 (2015).
136. Shefah Qazi, H.M.M., Royce A. Wilkinson, Kimberly McCoy, Trevor Douglas, and Blake Wiedenheft Programmed Self-Assembly of an Active P22-Cas9 Nanocarrier System. *Mol. Pharmaceutics* **13**, 1191-1196 (2016).
137. Daley, J. Gene Therapy Arrives. *Nature* **576** (2019).
138. Brandon J Aubrey, G.L.K., Ana Janic, Marco J Herold & Andreas Strasser How does p53 induce apoptosis and how does this relate to p53-mediated tumour suppression? *Cell Death & Differentiation* **25**, 104-113 (2018).
139. Wei-Wei Zhang, L.L., Dinggang Li, Jiliang Liu, Xiuqin Li, Wei Li, Xiaolong Xu, Michael J Zhang, Lois A Chandler, Hong Lin, Aiguo Hu, Wei Xu, Dominic Man-Kit Lam The First Approved Gene Therapy Product for Cancer Ad-p53 (Gendicine): 12 Years in the Clinic. *Hum. Gene Ther.* **29**, 160-179 (2018).
140. Burmester, D.C.a.J.K. Gene Therapy for Cancer Treatment: Past, Present and Future. *Clinical Medicine & Research* **4**, 218-227 (2006).

141. Alireza Shahryari, M.S.J., Saeed Mohammadi, Hadi Razavi Nikoo, Zahra Nazari, Elaheh Sadat Hosseini, Ingo Burtscher, Seyed Javad Mowla and Heiko Lickert Development and Clinical Translation of Approved Gene Therapy Products for Genetic Disorders. *Front. Genet.* **10** (2019).
142. Alireza Shahryari, I.B., Zahra Nazari, Heiko Lickert Engineering Gene Therapy: Advances and Barriers. *Advanced Therapeutics* **4** (2021).
143. Xi-Xi Ma, J.-L.X., Yi-Yang Jia, Ya-Xuan Zhang, Wei Wang, Chen Li, Wei He, Si-Yuan Zhou & Bang-Le Zhang Enhance transgene responses through improving cellular uptake and intracellular trafficking by bio-inspired non-viral vectors. *Journal of Nanobiotechnology* **18** (2020).
144. Christian Jreysaty, Q.S., Huijie Wang, Xingping Qiu, Françoise M. Winnik, Xiaoling Zhang, Kerong Dai, Mohamed Benderdour, and Julio C. Fernandes Efficient Nonviral Gene Therapy Using Folate-Targeted Chitosan-DNA Nanoparticles In Vitro. *ISRN Pharmaceutics* (2012).
145. Julien Villemejeane, L.M.M. Physical methods of nucleic acid transfer: general concepts and applications. *Br J Pharmacol.* **157**, 207-219 (2009).
146. TM., B. The Current Status of Gene Therapy for the Treatment of Cancer. *Biologics*. . *Biologics* **15**, 67-77 (2021).
147. Adenovirus Production, Toxicity and Tropism. *Molecular Therapy* **3**, S157-S174 (2001).
148. Lehrman, S. Virus treatment questioned after gene therapy death. *Nature* **401**, 517-518 (1999).
149. Tazio Storni, C.R., Katrin Schwarz, Reto A. Schwendener, Wolfgang A. Renner and Martin F. Bachmann Nonmethylated CG Motifs Packaged into Virus-Like Particles Induce Protective Cytotoxic T Cell Responses in the Absence of Systemic Side Effects. *J. Immunol* **172**, 1777-1785 (2004).
150. Le Chang, G.W., Tingting Jia, Lei Zhang, Yulong Li, Yanxi Han, Kuo Zhang, Guigao Lin, Rui Zhang, Jinming Li and Lunan Wang Armored long non-coding RNA MEG3 targeting EGFR based on recombinant MS2 bacteriophage virus-like particles against hepatocellular carcinoma. *Oncotarget* **7**, 23988-24004 (2016).
151. Rabbab Oun, Y.E.M.a.N.J.W. The side effects of platinum-based chemotherapy drugs: a review for chemists. *Dalton Trans.* **47**, 6645-6653 (2018).
152. Ho Lun Wong, R.B., Andrew M.Rauth, Yongqiang Li, Xiao Yu Wu Chemotherapy with anticancer drugs encapsulated in solid lipid nanoparticles. *Adv. Drug Deliv. Rev.* **59**, 491-504 (2007).

153. Feng, S.-S. Nanoparticles of biodegradable polymers for new-concept chemotherapy. *Expert Review of Medical Devices* **1**, 115-125 (2004).
154. Marcus J. Rohovie, M.N., James R. Swartz Virus-like particles: Next-generation nanoparticles for targeted therapeutic delivery. *Bioengineering & Translational Medicine* **2**, 43-57 (2016).
155. Young, T.D.a.M. Viruses: Making Friends with Old Foes. *Science* **312**, 873-875 (2006).
156. Yujie Ma, R.J.M.N., Jeroen J.L.M. Cornelissen Virus-based nanocarriers for drug delivery. *Advanced Drug Delivery Reviews* **64**, 811-825 (2012).
157. Marisa L. Hovlid, J.L.L., Kurt Breitenkamp, Cody J. Higginson, Burkhardt Laufer, Marianne Manchester, and M. G. Finn Encapsidated Atom-Transfer Radical Polymerization in Q β Virus-like Nanoparticles. *ASC Nano* **8**, 8003-8014 (2014).
158. W. H. Roos, I.L.I., A. Evilevitch & G. J. L. Wuite Viral capsids: Mechanical characteristics, genome packaging and delivery mechanisms. *Cellular and Molecular Life Sciences* **64**, 1484 (2007).
159. Ibrahim Yildiz, K.L.L., Kevin Chen, Sourabh Shukla, Nicole F.Steinmetz Infusion of imaging and therapeutic molecules into the plant virus-based carrier cowpea mosaic virus: Cargo-loading and delivery. *Journal of Controlled Release* **172**, 568-578 (2013).
160. Gao, D. et al. Multifunctional phototheranostic nanomedicine for cancer imaging and treatment. *Materials Today Bio* **5**, 100035 (2020).
161. Chen, F. & Cai, W. Nanomedicine for targeted photothermal cancer therapy: where are we now? *Nanomedicine (Lond)* **10**, 1-3 (2015).
162. Pinto, A. & Pocard, M. Photodynamic therapy and photothermal therapy for the treatment of peritoneal metastasis: a systematic review. *Pleura Peritoneum* **3**, 20180124-20180124 (2018).
163. Krysko, D.V. et al. Emerging role of damage-associated molecular patterns derived from mitochondria in inflammation. *Trends in immunology* **32**, 157-164 (2011).
164. Chen, G.Y. & Nuñez, G. Sterile inflammation: sensing and reacting to damage. *Nature reviews. Immunology* **10**, 826-837 (2010).
165. Hernandez, C., Huebener, P. & Schwabe, R.F. Damage-associated molecular patterns in cancer: a double-edged sword. *Oncogene* **35**, 5931-5941 (2016).
166. West, C.L., Doughty, A.C.V., Liu, K. & Chen, W.R. Monitoring tissue temperature during photothermal therapy for cancer. *J BioX Res* **2**, 159-168 (2019).

167. Li, L. et al. An Endogenous Vaccine Based on Fluorophores and Multivalent Immunoadjuvants Regulates Tumor Micro-Environment for Synergistic Photothermal and Immunotherapy. *Theranostics* **8**, 860-873 (2018).
168. Wang, C. et al. Immunological responses triggered by photothermal therapy with carbon nanotubes in combination with anti-CTLA-4 therapy to inhibit cancer metastasis. *Advanced materials (Deerfield Beach, Fla.)* **26**, 8154-8162 (2014).
169. Wangzhong, S., Sha, H., William, J.S. & Adah, A. Review of the progress toward achieving heat confinement—the holy grail of photothermal therapy. *Journal of Biomedical Optics* **22**, 1-16 (2017).
170. Yang, Z. et al. Advances in nanomaterials for use in photothermal and photodynamic therapeutics (Review). *Mol Med Rep* **20**, 5-15 (2019).
171. Jaque, D. et al. Nanoparticles for photothermal therapies. *Nanoscale* **6**, 9494-9530 (2014).
172. Lee, S. et al. Near-Infrared Heptamethine Cyanine Based Iron Oxide Nanoparticles for Tumor Targeted Multimodal Imaging and Photothermal Therapy. *Scientific Reports* **7**, 2108 (2017).
173. Wu, F. et al. Intriguing H-Aggregates of Heptamethine Cyanine for Imaging-Guided Photothermal Cancer Therapy. *ACS applied materials & interfaces* **12**, 32388-32396 (2020).
174. Li, X. et al. New application of phthalocyanine molecules: from photodynamic therapy to photothermal therapy by means of structural regulation rather than formation of aggregates. *Chemical Science* **9**, 2098-2104 (2018).
175. Zheng, B.-D., He, Q.-X., Li, X., Yoon, J. & Huang, J.-D. Phthalocyanines as contrast agents for photothermal therapy. *Coordination Chemistry Reviews* **426**, 213548 (2021).
176. Cheung, C.C.L. et al. Liposome-Templated Indocyanine Green J- Aggregates for In Vivo Near-Infrared Imaging and Stable Photothermal Heating. *Nanotheranostics* **4**, 91-106 (2020).
177. Holzer, W. et al. Photostability and thermal stability of indocyanine green. *Journal of Photochemistry and Photobiology B: Biology* **47**, 155-164 (1998).
178. Vines, J.B., Yoon, J.-H., Ryu, N.-E., Lim, D.-J. & Park, H. Gold Nanoparticles for Photothermal Cancer Therapy. *Front Chem* **7**, 167-167 (2019).

179. Sobhani, Z., Behnam, M.A., Emami, F., Dehghanian, A. & Jamhiri, I. Photothermal therapy of melanoma tumor using multiwalled carbon nanotubes. *International journal of nanomedicine* **12**, 4509-4517 (2017).
180. Estelrich, J. & Busquets, M.A. Iron Oxide Nanoparticles in Photothermal Therapy. *Molecules* **23**, 1567 (2018).
181. Zhou, B. et al. Near-Infrared Organic Dye-Based Nanoagent for the Photothermal Therapy of Cancer. *ACS applied materials & interfaces* **8**, 29899-29905 (2016).
182. Avirah, R.R., Jyothish, K. & Ramaiah, D. Infrared Absorbing Croconaine Dyes: Synthesis and Metal Ion Binding Properties. *The Journal of Organic Chemistry* **73**, 274-279 (2008).
183. Lei, S., Zhang, Y., Blum, N.T., Huang, P. & Lin, J. Recent Advances in Croconaine Dyes for Bioimaging and Theranostics. *Bioconjugate Chemistry* **31**, 2072-2084 (2020).
184. Tang, L. et al. Croconaine nanoparticles with enhanced tumor accumulation for multimodality cancer theranostics. *Biomaterials* **129**, 28-36 (2017).
185. Harmatys, K.M. et al. Selective photothermal inactivation of cells labeled with near-infrared croconaine dye. *Chemical Communications* **53**, 9906-9909 (2017).
186. Spence, G.T., Hartland, G.V. & Smith, B.D. Activated photothermal heating using croconaine dyes. *Chemical Science* **4**, 4240-4244 (2013).
187. Benjamin, C., Brohlin, O., Shahrivarkevishahi, A. & Gassensmith, J.J. in *Nanoparticles for Biomedical Applications*. (eds. E.J. Chung, L. Leon & C. Rinaldi) 153-174 (Elsevier, 2020).
188. Herbert, F.C. et al. Supramolecular Encapsulation of Small-Ultrared Fluorescent Proteins in Virus-Like Nanoparticles for Noninvasive In Vivo Imaging Agents. *Bioconjugate Chemistry* **31**, 1529-1536 (2020).
189. Wang, Q., Lin, T., Tang, L., Johnson, J.E. & Finn, M.G. Icosahedral Virus Particles as Addressable Nanoscale Building Blocks. *Angewandte Chemie International Edition* **41**, 459-462 (2002).
190. Chung, Y.H., Cai, H. & Steinmetz, N.F. Viral nanoparticles for drug delivery, imaging, immunotherapy, and theranostic applications. *Advanced Drug Delivery Reviews* (2020).
191. Park, J., Chariou, P.L. & Steinmetz, N.F. Site-Specific Antibody Conjugation Strategy to Functionalize Virus-Based Nanoparticles. *Bioconjugate Chemistry* **31**, 1408-1416 (2020).
192. Aanei, I.L. & Francis, M.B. Dual Surface Modification of Genome-Free MS2 Capsids for Delivery Applications. *Methods in molecular biology (Clifton, N.J.)* **1776**, 629-642 (2018).

193. Purwar, M. et al. Design, display and immunogenicity of HIV1 gp120 fragment immunogens on virus-like particles. *Vaccine* **36**, 6345-6353 (2018).
194. Benjamin, C.E. et al. Site-Selective Nucleation and Size Control of Gold Nanoparticle Photothermal Antennae on the Pore Structures of a Virus. *J Am Chem Soc* **140**, 17226-17233 (2018).
195. Fiedler, J.D., Fishman, M.R., Brown, S.D., Lau, J. & Finn, M.G. Multifunctional Enzyme Packaging and Catalysis in the Q β Protein Nanoparticle. *Biomacromolecules* **19**, 3945-3957 (2018).
196. Rampoldi, A. et al. Targeted Elimination of Tumorigenic Human Pluripotent Stem Cells Using Suicide-Inducing Virus-like Particles. *ACS chemical biology* **13**, 2329-2338 (2018).
197. Yin, Z. et al. Antitumor Humoral and T Cell Responses by Mucin-1 Conjugates of Bacteriophage Q β in Wild-type Mice. *ACS chemical biology* **13**, 1668-1676 (2018).
198. Shoeb, E. & Hefferon, K. Future of cancer immunotherapy using plant virus-based nanoparticles. *Future Sci OA* **5**, FSO401-FSO401 (2019).
199. Wang, C., Fiering, S.N. & Steinmetz, N.F. Cowpea Mosaic Virus Promotes Anti-Tumor Activity and Immune Memory in a Mouse Ovarian Tumor Model. *Advanced Therapeutics* **2**, 1900003 (2019).
200. Pitek, A.S., Hu, H., Shukla, S. & Steinmetz, N.F. Cancer Theranostic Applications of Albumin-Coated Tobacco Mosaic Virus Nanoparticles. *ACS applied materials & interfaces* **10**, 39468-39477 (2018).
201. Finbloom, J.A. et al. Stable Disk Assemblies of a Tobacco Mosaic Virus Mutant as Nanoscale Scaffolds for Applications in Drug Delivery. *Bioconjugate Chemistry* **27**, 2480-2485 (2016).
202. Mohsen, M.O., Speiser, D.E., Knuth, A. & Bachmann, M.F. Virus-like particles for vaccination against cancer. *WIREs Nanomedicine and Nanobiotechnology* **12**, e1579 (2020).
203. Klimek, L. et al. Virus-like particles (VLP) in prophylaxis and immunotherapy of allergic diseases. *Allergo J Int* **27**, 245-255 (2018).
204. Welch, R.P., Lee, H., Luzuriaga, M.A., Brohlin, O.R. & Gassensmith, J.J. Protein-Polymer Delivery: Chemistry from the Cold Chain to the Clinic. *Bioconjug Chem* **29**, 2867-2883 (2018).
205. Lee, H. et al. Supramolecular and biomacromolecular enhancement of metal-free magnetic resonance imaging contrast agents. *Chem Sci* **11**, 2045-2050 (2020).

206. Dharmarwardana, M. et al. Nitroxyl Modified Tobacco Mosaic Virus as a Metal-Free High-Relaxivity MRI and EPR Active Superoxide Sensor. *Mol Pharm* **15**, 2973-2983 (2018).
207. Lin, S., Liu, C., Han, X., Zhong, H. & Cheng, C. Viral Nanoparticle System: An Effective Platform for Photodynamic Therapy. *International Journal of Molecular Sciences* **22** (2021).
208. Rohovie, M.J., Nagasawa, M. & Swartz, J.R. Virus-like particles: Next-generation nanoparticles for targeted therapeutic delivery. *Bioengineering & Translational Medicine* **2**, 43-57 (2017).
209. Chen, Z. et al. Fluorescent Functionalization across Quaternary Structure in a Virus-like Particle. *Bioconjug Chem* **28**, 2277-2283 (2017).
210. Chen, Z., Detvo, S.T., Pham, E. & Gassensmith, J.J. Making Conjugation-induced Fluorescent PEGylated Virus-like Particles by Dibromomaleimide-disulfide Chemistry. *J Vis Exp* (2018).
211. Chen, Z., Li, N., Chen, L., Lee, J. & Gassensmith, J.J. Dual Functionalized Bacteriophage Q β as a Photocaged Drug Carrier. *Small* **12**, 4563-4571 (2016).
212. Chen, Z. et al. Viral chemistry: the chemical functionalization of viral architectures to create new technology. *Wiley Interdiscip Rev Nanomed Nanobiotechnol* **8**, 512-534 (2016).
213. Bear, A.S. et al. Elimination of metastatic melanoma using gold nanoshell-enabled photothermal therapy and adoptive T cell transfer. *PLoS one* **8**, e69073 (2013).
214. Mohsen, M.O., Gomes, A.C., Vogel, M. & Bachmann, M.F. Interaction of Viral Capsid-Derived Virus-Like Particles (VLPs) with the Innate Immune System. *Vaccines (Basel)* **6**, 37 (2018).
215. Zepeda-Cervantes, J., Ramírez-Jarquín, J.O. & Vaca, L. Interaction Between Virus-Like Particles (VLPs) and Pattern Recognition Receptors (PRRs) From Dendritic Cells (DCs): Toward Better Engineering of VLPs. *Front Immunol* **11**, 1100-1100 (2020).
216. Qian, C. et al. Recent Progress on the Versatility of Virus-Like Particles. *Vaccines (Basel)* **8** (2020).
217. Song, X. & Foley, J.W. A new water-soluble near-infrared croconium dye. *Dyes and Pigments* **78**, 60-64 (2008).
218. Liu, Y. et al. Dopamine-Melanin Colloidal Nanospheres: An Efficient Near-Infrared Photothermal Therapeutic Agent for In Vivo Cancer Therapy. *Advanced Materials* **25**, 1353-1359 (2013).

219. Kang, P. et al. Molecular Hyperthermia: Spatiotemporal Protein Unfolding and Inactivation by Nanosecond Plasmonic Heating. *Small* **13** (2017).
220. Marabelle, A. et al. Starting the fight in the tumor: expert recommendations for the development of human intratumoral immunotherapy (HIT-IT). *Ann Oncol* **29**, 2163-2174 (2018).
221. Steinman, R.M. Linking innate to adaptive immunity through dendritic cells. *Novartis Foundation symposium* **279**, 101-109; discussion 109-113, 216-109 (2006).
222. Wculek, S.K. et al. Dendritic cells in cancer immunology and immunotherapy. *Nature Reviews Immunology* **20**, 7-24 (2020).
223. Wang, J. et al. Designing immunogenic nanotherapeutics for photothermal-triggered immunotherapy involving reprogramming immunosuppression and activating systemic antitumor responses. *Biomaterials* **255**, 120153 (2020).
224. Guo, Y. et al. Magnetic-responsive and targeted cancer nanotheranostics by PA/MR bimodal imaging-guided photothermally triggered immunotherapy. *Biomaterials* **219**, 119370 (2019).
225. Mellman, I., Coukos, G. & Dranoff, G. Cancer immunotherapy comes of age. *Nature* **480**, 480-489 (2011).
226. Janeway, C.A., Jr. & Bottomly, K. Signals and signs for lymphocyte responses. *Cell* **76**, 275-285 (1994).
227. Mohsen, M.O., Gomes, A.C., Vogel, M. & Bachmann, M.F. Interaction of Viral Capsid-Derived Virus-Like Particles (VLPs) with the Innate Immune System. *Vaccines (Basel)* **6** (2018).
228. Grgacic, E.V.L. & Anderson, D.A. Virus-like particles: passport to immune recognition. *Methods* **40**, 60-65 (2006).
229. Kaczmarek, A., Vandenabeele, P. & Krysko, Dmitri V. Necroptosis: The Release of Damage-Associated Molecular Patterns and Its Physiological Relevance. *Immunity* **38**, 209-223 (2013).
230. Xu, P. & Liang, F. Nanomaterial-Based Tumor Photothermal Immunotherapy. *International journal of nanomedicine* **15**, 9159-9180 (2020).
231. Cheng, H.-W., Tsao, H.-Y., Chiang, C.-S. & Chen, S.-Y. Advances in Magnetic Nanoparticle-Mediated Cancer Immune-Theranostics. *Advanced Healthcare Materials* **10**, 2001451 (2021).

232. O'Melia, M.J. et al. Quality of CD8⁺ T cell immunity evoked in lymph nodes is compartmentalized by route of antigen transport and functional in tumor context. *Science Advances* **6**, eabd7134 (2020).
233. Buchwald, Z.S. et al. Tumor-draining lymph node is important for a robust abscopal effect stimulated by radiotherapy. *Journal for ImmunoTherapy of Cancer* **8**, e000867 (2020).
234. Li, C., Jiang, P., Wei, S., Xu, X. & Wang, J. Regulatory T cells in tumor microenvironment: new mechanisms, potential therapeutic strategies and future prospects. *Molecular Cancer* **19**, 116 (2020).
235. Tormoen, G.W., Crittenden, M.R. & Gough, M.J. Role of the immunosuppressive microenvironment in immunotherapy. *Adv Radiat Oncol* **3**, 520-526 (2018).
236. Kalyani, V.S.a.V.L. Nano-cavity coupled waveguide photonic crystal based biosensor detection of cervical cancer using nucleus and cytoplasm. *International Conference on Information, Communication, Instrumentation and Control (ICICIC)*, 1-5 (2017).
237. McMillan, P.J., Strovass, T.J., Baum, M. et al Pathological tau drives ectopic nuclear speckle scaffold protein SRRM2 accumulation in neuron cytoplasm in Alzheimer's disease. *Acta Neuropathol Commun* **9**, 1-14 (2021).
238. Lin Hou, Y.Z., Xuemei Yang, Chunyu Tian, Yingshan Yan, & Hongling Zhang, J.S., Huijuan Zhang and Zhenzhong Zhang *ACS Appl. Mater. Interfaces* **11**, 225-268 (2019).
239. Qian Cao, J.Y., Hang Zhang, Liang Hao, Gang-Gang Yang, Liang-Nian Ji and Zong-Wan Mao Traceable in-cell synthesis and cytoplasm-to-nucleus translocation of a zinc Schiff base complex as a simple and economical anticancer strategy. *Chem. Commun* **55**, 7852-7855 (2019).
240. Katrien Remaut, V.O., Kevin Braeckmans, Judith Klumperman, Stefaan C. De Smedt, Lysosomal capturing of cytoplasmic injected nanoparticles by autophagy: An additional barrier to non viral gene delivery. *Journal of Controlled Release* **195**, 29-36 (2014).
241. William B. Liechty, R.L.S., Julia E. Vela Ramirez, Nicholas A. Peppas, Cytoplasmic delivery of functional siRNA using pH-Responsive nanoscale hydrogels. *International Journal of Pharmaceutics* **562**, 249-257 (2019).
242. Sophia Antimisiaris, S.M., Konstantina Papadia Targeted si-RNA with liposomes and exosomes (extracellular vesicles): How to unlock the potential. *International Journal of Pharmaceutics* **525**, 293-312 (2017).

243. Kim D, J.C., Kim JH, Kim MS, Yoon CH, Choi IS, Kim SH, Bae YS. Cytoplasmic transduction peptide (CTP): new approach for the delivery of biomolecules into cytoplasm in vitro and in vivo. . *Exp Cell Res.* **312**, 1277-1288 (2009).
244. Wei Jiang, H.Z., Jilian Wu 1, Guangxi Zhai 1, Zhonghao Li 2, Yuxia Luan 1, Sanjay Garg 3 CuS@MOF-Based Well-Designed Quercetin Delivery System for Chemo-Photothermal Therapy. *ACS Appl. Mater. Interfaces* **10**, 34513-34523 (2018).
245. Yousif LF, S.K., Kelley SO. Targeting mitochondria with organelle-specific compounds: strategies and applications. *Chembiochem.* **10**, 1939-1950 (2009).
246. Lucia Ya. Zakharova, G.I.K., Dinar R. Gabdrakhmanov, Gulnara A. Gaynanova,^a Elena A. Ermakova,^c Alexander R. Mukhitov,^c Irina V. Galkina,^d Sergey V. Cheresiz,^e Andrey G. Pokrovsky,^e Polina V. Skvortsova,^c Yuri V. Gogolev^c and Yuriy F. Zuev Alkyl triphenylphosphonium surfactants as nucleic acid carriers: complexation efficacy toward DNA decamers, interaction with lipid bilayers and cytotoxicity studies. *Phys. Chem. Chem Phys.* **21**, 16706-16717 (2019).
247. Zielonka, J., Joseph, J., Sikora, A., Hardy, M., Ouari, O., Vasquez-Vivar, J., Cheng, G., Lopez, M., & Kalyanaraman, B. Mitochondria-Targeted Triphenylphosphonium-Based Compounds: Syntheses, Mechanisms of Action, and Therapeutic and Diagnostic Applications. *Chemical Reviews* **117**, 10043-10120 (2017).
248. Gantumur Battogtokh, Y.S., Dong Seop Kang, Sang Jun Park, Min Suk Shim, Kang Moo Huh, Yong-Yeon Cho, Joo Young Lee, Hye Suk Lee, Han Chang Kang Mitochondria-targeting drug conjugates for cytotoxic, anti-oxidizing and sensing purposes: current strategies and future perspectives. *Acta Pharmaceutica Sinica B* **8**, 862-880 (2018).
249. Murphy, M.P. Targeting lipophilic cations to mitochondria. *Biochimica et Biophysica Acta (BBA)-Bioenergetics* **1777**, 1028-1031 (2008).
250. C Gomes, A., Roesti, E. S., El-Turabi, A., & Bachmann, M. F. Type of RNA Packed in VLPs Impacts IgG Class Switching-Implications for an Influenza Vaccine Design. *Vaccines* **7**, 47 (2019).
251. Steinmetz, A.M.W.a.N.F. Design of virus-based nanomaterials for medicine, biotechnology, and energy. *Chem. Soc. Rev.* **45**, 4074 (2016).
252. Steinmetz, N.F. Viral nanoparticles as platforms for next-generation therapeutics and imaging devices. *Nanomedicine: Nanotechnology, Biology and Medicine* **6**, 634-641 (2010).
253. Oliver Ast, A.C., Linda Cashion, Brent Larsen, Gabor M. Rubanyi, Richard N. Harkins, Harald Petry In Vitro DNA Packaging and Gene Delivery Using JC Virus-Like Particles. *Molecular Therapy* **11**, S68 (2005).

254. Zhuo Chen, N.L., Luxi Chen, Jiyong Lee, Jeremiah J. Gassensmith Dual Functionalized Bacteriophage Q β as a Photocaged Drug Carrier. *Small* **12**, 4563-4571 (2016).
255. Wu W, H.S., Carrico ZM, Francis MB. Genome-free viral capsids as multivalent carriers for taxol delivery. *Angew Chem Int Ed Engl.* **48**, 9493-9497 (2009).
256. Pawel Kraj, E.S., Byeongdu Lee, and Trevor Douglas Polymer Coatings on Virus-like Particle Nanoreactors at Low Ionic Strength—Charge Reversal and Substrate Access. *Biomacromolecules* **22**, 2107-2118 (2021).
257. Minseok Kwak, I.J.M., Diana-Milena Anaya, Andrew J. Musser, Melanie Braschll, Roeland J. M. Nolte, Klaus Müllen, Jeroen J. L. M. Cornelissen, and Andreas Herrmann Virus-like Particles Templated by DNA Micelles: A General Method for Loading Virus Nanocarriers. *J. Am. Chem. Soc.* *2010*, *132*, *23*, 7834–7835 **132**, 7834–7835 (2010).
258. Steven D. Brown, J.D.F., and M. G. Finn Assembly of Hybrid Bacteriophage Q β Virus-like Particles. *Biochemistry* **48**, 11155–11157 (2009).
259. Candace Benjamin, O.B., Arezoo Shahrivarkevishahi, Jeremiah J. Gassensmith Chapter 11 - Virus like particles: fundamental concepts, biological interactions, and clinical applications. *Nanoparticles for Biomedical Applications, Elsevier*, 153-174 (2020).
260. Candace E. Benjamin, Z.C., Olivia R. Brohlin, Hamilton Lee, Arezoo Shahrivarkevishahi, Stefanie Boyd, Duane D. Winkler and Jeremiah J. Gassensmith Using FRET to measure the time it takes for a cell to destroy a virus. *Nanoscale* **12**, 9124-9132 (2020).
261. Duane E. Prasuhn Jr., P.S., Erica Strable, Steven Brown, Marianne Manchester, and M. G. Finn Plasma Clearance of Bacteriophage Q β Particles as a Function of Surface Charge. *J. Am. Chem. Soc.* **130**, 1328–1334 (2008).
262. Bingjie Hao, W.L., Sen Zhang, Ying Zhu, Yongjun Li, Aishun Ding and Xiaoyu Huang A facile PEG/thiol-functionalized nanographene oxide carrier with an appropriate glutathione-responsive switch. *Polym. Chem.* **11**, 2194-2204 (2020).
263. Guoyao Wu, Y.-Z.F., Sheng Yang, Joanne R. Lupton, Nancy D. Turner Glutathione Metabolism and Its Implications for Health. *The Journal of Nutrition* **134**, 489–492 (2004).
264. M. F. Ross, G.F.K., F. H. Blaikie, A. M. James, H. M. Cochemé, A. Filipovska, T. Da Ros, T. R. Hurd, R. A. J. Smith, and M. P. Murphy Lipophilic Triphenylphosphonium Cations as Tools in Mitochondrial Bioenergetics and Free Radical Biology. *Biochemistry (Moscow)* **70**, 222-230 (2005).
265. Tsu-Kung Lin, G.H., Aleksandra Muratovska, Frances H Blaikie, Paul S Brookes, Victor Darley-Usmar, Robin A J Smith, Michael P Murphy Specific modification of

- mitochondrial protein thiols in response to oxidative stress: a proteomics approach. *J. Biol. Chem.* **277**, 17048-17056 (2002).
266. Lee M. Booty, J.M.G., Filip Cvetko, Thomas Krieg, Richard C. Hartley, Michael P. Murphy Selective Disruption of Mitochondrial Thiol Redox State in Cells and In Vivo. *Cell Chemical Biology* **26**, 449-461 (2019).
 267. Wall, A. et al. One-pot thiol–amine bioconjugation to maleimides: simultaneous stabilisation and dual functionalisation. *Chemical Science* **11**, 11455-11460 (2020).
 268. Arianna Gennaria, J.W., Enrique Lallana, Nora Francini, Nicola Tirelli Thiol-based Michael-type addition. A systematic evaluation of its controlling factors. *Tetrahedron* **76**, 131637 (2020).
 269. Montserrat Marí, E.d.G., Cristina de Dios, Vicente Roca-Agüetas, Blanca Cucarull, Anna Tutusaus, Albert Morales and Anna Colell Mitochondrial Glutathione: Recent Insights and Role in Disease. *Antioxidants* **9**, 909 (2020).
 270. Mathew P. Robin, P.W., Anne B. Mabire, Jenny K. Kiviho, Jeffery E. Raymond, David M. Haddleton, and Rachel K. O'Reilly Conjugation-Induced Fluorescent Labeling of Proteins and Polymers Using Dithiomaleimides. *J. Am. Chem. Soc.* **135**, 2875-2878 (2013).
 271. Cowan, G.M.E.a.T.M. Glutathione as a Redox Biomarker in Mitochondrial Disease—Implications for Therapy. *J. Clin. Med.* **6**, 50 (2017).
 272. Yi, M.C. & Khosla, C. Thiol-Disulfide Exchange Reactions in the Mammalian Extracellular Environment. *Annu Rev Chem Biomol Eng* **7**, 197-222 (2016).
 273. Mark E. B. Smith, F.F.S., Chris P. Ryan, Lauren M. Tedaldi, Danai Papaioannou, Gabriel Waksman, Stephen Caddick, and James R. Baker Protein Modification, Bioconjugation, and Disulfide Bridging Using Bromomaleimides. *J. Am. Chem. Soc.* **132**, 1960-1965 (2010).
 274. Kneen M, F.J., Li Y, Verkman AS. Green fluorescent protein as a noninvasive intracellular pH indicator. *Biophys J.* **74**, 1591-1599 (1998).
 275. Zielonka, J. et al. Mitochondria-Targeted Triphenylphosphonium-Based Compounds: Syntheses, Mechanisms of Action, and Therapeutic and Diagnostic Applications. *Chemical Reviews* **117**, 10043-10120 (2017).
 276. Zhuo Chen, N.L., Luxi Chen, Jiyong Lee, Jeremiah J. Gassensmith Dual Functionalized Bacteriophage Q β as a Photocaged Drug Carrier. *Small* **12**, 4563-4571 (2016).
 277. Hong Chang, J.Z., Hui Wang, Jia Lv, and Yiyun Cheng A Combination of Guanidyl and Phenyl Groups on a Dendrimer Enables Efficient siRNA and DNA Delivery. *Biomacromolecules* **18**, 2371-2378 (2017).

278. Alessandro Laganà, D.V., Francesco Russo, Alfredo Pulvirenti, Rosalba Giugno, Carlo Maria Croce and Alfredo Ferro Computational Design of Artificial RNA Molecules for Gene Regulation. *RNA Bioinformatics* **1269**, 393-412 (2015).
279. Stacy L. Capehart, M.P.C., Jeff E. Glasgow, and Matthew B. Francis Controlled Integration of Gold Nanoparticles and Organic Fluorophores Using Synthetically Modified MS2 Viral Capsids. *J. Am. Chem. Soc.* **135**, 3011-3016 (2013).
280. Khvorova, A., Osborn, M.F. & Hassler, M.R. Taking charge of siRNA delivery. *Nature Biotechnology* **32**, 1197-1198 (2014).
281. Oiseth, S. & Aziz, M.S. Cancer immunotherapy: a brief review of the history, possibilities, and challenges ahead. *Journal of Cancer Metastasis and Treatment* **3**, 250 (2017).
282. Ventola, C.L. Cancer Immunotherapy, Part 1: Current Strategies and Agents. *P T* **42**, 375-383 (2017).
283. Zhang, Y., Zhang, G., Chen, L. & Li, Y. Modulation of the inflammatory tumor microenvironment: a new approach for photothermal-synergized cancer immunotherapy. *Nanomedicine* **14**, 2101-2104 (2019).
284. Muenst, S. et al. The immune system and cancer evasion strategies: therapeutic concepts. *Journal of internal medicine* **279**, 541-562 (2016).
285. Sambhi, M., Bagheri, L. & Szewczuk, M.R. Current Challenges in Cancer Immunotherapy: Multimodal Approaches to Improve Efficacy and Patient Response Rates. *Journal of Oncology* **2019**, 4508794 (2019).
286. Alatrash, G., Jakher, H., Stafford, P.D. & Mittendorf, E.A. Cancer immunotherapies, their safety and toxicity. *Expert opinion on drug safety* **12**, 631-645 (2013).
287. Waldman, A.D., Fritz, J.M. & Lenardo, M.J. A guide to cancer immunotherapy: from T cell basic science to clinical practice. *Nature Reviews Immunology* (2020).
288. Shofolawe-Bakare, O.T., Stokes, L.D., Hossain, M., Smith, A.E. & Werfel, T.A. Immunostimulatory biomaterials to boost tumor immunogenicity. *Biomaterials Science* (2020).
289. Ni, K. et al. A Nanoscale Metal–Organic Framework to Mediate Photodynamic Therapy and Deliver CpG Oligodeoxynucleotides to Enhance Antigen Presentation and Cancer Immunotherapy. *Angewandte Chemie International Edition* **59**, 1108-1112 (2020).

290. Song, H. et al. Injectable polypeptide hydrogel for dual-delivery of antigen and TLR3 agonist to modulate dendritic cells in vivo and enhance potent cytotoxic T-lymphocyte response against melanoma. *Biomaterials* **159**, 119-129 (2018).
291. Morishita, M., Takahashi, Y., Matsumoto, A., Nishikawa, M. & Takakura, Y. Exosome-based tumor antigens-adjuvant co-delivery utilizing genetically engineered tumor cell-derived exosomes with immunostimulatory CpG DNA. *Biomaterials* **111**, 55-65 (2016).
292. Park, J. et al. Combination delivery of TGF- β inhibitor and IL-2 by nanoscale liposomal polymeric gels enhances tumour immunotherapy. *Nat Mater* **11**, 895-905 (2012).
293. Manolova, V. et al. Nanoparticles target distinct dendritic cell populations according to their size. *Eur J Immunol* **38**, 1404-1413 (2008).
294. Shaobo Li, M.D., Raymond P. Welch, Yixin Ren, Dr. Christina M. Thompson, Prof. Ronald A. Smaldone, Prof. Jeremiah J. Gassensmith Template-Directed Synthesis of Porous and Protective Core-Shell Bionanoparticles. *Angewandte Chemie International Edition* **55**, 10691-10696 (2016).

BIOGRAPHICAL SKETCH

Arezoo Shahrivarkevishahi was born in Tehran, Iran. After graduating from high school in 2007, she entered Shiraz University in Shiraz, Iran where she received a Bachelor of Science with a major in Chemistry. During her bachelor's degree, she joined Dr. Hemmateenejad's research group to learn about chemometrics methods and worked on developing videometric assay to study kinetic behavior of different analytes. In 2012 she was accepted to an analytical chemistry master's program in Shiraz University as a top 1% (among more than 60000) participant. Her research focus in Dr. Hemmateenejad's lab concentrated on colorimetric assay development using metal-based composites for protein and antioxidant detection and determination. In 2016, Arezoo came to the United States and one year later she joined Dr. Jeremiah Gassensmith's lab at The University of Texas at Dallas (UTD) as a volunteer researcher. In June 2018 she entered the chemistry PhD program at UTD. In May 2021, she started a summer worker program at ligand binding assay group in Pfizer at Groton, CT where she closely worked with several clinical teams and projects. After her internship, in August 2021 she joined GC Therapeutic company in Cambridge, MA as an intern scientist to work on stem cell-based immunology projects. As of October of 2021, she published more than 12 papers in peer reviewed articles, including a first author paper in the Journal of the American Chemical Society (JACS). In October 2021, she accepted a position at Pfizer to pursue her interest in research development for clinical studies.

CURRICULUM VITAE

Arezoo Shahrivarkevishahi

Curriculum Vitae

Email: Arezoo.shahrivar@gmail.com

<https://www.linkedin.com/in/arezoo-shahrivarkevishahi-706671125/>

Education

Candidate for Doctor of Philosophy in Chemistry (Expected 2021)

University of Texas at Dallas, Richardson, TX, USA

Advisor: Professor Jeremiah. J. Gassensmith

Thesis Title: Chemically tuned virus like particles: from cancer therapy to targeted delivery

Master of Science in Chemistry (2014)

Shiraz University, Shiraz, Iran.

Advisor: Prof. Hemmateenejad

Bachelor of Science in Chemistry (2012)

Shiraz University, Shiraz, Iran.

Advisor: Prof. Hemmateenejad

Research Experiences

Scientist-Intern in GC Therapeutic, Cambridge, MA.

Aug. 2021-Current

- Intern-scientist: working on developing flow cytometry panel for programming STEM cells to different therapeutic relevant cells. Cellular characterization of produced cells using ELISA, different cellular and immunoassay.

Researcher at Ligand Binding Assay Lab at Pfizer, Groton, CT.

May 2021-Aug. 2021

- Associate researcher: study the affinity interaction of protein-drug and investigate their binding mechanism through protein biotinylation and investigating kinetic behavior using Octet and ELISA platforms.

Graduate Research Scientist (Doctor of Philosophy)

Aug. 2017-Nov

2021 University of Texas at Dallas, Department of Chemistry and Biochemistry

Advisor: Dr. Jeremiah J. Gassensmith

Graduate student researcher incorporating chemistry, biology, and immunology concepts/techniques on nano/biomaterials to fabricate systems with new and improved ability in biomedical applications as demonstrated in design and development of immunophotothermal virus based anti-tumor agent against primary-metastasis tumor, sustained release vaccine formulations against bacteria and melanoma cancer and developing intracellular protein and siRNA delivery systems. I characterized and assayed these formulations in vitro and in vivo through various immunological assays.

Graduate Research Assistant (M.S., Analytical Chemistry)

Aug.2012 to May

2014 Shiraz University, Department of Chemistry

Advisor: Prof. Bahram Hemmateenejad

- In Prof. Hemmateenejad group, I studied the capacity of metal-based composites for assay development to act as a superior sensitive method for bioanalytes such as protein and antioxidant detection and determination. I specifically applied the gold nanocluster and cationic cyanin dye for colorimetric measurement of protein. The assays showed a large range of response (pM- μ M) and were used for kidney disease diagnosis.

Undergraduate Research Assistant

Aug. 2008-May

2012 Shiraz University, Department of Chemistry

Advisor: Prof. Bahram Hemmateenejad- Dr. Fatemeh Shakeri-Shirazi

- Undergraduate researcher worked on designing a cost-effective and rapid method for the visual detection of analyte (kinetic and studies) based on the video-image analysis and chemoinformatic techniques on the partial least squares (PLS) and principal component analysis-artificial neural network (PC-ANN) models.

Publications

1. **Shahrivarkevishahi, A.**, Luzuriaga, M., Castro, F., Tumac, A., Brohlin, O., Wijesundara, Y., Gassensmith, J.J. Photothermal Phage: A Virus-based Photothermal Therapeutic Agent. *JACS* **2021**.
2. Jenica L Lumata, Darby Ball, **Arezo Shahrivarkevishahi**, Michael A Luzuriaga, Fabian C Herbert, Olivia Brohlin, Hamilton Lee, Laurel M Hagge, Sheena D'Arcy, Jeremiah J Gassensmith. Identification and physical characterization of a spontaneous mutation of the tobacco mosaic virus in the laboratory environment. *Scientific reports*. **2021**.11,10.
3. Luzuriaga, M. A.; Herbert, F. C.; Brohlin, O. R.; **Shahrivarkevishahi, A.**; Wijesundara, Y. H.; Veera, K.; Benjamin, C. E.; Popal, S.; Burton, M. D.; Ingersoll, M. A.; De Nisco, N. J.; Gassensmith, J. J.; "A Whole Cell Metal-Organic Framework Encapsulated Vaccine Against Septicemic UPEC Infection" *ACS Nano*, **2021**.
4. Michael A Luzuriaga, **Arezo Shahrivarkevishahi**, Fabian C Herbert, Yalini H Wijesundara, Jeremiah J Gassensmith. Biomaterials and nanomaterials for sustained release vaccine delivery. *Wiley Interdiscip. Rev. Nanomed. Nanobiotechnol.* **2021**.
5. **Shahrivarkevishahi, A.**, Tumac, A., Brohlin, O., Gassensmith, J.J. Endosomal escape and Intercellular siRNA delivery using glutathione sensitive virus like particle. *Submitted*. **2021**
6. Lee, H.; **Shahrivarkevishahi, A.**; Lumata, J. L.; Luzuriaga, M. A.; Hagge, L. M.; Benjamin, C.E.; Brohlin, O. R.; Parish, C. R.; Firouzi, H. R.; Nielsen, S. O.; Lumata, L. L.; Gassensmith, J.J., Supramolecular and biomacromolecular enhancement of metal-free magnetic resonance imaging contrast agents. *Chemical Science*, **2020**, 11, 2045-2050.
7. Herbert, F. C.; Brohlin, O. R.; Galbraith, T.; Benjamin, C. E.; Reyes, C. A.; Luzuriaga, M. A.;

- Shahrivarkevishahi, A.**; Gassensmith, J. J.; “Supramolecular Encapsulation of Small- Ultra Red Fluorescent Proteins in Virus-Like Nanoparticles for Non-Invasive In Vivo Imaging Agents” *Bioconjugate Chem.*, **2020**, 31 (5), pp 1529–1536.
8. Brohlin, O. R.; Benjamin, C. E.; **Shahrivarkevishahi, A.**; Gassensmith, J. J.; “Nanoparticles for Biomedical Applications: Chapter 11 - Virus like particles: fundamental concepts, biological interactions, and clinical applications” *Elsevier*, **2020**, 153-174.
 9. Benjamin, C.E.; Chen,Z.; Brohlin,O.R.; Lee, H; **Shahrivarkevishahi, A**; Boyd, S., Winkler, D; Gassensmith, J.J.; Using FRET to Measure the Time it Takes for a Cell to Destroy a Virus. *Nanoscale*, **2020**, 12, 9124-9132.
 10. Luzuriaga, M. A.; Welch, R. P.; Dharmarwardana, M.; Benjamin, C. E.; Li, S.;**Shahrivarkevishahi,A.**; Popal, S.; Tuong, L. H.; Creswell, C. T.; Gassensmith, J. J., Enhanced Stability and Controlled Delivery of MOF-Encapsulated Vaccines and Their Immunogenic Response In Vivo. *ACS applied materials & interfaces*, **2019**, 11, 9740–9746.
 11. Hemmateenejad, B.;* **Shahrivarkevishahi, A.**; Shakerizadeh-Shirazi, F., Reversible Photobleaching of Gold Nanoclusters: A Mechanistic Investigation. *The Journal of Physical Chemistry C*, **2016**, 120, 28215–28223.
 12. Hemmateenejad, B.; * **Shahrivarkevishahi, A.**; Shakerizadeh-Shirazi, F.; Rouhani, S.; Mohamadi-Gharaghani, F., A time-insensitive colorimetric sensor for the determination of total protein. *RSC Advances* **2016**, 6, 52026-52033.
 13. Hemmateenejad, B.; Shakerizadeh-Shirazi, F.; Heidari, S.; **Shahrivarkevishahi, A.**, Digital videometrics analysis for the kinetic determination of dopamine in the presence of ascorbic acid based on the formation of silver nanoparticles. *Analytical Methods*, **2015**, 7, 6318-6324.

Meeting and Conferences

The 2021 RSC poster conference (Virtual)	2021
2nd Annual Immune Modulation & Engineering Symposium (Virtual)	2020
ACS National Meeting, Orlando, FL.	2019
ACS National Meeting, San Diego, CA.	2019
ACS National Meeting, Boston, MA.	2018

Technical Proficiency

Techniques:

Flow Cytometry: Solid background and experience in the development of multi-parameter flow cytometry assays. Independently sets up assay-specific application settings and compensation matrices on a flow cytometer and monitors instrument and assay performance. Advanced knowledge of flow cytometry data analysis software (FlowJo).

Cell Characterization: Experience working with aseptic skills/technique for culturing wide range of cell lines including cancer cells (B6F10, 4T1, HeLa, etc.), immune cells, transfected cells (HEK293T/17, Vero-E6), and primary cells isolated from animal source (DCs, splenocyte, etc.) and

all immune cells including NK, T reg, Macrophages, DCs, Gamma Delta, etc. following best practices including subculturing, cell banking, cell harvest and processing.

Cell functional characterization assays (stimulation, suppression, viability, immunocytochemistry, proliferation and cytokine measurements)

Ligand Binding Assays: ELISA, Octet. *Imaging:* Laser confocal microscopy, EPI Fluorescence microscopy.

Protein and VLPs Composite Characterization: Circular Dichroism, Dynamic Light Scattering, Nanodrop, HPLC/FPLC, Fluorimeter, UV-Vis.

In vivo: Mice handling, tumor implantation, surgery, injection (subcutaneous, intramuscular, intravenous injection), bone marrow cell isolation, organ harvesting and single suspension.

Organic Synthesis: Chromatography methods, flash column, TLC, NMR, Analytical and preparative HPLC, mass spectroscopy.

Computer/ IT: E-Lab book Asana, E-Lab journal, FlowJo, Adobe Illustrator, Chemdraw, Chimera, TopSpin, Graph Pad, Origin, Image J, Image Lab, Microsoft Office.

TEACHING EXPERIENCE

- Undergraduate Research Mentor Sindhu Ponnam, The University of Texas at Dallas 2021-current
 - Project: Developing tumor vaccine based on sustained release of tumor lysate.
 - Undergraduate Student Research Mentor Abhinay Varma Adlooru, The University of Texas at Dallas 2020–current
 - Project: Enhancing immune checkpoint inhibitor efficiency using Immunophotothermal system
 - Undergraduate Student Research Mentor Alisia Tumac, The University of Texas at Dallas 2018-2020
 - Project: Design and development of intracellular delivery systems
 - Undergraduate Student Research Mentor Chayton T Creswell, The University of Texas at Dallas 2017-2018
 - Project: Virus like particle cellular cytosolic delivery using fusogenic and thermal liposomal formulations
 - Teaching Lab Lecturer- The University of Texas at Dallas 2018-2019
 - Teaching Lab Assistant- The University of Texas at Dallas 2018-2021
- Inorganic Chemistry Lab

